PRECIPITATION AND TRANSFORMATION OF NANOSTRUCTURED COPPER OXALATE AND COPPER/COBALT COMPOSITE PRECURSOR SYNTHESIS

THÈSE N^{O} 3083 (2004)

PRÉSENTÉE À LA FACULTÉ SCIENCES ET TECHNIQUES DE L'INGÉNIEUR

Institut des matériaux

SECTION DES MATÉRIAUX

ÉCOLE POLYTECHNIQUE FÉDÉRALE DE LAUSANNE

POUR L'OBTENTION DU GRADE DE DOCTEUR ÈS SCIENCES

PAR

Lucica Cristina SOARE

DEA de physique de la matière, Université Paul Sabatier, Toulouse, France
et de nationalité roumaine

acceptée sur proposition du jury:

Prof. H. Hofmann, directeur de thèse
Dr P. Bowen, rapporteur
Dr H. Cölfen, rapporteur
Prof. M. Pijolat, rapporteur
Prof. A. Renken, rapporteur

Lausanne, EPFL
2004

To my mother and my father

with gratitude… … …

Remerciements

Je tiens à remercier toutes les personnes qui ont contribué à la réalisation de ce travail, de prés ou de loin en particuliers:

Le ***Prof. Heinrich Hofmann***, mon directeur de thèse, le directeur du Laboratoire de Technologie des Poudres et initiateur de ce sujet, pour ses nombreux conseils et son intérêt tout au long de travail.

Le ***Dr. Paul Bowen***, pour son aide dans les moments clés de la thèse, les nombreuses discussions partagées, ses encouragements, sa patience, son aide pour la correction du manuscrit de thèse; il fut un chef et restera un ami; "*if you can't be good be careful*".

Le ***Dr. Jacques Lemaître***, pour son aide importante au début de ma thèse, son excellent enseignement scientifique et ses conseils.

Le ***Dr. Nathalie Jongen***, collègue de bureau et amie, qui a suivi de prés le début de ce travail de thèse.

Le ***Dr. Sandrine Rousseau*** pour son soutien et ses encouragements au long de la thèse et les analyses ICP.

Le ***Prof. Frank Kubel*** (*Wien, University of Technology*) - pour sa gentillesse et les nombreuses discussions sur la caractérisation des poudres par diffraction de rayons X, la détermination de la structure de l'oxalate de cuivre, et la visite d'une ville magnifique Wien.

Le ***Prof. A. Philippe Buffat*** (*Centre Interdépartemental de Microscopie Electronique - CIME Lausanne*), pour son aide dans un moment important de la thèse, pour les nombreuses heures qu'il m'a consacré pour les diffractogrammes TEM sur l'oxalate de cuivre, malgré les conditions difficiles d'observation. Je tiens à le remercier également pour l'opportunité d'accès au HRSEM.

Le ***Dr. Ollivier Pujol*** *(Centre Interdépartemental de Microscopie Electronique - CIME Lausanne)*, collègue de travail, je teins à le remercier pour toutes les discussions tout au long de ce travail et l'enseignement de la microscopie.

Mme. ***Daniel Laub*** (*Centre Interdépartemental de Microscopie Electronique - CIME Lausanne*), pour les superbes coupes qu'elle a réalisées ainsi que pour les diffractogrammes TEM sur les oxydes de cuivre et le cuivre métallique.

Les ***Prof. Michèle Pijolat*** et ***Dr. Francoise Valdivieso*** (*Sciences des Processus Industriels et Naturels - SPIN St-Etienne*), de m'avoir accueillie dans leur laboratoire, leurs excellentes explications scientifiques et la mise en œuvre du troisième chapitre de thèse.

Le ***Dr. Heinz Aminitsch*** (*Institute of Biophysics and X-ray Structure Research, Graz*), or "Planet Beam Time" pour la découverte du monde SAXS, son esprit et manière de travailler originale, pour la validation des mesures effectuées.

L'Office Fédéral de l'Education et de la Science pour son soutien financier projet COST 523 n° C90-0020 OFES: 20100-056643.99/1.

Mes étudiants de projet de semestre: ***Michael Siegfried***, ***Aude Hauert***, ***Alban Dubach***, pour leurs contributions à ce projet.

Je voudrais également remercier tous mes collègues du LTP pour la bonne ambiance et leur humeur spécifique.

Enfin je n'ai pas oublié mes amis, ***Sébastien Jiguet*** et ***Séverine Lamberet*** de m'avoir soutenue et encouragée dans les moments difficiles de la thèse, ma sœur ***Gabriela***, ***Frédéric Juillerat*** *et* ***Wolfgang Kerbe*** d'avoir eu la patience du corriger l'anglais du manuscrit, ***Ingrid Schneider***, ***Bernadette Müller*** *et* ***Petra Passuello*** avec qui j'ai partagé les vacances.

Summary

The aim of this thesis was to synthesise and control a nanostructured composite of copper/cobalt. Both the copper and cobalt oxalate exhibit a nanostructure. Attempts to produce nanocomposite particles in the size range of 10-70 nm were made via an oxalate co-precipitation route followed by the appropriate thermal treatment to finally obtain the metal nanocomposite. Much attention was focussed on the understanding of the copper oxalate precipitation and its further transformation into metal before the investigation of the co-precipitation system.

One major challenge of this thesis work was to achieve a better understanding of the copper oxalate precipitation mechanism. This was made by following kinetic parameters in order to shed light on the various steps of the precipitation from a supersaturated solution (nucleation, growth and aggregation of nanocrystals). Following the pH as a function of time and using the thermodynamic solubility data it was possible to propose a kinetic model of copper oxalate precipitation, with the co-precipitation of slight amounts (around 0.40% wt) of malachite ($CuCO_3 \cdot Cu(OH)_2$). The copper oxalate nanostructured particle growth mechanism, from the self-assembly of nanosized buildings blocks, was confirmed for intermediate precipitation times (1-15 minutes). Evidence for such organisation of the particles was shown by a combination of XRD diffraction, SEM and AFM measurements showing the presence of steps at the particle surface with a height that corresponds to a multiple of the mean crystallite size in that particular crystallographic orientation. Further investigations were performed for the early steps of the precipitation by SAXS but either the precipitated volume fraction was too low for detection of the particles or nucleation and growth kinetics were to fast (less than one second) to be followed. The TEM cross-section analyses showed a possible core-shell assembly mechanism. The core showed a random organisation of the crystallites with a size of around 25 nm, while the crystallite in the shell with a size of around 40 nm presented certain order along the 110 axis, particularly towards the particle surface. All these details provided the opportunity to propose a new and more detailed mechanism of the copper oxalate polycrystalline particle formation.

In order to master the conditions of the Cu/Cu oxalate decomposition, a good understanding of the simple copper oxalate decomposition was necessary. All along this thesis, much attention was paid to the transformation of the copper oxalate cubic particles into the metal. The objective was thus to conserve the particles cubic macrostructure morphology and their internal nanoscale spatial organisation. To this goal

two routes were investigated: a direct transformation and another, an indirect one, that required the formation of an oxide. Both the copper oxalate and the oxide showed an anisotropic behaviour during the transformation into the metal. It is shown experimentally that the anisotropy, nanostructure and inhomogeneity of the initial nanocrystallites of both the oxalate and the oxide have an important influence on the mechanism and evolution of transformation into the metal. The particle morphology was shown to be lost for a transformation yield of $\alpha>0.80$ in the case of the direct transformation from the oxalate whereas the morphology was kept up to the metallic state when passing via the oxide. A kinetic model was proposed for both systems using the method of the sudden change in temperature and pressure. The kinetics analysis did not permit a total understanding of the transformations studied, as several stages were shown to have complex and concurrently competing mechanisms. However, a geometrical model was proposed using the *ex-situ* analysis of the samples as a function of the reaction yield for both routes. For the initial stages of the copper oxide reduction under He/H_2 atmospheres, the kinetic analysis showed hydrogen dissociation as a rate-limiting step.

With a view to producing a cobalt/copper composite, preliminary experiments were carried out for the co-precipitation of the Co/Cu oxalate with different cationic ratios. Thermodynamic calculations showed the formation of the two solids was possible independent of the ratio Co/Cu. Experimentally, however a co-precipitation was obtained only for a ratio Co/Cu of 1, whereas for other ration only one single phase (either copper oxalate or cobalt oxalate) was formed. A second route was investigated using cobalt oxalate or cobalt oxide seeds. The amount of the cobalt detected by TEM in the precipitate using either the oxalate or from the oxide seeds was around 3%wt, which is lower than the value of 10%wt necessary to provide desired magnetic properties in the resulting precipitate. The exact nature and spatial distribution of the cobalt was not ascertained and further analysis of the nanostructure by TEM needs to be carried out to confirm the premise of the seed route.

This thesis has shown that it is possible to get to a deeper understanding of the kinetics and the mechanism of the copper oxalate precipitation using the appropriate techniques. The cubic macrostructure can be conserved from the initial CuO nanoparticles (13 nm) to metallic Cu (42 nm) by a controlled transformation in a reducing atmosphere. Preliminary experiments made on the possible formation of a Co/Cu composite via the use of the cobalt oxide seeds as heterogeneous nuclei for the copper oxalate precipitation seems most promising.

Version Abrégée

Le but de la thèse était de synthétiser et de contrôler la nanostructuration d'un composite métallique Co/Cu. Les deux oxalates de cobalt et cuivre montrant une nanostructure, avec crystallite de 10-70 nm. La production d'un nanocomposite de type "mosaïque" a été envisagée par la voie de la co-précipitation de ces deux oxalates, suivie par un traitement thermique approprié afin d'obtenir le nanocomposite métallique.

Un des points clé dans ce travaile de thèse était de comprendre le mécanisme de précipitation de l'oxalate de cuivre. Le suivi du pH en fonction du temps et l'utilisation des calcules de la solubilité ont ainsi permis de déterminer un modèle cinétique pour la précipitation de l'oxalate de cuivre. La précipitation de l'oxalate de cuivre entrain également une précipitation de malachite - hydroxycarbonate de cuivre ($CuCO_3 \cdot Cu(OH)_2$) estimée à environ 0.40% pds qui a une fort influence sur l'évolution du pH. D'autre part, le mécanisme de formation de l'oxalate de cuivre a été décrit par un auto-assemblage de nano "buildings blocks", confirmé dans ce travail par microscopie electronique effectuée pour des étapes intermédiaires de précipitation (1-15 minutes). L'auto-assemblage a été mis en évidence par la corrélation entre les analyses XRD, AFM et HRSEM. Les mesures AFM de la hauteur des "marches" à la surface des particules présentent le même ordre de grandeur que la taille calculée par XRD selon leur organisation cristallographique. Le SAXS constitue une méthode intéressante pour étudier les premières secondes de la réaction, cependant la fraction volumique de solide étant faible il est difficile de suivre *in-situ* les phénomènes de nucléation et de croissance. Il se peut également qu'ils se produisent pour des temps inférieurs à 1 second pour des sursaturations élève nécessaire pour accéder le domaine d'analyse SAXS. Les analyses de coupe TEM ont démontré pour l'oxalate de cuivre l'existence d'une structure "core-shell". Le cœur présente une organisation aléatoire des crystallites possédant une taille de 25 nm. Dans la couche externe, les cristallites deviennent plus organisés dans la direction 110 et leur taille augmentent jusqu'à 40 nm. Les détails qui découlent de ces observations de l'évolution de la précipitation de l'oxalate de cuivre nous ont ainsi amené à décrire son mécanisme de formation d'une manière plus appropriée.

Les conditions de décomposition ont été étudiées pour l'oxalate de cuivre, de morphologie cubique, vers le cuivre métallique avant la formation de l'oxalate mixte Co/Cu. L'objectif du présent travail est donc de parvenir à conserver la morphologie de l'état initial jusqu'à l'état final du métal. Les mécanismes de transformation directe de l'oxalate de cuivre vers le cuivre métallique et de transformation via la formation d'un oxyde ont été approfondis. L'oxalate de cuivre et l'oxyde de cuivre ont tous deux

montré un caractère anisotrope pendant la transformation,. Il est de fait que l'anisotropie de la nanostructure des particules et l'inhomogénéité ont tous une influence sur les mécanismes de transformation. Expérimentalement, il a été montré que pour le cas de la transformation directe de l'oxalate de cuivre vers le cuivre métallique, la morphologie cubique des particules est perdue pour une progression suffisante de la réaction (taux de transformation $\alpha > 0.80$). Par contre dans le cas de la transformation intermédiaire par l'oxyde de cuivre, la morphologie cubique est conservée jusqu'à l'état de métal. L'étude des cinétiques n'a pas permis de comprendre la transformation totale, du fait de la possibilité de cas complexes où plusieurs réactions consécutives peuvent avoir lieu. Cependant un modèle géométrique a été proposé tout en tenant compte des analyses ex-situ. Par ailleurs pour la transformation de l'oxyde de cuivre vers le cuivre métallique, sous atmosphère réductrice He / H_2, les analyses cinétiques mettent en évidence que la dissociation de l'hydrogène est un facteur limitant pour l'étape initiale de la transformation.

Pour la synthèse d'un composite cobalt/cuivre par la voie de la co-précipitation, plusieurs rapports Co/Cu ont été pris en compte. Les calculs thermodynamiques ont montré la formation de deux solides, était possible indépendamment du rapport Co/Cu. Cependant les expériences ont mis en évidence que la formation de deux solides avait lieu uniquement pour un rapport Co/Cu=1, sinon un seul composé peut précipiter. Une deuxième route pour la formation du composite consistait à utiliser des germes, soit d'oxalate, soit d'oxyde de cobalt. La quantité de cobalt présente dans les deux précipités a été évaluée par TEM à 3% pds, ce qui est inférieur à la valeur de 10% pds nécessaire pour obtenir les propriétés magnétiques souhaitées. La distribution du cobalt dans la matrice d'oxalate ou d'oxyde de cuivre reste à approfondir, par des études de coupe TEM.

Au cours de cette thèse il a ainsi été montré qu'il est possible de mettre en évidence la cinétique et le mécanisme de la précipitation de l'oxalate de cuivre métallique en utilisant les techniques appropriées. La macrostruture cubique initiale des nanoparticules de CuO (13 nm) a pu être conservé lors de la transformation contrôlée en cuivre métallique (42 nm) sous une atmosphère réductrice. Des expériences préliminaires effectuées quant à la possible formation d'un composite Co/Cu tout en utilisant des germes d'oxyde de cobalt pour la précipitation hétérogène de l'oxalate de cuivre semblent prometteuses.

Contents

Chapter 3: Transformation of copper oxalate into metallic copper particles

Chapter 4 . Co-precipitation

Chapter 5. Conclusions and Outlook

General Introduction

Granular magnetic materials that show giant magnetoresistance (GMR) have recently attracted a great deal of attention due to their potential application in magnetic data storage and reading. In the presence of a magnetic field these materials exhibit a large drop in resistivity. The (GMR) effect was first observed in Fe/Cr[1] multilayers and these materials are attractive for application in magnetoresistive devices, such as magnet recording head. At room temperature, the GMR effect can be as high as 65 % compared with only 2 or 3 % for bulk ferromagnetic materials. These increased magnetoresistive properties are attributed to the nanometric thickness between the magnetic (Fe) and non-magnetic conducting layers (Cr). The most common method of manufacturing such layered materials is by using sputtering deposition techniques, which takes place under ultra high vacuum (UHV) or an inert atmosphere (Ar). Although many theoretical and experimental studies have helped to elucidate many points, there are still open questions concerning the role of the local atomic order in GMR, mainly at the interface between magnetic and non magnetic regions (conducting matrix)[2]. If a GMR nanocomposite powder could be synthesised, other shapes with a 3D GMR structure and improved properties or new applications could be envisaged. A nanocomposite powder (3D GMR material) with a modulated size and distance between magnetic particles may help elucidate the interfacial interactions between the magnetic and non-magnetic materials. One route towards this goal of a powder nanocomposite is via chemical precipitation to produce 10nm magnetic particles (e.g. Co) dispersed in a conducting but non-magnetic matrix (Cu). These 10 nm particles need to be separated by more than 10 nm of the conducting matrix to produce the GMR effect. From geometric considerations for perfectly dispersed 10 nm cubic cobalt particles and an interparticle distance of 50 nm the relative volume fraction of cobalt in the composite would be 10%. At temperatures below 700°C the solubility of Co in Cu is less then 1.1 atomic % indicating that such a composite should be possible[3,4]. By the precipitation route it is possible to control the size of magnetic domains of cobalt. However the compounds of cobalt present a magnetic behaviour, which could induce a supplementary field on nanoparticles organisation like a mosaic nanostructured materials.

One of the main goals of the current thesis is to investigate the synthesis of a metallic Co/Cu nanocomposite powder via an aqueous precipitation route. Copper oxalate is known to precipitate as a nanostructured material – if cobalt can be incorporated into such a matrix either via coprecipitation or as nanosized seeds a GMR nanocomposite powder may result after transformation into the metallic state. Nanostructured copper oxalate has been studied in our laboratory over many years[5]. Detailed investigations were made on nanostructured particles of copper oxalate[6,7], which are mosaic particles made

up of organised nanosized crystals. Using organic additives the copper oxalate precipitation can be well controlled. The size and shape of both particles (a few microns) and the nanocrystals can be controlled. The particles shape can be varied from plates through cubes to rods. The shape control is linked to the anisoptropic crystal structure and specific interactions of certain crystal faces with cellulose derivatives. The anisotropy and well-controlled particle shape of the copper oxalate e.g. cubic particles also promise to be useful in a mesoscale organisation of particles towards the formation of macroscopic bodies. The previous work proposes a mechanism of the nanocrystals self-assembly but with only ex-situ analysis of the final precipitate.

Goals of thesis:

To better understand and confirm the proposed mechanism of copper oxalate to allow tailoring of the nanostructure to suit the synthesis of GMR composites. The precipitation is to be studied in a well-mixed mini-batch reactor allowing a finer control of experimental parameters (e.g. better mixing and temperature control). To this end kinetic studies of the precipitation mechanism following the evolution of the precipitating solution chemistry in conjunction with solubility calculations were made. Also reactions were stopped to investigate the structure of partially formed particles and attempts to follow the particle evolution by in-situ measurements using SAXS were made. Then the transformation of the copper oxalate into metallic the state was investigated before finally trying to incorporate Co via coprecipitation and by the use of Co oxalate or oxide seeds.

The thesis is divided into five sections:

The first section includes a literature survey where the state of the art is described in the different domains where this work is involved. An introduction to powder precipitation highlighting the need for a good understanding of each step in the building of precipitated particles. Highlighting in particular the various models proposed for the formation and self-organisation of nanostructured materials. Also there is a focus on the relationship between the initial nucleation step, molecular growth or growth by aggregation, with or without additives, and the influence of these early formation mechanisms on the mesoscale particles that may then be used to build higher order nanostructured materials. Then an accent was put on the thermal decomposition of the nanostructured oxalates and oxide materials. A review of work on the kinetics of the oxalate decomposition and the influence of different atmospheres on the structural evolution. The last part of the literature focuses on oxalate co-precipitation via aqueous routes. At the end of the chapter an overview is given of the "stage" in this field at the outset of this thesis.

In the second chapter the precipitation of copper oxalate in a well-mixed batch (mini-batch) reactor was studied. The advantage of a smaller volume (20ml) compared to the 250ml of previous studies, is a better control of mixing and kinetic parameters, resulting in more homogeneous precipitation

conditions. Previous work carried out in a fed batch reactor by a continuous addition of reactants was complicated to monitor and understand of the solution chemistry and particle growth. Monitoring of the solution composition as a function of time gives a direct link to the kinetics of precipitation. Using thermodynamic solubility data in conjunction with solution composition allows a possible mechanism hypothesis. Intermediate precipitate properties were investigated by stopping the reaction at various intermediate times and analysing the recovered precipitate using scanning and transmission electron microscopy, atomic force microscopy and X-ray diffraction. All these techniques help to elucidate a possible pathway to explain the precipitated particle architecture. At the end of this chapter we conclude on the precipitation mechanism and nanostructure control and characteristics is discussed in detail, important for the understanding of the next chapter where the copper oxalate precipitates are transformed into the metallic state.

In the third part of the thesis is focused on metallic copper synthesis. With the aim of conserving the morphology and the spatial organisation of metallic copper nanocrystals in particles by thermal treatment. In this case two pathways are possible, the direct transformation of the oxalate to metallic copper or via the copper oxide. The copper oxide was also synthesised from copper oxalate in air under isothermal conditions and then detailed kinetic studies carried out on the second stage of reduction to the metal. Thermogravimetric analysis was used to follow the reduction for both routes under controlled conditions of gas partial pressure (95.75% He and 4.25% H_2) and temperature. As a first step the overall evolution of the morphology and particle microstructure as a function of degree of reaction was first investigated. These experiments were then followed by a deeper study of the transformation mechanism on partially transformed reactants. These were characterised using different techniques such as XRD, HRSEM and cross section TEM. The chapter then concludes by focusing on the kinetic mechanism modelling and nanostructure control of copper metal particle synthesis by thermal treatment.

The fourth chapter will describe possible synthesis routes for the cobalt and copper composite. Attempts to co-precipitate Cu/Co mixed oxalates via an aqueous precipitation route were initially investigated. Solution solubility calculations were used to interpret the results. Preliminary experiments were made using cobalt oxalate nanoseeds from a precipitated cobalt oxalate nanostructured powder. Then the use of cobalt oxide nanoseeds with a suitable particle size distribution was attempted. The cobalt oxalate and oxide nanoparticles were envisioned as being heterogeneous nucleation sites for nanocrystals copper oxalate growth. An overview of the two approaches is described and future experiments suggested.
Finally in the fifth chapter the general conclusions and possible avenues for the continuation of this work are presented.

Chapter 1. Literature - State of the Art and Aim of the Work

1.1. Introduction:

The literature review will be presented in two parts. The first section deals with particle precipitation and the control of the particle nanostructure. More precisely, one will focus on the earlier stages of precipitation - nucleation, before treating the different types of growth mechanism for nanocrystals attachment, and the possible driving forces that control the building of particles from nanosized units. Afterwards, the second part constitutes an overview of literature the focusing on the thermal decomposition of oxalates, including the intensive and extensive parameters that control the transformation into metallic copper. Each part of this literature review will end with a short conclusion trying to give a general outlook of the theoretical knowledge and experimental limitations at this moment.

1. 2. Synthesis of oxalates by aqueous routes

1. 2. 1. Precipitation and Nanostructured materials

The precipitation process is an interesting method meant to control particle size, morphology and chemical composition. Precipitation from solution often involves a nucleation and growth process. Nucleation might be described as the birth of new crystals, while crystal growth is the growth of existing crystals to larger sizes by various mechanisms like molecular attachment or agglomeration. Preparation of colloidal particles by aqueous routes can be controlled by varying the experimental conditions, like reactant concentration, temperature, ageing time, agitation, mixing, additions of surfactants. Many examples of studies with well-controlled precipitation of particles with sizes ranging from nanometre to millimetres[8- 5, 17- 20, 31, 39 - 41] can be found in the literature.

The understanding of nucleation from solution is one of the most challenging problems in precipitation chemistry. For the analysis of fast precipitation reactions (induction time in the order of milliseconds) only a few techniques are available for the analysis. For many groups of research the challenge is to follow, within nanoseconds, the very first start of nucleation and to identity the forces, which control the growth process leading to particles with different nanostructures.

An important goal is to propose a possible mechanism for particle precipitation that takes into account all the phenomena occurring in the precipitation system and, by using this knowledge, to model

other chemical precipitation systems. This could finally allow the design specific particles for specific applications.

The subject of this thesis deals with precipitation via the oxalate route, because oxalates present the particularity of showing a low solubility in aqueous media. It has been reported in the literature that several oxalates as well as mixed oxalates such as NiMn[10] obtained via the precipitation route show nanostructures sometimes with a long-range ordering between nanocrystals such as copper oxalate[6], cobalt oxalate[9].

More specifically, the present work will focus on a nanostructured material built up by the self-organisation of copper oxalate polycrystalline particles[6]. In this case the aggregates consist of crystallographically aligned subunits. It has also been shown that the presence of an organic additive, i.e. the hydroxyropylmethylcellulose (HPMC), induces the formation of different particle and nanocrystallite shapes[2] and has an important influence on every stage of the precipitation. The surface energy and the hydrophilic/hydrophobic nature of nanocrystallites are supposed to govern the self-organisation process of nanostructured copper oxalate. This material will be studied in more detail especially for a better understanding of the earlier stage of precipitation, the formation of nuclei, their growth until a certain size and the forces that cause the nanocrystallite to finally build a long-range ordered material.

Cobalt oxalate nanostructured materials precipitated in aqueous media show a core/shell structure with an amorphous core and a polycrystalline shell[9]. O. Pujol *et al* have described an important correlation between the particles evolution and the chemistry of the solution. It has been shown that the particle evolution is linked to the solution chemistry, function of the pH behaviour, and a possible mechanism for the nanoparticles aggregation is proposed. One has to mention that the mechanism of particles assembly is a result of detailed microscopy analysis for different stages of reaction, using cryogenic methods.

Finally, as an example of a mixed oxalate, the nickel manganese oxalate has been synthesised by co-precipitation from a nitrate precursors and ammonium oxalate in an aqueous medium. After a thermal treatment this material also showed a nanostructure[10]. This nanostructure may come from either the fact that the initial powder is made up of nanounits, and each one transforming, with a high memory of the initial organisation, or it could be due to the growth mechanism of these initial nanounits during the transformation.

To achieve a high degree of control of specific particle precipitation, a systematic investigation is needed: first, one should identify the solute species that are involved in the solid phase formation and a second one has to understand and gain control over the various stages from the initial nucleation to the final particles.

1.2.2. Nucleation

A. Theory

The precipitation of a solid phase from solution is initiated by the creation of a supersaturation, whereby there is an excess of solute compound to solvent compared to the equilibrium state. The simplest and the most common methods of obtaining supersaturated solutions is by cooling, solvent evaporation, or chemical reaction, or the addition of third component to change the solubility of the solute. Cooling is a simple method employed where there is an increase in solubility with increasing temperature. Solvent evaporation results in an increase in the solute concentration as solvent is removed, until the solution is supersaturated. Chemical reaction involves the addition of soluble reagent to the solution; these may react and form a product of lower solubility, by changing the pH of the system or by altering the solvent composition.

Nucleation is the first stage of solid nanoparticles formation. This first burst of solid nanoparticles is the most complex process of solid state chemistry and the most poorly understood.

Three types of nucleation have been described in the literature: *primary* homogeneous nucleation, *primary* heterogeneous nucleation and *secondary* nucleation.

The homogeneous nucleation for example of two salts, starts in a system free of any impurities or foreign substance such as a substrate that could help starting the nucleation process.

The classical theory of nucleation considers the spontaneous formation of spherical molecular clusters with size dependent free energies that continue growing only for larger values than a threshold value of critical size. Early papers described the formation of monodisperse colloids using LaMer's[11] model according to which all particles must nucleate at the same time and grow up to the same size by diffusion of species from the solution towards the particles surface. If it is assumed that the clusters are spherical, an equation can be written that gives the change in Gibbs free energy, ΔG required forming a cluster of a given radius[24].

$$\Delta G = 4\pi r^2\sigma - \left(4\pi r^3 \big/ 3V_m\right) RT\ln(S) = \Delta G_s + \Delta G_v \qquad \textit{Eq 1}$$

where r is the cluster radius, σ is the solid-liquid interfacial tension, V_m is the specific volume of a solute molecule, and S is the supersaturation (supersaturation is defined in equation 1 by $S = C/C_{eq}$ where C is the concentration at a time t and C_{eq} is the concentration at equilibrium). The first term on the right hand side of equation 1, is the change in Gibbs free energy necessary to form the surface of a cluster, while the second term is the change in Gibbs free energy for forming the cluster's volume. In particular, the formation of solid particles implies a serie of changes in solubility of the precipitated solute as well as the free energies of activation and the structural composition.

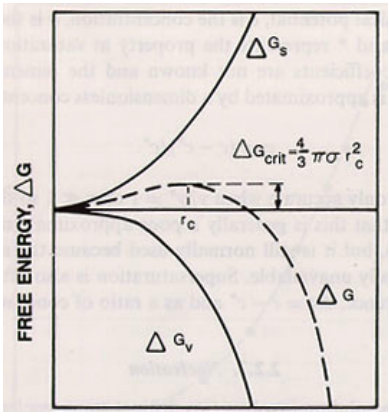

Figure 1: Gibbs free energy as a function of clusters radius[24]

The plot in Figure 1 shows the variation of ΔG as a function of the clusters size. Due to the competition occurring between the negative bulk term and the positive surface term, the free energy exhibits a maximum for supersaturated solutions (S>1). The maximum free energy occurs at a critical nucleus size given by equation (2). For smaller cluster sizes than (r_c), the free energy is positive and these clusters will dissolve, since all spontaneous processes requires a negative value of Gibbs free energy. Above r_c the crystals will grow.

$$r_c = 3V_m\sigma / RT \ln(S) \qquad \textit{Eq 2}$$

For a fixed temperature, the critical nucleus size decreases with supersaturation and increases with interfacial energy. The maximum free energy is the energetic barrier inhibiting the growth of a new phase. When a suspension of particles is suddenly quenched to a temperature below the particles solubility, clusters must grow to size larger then r_c to be thermodynamically stable. This r_c is at about 7.5 nm in the case of calcium carbonate with an interfacial tension of 47mN/m [(12)]. At low values of surface energy and large supersaturation levels, the critical size, r_c, approaches the size of an individual molecule[14].

A supersaturated solution is metastable in the region in which nucleation and growth occurs. Another property of supersaturated solutions, related to the metastable zone, is the nucleation induction time. The nucleation induction time is the time necessary for a given supersaturated solution to nucleate if left under constant conditions. The higher the supersaturation, the shorter the nucleation induction times[13]. This time can be thought of, as the time required for a critical sized cluster to form.

The nucleation described above is known as primary nucleation and is driven by the thermodynamics of the phase separation processes. Primary nucleation can be divided into the primary homogeneous nucleation and the primary heterogeneous nucleation.

Heterogeneous nucleation is often met in precipitation and takes place in the presence of solid surfaces other than the solute (dust, dirt or the container walls). These foreign uncontrolled surfaces may play an important role in the kinetic steps of precipitation, such as growth rate of nuclei, growth of particles; thus influencing the properties of the final product. This type of precipitation only takes place if

the foreign particles provide a certain gain in free energy when forming a precipitate surface[14]. For heterogeneous primary nucleation to take place, the free energy barrier (critical cluster size) must be lower than the primary homogeneous nucleation. So heterogeneous nucleation tends to take place at significantly lower supersaturation than homogenous nucleation and so the width of the metastable phase is often reduced[15].

Secondary nucleation can be defined as "nucleation, which takes place only because of the prior presence of crystals of the material being crystalized"[24]. This process develops in the presence of solid particles of the same nature as the solute and it can be the origin of different sources. Furthermore the secondary nucleation can be divided in three classes: apparent, true and contact secondary nucleation.

- ✓ The apparent secondary nucleation takes place when the nuclei are brought into the system along with inoculating crystals (seeding);
- ✓ The true secondary nucleation happened where new nuclei are formed due to crystal-solution interactions.
- ✓ The contact secondary nucleation, nuclei are formed by collisions between crystals or between crystals and the crystallizer[24].

The supersaturation, the mass nanoparticles density and the fluid mechanism interaction influence secondary nucleation. At this stage the particles may have a large hydrodynamic shear given by the motion, and a high contact frequency on the number of nanoparticles resulting from contact secondary nucleation.

B. Experimental results

The secondary nucleation process is found to be an important process in systems such as barium titanate or iron oxide for instance [16,17]. Precipitation of barium titanate from $TiCl_4$ and $BaCl_2$, at 90°C, and high supersaturation, involved a rapid primary nucleation. Lowering supersaturation below a critical value at this point induced further growth of the nucleus. The rate of secondary nucleation is then proportional to the total available surface area. The particles growth it can increase quickly after an initial period of time, like a self-catalytic process[16]. This is considered as a standard example because no phases with different solubility that can change the ions species evolutions in solution are involved such as in the case of iron oxide for example.

The precipitation of spherical hematite particles is obtained by ageing a 0.02 mol/L solution of $FeCl_3$ at 100°C for 2 days. This precipitate is constituted of initially spherical α-Fe_2O_3[17] particles in the akagamaite phase, which redissolves then, acting as a source of ferric cations, for the precipitation of final hematite particles. The initial precipitation of a metastable phase has often been observed, and is due to the creation of desequilibrium (supersaturation) in the solution with respect to several precipitating phases at the same time as schematically show in Figure 2. Usually, the more disordered phases, which are more soluble, precipitate first due to their lower surface energy. However, the system remains supersaturated

with respect to the more insoluble phases, which grows at the expense of the dissolved or metastable phases. The final precipitate can grow on the "metastable" phase as an example of secondary nucleation.

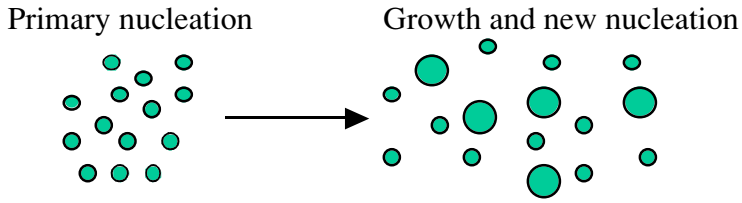

Figure 2: Schematic representation of the formation mechanism of α-Fe_2O_4 particles involved in the first stage of nucleation, secondary nucleation and growth

The early stages of the precipitation - nucleation process is thus an important period and is poorly comprehended because of the difficulties of monitoring small changes in 10 nm nuclei particles, often at low number density. The techniques available to catch the early stages of precipitation are Dynamic Light Scattering (DLS), Small Angle X- rays Scattering (SAXS) or Small Angle Neutron Scattering (SANS). The SAXS technique yields information about size and shape distribution from scattered X-rays, as well as other structure-related parameters. This technique provides information on particles dimension between ten and a few thousand angstroms and also depends on the solid/liquid volume ratio. The scattered intensity I (q) is given by [18]

$$I(q) = \int_{R_{\min}}^{R_{\max}} N(R) I_0(qR) dR \qquad \text{Eq 3}$$

where $I_0(qR)$ is the form factor of a sphere of radius R and N(R) is the number density of particles (as a function of the radius R), in a range between R_{min} and R_{max}. This method has been used to explain several precipitation steps with a resolution in the nanometre and milliseconds ranges.

SAXS was successfully used in the precipitation process of zinc oxide from zinc acetate and absolute ethanol[19]. The formation kinetics of colloidal particles was analysed under isothermal conditions at 40°C. Zinc oxide is a model system for studying controlled crystallisation processes, because only one crystalline phase is observed. Figure 3 a) shows the *in-situ* time evolution of the SAXS intensity, I(q), versus the modulus of the scattering vector, q, logarithmic scale, measured during the hydrolysis process at 40°C. The evolution of the shape of SAXS curves with the reaction shows two distinct domains. During the initial stage of particle formation up to 30 minutes, the SAXS intensity is nearly independent of the scattering vector in the range of large q due to fluctuations in the electronic density of the solutions that contains dissociated reaction species. After 30 minutes an increase in the scattering vector intensity with an intermediate q-range is apparent. This contribution becomes more important as time increases, showing the sensitivity of SAXS to the precipitation process of system like ZnO[19]. By deconvolution of experimental curves using equation (3), two main stages can be seen in Figure 3 b. During the first 30 minutes a continuous formation of 2 nm clusters is observed. The number of these particles increases with the reaction time, while their size remains constant. During the second stage, particles with a size of about

6 nm are formed, while the number of the 2 nm ones decrease. Initial nucleation and growth provide a continuous increase of the primary particles, meaning that the aggregation rate is lower than the rate of nanoparticles formation. Then, agglomeration of the 2 nm primary particles dominates as the nucleation rate decreases with decreasing ZnO species in solution.

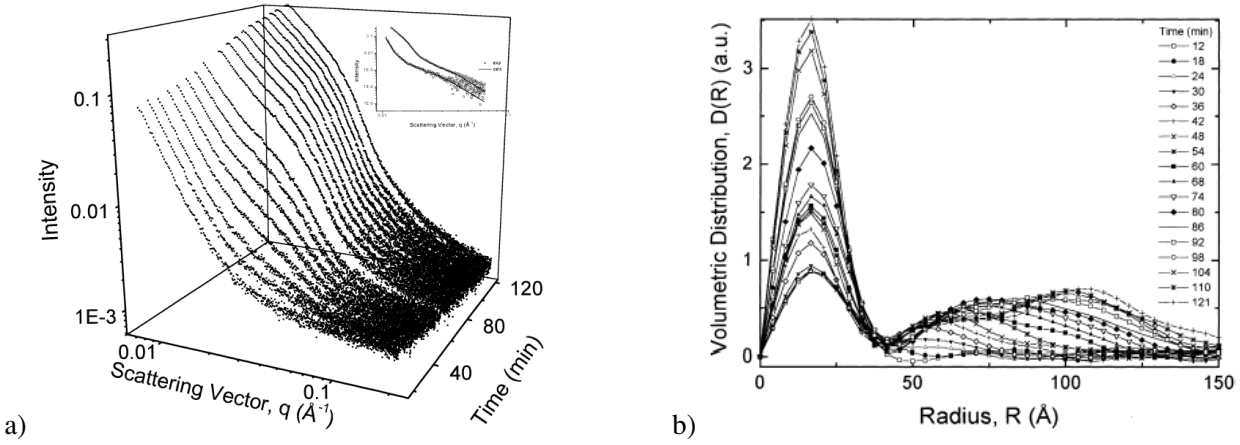

Figure 3: a) SAXS intensity as a function of the scattering vector q, and time of reaction; b) Volume distribution as a function of particles radius[19]

Another example of SAXS measurements, used to elucidate the particle formation mechanisms has been proposed for oxy-hydroxide iron[20]. Colloidal particles prepared from ferric chloride with or without urea, were aged at different temperatures and investigated by SAXS and optical transmittance. The particles showed a prolate ellipsoid morphology, which changed as a function of both the urea amount and the induction time for the observation of the first precipitates. In the absence of urea, the aspect ratio of particles is 5 with an induction time of about 150s, at 60°C, and this aspect ratio increases to 80 at 80°C. In the presence of urea the aspect ratio of the particles decreases. This difference in the growth process is frequently attributed to limited hydrolysis due to the presence of complexing anions, by a rapid exchange of chloride and hydroxyl ions in polymer complexes. This phenomenon occurs by increasing the amount of OH^- in solution due to urea decomposition. A lateral growth takes place, which reduces the aspect ratio of the particles. From SAXS measurement of the iron oxide precipitates, with or without urea, it was possible to establish the influence on particle growth. Without urea the particle morphology was cigar-shaped and with urea it changed to ribbons. The size and the aspect ratio of nanocrystallites are controlled by the conditions of hydrolysis[20] and urea concentration. Another method to detect the initial stage of precipitation has been using DLS (dynamic light scattering) as demonstrated the *in-situ* study of zirconia with a size detection limit larger than 5 nm[21].

The stage of cluster formation with sizes approaching the atomistic scale can be followed by scanning the adsorption along an ultracentrifuge cell, using analytical ultracentrifugation (AUC)[22]. The adsorption is transformed into particle size using the Mie theory. The wavelength of adsorption depends on the concentration and size of nanoparticles in the suspension. AUC seems to be an excellent and rapid

tool for the study with almost an atomic resolution of particles with radii less then 1 nm, as it was demonstrated for materials like ZnO, Pt[22], Au or CdS. After the nucleation steps, nuclei can grow by different mechanisms, which will be described in the next section.

1.2.3. Particle Growth

When a nucleus is formed, it is the smallest size crystalline entity that can exist under given set of conditions. Crystal growth involves the transport of dissolved species to and from the surface of a crystal inducing various chemical reactions to occur at this surface. The latter includes adsorption, ion exchange, dehydration of ions, formation of two-dimensional nuclei on the surface, diffusion along the surface and ion pair formation. The growth rate is limited by the slowest step within a whole chain of processes and the nature of the rate-limiting step is usually not known. Crystal growth is linked to the thermodynamics of the crystal chemistry and the factors that control the growth rate.

The total free energy of a crystal is the sum of the free energy associated with its volume, surface, edge and corners. The relative contribution of the surface free energy decreases in proportion to the crystal size. For a crystal at constant volume, the equilibrium shape will occur for the minimum value of total surface energy. Growth rates often exhibit different dependence as a function of surface characteristics. Two processes that exert a decisive influence during the growth of crystals from solution are mass transport from solution to the crystal surface (by volume diffusion or convection or a combination of both mechanisms), and incorporation of material into the crystal lattice through surface integration. The boundaries between the regions in which growth is controlled by any of these mechanisms can be specified by determining the set of values of S and r for which the mechanism on either side of the boundary are equally important.

The crystal growth process can be described at several different levels of magnification. Various theories have evolved to represent the processes taking place at these different size scales: molecular (nanometric level), microscopic and macroscopic scale.

- ✓ At the *molecular* level, the " growth units" are envisaged to attach themselves to the crystal surface, diffuse over this surface and eventually either integrate into the lattice at an energetically favourable site or return to the fluid phase.
- ✓ At the *microscopic* level, surface layers or "step bunches" are often observed. These are many hundreds of atomic dimensions high and are made up of groups of smaller steps that become bunched together.
- ✓ At the *macroscopic* level, effects of transport limitations on growth rate can be obtained. A low supersaturation in solution can influence the surface profiles and cause instabilities in the growth process. All of these processes have a high influence on particle morphology and size at the macroscopic scale.

The structure of the crystal/solution interface imposes constraints on the mechanism by which a crystal can grow. In the literature different kinds of crystals growth as a function of supersaturation and the surface nucleation are mentioned [13]. When the surface nucleation is fast each layer of the crystal is the result of the intergrowth from many individual surface nuclei. A "polynuclear" growth model can describe this rate of crystal growth. These new layers are produced by a crystal dislocation, which is a continuous source of step and kink sites. At a low values of the supersaturation screw dislocation growth is more relevant. In this case the growth rate for screw dislocations depends on the shape of the growth spiral. A summary of mathematical expressions for the growth mechanisms is presented in Table 1[14].

Table 1: Effect of supersaturation and particles size on the crystal growth rates for various types of growth mechanism [14]

Growth mechanism	Supersaturation function f(S)
Monosurface nucleation	$\text{Exp } (-\Delta G^{s}_{max}/k_B T)$
Mono/poly crossover point	S - 1
Polysurface nucleation	$(S-1)^{2/3}\exp(-\Delta G^{s}_{max}/k_B T)$
Screw dislocation	$(S^2/S_1)\tanh(S_1/S)$
Bulk diffusion	S - 1

In order to determine the controlling growth mechanism in a particular case, the point representing the initial supersaturation of the system and the final average crystal size can be calculated from[13]:

$$r = \left[V_m \left(c_0 - c_{eq} \right) / k_B N \right]^{1/3} \qquad Eq\ 4$$

where V_m – is the molecular volume, c_0 – is the initial concentration, c_{eq} the equilibrium concentration, k_B the Boltzamnn constant, N_A-the Avogadro number.

Equation 4 is plotted in Figure 5 as a consequence of different types of growth processes.

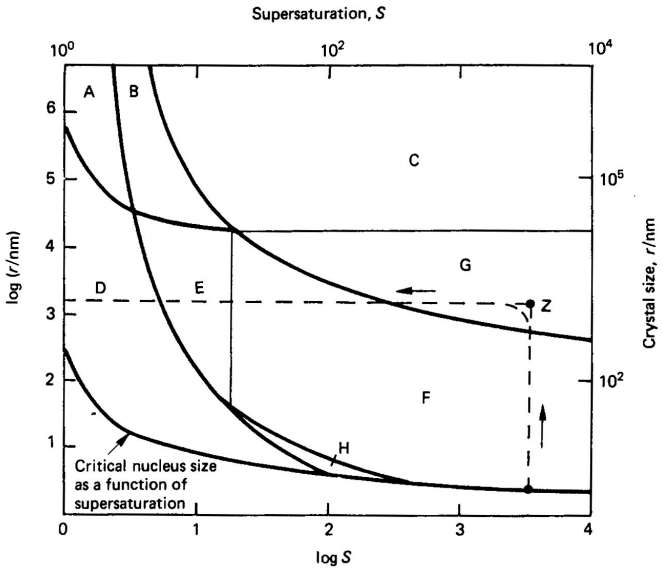

Figure 4: Precipitation map for $BaSO_4$. Controlling growth mechanism in the individual regions are: A - mononuclear or convection, B - polynuclear or convection, C - convection, D - mononuclear or screw dislocation, E - polynuclear or screw dislocation, F polynuclear, G diffusion, H - mononuclear[24]

Point Z in Figure 4 is located in the region corresponding to an arbitrary initial supersaturation. The dotted line represents the "life history" of the crystals during their growth; the crystals moving along this path in the direction of the arrow. Very small crystals are formed in the beginning of precipitation and start growing. Although their size rapidly increases, supersaturation remains almost constant because the mass of solute deposited on the crystals is very small. A line almost parallel to the size axis therefore represents the initial portion of the life history. With increasing the crystal size, the mass deposited on the crystals increases and the supersaturation begins to fall. In this region, the precipitation process is represented by a curve. In the last stage of precipitation supersaturation decreases to its final value by the crystal size change little, as here a large amount of mass is required to produce even a small increase in crystal size. Therefore in this final stage the life history curve is almost parallel to the supersaturation axis.
During the course of their growth, crystals pass through a number of regions representing different controlling mechanisms. In the case of $BaSO_4$, growth is initially controlled by the mononuclear mechanism and then passes through polynuclear, diffusion, and polynuclear again and finally screw dislocation control. For the process as a whole, the dominating mechanism is the one that controls the region where the major part of the mass deposition takes place and where the crystals remain for most of their life history. This corresponds to the part of the life history curve where curvature is the greatest and close to point Z; in this case the region is characterised by a diffusion-controlled mechanism[24].
From the above it can be understood that during growth, several mechanisms may combine to control the overall process.

The kinetics of crystal' growth strongly depends on the structure of the material, the properties of the solution, and the nature of the interface between crystals and the surrounding solution.

In any precipitation system the two main mechanisms for size enlargement are growth, (by which the deposition of ionic or molecular species on the crystal surfaces is meant) and aggregation, (the process by which crystals collide, adhere to each other, and form new stable particles). Growth by molecular attachment has been well studied on macroscopic crystals larger than 100 µm and the various mechanisms are known in detail[13,14,15,24]. Growth by agglomeration has been discussed for many years but over the last 20 years, as equipment has allowed a better discrimination, the structure of micron sized particles, and their growth by agglomeration has been more frequently identified as a dominant mechanism. The following sections discuss the various aspects of particle growth particularly related to nanostructured particles. Specific examples will be used, many more can be found in the literature. Many are discussed and described in a recent review[23].

A. Growth by molecular attachment

A detailed understanding of the growth behaviour is essential for a fine control of particle properties (size, distribution and morphology). The growth by molecular attachment implies a critical supersaturation, leading to nucleation. The resulting nucleus then grows uniformly by diffusion of solutes toward the particle surfaces until a stable size is attained. Particle growth has typically been thought to occur atom-by-atom addition to an inorganic or organic template from solvated species or by dissolution of unstable phases (small particles or metastable polymorphs that are the result of a rapid nucleation process (see section 1.2.2. B). The particle growth process involves the incorporation of grow units into the crystal lattice. These grow units can be either molecules, atoms, or ions depending on the type of surfaces and the type of growing particle. These growth units must find their way to an appropriate site on the particle surface where it can then be incorporated into the particle. A possible surface structure and pathway for a growing particle is shown in Figure 5.

a) 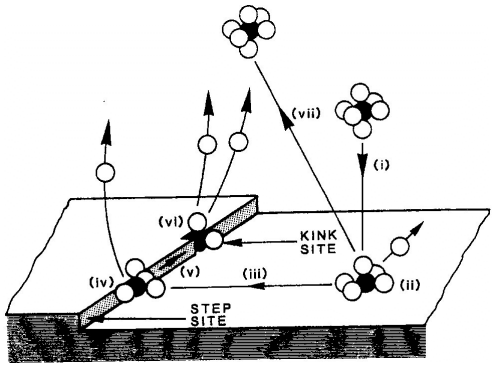

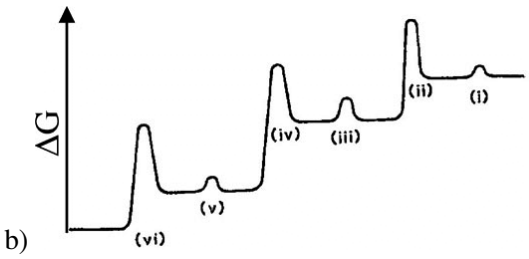

Figure 5: Energetic evolution of particle growth from solution: a) movements of the solvated solute molecules; b) corresponding energy changes for each step evolution[13]

During the molecular attachment, three types of surfaces sites are known where the atoms (or growth units) can be integrated into the particle structure. The first type of site is a flat surface, which is atomically smooth. If a growth unit attempts to become incorporated at this site (figure 5a_ii), it can bond only in one place. The second site is known as a step (figure 5a_iv), provides two places for the growth unit to bond to the particle, while the third site, known as a kink (figure 5a_vi), provides three places in which the growth unit can bond. These steps of attachment can be described by different energy levels and barriers (Figure 5b). The first energy level is the molecular transport from the bulk solution to the particle surface (figure 5b_i), then the adsorption on the particle surface (figure 5b_ii) or return to solution (figure 5a_vii). This step is characterised by a relatively high-energy barrier given by the single "bond" with the nearest neighbour. The second type involves diffusion of the atoms (figure 5a_iii) along the surface and their further incorporation into the lattice of a step (figure 5a_iv). This phase involves a low energy transfer on growth unit attachment. The third type, kinks, involve diffusion along a step (figure 5 a_v) and then combination into the lattice of the step (figure 5 a_vi). In this part the energy to attach decrease and the free energy of the system also decrease (figure 5 b_vi). Diffusion of solvent molecules away from the crystal surface released as a solute molecule becomes incorporated may limit the diffusion of the new solvated solute toward the crystal surface and thus limit the growth rate. In summary the energetic analysis of this process shows that the most favourable spot on the surface at which growth unit can incorporate into the lattice is at “kink” sites as illustrated in Figure 5. The concentration of such sites on the surface is determined by the “entropic factor”

$$\varepsilon = {}^{4\omega}\!/_{kT} \qquad \textit{Eq 5}$$

where ω represent the energy gain for the formation of a bond between a solid and a fluid phase at the boundary and is given by:

$$\omega = 0.5\phi_{ss} + 0.5\phi_{ff} - \phi_{sf} \qquad \textit{Eq 6}$$

where ϕ_{ss}, ϕ_{ff} , ϕ_{sf} are the potential energies of interaction between the growth units in the solid, in the fluid and between the two phases respectively.

If $\varepsilon < 3.2$ the particle surface is rough at the molecular scale and contain numerous kink sites. If $3.2 < \varepsilon < 4.0$ the particle surface is smoother and better defined. When $\varepsilon > 4$ the surface is smooth at the molecular level and the particle can only grow if steps are present on the surface[24].

This model of molecular attachment of ionic species can be extrapolated to the block units of growth on different types of surface (smooth or rough).

It should be noted that some of the processes (i) to (vii) occur in series but some occur in parallel so that not all stages are necessarily involved in the growth of a chosen material. Practically for crystal growth it is important to know which process is determinant for the growth rate. If, however, the processes take place in series, as is the case of bulk diffusion followed by surface reaction, the slower participating mechanism thus controls the overall rate. These features can be illustrated for particle growth in a closed batch system in which the solute concentration decreases as growth proceeds (see Figure 6)[14]. For a concentration c_C, the reaction rate is high as the concentration is high and the slower diffusion rate dominates growth. When the concentration reaches c_B the surface reaction becomes the controlling mechanism because both reaction processes are slower than diffusion. In the region located between c_B and c_A, the nucleation mechanism is the faster of the two surface processes and so is the controlling process. Finally for concentrations lower than c_A the screw dislocation mechanism becomes the controlling and, under these conditions, results in the fastest growth. The overall growth rate will thus follow the solid curve in Figure 6.

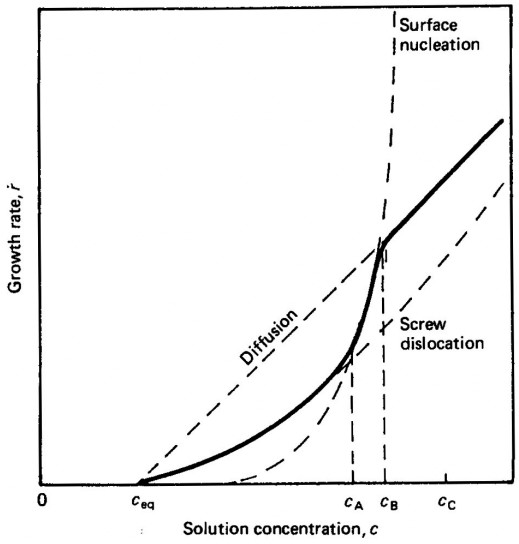

Figure 6: Growth rate of a particle in a closed system with decreasing supersaturation as a function of the solution concentration (24)

A particle will grow until enough material is removed from solution, that supersaturation is relieved and equilibrium is reached.

The smallest faces on a growing crystal are the fastest growing faces, while the largest faces are the slower. The fast-growing faces grow so rapidly that they effectively disappear on the particle. Impurities often change the habit and morphology of particles through specific interactions with particular

surfaces, thus retarding the growth rate of these faces. The rapid kinetics associated with nucleation, growth and agglomeration, for high supersaturation, sometimes necessitates studies under different conditions, to identify some of these growth factors. This is often necessary to understand the growth of nanostructured particles. Several methods can be used to that purpose, like by decreasing the solubility rate, or by cooling, but they do not always produce the same type of nanostructured particles. One of the most popular methods to obtain a monocrystal consists of growing particle in a gel.

B. Growth by aggregation

In this part, a general discussion will deal with the phenomena of nanostructured particles assembly, going further on different proposed mechanisms for various nanostructured materials.

As discussed above, precipitation at high supersaturation gives an initial burst of nucleation, with a high nucleation rate, and a fast growth of the nuclei until a certain size generally in the nanometre size range. Then aggregation starts becoming a competing mechanism. The alteration in particle interactions due to changes in the solution conditions during a reaction can result in large changes in the manner of particle aggregation. The aggregation process can take place by collisions, the "sticking" efficiency of relative magnitude of the interparticles forces: attractive van der Waals forces, repulsive electrostatic and steric forces. When the "sticking" efficiency is high, a random arrangement of nanounits results. Repulsive forces that naturally appear between particles, in precipitation reactions carried out in polar media typically have electrostatic and steric origins. Electrostatic repulsion arises because of the dissociation of covalently bound groups or the adsorption of ions from the continuous phase. Steric forces arise from adsorption of low or high molecular weight species which act by blocking access to the primary van der Waals attractive minimum and/or generate repulsion due to the restricted configuration of polymer segments between particles. The particle aggregation involves a summation of all these forces. The kinetics of particle growth strongly depends on the size, number density, crystallographic structure of the material, the properties of the solution, and the nature of the interface between the particles and the surrounding solution.

Self-assembly of small solid nanocrystals into ordered structures have been described by the contribution of three factors[25]. First, the aggregates are energetically more stable than the individual dissociated objects or disordered aggregates. Second the formation of aggregates is reversible when the system is agitated: formation and dissociation of the aggregates compete. The aggregates are therefore able to reach the energetically most stable form. Third, if there is an anisotropy or surfaces at different polarity the more hydrophobic sides are attracted to one another over large distance, leading to the rapid assembly.

The nanostructure obtained for particles can be characterised by either a long range order of nanocrytals[6,20,21,22,38,44,45], or a random architecture but also by a combination of the both e.g. a random core with an ordered outer shell[9]. The nanocrystals assembly can be influenced by many factors like the

crystallographic structure, the differences in energy between the different crystals surfaces, the crystalline field, interaction of additives with the crystals surfaces, their preferential adsorption and finally the experimental conditions such as pH and ions and complex formation during the precipitation of nanocrystallites and their evolution with time. Competiting molecular interactions like hydrophobic/hydrophilic components, gravitational, Van der Waals or coulomb interaction, amongst others drives organisation during self-assembly processes.

Several research groups have shown aggregates grown in aqueous suspension with a specific orientation made up of 5 - 70 nm primary nanocrystals[26,17,35,28,30,38,44]. The primary particle orientation was studied for different nanostructured materials such as TiO_2, Fe_2O_3, ZnS, CuC_2O_4, CoC_2O_4, and $BaSO_4$.

A mathematical model of growth by hetero-coagulation in seeded colloidal dispersions considering electrostatic interactions, forces dispersion, Brownian motion, was developed by Zukoski[27]. The interfacial energy of nanoparticles in solution plays a major role in the ordering process of particles aggregation. Examples of random aggregates that give narrow final PSD's which may have in previous years been attributed to growth by molecular attachment have been illustrated. For silver nanoparticles formation obtained by reduction of silver perchlorate with sodium borohybride[36]. The growth rate and the particles size have been shown to be sensitive to the solution properties, which are not expected to promote growth by molecular addition. Furthermore, if an indifferent electrolyte is added, particles tent to grow more rapidly and retain their narrow size distribution, up to a critical ionic strength where the aggregation takes place. These observations support the fact that silver sols grow by slow aggregation. The repulsive barriers produced by electrostatic forces are not sufficient enough to stop aggregation into the primary minimum in the time scale of experiment. A typical model for the kinetic of silver nanoparticles aggregation eliminated the aggregation effect using a steric barrier by a polymer addition. With this pathway the growth rate and delays in the aggregation mechanism can be controlled[35].

In summary one can say that, mechanisms of particles aggregation can be controlled by several forces involved in the precipitation event at the nanoscale level and by the crystalline field.

Detailed studies performed on TiO_2 have highlighted several key factors in the "oriented" attachment during growth mechanism for 3-4 nm primary particles. Brownian motion may also allow adjacent particles' rotation to help them find the lower energy configuration, which is represented by a coherent particle-particle interface[28]. The mobility of the surface ions, which is related to the hydrated layer, can be at the origin of inter - crystals bonding. When hydrated particles surfaces come in close proximity, the ion mobility allows adaptation of the surface topologies[29]. Several defects may be introduced when growth occurs by oriented aggregation[30]. These defects usually impact subsequent coarsening (spiral growth) and deformation. The oriented attachment could give rise to the presence of particles separated by twin boundaries or other planes or defects. Note that by definition a twinned crystal present two individual single crystals joined in a single particle, characterised by low lattice energy[31] like

in the case of saccharin crystals for example. Finally there is a strong thermodynamic contribution for oriented attachment, because the surface energy is substantially reduced when the interface is eliminated[32].

Molecular simulation of the crystallographic surfaces and an estimation of the surface energy of each surface can help predicting the formation of dislocations during precipitation and also predicting the rotation of contacting particles, such as for TiO_2. Particles synthesised by a sol gel method in hydrothermal condition at 250°C and 40 bars[30], show a rapid evolution of the particle morphology, leading to crystals primarily bounded by high surface energy planes. The microscopy analysis showed a group of three crystals attached with very similar orientation. A detailed analysis of the lattice orientation indicated that the interface between the two uppermost particles involved a relative rotation of one particle to the other. This mechanism was interpreted to be the result of a series of edge dislocation. When surface of particles are brought in close contact, that have closely related crystallographic structure there will be a driving force to form chemical bonds between atoms at this interface. These types of surfaces are not atomically flat, causing an imperfect attachment, itself involving simple rotation of two particles about an axis normal to the interface. A substantial driving force for particle rotation to achieve full alignment would be expected, but some positions may be metastable and may be preserved by the formation of a coincident site array. Moreover, stresses associated with defects caused by initial mismatching at the particle-particle interface might be sufficient to induce rotation of the crystallites into an aligned configuration. Predicting the rotation is of importance as it is strongly related to the driving forces for particles orientation. These forces are expected to play a significant role in a wide range of experimental conditions.

The special case of self-assembled aggregation leads to the formation of highly ordered particles, which often possess a porous internal structure. The growth mechanism for small particles is induced by aggregation and coalescence of small particles, which grow together and finally form larger particles. This mechanism could lead to solution inclusions and to a porous internal particle structure. The most well known example to treat this effect concerns the precipitation of barium sulphate in nonstoichiometric conditions[33]. It has been observed that precipitation sometimes took place with an excess of barium, and other times with an excess of sulphate. Furthermore, at some moments in time, the crystals' surfaces is only slightly charged or even uncharged. The adsorption of one or more ion species is responsible for the homogenous distribution of cavities, as the ions are not able to block a kink permanently. The same behaviour has also been observed for precipitation in a stoichiometric ratio of precursors[33]. This particles growth behaviour is similar to the Ostwald ripening, where small crystals dissolve in favour of the larger ones due to the dependence of solubility on surface curvature. As the particles chemical potential increases with decreasing particles size, the equilibrium solute concentration near a small particle is higher than near a large particle. The resulting concentration gradients lead to the transport of solute from small particles to the larger ones[34]. This mode of growth may result in the formation of faceted particles if it

occurs near equilibrium and if there is a sufficient difference in the surface energies of different crystallographic faces[35]. This pathway may dominate over dissolution - recrystallisation if the phase is relatively insoluble. The large number of cavities involved in porous particles induces curved surface that increases the surface energy. Barium sulphate particles analysed by transmission microscopy show a higher porosity in their core than on the surface. This is correlated to the age of both the core and the shell of the particles. The zones in the core have more time to recrystallise, whereby the size of the pores increases and the surface decreases. At high concentrations, the pore size increases due to an increase in supersaturation, shorter induction times and an increase in the particles' density. At lower level of supersaturation, at the end of precipitation, the amount of small nanocrystallites is low and so presumably, in addition to aggregation, molecular growth takes place.

C. Organic additive control

Specific additives can also control the nanoparticles' size, shape and assembly. Specific additives can influence the various stages of precipitation already at the early stage of nucleation. Then, nanocrystallites[6] can show a preferential growth process induced by organic additive adsorption and consecutive modification of the surface growth.

The aggregation mechanism of inorganic precipitates with an inorganic core and organic shell is also influenced by the steric effect[6,36]. Additives may influence both the morphology and the internal structure of the precipitates. Steric forces in some systems can even organise the nanocrystallites in a high long-range order[23]. The presence of an additive in solution can also change the solution chemistry, influencing the competing molecular attachment mechanisms.

Nanoparticles of ZnS synthesised from the aqueous solution of sodium sulphide and mercaptoethanol at a pH of 10.2 show an intimate physical mixture of two phases: sphalerite and wurtzite[37]. The kinetic analysis of the ZnS nanoparticles' precipitation shows two mechanisms. The particles initially grow by oriented attachment up to 3 nm. Then, in the second stage growth took place via Ostwald ripening. However, oriented attachment could also occur in the prophase of the second stage and may even predominate if oriented attachment kinetics adopt an aspect similar to Ostwald ripening. The two-stage growth is primarily attributed to the presence of organic ligands, which control the stage of nanoparticles aggregation. It has been observed that in the first stage the particles volume doubles. Despite polymer adsorption, coarsening is controlled by oriented attachment. This behaviour has important effects on particle growth leading to distinct morphologies. After the first stage, growth ceases until surface-bound ligands are removed, and the growth mechanism can be understood by an Ostwald ripening bulk diffusion model[37], despite the fact that growth simultaneously occurs by oriented attachment and Ostwald ripening.

Similar behaviour was observed in the microstructure evolution of the zinc oxide particles precipitated in the presence of di-block copolymer from aqueous solution, investigated by electron diffraction for a better understanding of the formation mechanism[38]. Both polymer composition and concentration seem to have a significant influence on the particle morphology and size. Particle precipitates without polymer show a specific needle-like morphology, while in the presence of the block co-polymer, they become more like a "stack of pancakes". This behaviour comes from the fact that polymer preferentially adsorbs on a specific surface of the crystal thus reducing the overall growth rate. The diffraction patterns of particle precipitated in the presence of polymers show multiple domains with an orientation distribution of 5-10 degrees. These diffraction patterns show the evidence of two types of crystal alignment, higher order at a further distance from the central grain boundary and a region closer to the grain boundary with a somewhat shorter-range order. The increase of order with increasing distance from the grain boundary is presumably due to a fast initial growth regime, followed by a much slower growth regime after some of the Zn^{2+} have been removed from the solution[38]. A higher correlation even in the region close to the central grain boundary may arise from the intrinsic electric fields of the nanoparticles polar crystal lattice. For later reaction stages, the crystals grow via addition of ions rather than nanocrystals aggregation, which leads to this higher order effect further away from the central grain boundary and a decrease in the defect number. HRTEM clearly demonstrates a transition from very highly ordered bulk particles to a series of thin, defect-rich, and locally misorientated lamellae. The structure of these two regions shows that a metastable intermediate is first formed by a central hexagonal particle. The polymer can only adsorb at the core crystal after its release from an intermediate state. This finally leads to the presence of these 10 nm lamellae features as the crystal can only grow from its polymer free surface. Polymer adsorption also induces a slight misorientation of the lamellae, which then induces defects in the lamellae.

The crystallographic structure of stable solid nanocrystals plays an important role in particles alignment, often due to the different nature of the surfaces. The crystallographic structures of copper oxalate nanostructured particles have been noticed to show two distinct surfaces of different hydrophobic/hydrophilic[39] nature. As the particles' growth takes place in the presence of attractive van der Waals forces, oriented attachment involves spontaneously self-organisation of adjacent particles for them to share a common crystallographic orientation, and then join with creation a planar interface[6].

Precipitation of copper oxalate nanostructured particles has been studied in detail in our laboratory. The particle morphology was modified using an organic polymer, hydroxypropyl methylcellulose (HPMC). Without polymer the copper oxalate precipitates showed a cushion-like morphology for a precursor concentrations of 0.02M. Increasing the polymer concentration modified both the size and the shape of the particles. As the polymer concentration increased, the size of the primary particles decreased and they became more elongated, with a specific growth in the 001 direction. This type of specific adsorption can

explain the influence of the polymer in the growth process of nanocrystals similar to that of ZnO and their assembly to form aggregates[38] described above. The polymer has been shown to affect the nucleation crystal growth and aggregation, as shown in (Figure 7). The crystallographic structure of the copper oxalate showed two distinct surfaces one hydrophobic and one hydrophilic. The polymer is assumed to adsorb on the more hydrophobic ε surface to minimise the surface energy of system taking into account the relative surface area of the copper oxalate crystal.

In the final product, the amount of the adsorbed polymer corresponds to the geometrical external ε-surfaces. These means that the particle assembly is governed by a dynamic mechanism of polymer adsorption and desorption. The TEM results obtained for the nanostructured material showed an alignment of the nanocrystals parallel to the 110 direction. The copper oxalate showed a high anisotropy given by the structure and particles morphology. The mechanism of nanoparticles assembly is thus governed by two different rates of agglomeration, higher along the 001 direction and slower along 110, where the polymer is adsorbed. The forces involved in the particles assembly process are the steric forces created by polymer adsorption, van der Waals forces and hydrophobic/hydrophilic forces arising from the structure and chemical nature of the nanoparticles. The process of the particles growth takes place in the presence of weak forces and nanocrystallites have time to orient and decrease the energy of system. The precipitates showed the smooth surfaces and their surface is closed and the specific surface area is measured by nitrogen adsorption (BET) surface is the same order of magnitude as the geometrical external surface of the micron sized particles.

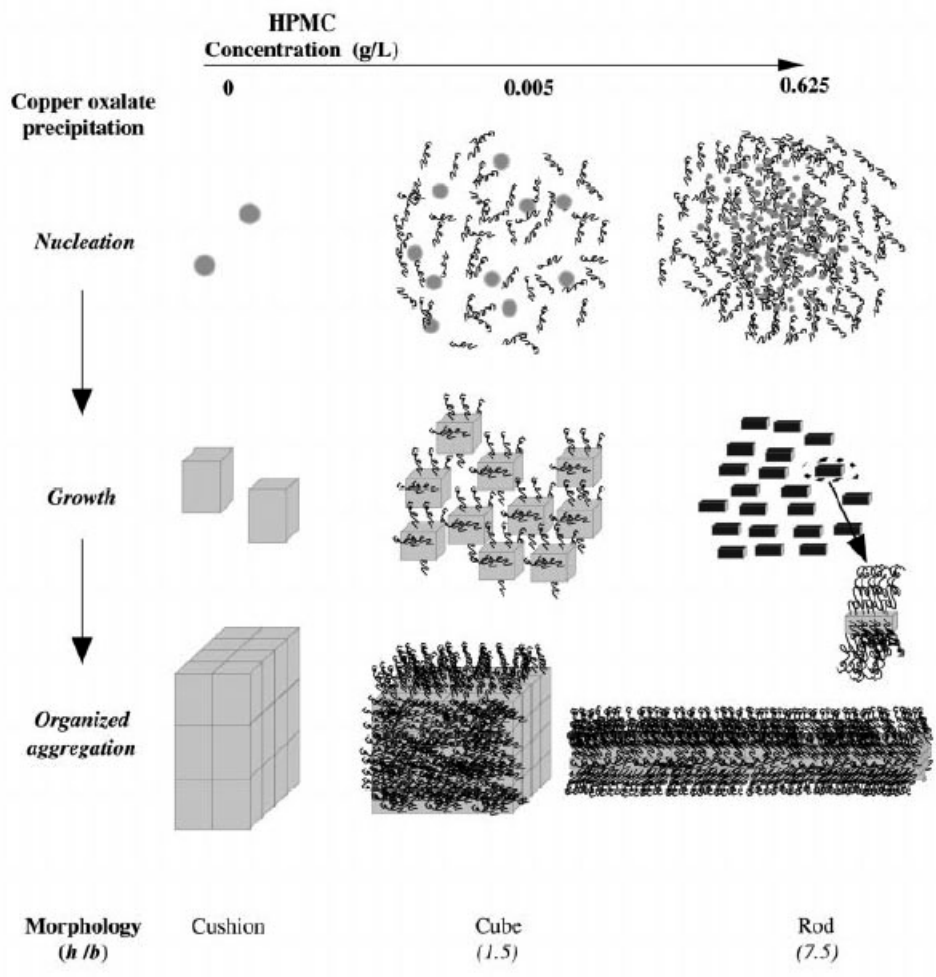

Figure 7: Polymer influence on the nanoparticles precipitation process in the case of copper oxalate nanostructure particles[6]

A dynamic adsorption - desorption effect has been involved during the aggregation, the polymers can be still adsorbed on the preferential surface of the crystals, remaining as inclusion in the final particle (ZnS)[37] or adsorbed only at the external surface like for copper oxalate[6].

The synthesis of barium chromate ($BaCrO_4$) monocrystalline particles from barium is (2-ethylhehyl) sulphosuccinate in the presence of sodium chromate Na_2CrO_4 have been reported to exhibit chain-like arrays. These particles form chains of 50-500 nm and consist of rectangular -shaped primary particles, uniform in length, 16 nm, and width, 6 nm, and are perfectly aligned perpendicular to the particles longer axis[40]. A regular 2 nm spacing, corresponding to the thickness of an adsorbed surfactant layer separates each crystal along the chain. Transmission electron microscopy observation, which was performed after the initial stages of chain assembly, showed stripped patterns rather than isolated nanoparticles with prismatic morphology, suggesting that $BaCrO_4$ growth occur in sequential attachment of the individual nanoparticles. This is understood as a spontaneous linear self-assembly in the

microemulsion fluid arising from the interaction between the hydrophobic surfactant tails adsorbed onto the flat faces of the developing $BaCrO_4$ prismatic crystallites.

As already pointed out above, the solution chemistry and the nanocrystals energy play an important role on the particles assembly. Many mechanisms concerning calcium carbonate are proposed in the literature[41,42,43]. Our attention will focus on the mechanism describing the alignment of the nanocrystals[43]. When two adjacent crystals have a perfect lattice alignment, a strong decrease in free energy is involved. This provides a strong driving force for the re-alignment of the crystals within an aggregate. A possible explanation for this behaviour has been proposed to be due to the thickness of the electric double layer surrounding the particles that changes with the ionic strength of the solution. Increasing the thickness of the electric double layer at low ionic strength may slow down the approach process of the crystals, allowing them to rotate before cementing. A similar behaviour has recently been observed for TiO_2, where the two crystals are fully aligned[44]. In this case, the thermodynamic driving forces are responsible for the oriented attachment because the surface energy is substantially reduced when the interface is eliminated.

Supplementary forces such as the local magnetic fields many also influence the mechanism of the nanoparticles aggregation. When a cobalt colloidal suspension is slowly evaporated in a controlled atmosphere, the particles can diffuse to their lowest energy sites producing a well-defined superstructure. The nanocrystals assembly is driven by the balance of surface tension, van der Waals forces, and magnetic interactions that allow the ordering of the nanodomains of cobalt[45]. The magnetic interactions depend on the nanocrystals size and involve different magnetic behaviour, such as superparamagnetism or ferromagnetism and permit a free orientation to lower the system energy.

The precipitation of α-Fe_3O_4 particles occurring in the presence of phosphate ions leads to their aggregation in an ordered manner resulting in an ellipsoid-like shape. This behaviour suggests a high influence of the magnetic moment that the hematite exhibits along the c axis[46]. When a magnetic field is applied during the precipitation, the shapes of the particles are modified to produce even more elongated particles with a high aspect ratio higher then 5.

To summarise, Van der Waals attractive forces, electrostatic repulsion, and possible magnetic forces, depending on the particles properties and the steric forces when in the presence of organic additives govern the aggregation mechanism of particles. The addition of all these distinct contributions affects the evolution of the particles. All proposed mechanisms for the aggregation of the particles have been studied in detail by ex-situ microscopy technique with very little information concerning the evolution of ionic species in solution, except for the cementing of $CaCO_3$. The balance of ionic species and the resulting complexes strongly influence the surface charge and the ionic strength, and consequently the electrostatic interactions and the particles' aggregation behaviour. The competing growth by molecular

addition will also be influenced by the specific ions, molecules or complexes that may exist in solution during the particles' growth. The next section will discuss some examples on this subject.

D. Supersaturation - controlled growth - solution chemistry

The importance of nucleation and growth is determined by the relative supersaturation of the solution. The supersaturation process is sensitive to temperature, concentration and mixing conditions. The formation of the particles and the growth processes in precipitation, which directly depend on the supersaturation of solution, vary with both feed concentration and flow rate. A modification of the particle morphology and the variation of particle size can result from the excess of a particular species in solution, which could be caused by nonstoichiometric reaction conditions. A complete detailed understanding of the solubility data of each system; of all the ionic species able to influence the physical behaviour of nanocrystals growth is of great interest. It is well known that a higher supersaturation produces smaller primary particles as it promotes high nucleation rates. Supersaturation can also play a role in determining the rate of aggregation, which is itself the result of the balance between the formation of aggregates and their almost immediate disruption by fluid shear. It is often suggested that a role for supersaturation is to provide new material to bond or "cement" two colliding crystals together[48]. Also interactions between molecules and ions in solution and species that represent the termination of the bulk crystal structure are critical as they determine reactivity and free energy at the solid-liquid interface. Two important considerations related to processes occurring at surfaces are the mechanism and the rates of reactions. The mechanism is the series of steps involved in the process of reaction. One of these steps will be slower than another and will thus determine the rate. Although a variety of distinct surface sites may contribute to the reaction, the overall rate is dominated by the most abundant of the most reactive sites. Rates for specific processes can be suppressed by diffusion of reactants and products to and from surfaces and are affected by the characteristics of the solid composition (pH, saturation, and ionic strength) of the solution and by temperature.

Solubility isotherms have been calculated for the system ($Y(OH)_3$-$Ba(OH)_2$-$Cu(OH)_2$-$H_2C_2O_4$-(HNO_3/NaOH)-H_2O)[47], involving a numerical algorithm and several equilibrium between different possible precipitated complexes and the ionic strength. This type of approach highlights the importance of the complex formation, their sensitivity to pH and supersaturation.

A lot of work has been carried out on calcium oxalate monohydrate precipitation from supersaturated solution, with varying the ratio of calcium to oxalate ions[48]. Using the solution thermodynamics, population balance data of solution it is possible to select the growth and aggregation rates and to calculate the calcium concentration from the experimental particle size distributions (PSDs)[48]. Figure 8 shows a linear rate of crystal growth taking into account the calcium to oxalate ions ratio in solution. Figure 8 also shows that the solutions were supersaturated throughout the experiments, and

indicates that supersaturation (defined as $S = \sqrt{P_s / K_s}$ with P_s solubility product and K_s solubility constant) decreases from the initial value of 2.9 to approximately 1.1.

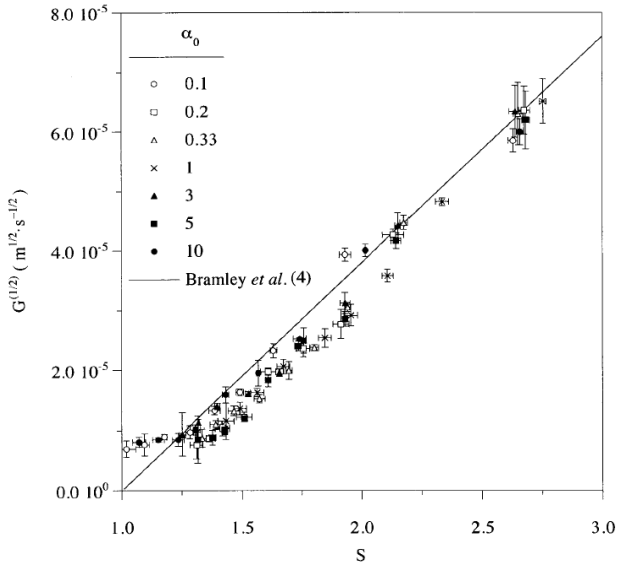

Figure 8: Dependence of the growth rate with relative supersaturation for α_0 varying from 0.1 to 10, where α_0 is the ratio of $Ca^{2+}/C_2O_4^{2-}$ (48)

A critical parameter is the control of the crystal size. The size is determined by the number of the crystals formed (nucleation), by the following growth and by consequent aggregation. In the case of the calcium oxalate precipitation the final particle formation is explained by the growth between agglomerated particles at a cementing site. The cementing process requires the transport of the solute to the cementing site by diffusion followed by a reaction at the surface of the two contacting particles. Further disruption by agitation or particle collisions may occur if the Van der Waals forces alone are not strong enough to keep the aggregate together. The surface reaction rate, r_s, may be calculated from the linear rate of crystal growth by:

$$r_s = \frac{\rho_m}{2} \cdot G \qquad \textit{Eq 7}$$

where ρ_m represents the molar density. The growth rate of the cementing, process expressed here by G depends on the transport properties of the ionic species, the surface reaction kinetic and the bulk solution composition. Thus as supersaturation decreases during the experiment, the growth rate and the cementing rate G will also decrease. Moreover, taking into account the ions concentration in solution, the rate of diffusion at a constant temperature and the agitation rate, one finds that the aggregation rate constant depends on the cementing rate only for this calcium oxalate system. At the same time, the aggregation rate constant varies with the surface reaction rate. A pore diffusion reaction describes the growth of new material, or cement, at the point of contact among the particles. The model highlights the dependence of the aggregation process on supersaturation and solution composition.

The chemistry of ZnS[49] particles synthesised from the aqueous solution has been studied on a range of pH from 2 to 6 in order to understand the physical characteristics of the powders in the presence of the acetate and acetylacetonate. The chemical composition of ZnS was shown to be sensitive to pH, which also influences the morphology, size and aggregation mechanism. For pH > 2, the agglomeration of the particles increases, particularly at pH near 4, which is close to the isoelectric point of ZnS. In this range of pH the particles' size is of 20-40 nm. In the presence of the acetate, the particles size grows up to 70 nm. Considering the concentration of the ions in solution and the complex formation provides an explanation of this behaviour[49]. The complexation of the precipitating cation with a chelating agent like acetylacetonate, leads to a lower concentration of free Zn^{2+} cation in solution reducing supersaturation and thus influencing the kinetic of precipitation. The Acac-Zn is the dominant species in a pH range of 1.5-7, whereas acetato complexes are present in majority for pH<1. Precipitating cation with a chelating agent acetylacetonate, leading to a limited concentration of free Zn^{2+} cations in the solution, is an efficient way of influencing the kinetic of ZnS precipitation. In the presence of Acac ligands, acetate ions are not expected to complex the cation. In the contrary, when the acetate ligands are substituted to acetylacetonate, a strong interaction with the Zn^{2+} cation occurs, which results in the formation of trioacetato complexes as the preponderant species in a pH range of 0 to 3. The resulting complexes act as an intermediate species in the formation of the crystalline phase, giving a "buffer" source of Zn^{2+}. All the experimental data were interpreted using the solubility isotherm. The chemical equilibrium considered the phenomena of dissolution and protonation and the complex formation. All the experimental results obtained can be accounted for by using the isothermal solubility, the interaction between the different ionic species in solution and the complex formation as a function of pH. These fundamental solution parameters have a significant influence on the mechanism of aggregation, size and morphology.

In recent years several particle growth/formation assembly mechanisms have been clarified using cryogenic microscopy measurements. These measurements were performed at the different stages of cobalt oxalate particle formation[9]. The particle evolution was linked to the ionic concentration in solution, and consequently with pH. A possible mechanism was finally proposed showing a disordered core and an ordered nanostructured shell.

In summary precipitation needs a supersaturated solution before several steps can take place for the particle formation. The nucleation process is the least controlled step at this time, necessitating the most powerful devices, especially as nucleation happens in milliseconds for high supersaturation that produce nanostructured particles. Then the growth of the nuclei, up to a certain stage, can be influenced by different parameters. The chemical environment of the nuclei has a high influence on the particles' growth. Another important parameter that should be highlighted is the number of the synthesised crystals and hence the solid/liquid ratio, the particle velocity in solution and the frequency of collisions among particles. When particles grow by molecular attachment or by aggregation, other factors might disturb the

system such as the internal forces among the particles surfaces', hydrophobic / hydrophilic forces, electric field, magnetic forces or the crystalline field. If a polymer is added to the physical system of precipitation and adsorb on crystal surfaces steric forces will come to complete the force balance as seen previously. When molecular attachment or aggregation forms the particles, the supersaturation of the solution decreases as a function of the particle formation and the cementing process can occur. In the end, nanostructured particles are obtained with a high order or a random arrangement. All of these parameters, which have been briefly described above for the particle evolution, must be considered for a discretization of the different mechanisms taking place in the particles organisation process. Although the use of the "population balance approach" is beyond the scope of this thesis, a brief description is given as current developments[50] and will in the near future provide a tool that may be applied to the copper oxalate system studied in this thesis.

E. Population Balance

In recent years, much research has been focused on the discretized population balance in order to model the nucleation, growth and aggregation processes[51-56]. In seeking a solution to such an equation, one is essentially looking for a description of how particles are distributed in size as a function of time. The population balance technique is applied to develop a mathematical description of the system under consideration. The particles are characterised by internal velocities that are assumed to be a unique function of the state of the particles. An example of internal velocity is that of the linear rate of growth of a crystal in a supersaturated solution, determined by the size of the particle and the level of surrounding supersaturation. In the case of the crystal growth, evidence indicates that crystals of identical size and environments do not necessarily grow at the same rate, but there is an inherent dispersion of the particles growth rates under identical conditions. If a given particle has a repeatable growth rate under identical conditions, then it behaves properly in its particle phase space and one can view the growth dispersion phenomenon as the result of a distribution of particle phase planes in the suspension with each particle being a member of one of the phase planes[51].

The discretized population balance is used to simulate changes in a particle size distribution for given growth and aggregation rates. In a multiparticle system the rate of aggregation r_{agg}, at which particles of size (L, L+dL) aggregate with particles of size ($\lambda + d\lambda$). The aggregation is a measure of the frequency with which a particle of size L aggregates with one of size λ. In the assumption that all particles collisions are binary; this is usually taken to mean that particle concentration are sufficiently low, the aggregation rate can be written as a product of two factors:

$$\beta(L,\lambda) = \beta_0 \cdot f(L,\lambda) \qquad \textit{Eq 8}$$

where β_0 depends on the operating conditions such as the local fluid velocity field and the chemical environment and is independent of size. The second factor, $f(L,\lambda)$, is a function of the particle size. The size dependence of the function reflects the mechanism thought to be at the origin of the aggregation, such

as, for example, the Brownian motion, gravitational settling, and shear or particle inertia. These functions are summarised in Table 2.

Table 2: Aggregation function used to model aggregation during precipitation[53]

Mechanism	Function β (L, λ)
Brownian motion	$\beta_0(L+\lambda)\cdot(L^{-1}+\lambda^{-1})$
Gravitational	$\beta_0(L+\lambda)^2\cdot(L-\lambda)$
Shear	$\beta_0(L+\lambda)^3$
Particle inertia	$\beta_0(L+\lambda)^2\cdot(L^2-\lambda^2)$
Empirical function	$\beta_0(L^3-\lambda^3)^2/(L^3+\lambda^3)$

For a well-mixed batch system of constant volume, the population balance is given by:

$$\frac{\partial n}{\partial t} + G \cdot \frac{\partial n}{\partial L} = B - D \qquad \textit{Eq 9}$$

where n is the number density function, D is the death rate ($m^{-4}\cdot s^{-1}$), B is birth rate ($m^{-4}\cdot s^{-1}$) and G is the growth rate ($m\cdot s^{-1}$) If one considers a system containing dN particles per unit volume of suspension in the size range of L to L+dL then at that size and time the density function is:

$$n(L) = \frac{dN}{dL} \qquad \textit{Eq 10}$$

Equation (9) relates the rate of change of the particles' number in the differential size range of L to L+dL to the rates of growth into and out this range and the rates of birth and death in this size range[52].

Solving the population balance equation requires determination of the particle size distribution PSD and n(L,t), that satisfies the population balance equation for the system. Perhaps the most difficult problem associated with the modelling of a process simultaneously involving growth and aggregation is the selection of an aggregation function[53]. A function for the aggregation process is often chosen arbitrarily and the procedure for determining the rate constants described is applied to a set of experimental data. Usually, both the aggregation and growth rates will depend on supersaturation, as it has been observed experimentally. Nucleation rate may be correlated with supersaturation. From the experimental PSDs and the initial solution composition a mass balance can be used to calculate the variation in the reactant concentration with time. The aggregation process has the potential to produce large particles in a short period of time with no relief of supersaturation. For the process of nanoparticles aggregation it may even be a source for increased supersaturation[9].

Several studies have been performed on the precipitation of calcium oxalate, using the population balance to the discriminate particle assembly mechanisms. Calcium oxalate was precipitated using $CaCl_2$ and $Na_2C_2O_4$ at 37°C, in a solution with an ionic strength of 0.16 mol/l[48]. The precipitation was studied in a batch system using solutions of constant initial supersaturation, but with different calcium to oxalate

ions ratios. During the experiments, PDS were measured at regular intervals, the supersaturation was calculated in terms of free ion concentration, and four experiments were conducted for each degree of reaction advancement. It was found that the particles growth rate was a second order function of supersaturation.

This method is capable of characterising two main tasks: extracting growth and aggregation rate constants from experimental data and simulating changes in particle size distribution during an experiment. The advantage of batch reactions is the possibility to determine the effect on growth and aggregation rate of potentially inhibiting physico-chemical factors.

All calculations impose a correlation between concentration, supersaturation, PSDs, and particles death and birth. The isothermal solubility is a key factor for the discretization of the different mechanisms of growth and aggregation. Thus the solution chemistry plays an important role in crystal growth and in the mechanisms of particle attachment to provide a long-range order of nanocrystals, accessible via the type of solution thermodynamics calculation described in section C.

1.2.4. Conclusion

The precipitation process via aqueous routes is initiated from a supersaturated solution. A high supersaturation first implies a short burst of nucleation, then a growth process and after a final stage of aggregation. The initial stage of nucleation is the least understood at this moment. The most powerful techniques available to catch the first part of the precipitation are SAXS, AUC, and DLS in the range of milliseconds. These methods are useful within their detection limits of nanosize particles and the process rate of reaction.

After nuclei have formed, growth will occur until a certain size before the competition between growth by molecular attachment and aggregation begins. Whether one or the other of the growth mechanisms dominates will depend on the number density of the nanoparticles and the relative molecular growth and aggregation rates. The aggregation rate itself depends on attractive forces like van der Waals, repulsive electrostatic forces and steric forces initiated by the presence of an organic additive, or of magnetic forces. The proposed mechanisms of particle assembly described in the current literature have generally been studied using microscopy and X-rays diffraction patterns. It should also be noted that a stop of the particle growth has been demonstrated by using polymers of high molecular weight[36] that are able to block the aggregation mechanism. Furthermore, some research groups took into account the particles nearest neighbour in solution and the effect of double layers[47,49,50,53]. The aggregation mechanism may change as a function of the ionic strength and the presence of a possible complexes that could be formed depending on chemical conditions and temperature[24,20,54]. The complex formation during precipitation present different equilibrium velocity, as a function of ionic species and solid phases in solution and thus affect the supersaturation and the growth kinetic.

Another important factor that starts being more and more useful in discerning aggregation mechanisms is the modelling of nucleation and crystal growth using the population balance approach. This method can be applied by controlling the chemistry of the solution and monitory the particles size distribution during the aggregation process. Until now the population balance has not been frequently used as a possible tool to help distinguish between the early steps of precipitation and growth mechanisms.

The presence of specific organic additives in solution is assumed to change the surfaces growth rates by a preferential adsorption on the nanoparticles surfaces. These additives were considered as a possible way to control the particles' assembly[6,23,38,49]. They are either incorporated in the particle nanostructure[55] or they can still be adsorbed only on the external surface[6].

1.3. Transformation of oxalate precursors into oxides and metals

1.3.1. Transformation

The possible applications for powders produced via the controlled precipitation of nanostructured copper oxalates are expected to be in the form of copper oxide (catalysis) or metallic copper (matrix for GMR's). This necessitates the transformation from the oxalate in a controlled manner with view to retaining both the nanostructure and particle shape (which has been shown in the oxalate precipitation step). An understanding of the transformation / decomposition mechanism and kinetics is a key step in helping the materials scientist to control and tailor the final nanostructured products for a specific application.

In this section we shall look at the literature on the decomposition of different metal oxalates in general, before discussing the texture of the oxalate precursors and finally a brief description of kinetic models that will help interpret the transformation mechanism and kinetic.

Metal oxalates as precursors in the preparation of oxides or metals, possessing high surface area,[56] at relatively low temperature has generated great interest in the investigation of the thermal decomposition of these salts. The preparation of a metal by the thermal decomposition of an oxy-salt leads to the production of a powder product at temperatures, which are below the melting point of the metal. Furthermore, as the metal can be produced in fine particles form, it has potential use as a catalyst, a reactive chemical, or in metallurgy can be formed to give shapes of controlled porosity[56].

For multi element compositions co-precipitation can be used. Using precipitation techniques various metal ions can be precipitated in the desired stoichiometric proportion and in several cases a single-phase solid solution precipitation is achieved assuring homogeneity at a molecular level. The thermal decomposition of the simple or mixed oxalates obtained via the precipitation method has been

studied using different gaseous atmospheres in order to understand the atmospheric influence on the decomposition process [58].

For the simple or mixed oxalate the physico-chemical or geometrical mechanistic models have not been investigated in detail. Many studies have focused on the final product simply as a function of temperature and gaseous atmosphere. For oxalates the nanostructured nature of the particles has not been taken into consideration. Also the effect of the gaseous atmospheres on the particles evolution and the kinetic mechanism have been little studied.

The decomposition routes of the oxalate are affected by various factors such as: nature of cations, heating rate, partial pressure and elimination gases, nature of the interface between the solids, size and architecture of samples under investigation, crucible nature. If the platinum crucible is used this can behave as a catalyst [57] in a reducing atmosphere.

In the literature, investigations on the thermal decomposition of several oxalates under different atmospheres such as nitrogen, air, and oxygen has been well documented. In the following paragraphs a review of thermal analysis data on oxalate decomposition under nitrogen and oxygen atmospheres will be made. Also the oxalates have been classified as a function of their decomposition product.

A. Types of cations

In general hydrated oxalates decompose in a first step under all atmospheres to an anhydrous product, by loss of water. The mechanism can sometimes be more complicated as a function of the gaseous atmosphere. From differential thermal analysis (DTA), oxalates have been classified in two groups[58] as a function of the final product of decomposition in an inert atmosphere and subsequent behaviour on contact with oxygen. Those, which on admission of oxygen underwent oxidation of their decomposition products under nitrogen, are Type I and include oxalates of copper, cobalt, antimony, bismuth, cadmium, iron (II), iron (III), lead, manganese (II), nickel and tin (II). The other group of oxalates, termed Type II, did not undergo oxidation at the end of the DTA experiment in nitrogen upon admission of oxygen and these included aluminium, barium, calcium, cerium, chromium, lithium, magnesium, potassium, sodium, strontium and zinc.

For those oxalates which produce the metal in nitrogen the decomposition temperature represents the temperature at which the metal-oxygen bond is ruptured and will depend critically on the size and charge of the metal ion, whereas where the oxide is produced in nitrogen the decomposition temperature represents the energy required to break the carbon-oxygen bond and this will depend less critically on the cation nature[59]. Other authors have suggested that these oxalates may be classified according to three principal reactions[60,61], taking into consideration the final product formed (again under a nitrogen atmosphere):

i) alkali and alkali-earth oxalates which decompose into carbonate and carbon monoxide:

$$MC_2O_4 \rightarrow MCO_3 + CO \qquad \text{(a)}$$

ii) oxalates, the decomposition of which results in the formation of a metal oxide as the solid and a mixture of carbon monoxide and dioxide as the gaseous products:

$$MC_2O_4 \rightarrow MO + CO_2 + CO \qquad \text{(b)}$$

this group includes some of the transition metal oxalates such as zinc, iron, chromium, cobalt and copper.

iii) oxalates decomposing into metal and carbon dioxide according to the reaction:

$$MC_2O_4 \rightarrow M + 2CO_2 \qquad \text{(c)}$$

for the oxalates of bivalent metals, the greater the metal-oxygen bond is covalent the more likely the decomposition will give directly a metal. The decomposition into metal starts at the temperature at which the rupture of the Me-O link is possible or at which the rupture of the C-O bond occurs. If the reaction proceeds by breaking the carbon-oxygen bond, it will be followed by the rupture of the second Me-O bond because of the inability of the metal to accommodate two oxygen atoms [56]. The total reaction would lead to the evolution of equimolar amounts of CO and CO_2. The second possibility is the direct rupture of the two Me-O bonds resulting in the formation of a metal and the two molecules carbon monoxide.

In other variable valance oxalate decompositions, the reaction under nitrogen leads to the formation of the lowest valency oxide. This makes the decomposition route particularly dependent on the surrounding gaseous atmosphere. The decomposition of manganese oxalate yields a series of different oxide products depending on the experimental conditions. The product in nitrogen atmosphere or any other inert gas is the green oxide, MnO, whilst the product in oxygen is one of the other manganese oxides MnO_2, Mn_2O_3 or Mn_3O_4. In order of increasing temperature the transformation temperature for these oxides in air has been given by the following series [(62)]:

$$MnO_2 \rightarrow^{535°C} Mn_2O_3 \rightarrow^{933°C} Mn_3O_4 \rightarrow^{1160°C} MnO \qquad \text{(d)}$$

In summary these examples show that the thermal decomposition of oxalates can proceed by several routes. Some oxalates such as calcium oxalate decomposes to a carbonate, others such as zinc oxalate decompose to an oxide. A further group of oxalates if decomposed in inert atmosphere produce a metal as the solid product and when expose to air produce a metal oxide.

It has also been observed that the types of sample cell used can have an important influence on the thermal decomposition reaction. This behaviour has been studied in the case of magnesium oxalate[63]. The DTA results using a platinum sample holder in air will result in an endothermic decarboxylation. Another DTA trace again in air but using an inert sample holder (porcelain) results in an endothermic decarboxylation. This reaction is:

$$MgC_2O_4 \rightarrow MgO + CO_2 + CO \qquad \text{(e)}$$

but in the case where platinum samples holders are used, and in the presence of oxygen:

$$CO + \tfrac{1}{2}O_2 \rightarrow CO_2 \qquad \text{(f)}$$

If either oxygen is absent or the holder is inactive the reaction (f) does not take place. The catalytic process is exothermic and the net result is an exothermic peak. Magnesium oxide, the final product, is an insulator and is a poor catalyst for the oxidation of carbon monoxide.

Oxalates such as: chromium, manganese, iron and zinc, which produce oxides as a results of decomposition both in air and in nitrogen are expected to show endothermic reaction depending on the crucible. The same behaviour should be expected for cobalt, nickel and copper which gives the oxide on decomposition in air but metal in nitrogen. Copper oxalate[64], mercuric oxalate and silver oxalate, all decompose in nitrogen with an exothermic reaction.

Table 3: Oxalates transformation under nitrogen atmosphere and the types of reaction that takes place as a function of temperature from DTA analysis

Reactant	Temperature (°C)	Type of reaction
Potassium Oxalate	95 - 132	Endo dehydration
	370 - 388	Endo phase transition in oxalate
	481 - 525	Endo decomposition to carbonate
	860 - 898	Endo melting point of carbonate
Magnesium Oxalate	172 - 221	Endo dehydration
	426 - 505	Endo decomposition to oxide
Calcium Oxalate	134 - 201	Endo dehydration
	425 - 646	Endo decomposition to carbonate
	719 - 797	Endo decomposition to oxide
Strontium Oxalate	136 - 184	Endo dehydration
	424 - 501	Endo decomposition to carbonate
	911 - 924	Endo phase change in carbonate
	980 - 1069	Endo decomposition to oxide
Barium Oxalate	132 - 161	Endo Dehydration
	468 - 487	Endo decomposition to carbonate
	795 - 802	Endo phase change in carbonate
Aluminium	225 - 264	Endo dehydration
	295 - 321	Endo decomposition
Manganese	112 - 131	Endo dehydration
	343 - 396	Endo decomposition to oxide
	760	Exo very large, on admission of air
Iron	161 - 196	Endo dehydration
	315 - 364	Endo decomposition to oxide and metal
	960 - 975	Small exo in this region
	1050	Large exo on admission of air
Cobalt Oxalate	*149 - 197*	*Endo dehydration*
	355 - 371	*Endo decomposition to metal*
	1100	*Large exo on admission of air*
Nickel Oxalate	185 -231	Endo dehydration
	318 - 349	Endo decomposition
	450	Large exo on admission of air
Copper oxalate	*255 - 280*	*Exo decomposition to metal*
	500	*Exo very large on admission of air*
Zinc oxalate	109 - 156	Endo dehydration
	342 - 383	Endo decomposition to oxide

Table 4: Oxalate transformation under oxygen atmosphere and the types of reaction that takes place as a function of temperature form DTA analysis

Reactant	Temperature (°C)	Type of reaction
Potassium Oxalate	82 - 129	Endo dehydration
	370 - 388	Endo phase transition in oxalate
	458 - 534	Endo decomposition to carbonate
	856 - 898	Endo melting point of carbonate
Magnesium Oxalate	182 - 212	Endo dehydration
	279 - 312	Exo
	455 - 486	Exo decomposition to oxide
Calcium Oxalate	137 - 205	Endo dehydration
	394 - 444	Exo decomposition to carbonate
	643 - 653	Exo phase change in carbonate
	698 - 794	Endo decomposition to oxide
Strontium Oxalate	135 - 185	Endo dehydration
	407 - 502	Exo decomposition to carbonate
	920 - 925	Endo phase change in carbonate
	967 - 1057	Endo decomposition to oxide
Barium Oxalate	128 - 155	Endo Dehydration
	390 - 433	Exo decomposition to carbonate
	795 - 802	Endo phase change in carbonate
Aluminium	228	Large exothermic reaction complex peak
	262 284	Endo dehydration
	329	Exo peak decomposition
Manganese	99 - 127	Endo dehydration
	227 - 269	Exo decomposition to oxide
	1004 - 1011	Endo oxide dissociation
Iron	161 - 178	Endo dehydration
	178 - 221	Exo decomposition to oxide
Cobalt Oxalate	*147 - 187*	*Endo dehydration*
	219 - 261	*Exo decomposition*
	955 - 968	*Endo Co_3O_4 -> CoO*
Nickel Oxalate	173 - 329	Endo dehydration
	312 - 350	Exo decomposition
Copper oxalate	*255 - 302*	*Exo decomposition to oxide*
	1088 - 1102	*Endo on cooling*
Zinc oxalate	109 - 156	Endo dehydration
	342 - 389	Exo decomposition to oxide

General conclusion of the oxalate decomposition under nitrogen and oxygen atmosphere described in detail in Table 3 and Table 4 are:

- ✓ all dehydration peaks are endothermic;
- ✓ all primary decomposition peaks in oxygen are exothermic irrespective of whether the product is an oxide or a carbonate;
- ✓ with one exception, e.g. copper oxalate[65], all primary decomposition peaks in nitrogen are exothermic;
- ✓ the peaks for the decomposition of the carbonate to the oxide are endothermic both in nitrogen and oxygen and of a characteristic shape.

B. Phase transition and texture of initial product

Phase changes intrude upon the decomposition sequence in a number of cases associated with the solid products of oxalate decomposition. An example is the phase change occurring in barium carbonate. At low temperature 495°C the stable phase is γ-$BaCO_3$ and at around 850°C is present the transition of the γ-$BaCO_3$ to β-$BaCO_3$, these experiments have been verified by the simple measurement of density.

Some features of textural and surface chemistry have also to be considered. The factors which matter are the shape and size of the original reacting particles, the degree of compaction and adhesion between the particles imposed on the materials under investigation, and whether the product gases are removed as quickly as possible under vacuum conditions or at atmospheric pressure under specified flow conditions. Quantitative correlation's have been made between the kinetic of decomposition and the surface area, and have been applied to the decomposition of lithium oxalate[66]. A shattering of the particles causes the increase in surface area or the decrease of particles size. This is caused by the stresses and strains set up due to differences in the densities of the solid reactant and product causing a distortion of the reaction interface.

A metal in product from oxalate decomposition may undergo sintering at the end of the decomposition before the end of the thermal cycle. This results in increases in particle size and decrease of surface area. The sintering process is a function both of temperature and time. Isothermal heating runs show that the decrease in surface area occurs towards an equilibrium value determined by the initial physical condition of the metal and the temperature of experiment. The process of sintering can be considered as a growth in particles size brought about of diffusion. Sintering mechanisms and dominant diffusion process may change during a non-isothermal decomposition. In fact the three following processes may be distinguished[59]:

- ✓ adhesion between particles, which leads to solid joints at points of contact;
- ✓ surface diffusion, in which the coalescence of particles occurs by movement of metal atoms along the surface

- ✓ bulk diffusion, in which further coalescence is brought about by diffusion of the metal atoms through the bulk material [(59)].

C. Copper Oxide reduction

The reduction of copper oxide into metal is one way to synthesis metallic copper. During this thesis, one of the goals was to synthesis metallic copper with a cubic morphology with possible applications for GMR and as a catalyst.

CuO with the following composition 80% Cu(I), 15% Cu(II), and about 5% Cu(0), and a surface area of $20m^2/g$ has an important catalytic activity for 2-nitrophenol degradation[67]. It was shown that the Cu(I) seems to be the active species involved in the observed oxidation. Also CuO is used as a catalyst or a catalyst precursor in many chemical reactions that involve hydrogen as a precursor product: e.g. methanol synthesis from CO ($CO + H_2 \rightarrow CH_3OH$).

Much attention has been paid to the kinetics of the reduction of copper oxide into metal and the possible formation of intermediate states or directly transformation[69,70].

The exact process by with the reduction of copper oxide under different atmospheres is still under discussion, as there is a discrepancy between the results obtained in *in-situ* or *ex-situ* XRD measurements[69,70,68]. A CuO commercial powder (99.9999% purity) was studied using *in-situ* XRD (heating rate 10K/min) under a flow of 5% H_2 and 95% He. These measurements showed that the oxide starts to reduce near 300°C and becomes metallic Cu. In this case no intermediate phase is observed during the reduction (i.e., direct transformation from Cu^{2+} to Cu^0). However changes in the experimental conditions, involved the presence of the intermediate and suboxides formation. XRD patterns collected for a heating rate less 10K/min showed no hint of an intermediate phase formation. When the heating rate if increased to 20K/min, however a slight, but clear, hint of Cu_2O phase formation was observed. At a higher rate (40K/min), the existence of the intermediate phase became clear. This study using XRD and EXAFS measurements demonstrated that under normal supply of hydrogen, CuO reduces directly to metallic Cu without formation of intermediates of suboxides. The reduction of CuO is easier than Cu_2O. The apparent activation energy for the reduction of CuO is about 14.5 kcal/mol, while the value is 27.4 kcal/mol for Cu_2O. To see the formation of Cu_2O, one has to limit the flow of hydrogen and change the heating rate[69]. These results show the importance of kinetic effects for the formation of well-defined suboxides during a reduction process and the activation of oxide catalysts.

A systematic study of the reduction of H_2 with a pure film of CuO prepared by laser deposition in a UHV chamber on a clean Mo substrate was carried out using *in-situ* time-resolved XRD and surface science techniques. Under normal process conditions, *in-situ* time resolved XRD showed that Cu^+ is not a stable intermediate in the reduction of CuO. Instead of a sequential reduction ($CuO \rightarrow Cu_3O_4 \rightarrow Cu_2O \rightarrow Cu$), a direct $CuO \rightarrow Cu$ transformation occurs. To facilitate the generation of Cu^+ in a catalytic process one can limit the supply of H_2 or mix molecules that act as oxidant agents (O_2, H_2O). The kinetics of CuO

reduction could be associated with the production of sites on the oxide surface with a high efficiency for the adsorption and dissociation of H_2. Once a large coverage of H is available on the surface, then the efficient removal of O from the bulk or the nucleation of the new Cu phase can become rate-limiting factors. On the other hand the XRD data for the reaction of O_2 with the metallic Cu at 400-600°C show a sequential oxidation process: $Cu \rightarrow Cu_2O \rightarrow CuO$. In clear contrast to the behaviour observed for the reduction of CuO, Cu^+ is a stable intermediate in the oxidation reaction[70].

D. Kinetics of solid state reactions

Some of the most frequently observed kinetic characteristics for the reactions of a solid alone or with a gas are given in Table 5. Reaction kinetics is presented here in terms of the various rate-limiting steps of mass and heat transfer, as well as surface reaction. The following processes may control the rate of growth (product formation).

- ✓ a chemical reaction at an advancing interface (following a nucleation step);
- ✓ a chemical reaction at a static interface (following diffusion of appropriate species to that interface);
- ✓ diffusion of reactants (in a homogeneous phase or across a barrier of product) to the reaction interface at which the chemical step is fast.

The significance of diffusion generally increases with reaction rate in the sequence of gas, and solid reactants and (sometimes) with reaction yield (α), and particles size. The controlling factor (a chemical step or diffusion) may change during the pathway of reaction. It is a primary objective of most fundamental kinetic investigations to identify the rate-limiting process as function of reaction yield.

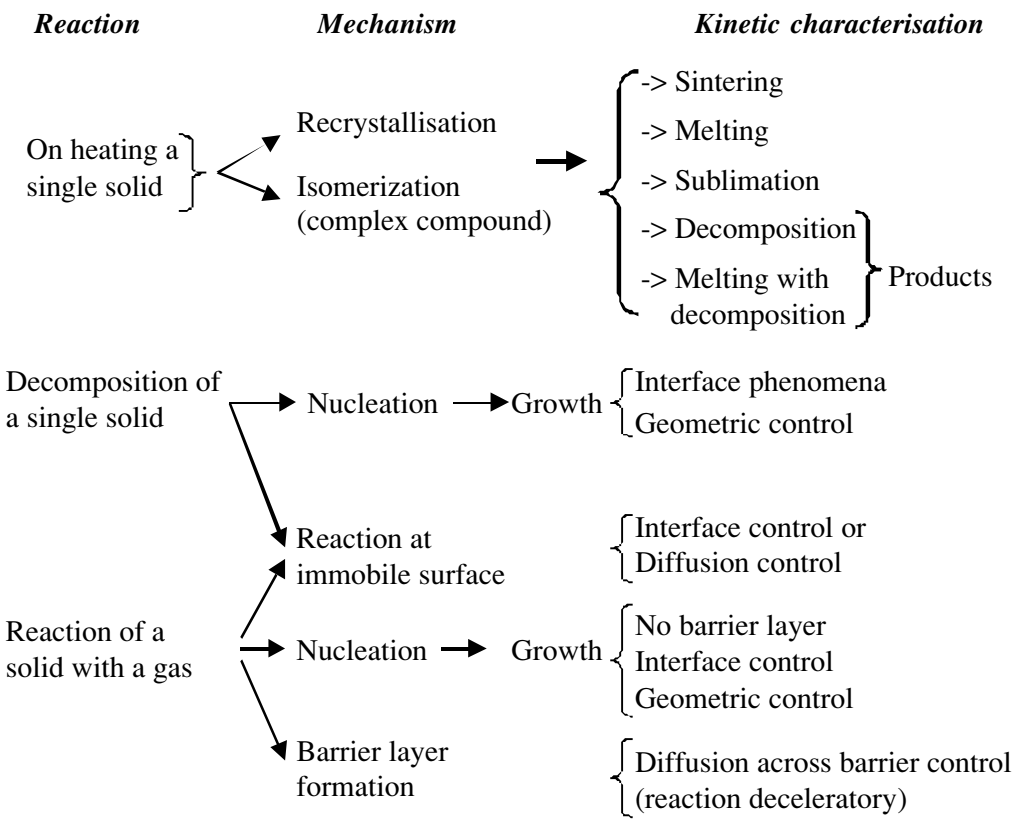

Table 5: Reactions of solids. Scheme of reaction pathways indicating relationships with kinetic characterisation[59]

Sintering processes are very often studied as phenomena distinct from the decomposition reaction. Growth of particle sizes of reactant and/or product at the decomposition temperature may influence kinetic characteristics[71]. The shape of α - t curves are sensitive to the relative ease of nucleation: where many product particles are formed rapidly at the onset of reaction, the rate process is decelatory throughout, whereas the slow development of a restricted number of nuclei results in a sigmoid shaped α - t relation.

Two alternative methods have been used in kinetic investigation of thermal decomposition and, indeed, other reactions of solids:

i) isothermal where yield - time, measurements are made while the reactant is maintained at a constant (known) temperature

ii) dynamic or non-isothermal, where the sample is subjected to a controlled rises temperature.

The kinetic investigations using the dynamic approach is governed by the equation 11:

$$d\alpha/dt = Af(\alpha)\exp\left(-E/RT\right) \qquad \textit{Eq 11}$$

where α is fraction reacted; t is the time, A pre-exponential factor, E activation energy, R gas constant, T temperature.

It is sometimes argued that it may be possible to vary temperature in a systematic and controlled manner and so determine the complete kinetic behaviour (f(α)-time, A and E).

Assuming these requirements to be met, the kinetic analysis requires comparison of measured (α, T, t) data with an appropriate form of (equation11).

The kinetics of solid state reaction followed for different gaseous atmospheres and temperature have to considered:

- ✓ there may be a period of initial relatively slow growth of nuclei;
- ✓ the rate of interface extension across a surface may be different for rate of bulk penetration;
- ✓ reactivity of surfaces and rates of interface advance may vary with crystallographic direction;
- ✓ subsidiary interfaces may develop from the reactant/product contact resulting in a zone, rather than a surface, of reaction;
- ✓ the volume of product will generally be different from that of the reactant from which it was derived, and thus the effective interface may not extend across the whole surface of the nucleus;
- ✓ in reversible reactions, a volatile product may be absorbed on the surface of the residual phase and diffusive escape from the reaction interface may be hindered;
- ✓ diffusion control may become significant in reversible reactions;
- ✓ the size and distribution of sizes of reactant particles may influence kinetic characteristics of rate processes[60].

The kinetic data for the different systems have been collected using programmed temperature experiments. This method for the kinetic parameter characterisation it is difficult to place confidence in the individual values of Arrhenius parameters, because two parameters vary at the same time; the temperature and the reaction yield (some times also the partial pressures).

For heterogeneous reactions where it is considered that the combination of various elementary steps such as nucleation and growth, occur in different regions the following theorem that "separates" key parameters may be used to develop the kinetic modelling[72].

$$d\alpha/dt = \phi(Y_i) \cdot E(x) = \phi(Y_i) \cdot E(t, Y_i(0,t)) \qquad \textit{Eq 12}$$

where dα/dt is the reactance, Φ the reactivity and E the space function. Φ is a function of the intensive stresses (temperature and partial pressure) and thus not depend on time, and E is a function related to the shape and size of the region in which the rate-limiting step occurs. In heterogeneous reaction two reactivities may be found, one for the nucleation and a second for the growth. As a consequence of this theorem it will be possible to establish separate models for the kinetics of a reaction: those corresponding to the space function will be called "geometrical model" and those corresponding to the processes of nucleation and growth will be called "physico-chemical" model[73]. The theorem of the separation model is

also useful when the transformation involves a modification of the texture of the initial solid. It is also a pathway to obtain information on the behaviour solid transformation in non-isothermal and non-isobaric conditions[73].

The kinetics of U_3O_8 reduction studied under a hydrogen atmosphere under non-isothermal conditions showed a complex behaviour involving steps of nucleation and anisotropic growth in which the rate limiting step of growth is located at the external interface[74]. The same sample was investigated in more detail under isothermal and isobaric conditions and the previous mechanism proposed was fitted with an appropriate model. This was possible by making a sudden change in the reaction temperature for different yield of reaction. A good correlation was found between the calculated and experimental $d\alpha/dt$ *vs.* α curves and the hypothesis made was thus confirmed by another route[75].

1.3.2 Conclusions

In order to establish a kinetic model for a solid state transformation it is important to control in detail the partial pressure of gases where the transformation process takes place. The shape of the kinetic curves can be affected by the powder texture such as the size of the primary particles, their preferential organisation, function of the crystallographic orientation. Single crystals of a sufficiently large size for a decomposition study are often difficult to obtain. Studies using individual well-defined and relatively perfect crystals can, in principle, provide deeper insights into the factors controlling the reaction than some others studies putting forth the use of less well-defined reactants, such as powders, with a range of particles size. Work with a single crystal enables the relative reactivities of the different crystals faces to be compared. Such ideal reactants differ considerably from the type of material usually used in industrial processes where reactants are often fine powders. Particle size and crystal perfection are often important parameters in controlling the reactivity of a solid reactant sample, so that single crystals are preferable in mechanistic studies[76].

A link between the kinetic model and the thermodynamic data can help tailor powders with desired properties mixed phases, size of primary particles and surface area one of the aim of this thesis.

For the phases involved during the transformation the more coherent analyses are the diffraction patterns *in-situ* measurements which seem to give the most representatives results.

1.4. Aim of the thesis

Finally the above concepts will be used to study the precipitation of the copper oxalate to further shed light on the growth mechanism from the earlier stage of precipitation to final particles. Previous studies used classical tools, such as X-ray diffraction, microscopy and solubility calculations as the starting and end points only of the synthesis. The precipitation was previously studied in the presence of a mother liquor in a large volume of 250 ml, using a fed batch reactor were the control of early stages of precipitation was difficult to monitor and model. The proposed "brick by brick" model was developed using *ex-situ* characterisation of final particles only.

To put it in a nutshell, this thesis work aims at further elucidating the proposed mechanism of copper oxalate precipitation. The literature has stressed out the influence of supersaturation and of the organic additives on particle formation and nanostructure organisation for several systems. The effect of ionic species in solution and their complex formation has also seen to play an important role on the stability and growth of the nanoparticles. This thesis will try and highlight the effect of complex formation in well-defined conditions of precipitation and pH evolution on particles precipitation. The aggregation process has been considered to be a consequence of forces involved among the particles in suspension, depending on size, surface energy and anisotropy of nanoparticles. These factors govern the route of particles formation from the earlier stage to final aggregates is they ordered or disordered. The early stages (first burst of nucleation) in general are difficult to study because of the small particles size (less than 10 nm) and rapid kinetics (less than one second). Attempts to get more information on this key stage of copper oxalate precipitation will be made using SAXS, successfully applied in several others precipitation systems.

Thus, this thesis' main goal is to produce metallic copper conserving the initial particle morphology and nanostructure. The transformation of the copper oxalate into metallic copper has not been much studied. The mechanism of the transformation will also be investigated in more detail than is usually made in the literature by following the kinetics of transformation. The transformation of copper oxalate and copper oxide nanostructured particles with cubic morphology will be made under a reducing atmosphere. The kinetic modelling will apply the separation model by making several sudden changes in isobaric and isothermal conditions, to help understand the mechanism and allow better control of nanostructure evolution.

Very little work has been previously carried out on either the co-precipitation of the synthesis of nanostructured bulk Cu/Co composites. A preliminary investigation of the possible co-precipitation of Co-Cu oxalate/oxide particles by using several methods, such as: simple co-precipitation of the oxalates or seeds of Co oxalate or oxide will be made.

Chapter 2. Copper oxalate precipitation

2.1. General introduction

This chapter describes the strategy used for the precipitation of copper oxalate nanostructure particles. Previous studies of N. Jongen[7] (1998) were made at concentrations of $2.4 \cdot 10^{-2}$ M at room temperature in a fed batch reactor of 250ml volume. These previous studies were focused more on particle morphology, and the influence of the organic additives like Hydroxylpropylmethylcellulose (HPMC) on particle shape evolution and substructure. All this work was undertaken in a fed batch reactor where it is difficult to follow the kinetic parameters, and the nanostructure evolution as a function of the degree of supersaturation. The current study used a smaller (25 ml) batch reactor in well-mixed conditions, which will allow the investigation of particle growth as a function of time. The use of a well-mixed batch reactor also allows the link between the solution chemistry and particle growth to be made.

Several experimental tools were used for the particle nanostructure characterisation. At first, the solution chemistry was studied using thermodynamic solubility calculations to follow the process of the precipitation. Then, further characterisation of particles nanostructure as a function of reaction yield (time) by different methods such as SEM, AFM and TEM cross-section were carried out. By putting together the available data of the ion concentration, ionic strength, particle size distribution and particle substructure, it becomes possible to evaluate a physico-chemical model for particle evolution during the precipitation of copper oxalate in aqueous solutions.

2.2. Copper oxalate precipitation - Theory & Procedure

2.2.1. Solution Chemistry

The precipitation of copper oxalate was carried out in aqueous media at room temperature using salts of sodium oxalate and copper nitrate in a stoichiometric ratio. Modelling of the solution chemistry as a function of precipitation yield presents a tool to follow and understand a kinetic model of the precipitation. The knowledge of the solubility equilibrium in a large variety of experimental conditions provides a relatively efficient and simple method of following facts that cannot easily be shown experimentally. These types of calculations take into account the effect of the presence of many species. For this proposes an iterative procedure will be used similar to that described by M. Donnet[12] (2002). The numerical calculations consider much different equilibrium, including dissolution, protonation and

complex formation that must satisfy electrical neutrality. These are well studied for the copper oxalate as well as for the copper and cobalt oxalate systems[81].

As input parameters the typical characterisation of the precipitation system uses concentration of solutions, temperature, carbonic gas partial pressure p_{CO2}, pH. The degree of supersaturation directly influences the rate of nucleation and growth, which in turn can affect the rate of aggregation. From the solubility calculations alone the correlation of system parameters such as pH and yield cannot be directly fixed as a function of time. Thus for the comparison of the kinetics between the experimental and theoretical some points have to be fixed.

For the reaction of the ions in solution, the rate of reaction depends not simply on the ions concentration, but moreover on the activity coefficient γ. In dilute solutions the interaction of the ions is low enough, the activity coefficient value is close to 1. The relation between the concentration and the ion activity in solution is given by:

$$\left(M_i\right) = \left[M_i\right] \cdot \gamma \qquad \textit{eq 13}$$

where (M_i) is the ion activity, $[M_i]$ the ion concentration.

The activity coefficient γ depends on ionic charge, the ionic strength of the solution and the radius of the ionic species, and can be calculated using the Debye -Hückel approximation:

$$\log \gamma_i = -A \cdot Z_i^2 \cdot \frac{\sqrt{I}}{1 + B \cdot r \cdot \sqrt{I}} \qquad \textit{eq 14}$$

where $A = 1.8246 \cdot 10^6 \ (\varepsilon T)^{3/2}$ ($mol^{-3/2}L^{1/2}K^{3/2}$) and $B = 502.9 \ (\varepsilon T)^{1/2}$ ($nm^{-1}\ mol^{-1/2}L^{1/2}K^{1/2}$), ε is the solvent dielectric constant (for water $\varepsilon = 251.629 - 0.803 \cdot T + 0.000744 \cdot T^2$) T is the temperature in Kelvin, r_i is the recovering radius of the ionic species in nm and I is the ionic strength. Equation 14 gives a good estimation of the activity coefficient if the value of ionic strength is ≤ 0.1mol/L. If the value of the ionic strength is higher several corrections parameters[24] must be added.

The ionic strength of a solution is defined as:

$$I = \frac{1}{2} \cdot \sum Z_i^2 \cdot \left[M_i\right] \qquad \textit{eq 15}$$

where Z_i is the valency of ion *i* and $[M_i]$ is the molar concentration.

If one considers the simple reaction dissolution/precipitation, in this study copper oxalate, the chemical equilibrium could be written as:

$$CuC_2O_{4(s)} \leftrightarrow Cu^{2+}_{(aq)} + C_2O_{4(aq)}^{2-} \qquad \textit{eq 16}$$

Each reaction of dissolution is characterised by an equilibrium constant denoted as K_s and defined as:

$$K_s = (Cu^{2+})_{eq} \cdot (C_2O_4^{2-})_{eq} \qquad \textit{Eq 17}$$

where K_s is called constant solubility at which is the value of the activity product at equilibrium.

The relation between the ionic activity in solution for dissolution and the free energy of dissolution is given by:

$$\Delta G_s = \Delta G_s^0 + RT \ln\left[\left(Cu^{2+}\right)\cdot\left(C_2O_4{}^{2-}\right)\right] \qquad \textit{eq 18}$$

where G^0 is the standard free energy of dissolution, R is the gas constant, and T is the temperature in Kelvin. At equilibrium ΔG_s is equal to zero and the free energy of dissolution is:

$$\Delta G_s^0 = -RT \ln\left[\left(Cu^{2+}\right)_{eq}\cdot\left(C_2O_4{}^{2-}\right)_{eq}\right] = -RT\ln(K_s) \qquad \textit{eq 19}$$

The free energy of dissolution depends on the ionic product of the species in at equilibrium solution and the solubility constant.

$$\Delta G_s = -RT\ln(K_s) + RT\ln\left[\left(Cu^{2+}\right)\cdot\left(C_2O_4{}^{2-}\right)\right] = RT\ln\left(\frac{P_s}{K_s}\right) \qquad \textit{Eq 20}$$

The variation of the free energy of dissolution represents the energetic state of the system of precipitation. In equation 20, P_s is called the solubility product and is defined using the activity ions concentration in solution out of equilibrium[77],[78]:

$$P_s = \left(Cu^{2+}\right)\cdot\left(C_2O_4{}^{2-}\right) \qquad \textit{Eq 21}$$

The supersaturation is expressed as S:

$$S = \ln\left(\frac{P_s}{K_s}\right) \qquad \textit{Eq 22}$$

A system under investigation can be found in three distinct conditions as a function of S:

- ✓ if $P_s > K_s$, $S > 0$: the solution is supersaturated and the process of precipitation takes place
- ✓ if $P_s < K_s$, $S < 0$: the solution is undersaturated and the dissolution is expected
- ✓ if $P_s = K_s$, $S = 0$: the system under investigation reaches the equilibrium state, $\Delta G = 0$.

During the entire thesis the chosen definition of the supersaturation is:

$$S^* = \frac{1}{x}\cdot\log\left(\frac{P_s}{K_s}\right) \qquad \textit{Eq 23}$$

S* is called the reduced supersaturation, where x is the number of the primary ionic species released by the dissolution process. In this case x is 2 because the only ions for the precipitation/dissolution involves are Cu^{2+} and $C_2O_4{}^{2-}$. If there are more complex solids involved in the precipitation/dissolution system such as $CuCO_3{\cdot}Cu(OH)_2$, x is 5 because of 2 ions of Cu^{2+}, one ion of $CO_3{}^{2-}$ and 2 ions of HO^- ions.

A simpler definition of supersaturation is often used in the literature[48] as: $S = \sqrt{P_s / K_s}$.

Based on the considerations above, the supersaturation of the copper oxalate in a solution for a precursor concentration of 0.005 M can be calculated taking into account all possible complexes that can form in solution using the copper ions activity. For the copper oxalate, the formation of ion-pairs, considering the activity (i.e. equation equation 23), S* is 0.70.

Data for the solid phases used in the following solubility calculations are listed in Table 6. The approach taken here considers all complex formation in solution as a function of pH, as described in Table 7. The supersaturation is then calculated from the activities of the Cu^{2+} and $C_2O_4^{2-}$ ions actually present in solution (eq 23).

Table 6: Dissolution reactions taken into account for the copper oxalate system at 25°C

Chemical	Chemical	Reaction	pKs
Copper oxalate (Moolite)	$CuC_2O_4 \cdot 0.5\ H_2O$	$Cu^{2+} + C2O_4^{2-} + H_2O$	9.65
Copper carbonate	$CuCO_3$	$Cu^{2+} + CO_3^{2-}$	9.63
Azurite	$2CuCO_3 \cdot Cu(OH)_2$	$3\ Cu^{2+} + 2CO_3^{2-} + 2OH^-$	33.78
Malachite	$CuCO_3 \cdot Cu(OH)_2$	$2\ Cu^{2+} + CO_3^{2-} + 2OH^-$	45.95

Table 7: Complex formation in solution for the system: $Cu(OH)_2$-$H_2C_2O_4$-(CO_2)-[HNO_3-NaOH]-H_2O

Number	Reaction	Log $K_{298}^{(79)}$
1	$HO^- + H^+ \rightarrow H_2O$	13.99
2	$C_2O_4^{2-} + H^+ \rightarrow HC_2O_4^-$	1.25
3	$HC_2O_4^- + H^+ \rightarrow H_2C_2O_4$	4.26
4	$Cu^{2+} + HO^- \rightarrow Cu(OH)^+$	6.00
5	$Cu(OH)^+ + HO^- \rightarrow Cu(OH)_2$	4.70
6	$Cu(OH)_2 + HO^- \rightarrow (Cu(OH)_3)^-$	3.50
7	$(Cu(OH)_3)^- + HO^- \rightarrow (Cu(OH)_4)^{2-}$	2.20
8	$2\ Cu^{2+} + Cu(OH)_2 \rightarrow (Cu_2(OH)_2)^{2+}$	6.93
9	$Cu^{2+} + C_2O_4^{2-} \rightarrow CuC_2O_4^0$	5.71
10	$CuC_2O_4 + C_2O_4^{2-} \rightarrow (Cu(C_2O_4)_2)^{2-}$	4.62
11	$Cu^{2+} + HC_2O_4^- \rightarrow Cu(HC_2O_4)^+$	2.90
12	$CuCO_3 + CO_3^{2-} \rightarrow (Cu(CO_3)_2)^{2-}$	3.17
13	$Cu^{2+} + CO_3^{2-} \rightarrow CuCO_3$	6.75

Table 8: Diameters of hydrated ions at 298K

Ionic species	Diameter (nm)[79]
Cu^{2+}	0.60
HO^-	0.35
H^+	0.90
$C_2O_4^{2-}$	0.45
$HC_2O_4^-$	0.40
$Cu(OH)^+$	0.30
$Cu(OH)_3^-$	0.30
$Cu(OH)_4^{2-}$	0.45
$Cu_2(OH)_2^{2+}$	0.50
$Cu(C_2O_4)_2^{2-}$	0.50
$Cu(HC_2O_4)^+$	0.50

These data permit us to estimate another important parameter of precipitation, the reaction yield of the precipitation ξ, which is defined as:

$$\xi = \frac{\{Cu\}_0 - \{Cu\}}{\{Cu\}_0 - \{Cu\}_{eq}} \qquad \textit{eq 24}$$

For example in the case of a 1:1 electrolyte, which is the case for the copper oxalate, a copper ion needs an oxalate ion for the precipitation of a mole of the oxalate. The reaction yield varies from 0 in the initial stage up to 1 where the reaction equilibrium is achieved.

Example of solubility data for copper oxalate

For a simple reaction of the precipitation of two salts, namely the formation of the copper oxalate from copper nitrate and sodium oxalate, it is possible to calculate the distribution of various species in solution as a function of pH. This type of calculation was made for the system $Cu(OH)_2$-$H_2C_2O_4$-(CO_2) -$(HNO_3/NaOH)$-H_2O at 25°C, for a ion concentration of Cu = C_2O_4 = 0.005 M. In a first step the pH value of the solution was calculated to be around 5.34 under a partial pressure of carbonic gas of $p_{CO2} = 3.3 \cdot 10^{-4}$ bar. Then the pH values were modified adding HNO_3 to the solution for an acidic pH or NaOH for a basic pH. The simulation results of the copper ionic species distribution in solution as a function of pH are shown in Figure 9. In a pH range from 2 to 7 the dominant species contain the copper ions is the neutral oxalato, $CuC_2O_4^0$. Another part of the copper is found in the complex $Cu(C_2O_4)_2^{(2-)}$, or it exists as free ion Cu^{2+} . The other species seem to be present in minor quantities.

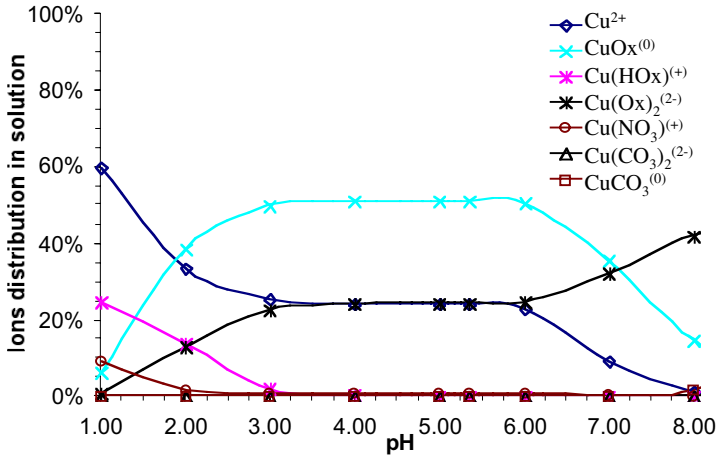

Figure 9: Copper ionic species distribution in solution as a function of pH and their complex formation for the system $Cu(OH)_2$-$H_2C_2O_4$-(CO_2)-HNO_3-NaOH-H_2O (whereC_2O_4 = Cu)

By using this tool it is possible to access to the reaction yield as a function of pH. For copper oxalate precipitation the yield of reaction was simulated, with or without carbonic gas with a partial pressure of $3.3 \cdot 10^{-4}$ bar as illustrated in Figure 10. These simulations were based on the hypothesis that the precursor solutions are stoichiometric 1:1 (Cu/C_2O_4 = 1) at room temperature. In the first step the initial pH was estimated at all precipitate phases able to be formed in solution in these conditions were found. Then the pH was modified by changing the supersaturation values of the copper oxalate, in this case from 0.72 to equilibrium 0. The supersaturation was calculated using the eq. 23.

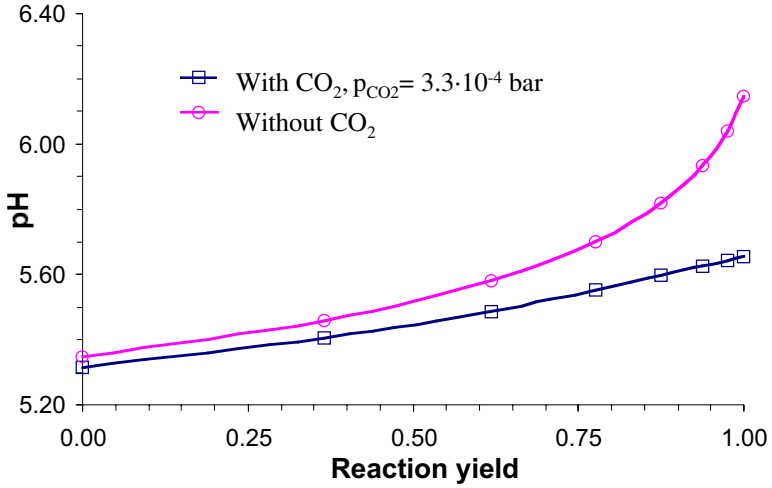

Figure 10: pH evolution as a function of reaction yield with and without the influence of the partial pressure of carbonic gas

Figure 10 shows the pH evolution as a function of the reaction yield at a concentration of 0.005M after mixing of the precursors. The presence of the carbonic gas seems to have an important influence on the pH behaviour. The large increases of pH from 5.40 to 6.20 was obtained without carbonic gas,

whereas a smaller increase from 5.31 to 5.65 was obtained in the presence of carbonic gas of $3.3 \cdot 10^{-4}$ bar. These curves show the sensitivity of the copper oxalate precipitation to the pressure carbonic gas.

Using this simulation approach in the system $Cu(OH)_2$-$H_2C_2O_4$-(CO_2)-$(HNO_3/NaOH)$-H_2O at 25°C it is possible to draw the supersaturation, S, as a function of pH evolution (Figure 11 a). If there is carbonate in the precipitation system it is possible to precipitate several copper compounds such as copper oxalate (Moolite), Malachite ($CuCO_3 \cdot Cu(OH)_2$) and Azurite ($2CuCO_3 \cdot Cu(OH)_2$). S has been calculated as a function of pH for different p_{CO2} values (Figure 11 a and b).

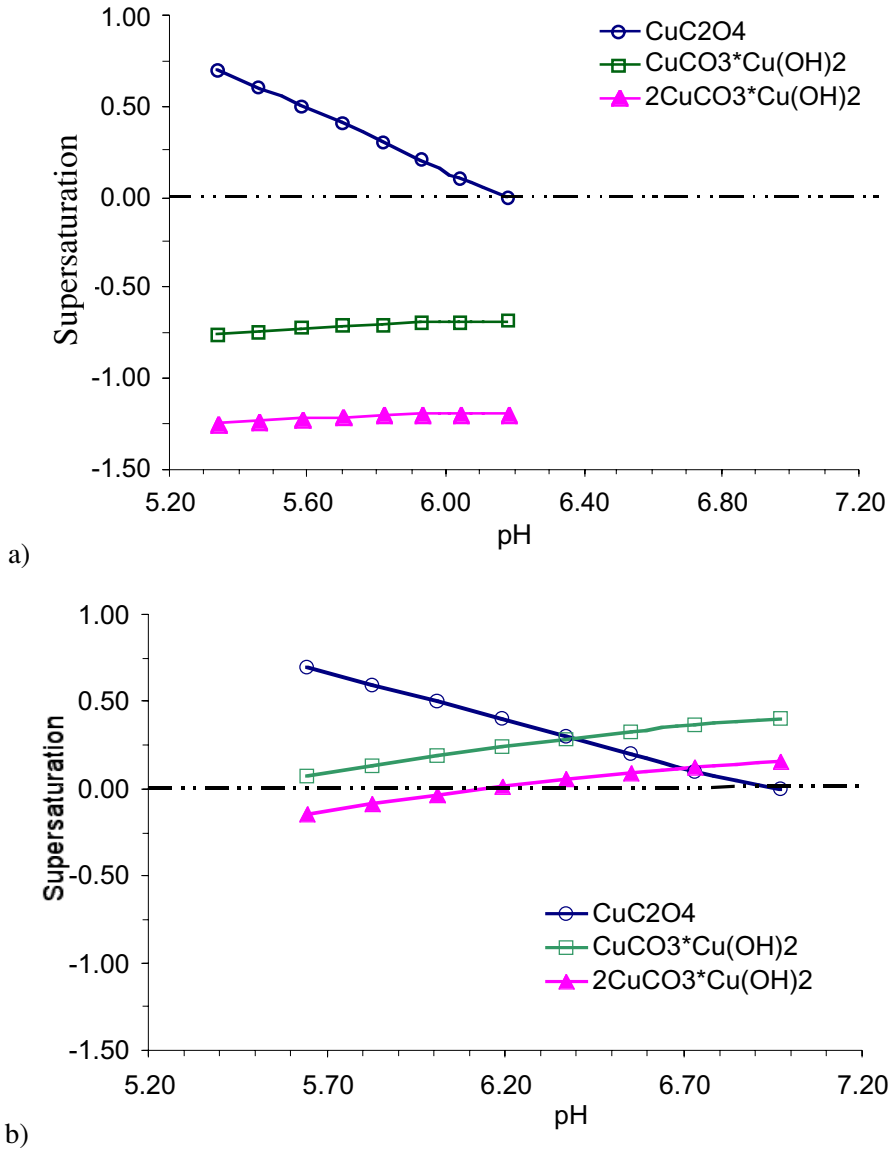

Figure 11: Copper oxalate precipitation as a function of pH: a) the phases likely to precipitate without carbonic gas in the system; b) the phases likely to precipitate in the presence of a carbonate concentration of 10^{-5} M ($p_{CO2}=2.66 \cdot 10^{-4}$ bar)

It is important to note that with the low p_{CO2} only copper oxalate can precipitate. The other solid phases malachite and azurite are undersaturated (Figure 11a). However, a small increase in the amount of carbonate in the system changes the phase equilibrium and the formation of two hydroxy carbonates of copper azurite and malachite becomes possible. As the supersaturation of the copper oxalate decreases (increasing pH) the supersaturation values of malachite and azurite increase (Figure 11 b).

Experimentally, it is possible to follow the pH behaviour as a function of time and compare them with the theoretical values. Using this simulation tool is possible to estimate the reaction yield of copper oxalate precipitate as a function pH, in well-defined conditions of temperature and partial pressure of carbonic gas. The employment of this tool facilitates the understanding of the thermodynamic behaviour of the precipitation.

The chemistry of the copper oxalate solutions is complex because the copper not only forms strong complexes with oxalate but there is also the possibility of carbonic gas adsorption and the precipitation of the above phases. Copper hydroxides are not precipitated from these solutions, but the large number of carbonates, particularly basic carbonate solids of different composition indicate that many complexes of different constitution may exist in solution. The above simulations stress the fact that the influence of all species that must be taken into account in the description of the precipitation and the chemistry may be controlled by complicated equilibrium. The chemistry of the solution and the supersaturation of different solids play an important role in determining the real route of precipitation and to correlate them with the early stage during nucleation, growth and the rate of aggregation, should help towards a better understanding of precipitation reactions.

2.2.2. Copper oxalate precipitation - Procedure

A. Experimental approach and solution control

The reactants used to carry out the precipitation experiment were copper nitrate (Merck 1.02753 p.a.) and sodium oxalate (Merck 1.06557 p.a.). The solutions were prepared by diluting the necessary amount of powder in ultrapure water. The ultrapure water was boiled and filtered at 200 nm in order to avoid possible dust. Both stock solutions were then filtered using a ceramic membrane of 20nm (Whatman). The exact concentration of the stock solution of copper nitrate was measured by Inducting Coupled Plasma Atomic Emission Spectroscopy (ICP-AES, Perkin-Elmer). The experiments of precipitation were carried out by mixing 10 ml of copper nitrate at a concentration of 0.010 M and 10 ml sodium oxalate at a concentration of 0.01 M. The precipitation was accomplished at room temperature in a small volume of 20 ml, by rapid injection during 6 seconds, allowing us to assume that the precursors were well mixed. The reactants were injected at high speed (127cm/s) into the bottom making sure that

mixing energy is sufficient. The mixing time was estimate to be less then 50 miliseconds[12]. In these conditions we measured the pH for a period up to 90 minutes. The reactor design is shown in Figure 12.

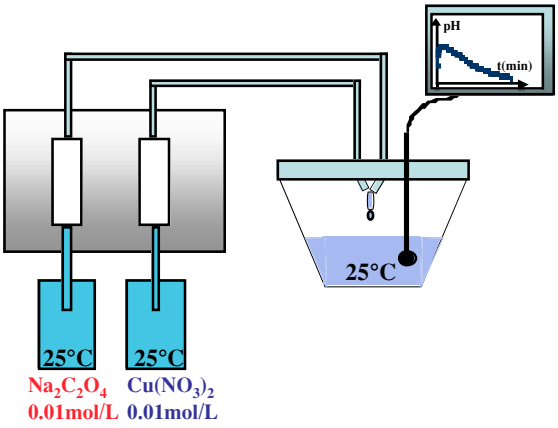

Figure 12: The design of the small reactor used for the precipitation of the copper oxalate

In the previous section the possible influence of the carbonic gas on copper oxalate precipitation was mentioned. Both precursor solutions were stored in a chamber where the p_{CO2} was controlled with a carbonate/bicarbonate solution. The aqueous solution of 0.10M $NaNO_3$ and 0.01M $NaHCO_3$ was prepared under the same conditions as the precursors (with the boiled water and filtered through 200 nm). This solution at room temperature should have a CO_2 partial pressure of $3.3 \cdot 10^{-4}$ bar and a pH of 8.11. After reaching the equilibrium with CO_2 of atmospheric pressure in the chamber the pH of the solution should increase to a value of 9.04. In these conditions it is possible to estimate the p_{CO2} in the chamber. The pH values of the three solutions were measured just before and after an ageing time of 3 days in the chamber, as indicated in Table 9.

Table 9: pH values of standard and precursor solutions before and after equilibrium with the carbonic gas in the chamber

Solution	Initial pH	Final pH
$Na_2C_2O_4$	7.65	7.14
$Cu(NO_3)_2$	4.64	4.69
$NaNO_3$-$NaHCO_3$	8.19	8.88

The partial pressure of CO_2 in the chamber was calculated using the pH values of the carbonate-bicarbonate solution. Considering this value and the pH measurement of copper nitrate and sodium oxalate it is possible to estimate the amount of the carbonate dissolved in the solution using thermodynamic data.

To fit the experimental to the theoretical pH behaviour for copper oxalate precipitation it is necessary to calculate the stoichiometry of the precursor solutions $Na^+ /C_2O_4^{2-}$ and Cu^{2+} / NO_3^-. The results are summarised in Table 10.

Table 10: Carbonic gas dissolving in both precursor solutions and their stoichiometry

Solution	Carbonic (mol/L)	stoichiometry
$2\ Na^+ / C_2O_4^{2-}$	1.48e-04	1.01
$Cu^{2+} / 2\ NO_3^-$	1.83e-05	1.00

For a first approach for the copper oxalate precipitation the reproducibility of the reaction was investigated (Figure 13).

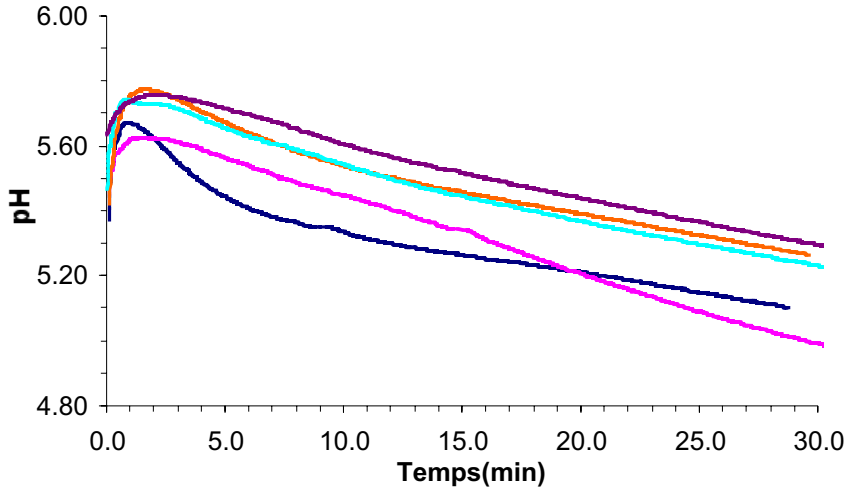

Figure 13: pH evolution as a function of time for several precipitations experiments with a concentration of 0.005M of copper nitrate and sodium oxalate

In the first few minutes the pH increases rapidly to a maximum value of 5.80 and then slowly decreases in time to around 5.20. The general allure of each experiment is similar with variation of ± 0.2 pH units in the 5-30 minutes region.

Table 11: Summary of the samples studied in the mini-batch reactor with the concentration of the precursors and the organic additive concentration

Name of sample	Precursor concentration (mol/L)	Organic additive HPMC (g/L)	Supersaturation CuC_2O_4
W_000	*0.005*	*0.000*	*0.69*
W_005	*0.005*	*0.005*	*0.69*
B_000	0.025	0.000	0.99
B_125	0.025	0.125	0.99
B_500	0.025	0.500	0.99
B_1000	0.025	1.000	0.99
C_000	0.050	0.000	1.10
D_000	0.100	0.000	1.22

Table 11 contains a description of the concentration of the reactants and organic additives for the various copper oxalate precipitates sample studied during this thesis work. Supersaturation values were also calculated using the ions activity in solution as discussed above. The samples W_000 and W_005, were investigated in detail following the particle evolution as a function of reaction time by scanning electron microscopy (SEM,) particles size distribution (PSD), cross - section transmission electron microscopy (TEM), atomic force microscopy (AFM) and X-rays diffraction patterns (XRD). The samples B, C and D have been analysed in detail by SEM, XRD and Small Angle X-ray Scattering SAXS.

B. Results and comparison with simulation

In chapter 2.2.1. the theoretical behaviour of pH in standard conditions of precipitation has been discussed (0.01M copper nitrate and 0.01M sodium oxalate). The samples showed an increase of the pH in both cases with or without carbonic gas at $p_{CO2} = 3.3 \cdot 10^{-4}$ bar. The experimental and simulated curves as a function of time show a significant discrepancy (Figure 14). At the beginning both curves show the same behaviour the pH increases. Then the experimental curve decreases instead of the continuous increase, seen for the theoretical curve. The link between the theoretical curve of the pH and time has been done by the analytical concentration of copper measured by ICP-ASE and calculated as a function of time.

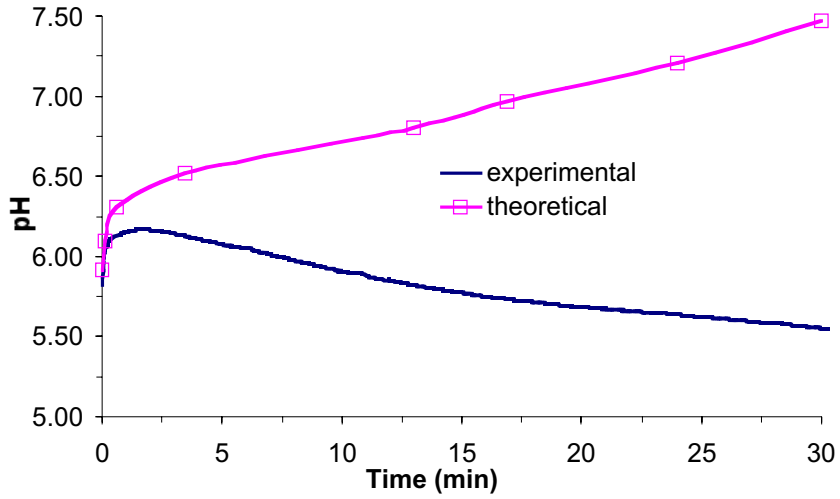

a)

Figure 14: Experimental and theoretical pH evolution as a function of time for the copper oxalate precipitation

Four hypotheses were made to try and understand the difference between the experimental and calculated pH evolution.

1. *first hypothesis* - precipitation of one single phase, copper oxalate. The theoretical pH increases as shown in Figure 10, which is not the case, for the experimental pH (Figure 14).

2. *second hypothesis* - two solutions are mixed in an equimolar ratio. The amount of carbonate dissolved is equal to the carbonate content estimated in each solution from thermodynamic calculation at $8.31 \cdot 10^{-5}$ M. We have to remark that the initial solution of sodium oxalate is not perfectly stoichiometric as calculated in Table 10.

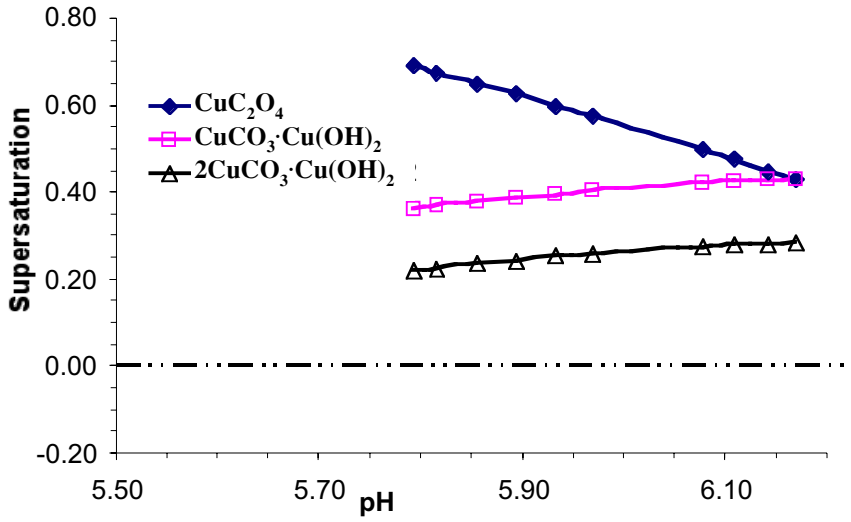

a)

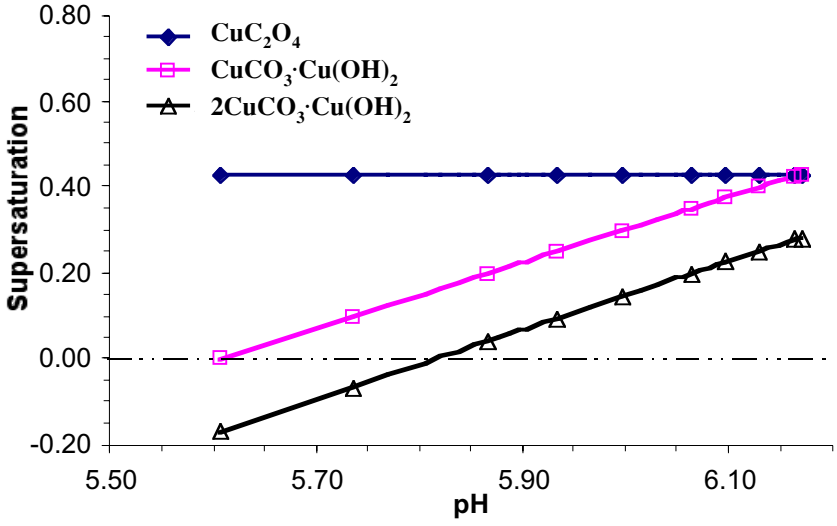

b)

Figure 15: Supersaturation behaviour of copper oxalate, malachite and azurite as a function of pH: a) period of pH increase 0-2 minutes; b) period of pH decrease 2-30 minutes

The pH behaviour was monitored using the thermodynamic approach. In the first part of precipitation the experimental pH increases and then decreases as illustrated in (Figure 14). The beginning has been simulated by copper oxalate precipitation changing the supersaturation value of this phase from 0.69 in the initial stage to 0.42 which corresponds to the maximum pH of 6.17 (Figure 15 a). It was shown (Figure 11 b) that if there is a small amount of carbonate in solution several phases can supersaturate. During the precipitation of copper oxalate, the system starts to supersaturate with respect to the hydroxycarbonic phases of copper as summarised in Table 12. The descent of pH was also simulated by stopping copper oxalate precipitation at S = 0.42. At this point the malachite reaches a supersaturation of about S = 0.42 above that of the copper oxalate. The simulation then considers that only malachite precipitates in this decreasing pH region. The azurite phase saturates but at much lowers value and becomes undersaturated as the malachite precipitates. It was therefore assumed that azurite does not precipitate under these simulation conditions. The evolution of supersaturation as a function of pH is given in Figure 15 b for this decreasing pH region. The precipitation of malachite shows the pH decreasing form 6.17 to 5.60. The supersaturation values at this pH are given in Table 12.

Table 12: Supersaturation value of the three compounds that might be considered at specific values of experimental pH

pH	Copper oxalate CuC_2O_4	Malachite $CuCO_3{\cdot}Cu(OH)_2$	Azurite $2CuCO_3{\cdot}Cu(OH)_2$
6.17	0.42	0.43	0.28
5.60	0.42	0.00	-0.18

3. third hypothesis - the ratio of two precursor solutions is equal to one. For the experimental and theoretical pH are made by varying the amount of carbonate in solution. The amount of carbonate dissolved varies around of $5.77 \cdot 10^{-5}$ M. Theoretical curves obtained using solubility data are illustrated in Figure 16. The same approach was done as for the hypothesis 2, initially copper oxalate precipitates (increasing pH region) then only malachite precipitates (decreasing pH). The supersaturation values of three compounds in solution are given in Table 13; it represents the supersaturation at a maximum pH and following the malachite precipitation.

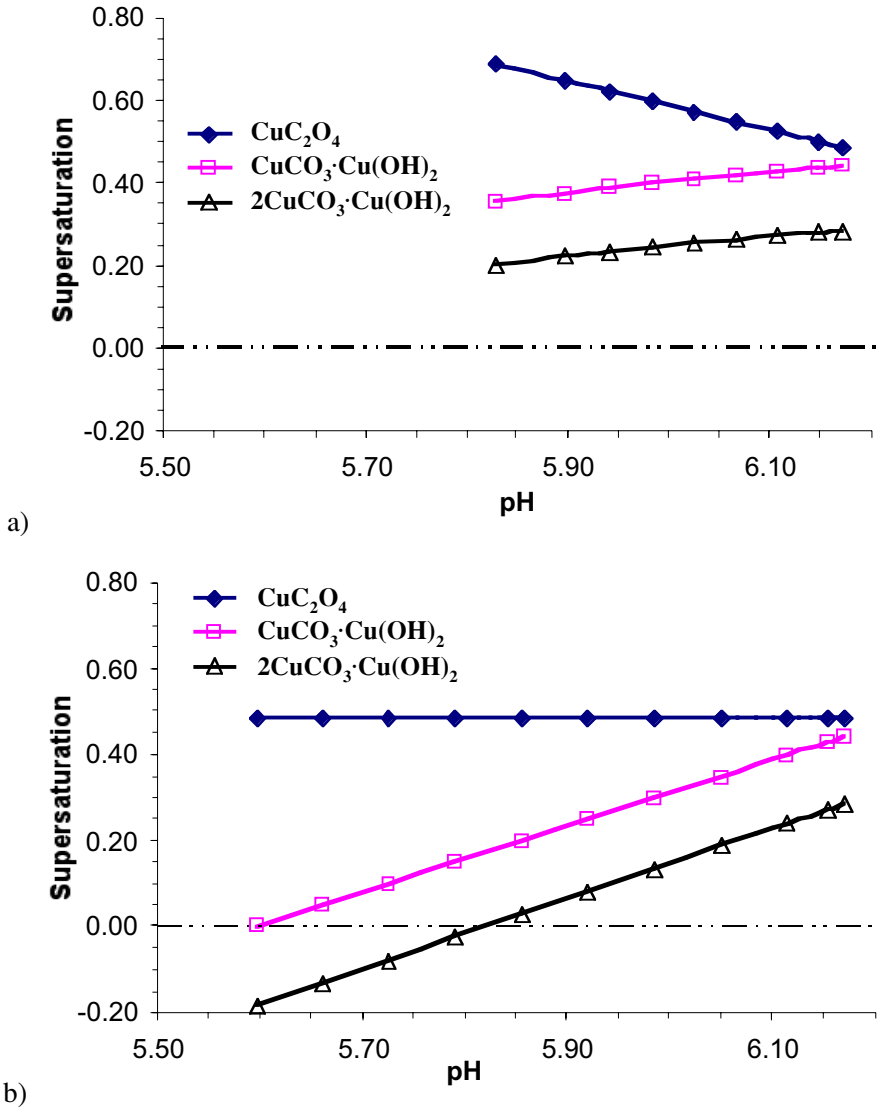

Figure 16: supersaturation behaviour of copper oxalate, malachite and azurite precipitation as a function of pH: a) pH increase; b) pH decreases

Table 13: Supersaturation value of the three compounds that might be considered at a maximum value of the experimental pH

pH	Copper oxalate CuC_2O_4	Malachite $CuCO_3 \cdot Cu(OH)_2$	Azurite $2CuCO_3 \cdot Cu(OH)_2$
6.17	0.48	0.44	0.28
5.60	0.48	0.00	-0.18

The supersaturation of copper oxalate is higher than in the case of hypothesis number 2, for malachite and azurite the supersaturation values are nearly the same as the previous case. The amount of copper oxalate precipitated is 10% wt less than the preceding hypothesis. Again azurite is assumed to not precipitate.

4. *fourth hypothesis* - the two precursor solutions are not in a stoichiometric ratio (given by possible bubble formation in syringes) and the amount of carbonate was recalculated at $8.43 \cdot 10^{-5}$M, taking into account this non-stoichiometric and the fixed initial pH.

For this hypothesis the theoretical simulations were carried out in the same way, as 2 and 3 and the results are shown in Figure 17.

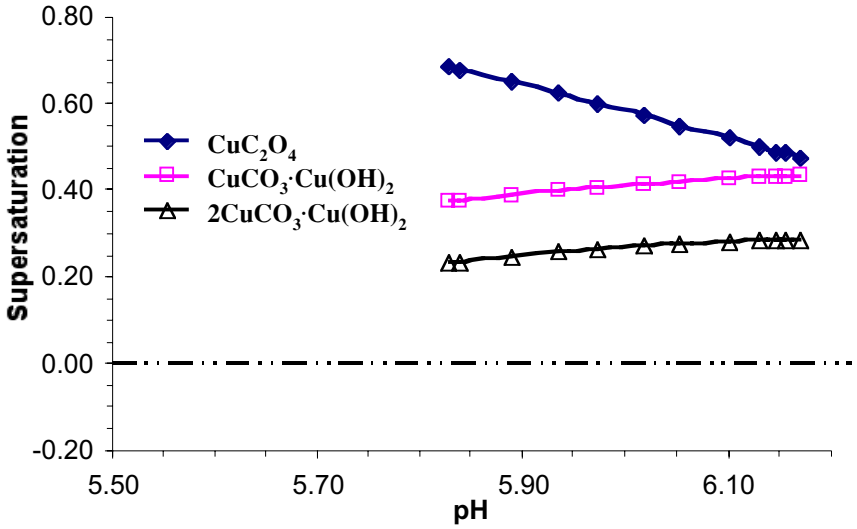

a)

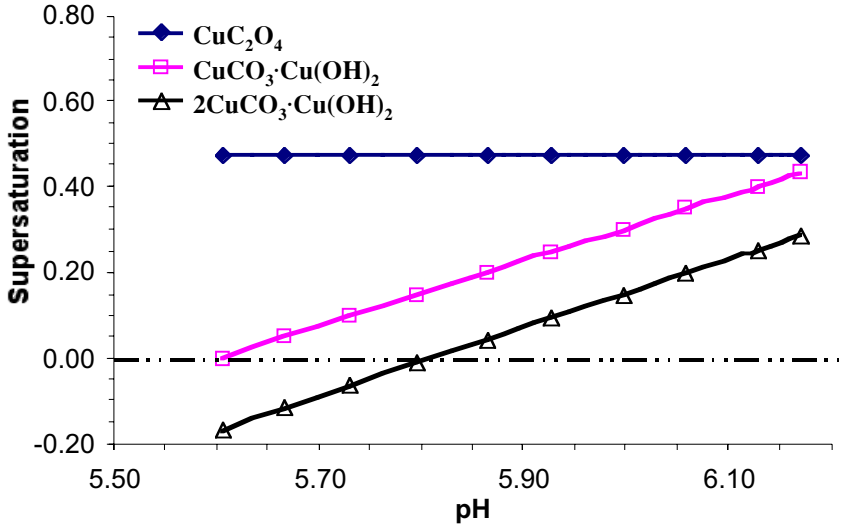

b)

Figure 17: supersaturation behaviour of copper oxalate, malachite and azurite precipitation as pH: a) pH increases; b) pH decreases

In Table 14 the supersaturation values of the simulation at pH 6.17 (maximum value) and their value after total precipitation of malachite are summarised, again using similar values to hypotheses 2 and 3 are found.

Table 14: Supersaturation value of the three compounds that might be considered at a maximum value of experimental pH

pH	Copper oxalate CuC_2O_4	Malachite $CuCO_3{\cdot}Cu(OH)_2$	Azurite $2CuCO_3{\cdot}Cu(OH)_2$
6.17	0.45	0.44	0.28
5.60	0.45	0.00	-0.16

In the cases 2 and 3 the presence of the hydroxy carbonate phases malachite or azurite the supersaturation value of copper oxalate changes slightly from 0.42 to 0.48, whereas the supersaturation of malachite remains constant and the azurite becomes undersaturated.

The case of hypothesis 2 is the only use where malachite has a higher supersaturation than copper oxalate at to pH maximum of 6.17.

The hypothesises 2, 3 and 4 fit well with the experimental curves as illustrated for 2 and 4 in Figure 18.

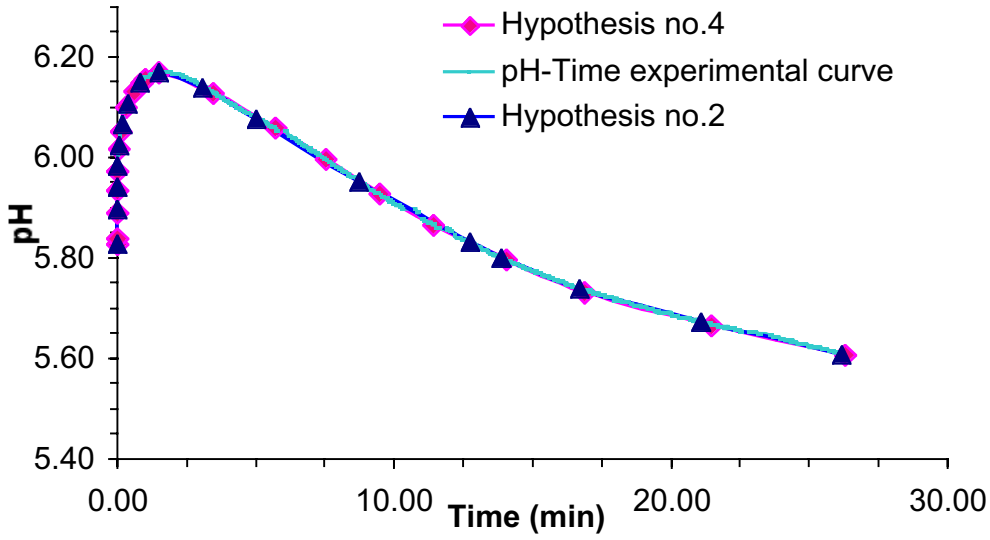

Figure 18: pH behaviour for an experiment and the fit with the hypotheses no. 2 and 4

Figure 18 shows two domains of pH that can be explained by a precipitation of copper oxalate in a short period of time at around 3 minutes. Then the pH decreases slowly in a long period of time where the precipitation of malachite is expected.

Of all these hypothesis able to give a kinetic approach of the pH behaviour the most close to experiments and simulations seem to be the hypothesis number 2 where malachite becomes more supersaturated than copper oxalate and the p_{CO2} is that calculated from the controlled chamber.

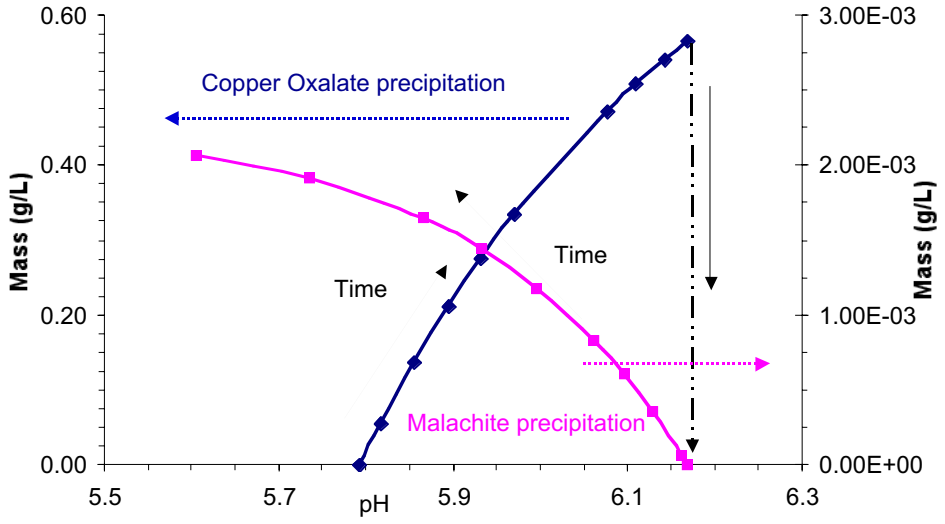

Figure 19: Mass evolution of the copper oxalate precipitation and malachite as a function of the pH in the case of hypothesis 2

The Figure 19 shows the mass evolution of copper oxalate during the precipitation as a function of pH for hypothesis 2. The mass balance indicates a low amount of malachite precipitation of about 0.40 %wt. This small amount has a significant influence on the pH behaviour. This quantity of malachite would

be difficult to detect as will be seen in the later section of precipitate characterisation. At the maximum value of the pH the solution is still supersaturated with respect to oxalate. Ratio of copper oxalate precipitated for hypothesis 2 compared to that expected at equilibrium, as a function of the pH is illustrated in Figure 20. At the maximum value of the pH only 73% wt of the total copper oxalate has precipitated, before the malachite precipitation starts. Under hypothesis 2 the other 27 % wt of copper oxalate can not precipitate i.e. growth is disrupted or equilibrium could be reached between the ionic species in solution and the solids formed at 25°C under these conditions. If the copper oxalate precipitation continue the pH must increase, which is not the case consider the experimental results.

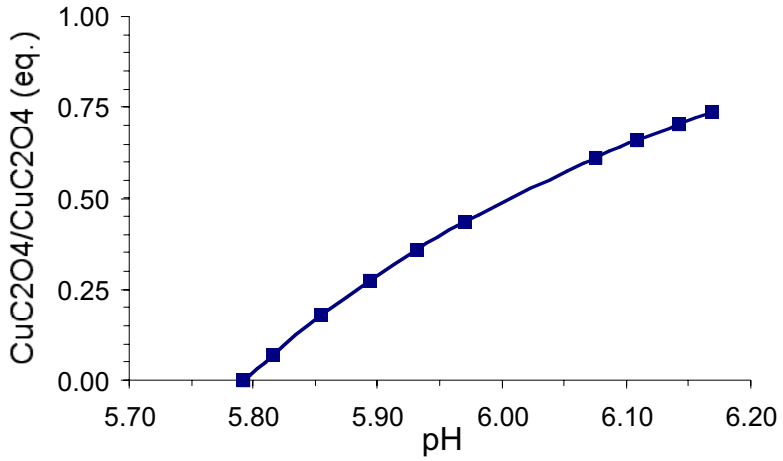

Figure 20: Ratio of copper oxalate precipitated as a function of the pH compared to expected yield at equilibrium

Using this approach of thermodynamic equilibria of several phases involved in precipitation it was possible to make a link between experimental and simulated pH behaviour. It was also possible to estimate the amount of copper oxalate and malachite precipitates, using this method. After a precipitation model that expected a burst nucleation, growth and then agglomeration, we predict the formation of a thin layer of the malachite on the primary particle surface of copper oxalate using only this approach of thermodynamic equilibria. The possible ramifications of this simulation will be discussed in the last section of this chapter in the context of particle formation.

2.2.3. Characterisation methods

A. Microscopy - SEM, HRSEM and TEM

The samples were characterised by high resolution scanning electron microscopy (HRSEM) Philips Sirion XL30-FEG at U = 3KV or 1KV, spot size 3 and a working distance of 5 mm, without coating, to avoid possible artefacts on the nanograins growing on the particles. The samples analysed using SEM (Scanning Electron Microscopy) Philips XLF 30 at 3kV, spot size 3 and working distance of 10 mm, are coated with a thin layer of gold to make them electrically conductive and to eliminate charging effects in the microscope. The samples under investigation have been prepared by deposition of a small

amount of dry powder on an aluminium holder and those collected on ceramic membranes have been investigated directly without any further preparation.

The samples investigated by transmission electron microscopy TEM needed a rigorous preparation. This technique gives an estimation of crystallite size, and the internal organisation of the precipitates. The cross section has been obtained by ultramicrotomy. The dry powder of copper oxalate with cubic morphology was embedded in an epoxy resin matrix of Agar100, dodecenyl succinic anhydride (DDSA), methyl nadic anhydride (MNA) and 2,4,6-tri (dimethylamonimethyl) phenol (DMP 30). The mixture of the resin and powder was put in a drier at 60°C during 12 hours for the polymerisation. Then the block has been cut in a dry environment at room temperature with a 35° Diatom diamond knife (radius of 5nm) mounted on Reichert-Jung Ultracut E ultramicrotom. The thickness of the cross section was of the range of 80nm. The particles structures were studied on a Philips CM 200 TEM operating at 200 kV at room temperature in the case of copper oxalate and Philips CM 430 TEM operating at 300 kV at room temperature for the oxides and metallic copper.

B. X-ray diffraction patterns XRD

XRD was used in order to determine the phase under investigation and then to estimate the coherent crystalline domain, crystallite size.

The diffraction patterns have been collected using two devices. One was the diffractometer SIEMENS D 500 with a copper radiation, U = 40 kV, I = 35 mA and with a window angle of 0.3°, 0.3°, 0.3° and 0.05°. The range under investigation has been chosen as a function of the samples. For example for copper oxalate the range is 20-60°, for copper oxides and copper the range is 20-90°. The step scan is 0.02 and the time for each step is 5 seconds. Quartz was used to estimate the instrumental contribution to the line broadening.

Another diffractometer used during the thesis work was an X-Pert Philips with copper radiation, wavelength λ (Cu $K_{\alpha 1}$) = 0.1506 nm, U = 50 kV I = 40 mA. Samples were rotated in order to minimise textural effects, in a range of 20-90°. This device has been used to characterise the intermediate states of copper oxide transformation into copper metal.

The average diameters of crystallites of powder under investigation were calculated from line broadening of the X-ray powder diffraction (XRD), using the following Scherrer equation (eq 25):

$$l = \frac{K \cdot \lambda}{B \cdot \cos(\theta)} \qquad \textit{Eq 25}$$

where λ is the wavelength of the X-ray source (nm), B is the line width at half of the maximum intensity (radians), Θ is the diffraction angle, l is the average diameter of the crystallites (nm) and K is a factor related to the crystallite shape which is assumed to be 0.89 [80]. Some powder diffractogrammes have been

fitted using TOPAS 2000, a software that takes into consideration the crystallographic parameters. JCPDS files used for the different phases are given in Table 15:

Table 15: JCPDS files used during the thesis work

CuC_2O_4	β-$CoC_2O_4 \cdot 2H_2O$	$CoC_2O_4 \cdot 4H_2O$	Co_3O_4	CuO	Cu_2O	Cu
21-0297	25-250	37-534	42-1467	05-0661	05-0667	04-0836

C. Atomic Force Microscopy - AFM

Certain samples were characterised in more detail using Atomic Force Microscopy AFM, Park Instrument Autoprobe CP, 0.6 µm "Ultralever SIN, contact mode: force ~ 1-2 nN. The samples under investigation were placed on ceramic membranes and coated with a thin film of gold.

D. Specific surface area SSA

The specific surface area measurements were made by nitrogen adsorption evaluated using the Brunauer Emmett Teller (BET) model with a Micromeritics GEMINI 2375 instrument. Before measurement, a specific treatment was applied depending on which powder was investigated. For copper oxalate the powder was dried under nitrogen atmosphere at 85°C for 60 minutes. For the copper oxide the temperature was increased to 200°C for 1h, then for the mixed oxides the temperature has been established at 85°C. All the temperatures have been chosen as a function of the thermal stability of the powder the start of dehydration (copper oxalate) and the synthesis of the oxides (copper oxide 275°C, mixture 110°C). For copper oxalate measurements, the amount of powder was around 1g. In the case of oxide particles the amounts of powder for the measurement were around 100 mg. Applying this method it is possible to estimate the primary particles size using the equation 26, assuming they can be represented by monodispersed spheres,

$$d_{BET} = \frac{6}{S_{BET} \cdot \rho} \qquad \textit{Eq 26}$$

where d_{BET} is the diameter of particles in µm, S_{BET} is the specific surface area in m^2/g and ρ the powder density in g/cm^3.

E. Particle density

The particles density measurement has been carried out by helium pycnometry (Microline 380 MIcrometrics). Before the measurement the powder under investigation was thermally treated. The copper oxalate powder was kept for 4 hours under air at 85°C to eliminate possible adsorbed water on the particle surface. For each sample 10 measurements were carried out.

F. Small Angle X-ray Scattering SAXS

The SAXS measurements were conducted at the Austrian SAXS beamline of the Synchrotron radiation Laboratory, ELETTRA, Trieste, Italy. SAXS measurements have been carried out for the early stage of copper oxalate precipitation using a self-made stopped flow device (y) mixing. The Y- capillary has a diameter of 1 mm with a wall thickness of 10 µm. A small volume of 60 µl of each precursor solutions was used. The intrinsic mixing time was estimated at about 50 milliseconds. The data was collected every 0.1 seconds for the first 60 seconds, every 0.5 seconds for the following 120 seconds and for the next 7 minutes every minute. Above each measurement a background have been using decarbonated water and filtered through a 20 nm ceramic membrane to avoid dust that can disturb the measurements[83]. The scattering curves were corrected for variation of the primary intensity and for background scattering using standard procedures for SAXS.

G. Particles Size Distribution PSD

Measurements of the particle size evolution of copper oxalate precipitates have been carried out *in-situ* using laser diffraction Malvern Mastersizer S. The total volume of the cell is about 100 ml. Before starting the measurements with the two reactants solutions of copper nitrate and sodium oxalate a background was measured. The background measurement was carried out using decarbonated water that had been filtered through a 20 nm ceramic membrane to avoid possible dust and bubbles. 50 ml of each reactive solution were injected within 20 seconds and then stirred with a velocity of 1400 rpm. The precipitate experiments investigated used the some solution concentration as described above in 2.2.2. The data was collected every minute up to 25 minutes then every 5 minutes up to 30 minutes and then up to 60 minutes each 15 minutes. To transform these types of measurements from diffraction patterns into PSDs the optical data for the copper oxalate is needed. A detailed investigation of optical data will be described in more detail in Appendix (chapter 2) values are given in Table 16.

Table 16: Optical parameters used for copper oxalate for PSD evolution using laser diffraction

Devices	Refractive index (CuC_2O_4) real part	Refractive index (CuC_2O_4) imaginary part	Refractive index H_2O
Mastersizer S	1.77	0.01	1.33

Another device used during the thesis work for PSD measurement was a centrifuge (Horiba CAPA 700). The particle evolution during the sedimentation is measured by light extinction. For this instrument we disperse 10 mg powder of copper oxalate in 200 mL of a saturated solution of copper

oxalate filtered through 20 nm. The background was made with the saturated solution of copper oxalate. Physico-chemical parameters used for the measurements are given in Table 17:

Table 17: Physico-chemical parameters utilised for copper oxalate PSD using the HORIBA device

Device	Powder density (CuC_2O_4)	Dispersion viscosity	Dispersion density
Horiba CAPA 700	3.5 (g/cm^3)	0.91 cP	0.99 (g/cm^3)

H. ICP-ASE analyses

The quantities of various ions in solution, in this case copper and cobalt were measured using ICP-ASE PERKIN ELMER type Plasma 2000 device. Each element is characterised by a specific wavelength of emission, which permit their identification by Atomic Emission Spectroscopy. The solution under investigation is sprayed into plasma. Using this technique the over all amount of copper/cobalt in solution as ions, complex and solids can be measured. The samples were prepared by dissolution in a matrix of 0.60M HNO_3. The standard samples were prepared in the same matrix of HNO_3.

I. Thermogravimetric Analysis TGA

The thermogravimetric analyses have been made using a SETARAM TG/ATD 92 with alumina crucibles. The powder under investigation was kept at a constant weight at around 15 mg. The decomposition measurements have been done under reducing atmospheres of helium/hydrogen (960 mbar and 40 mbar). A flow meter instrument calibrated previously fixed the partial pressures of the gases. The kinetic analyses have been carried out in isothermal conditions. The temperature parameters depend on the type of powder and are given in detail in the relevant section.

2.2.4. Nanostructure evolution - Results

A. HRSEM and AFM measurements

The particle evolution can be followed as a function of reaction time by stopping the precipitation process of reaction. Several experiments were undertaken in this aim using filtration through 20 nm ceramic membranes to stop the reaction. The reactants for precipitation, copper nitrate and sodium oxalate, have been prepared with the same precautions as described previously (section 2.2.3). The precipitation process took place in a well-mixed minibatch reactor of 20 ml volume at 25°C. For all experiments the pH evolution was monitored as shown in Figure 21. A quantitative estimation of powder weight is difficult to obtain for small suspension volumes (20 mL), for comparison with the thermodynamic solubility simulations were not possible.

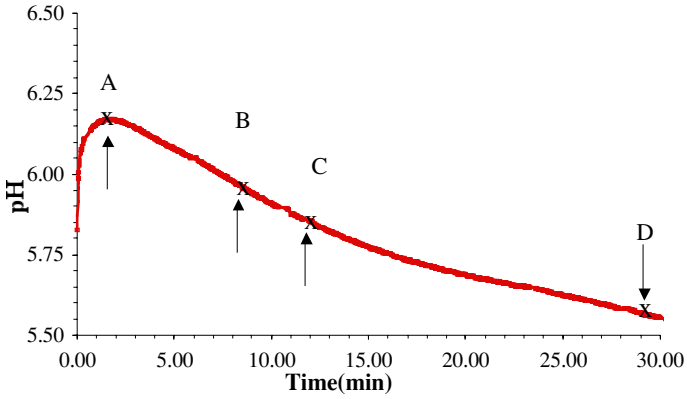

Figure 21: pH evolution as a function of time with the points A, B, C, D corresponding to filtration time and HRSEM analysis

Samples collected after 2, 5, 8, 12, 30, 60 minutes (shown on pH curves as a function of time in Figure 21) and two weeks were analysed using HRSEM. The copper oxalate particle evolutions as a function of time are shown in Figure 22.

High resolution **Low resolution**

a) 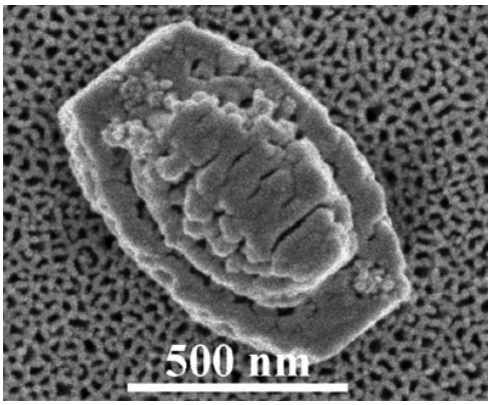

2 min

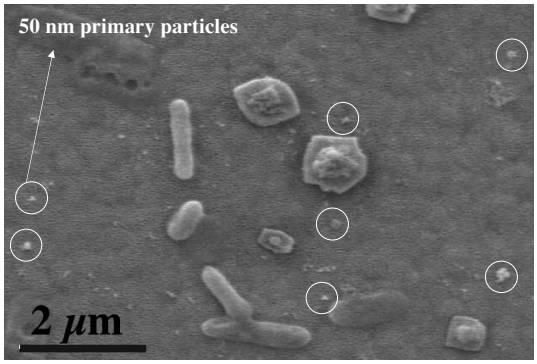

b) 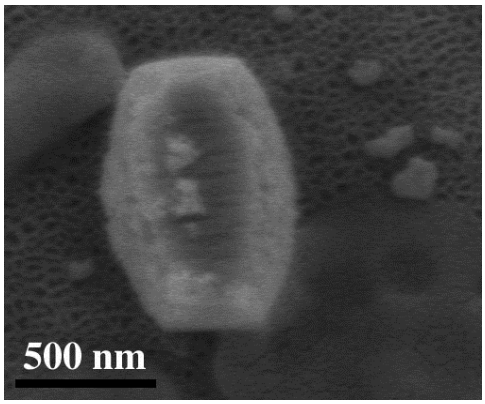

8 min

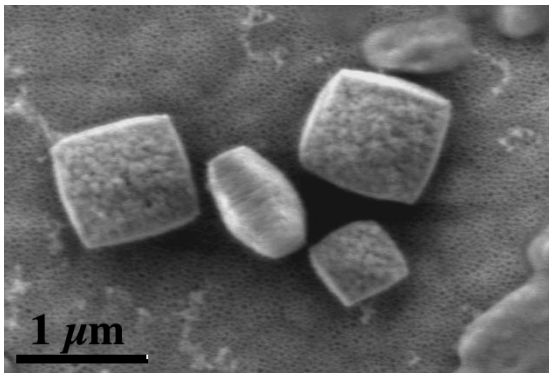

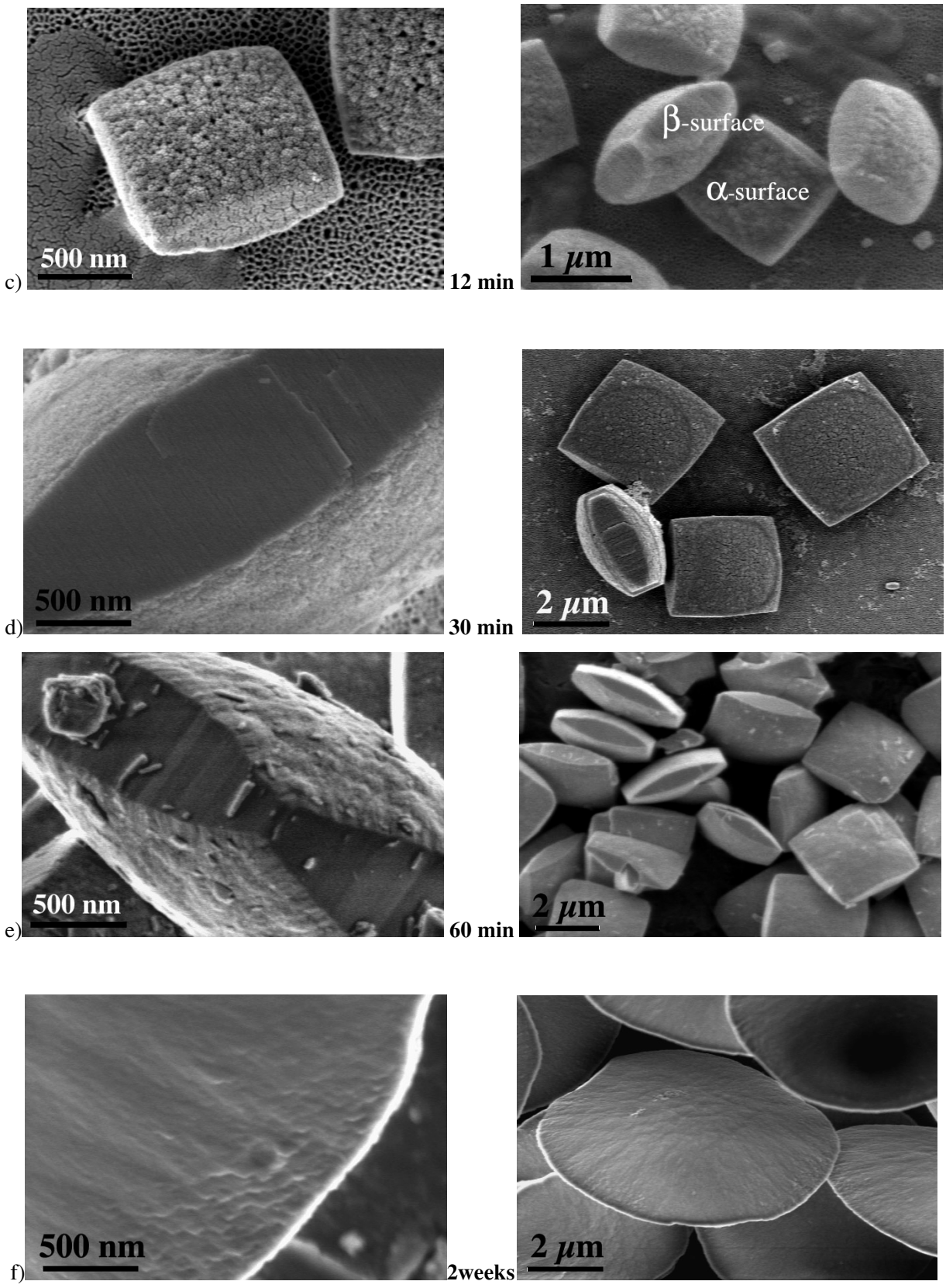

Figure 22: SEM image for copper oxalate particles as a function of precipitation time at high and low resolution: a) after 2 minutes, b) after 8 minutes, c) after 12 minutes, d) after 30 minutes; e) after 60 minutes; f) after 2 weeks

To link between pH evolution and particles evolution (Figure 21 and Figure 22) the first micrograph corresponds to the maximum value of pH (A). At this moment the precipitation of the majority of copper oxalate is expected. This micrograph of the sample with an ageing time of 2 minutes illustrates a mixture of large (550 nm) and smaller (50 nm) particles. Most of the large particles are "under construction" with steps clearly visible and with smaller particles distributed around them. A typical particle is represented in Figure 22 a. The central island consists of several layers assembled on the particles surface in the process of growth. After 8 minutes the particles reach a size around 0.9 - 1 µm, they have a cushion like shape and the steps are no longer visible. In addition the small particles that make-up the surface and several of these smaller 50-70 nm units are still observed on the filtration membrane. There is a further population with size about 100 - 200 nm showing a cubic shape. After 12 minutes the larger surfaces have a rough appearance while the four lateral ε surfaces are smooth. This is even more accentuated after 30 minutes. The particles precipitated after 60 minutes show a very smooth surface at the lateral surface (Figure 22 e) suggesting the nanocrystallites buildings blocks have been cemented together with the remaining solute as the reaction approaches the equilibrium state. After 2 weeks the morphology has continued to evolve and smaller surfaces have more or less disappeared. These last stages (60 minutes, 2 weeks) could be expected from the residual copper oxalate supersaturation predicted by the solubility simulation (S=0.40 after 30 minutes).

Several particles with an ageing time of 2 minutes were studied using AFM in order to determine the height and width of the growth steps.

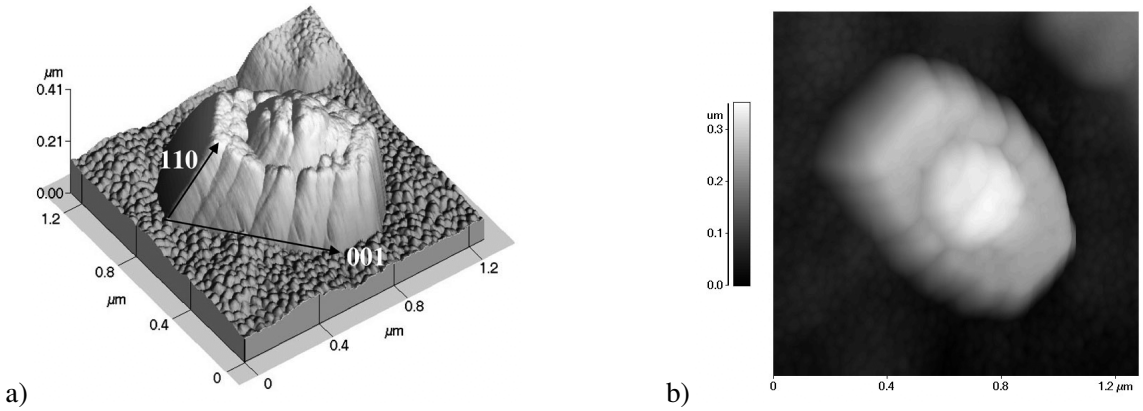

Figure 23: a) Topography of a typical particle with an ageing time of 2 minutes measured with Atomic Force Microscopy (AFM); b) 3D view of typical particle under construction

Figure 23 shows a typical particle measured by AFM with an ageing time of 2 minutes. The step of particles under construction is clearly visible. The height and the width of the steps measured for several particles are summarised in the Table 18.

Table 18: Dimension of the particles and of their corresponding step size determined by Atomic Force Microscopy

Particle	Particle			Step		
	Length(nm)	Width(nm)	Height(nm)	Length(nm)	Width(nm)	Height(nm)
1	1000	700	280	420	360	73 ± 10
2	1300	780	450	800	380	214 ± 10
3	1100	927	505	710	650	287 ± 10
4	1530	1225	275	760	900	210 ± 10
5	1000	875	280	500	448	145 ± 10

The experimental error of the method is about 10 nm, which corresponds to the instrument pointer. In a previous study of copper oxalate precipitation particles with an ageing time of 18 hours have been investigated using X-ray diffraction. The primary particle size has been estimated using the Scherrer equation and the particles crystallography to be 69 nm in 110 direction and 49 nm in 001 direction[6]. The height of the step has the same order of magnitude as in the XRD peak broadening measurements. The height of the step could be considered as one layer of particles (73±10 nm) as for the typical particles depicted in (Figure 23 a) or several layers e.g. 4 x 70 nm as for the particle number 3 (287±10 nm). These step height values are all more or less a multiple of 70nm. These steps and their correspondence with the XRD line broadening crystallite size adds significant weight to the "brick-by-brick" growth mechanism previously proposed for copper oxalate[6]. Finally the particles reach the same size with cushion morphology independent of the time and condition of birth of particle.

The mechanism of copper oxalate particles assembly proposed previously[6] starts with a simple fast burst of nucleation, growth and growth of crystallites by molecular attachment then growth by aggregation. HRSEM images of copper oxalate as a function of reaction time suggest that more than one process may take place at the same time, and that the formation of copper oxalate may involve a more complicated mechanism. However each process of nucleation, growth by molecular attachment, or by aggregation may be influenced by the distribution of ions and complexes in the precipitation system. This will be discussed later incorporating information from the solubility simulation.

B. Copper oxalate morphology & cross-section TEM

A copper oxalate nanostructured material was investigated in detail in a previous work[81]. This study focused on particle morphology and the influence of the organic additive Hydroxypropylmethyl cellulose (HPMC) on particles shape and substructure. It has been established that the HPMC can change both the size and shape of primary particles by a preferential adsorption and affecting the growth process and consequently the particles morphology as shown in Figure 24. The primary particles present a high anisotropy linked to the anisotropic nature of the crystal structure. Two types of terminating surfaces are postulated[7] ε-surface (hydrophobic) and α-surface (hydrophilic).

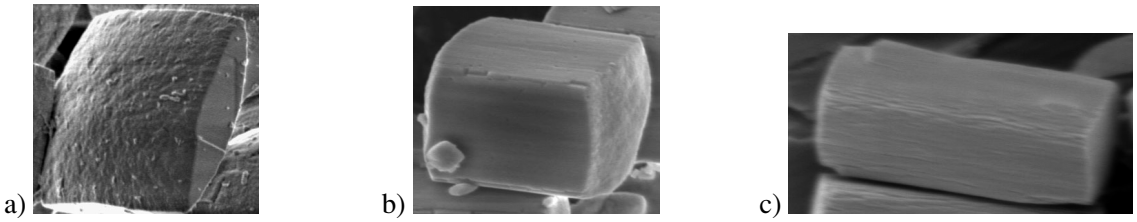

Figure 24: Copper oxalate particle morphology: a) cushion morphology without organic additive; b) cubic morphology with organic additive 0.005mg/l; c) rod morphology with organic additive 125mg/L

Increasing the HPMC concentration, the volume of primary particles decrease this can be interpreted as a preferential adsorption phenomenon on the primary particles surface ε as shown in Figure 26. The particles were characterised using XRD (Figure 25), calculating the size of primary particles from the Scherrer equation for 001 and 110 direction. The results are described in Table 19.

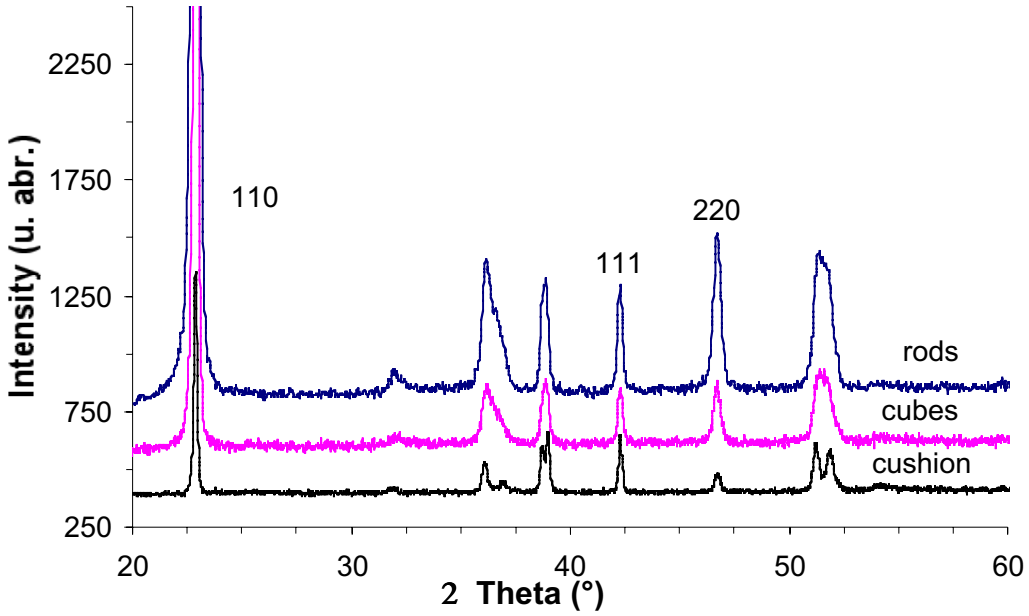

Figure 25: XRD diffraction patterns for the three morphologies of copper oxalate studied in details[81]

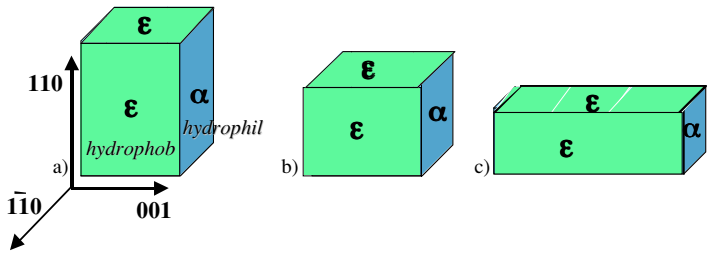

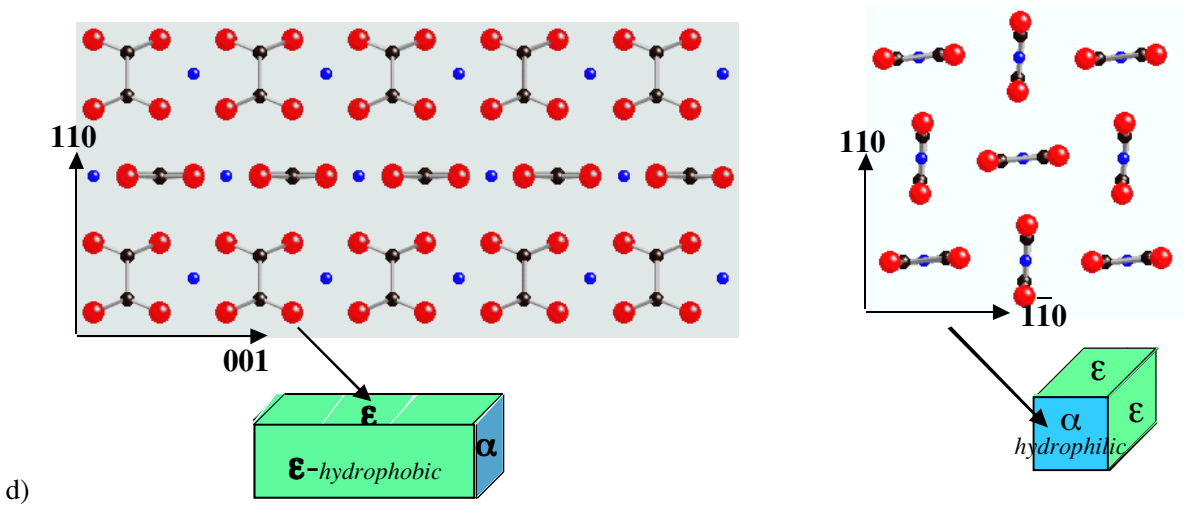

d)

Figure 26: Size of primary particles of copper oxalate as a function of polymer concentration: a) for the cushion; b) for the cubes; c) for the rods[81] d) copper oxalate structure with the two distinct faces hydrophilic and hydrophobic

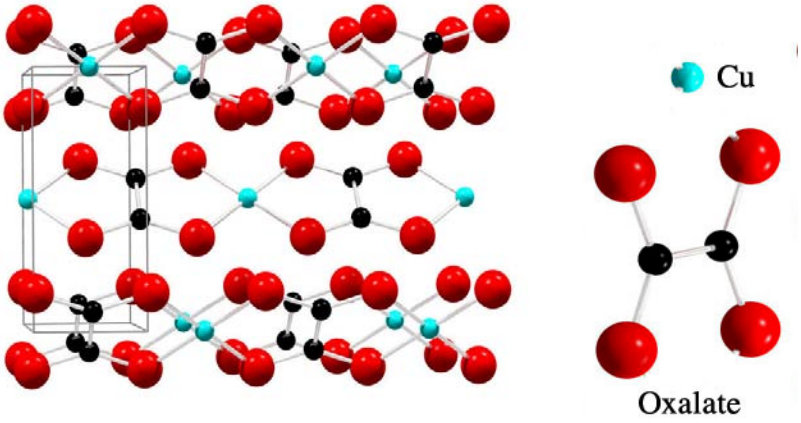

a) b)

Figure 27: a) Copper oxalate disordered structure; b) copper oxalate unit[92]

Table 19: Primary particles of copper oxalate crystallographic directions and particles morphology[81]

Morphology	Direction 001	Direction 110
Cushion	49	69
Cubes	46	31
Rods	41	19

The polymer is expected to adsorb only on the ε surfaces of primary particles. However increasing the polymer concentration the volume expected to a single of primary particle decreases. During the mechanism of the primary particles assembly, the polymer is desorbed and finally is found only on the external ε surface of the particles.

These three morphologies were analysed more carefully by the pycnometry in order to determine the particles density.

To determine the density for the three morphologies 10 measurements on each powder were made. All of them indicated a density of 2.95 g/cm^3. This value is smaller than that of the particles density calculated from the crystallographic unit estimated to be 3.50 g/cm^3. This suggests that the particles have up to 14% internal porosity, which does not depend on the particles morphology.

Only the particle with cubic morphology was investigated by TEM cross-section, which is the particle shape to be most interesting for certain application. The particles were embedded in a polymer matrix and then cross-section by ultramicrotomy was made as described in section 2.2.3.A.

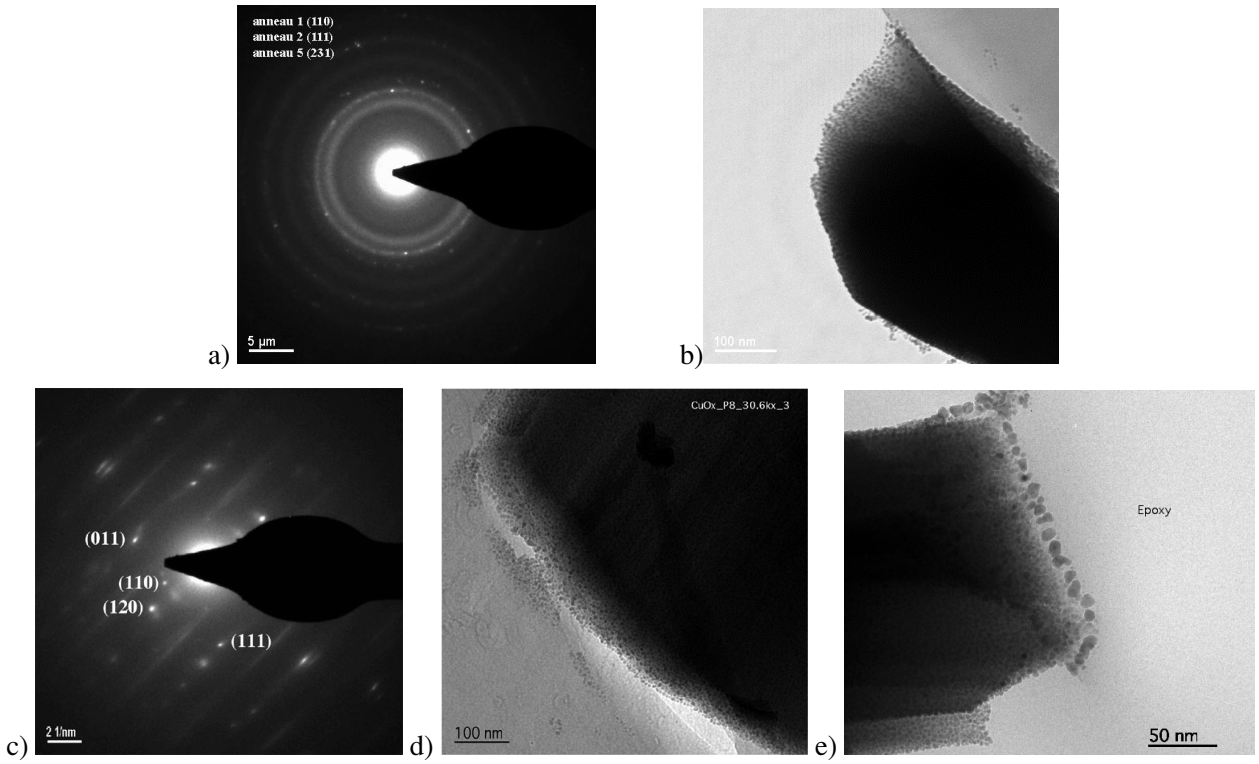

Figure 28: copper oxalate cross-section a) diffraction patterns for the image b); c) diffraction patterns for the image d); e) cross section of one particle

In Figure 28 e it is possible to distinguish two types of primary particles size: one in the particle core with a size of about 15 nm and the second on the particles shell with a size of about 25 nm. The diffraction patterns obtained on the core showed a poor order of primary particles or amorphous contribution possibly due to beam in stability of copper oxalate (Figure 28 a). Towards the corner of the particles the diffraction patterns (Figure 28 c) showed an well-ordered structure and was indexed as copper oxalate.

Using XRD diffraction patterns the particles average size is determined to be around 40 nm. The size has been estimated using the software TOPAS 2000. For the refinement the copper oxalate anhydride structure was assumed. The two different types of measurements indicate divergent values on primary particles size. This could be in point due to the inaccuracy of the time broadening method (40 ± 0.5 nm) and the geometrical factor for 2D cuts of a 3D structure. From the indexing of the diffraction patterns the

ransom of poorly ordered core seen in Figure 28 a, is perpendicular to the 110 direction, whereas the well ordered zones towards the outside of the particle is parallel to the 110 direction, the copper oxalate ribbon direction of the crystal structure. So they may be a directional preference for the "ordered primary particles".

C. Evolution of Particle Size Distribution by Laser Diffraction

The precipitate evolution of copper oxalate nanostructured materials with cushion morphology was studied in more detail by laser diffraction in order to try and follow the precipitation and the growth process as a consequence of particles assembly.

The *in-situ* PSD measurement of copper oxalate was carried out in the Malvern Mastersizer S at a precursor concentration of 0.005 M after mixing. The precursors have been prepared with the same precautions as described previously.

The two precursors copper nitrate and sodium oxalate were injected at the same time into the Malvern cell with a volume of 100 ml in a time of 20 seconds. After the injection time the measurements were made each minute for a period of 15 minutes then each two minutes for the next period up to 30 minutes and then each 15 minutes up to 60 minutes. The results are shown in Figure 29 and 31 and summarised in Table 20 and 21.

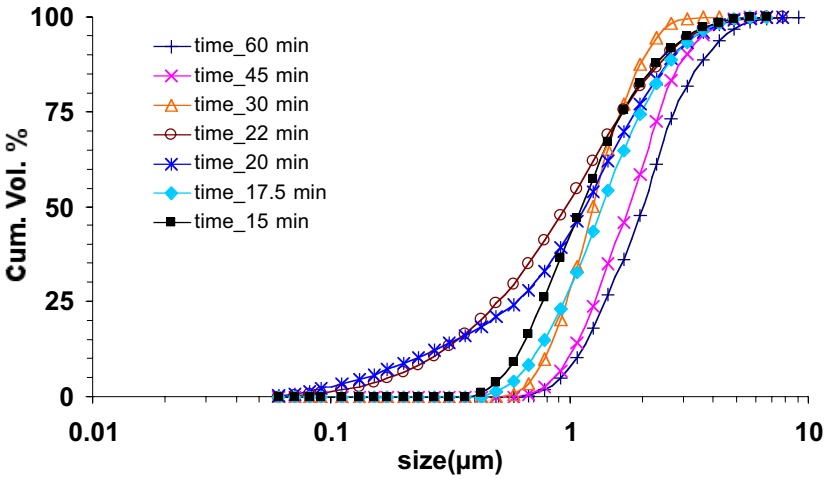

Figure 29: Particles size distribution of copper oxalate as a function of time

Table 20: Particle size distribution data in aqueous solution determined by Malvern instrument as a function of time.

Time (min)	D_{v10} (µm)	D_{v50}(µm)	D_{v90}(µm)	Span
15	0.59	1.10	2.45	1.68
17.5	0.70	1.23	2.74	1.51
20	***0.22***	***1.14***	***2.73***	***2.19***
22	***0.26***	***0.95***	***2.53***	***2.38***
30	0.78	1.23	2.05	1.02
45	0.98	1.76	3.05	1.17
60	1.05	2.00	3.72	1.32

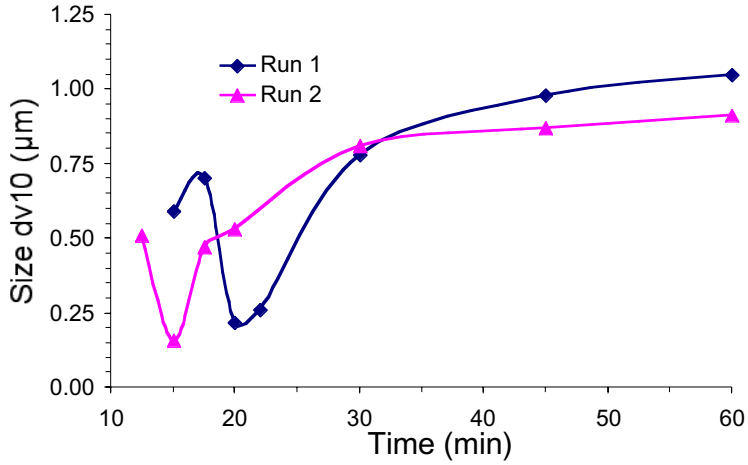

Figure 30: Particle size evolution of copper oxalate versus time for d_{v10} (µm)

Before 15 minutes it was not possible to detect the formation of particles the scattered light intensity being to low. This is perhaps due to two contributing factors, a low particle volume concentration and the low scattering coefficient for particles less then 100 nm which are expected to be most numerous in the initial stages of precipitation[82]. After 15 minute the particles larger than 500 nm are detected and a d_{v50} 1.1 µm is measured. The particles then increase in size with a d_{v50} of 1.23 µm (Figure 30). After 20 minutes the PSD shows a significant decrease with small particles under 200 nm being detected. This transition takes place during a short period of about 5 minutes when the smaller particles are formed and then growth process continues the d_{v50} increases again. A plot of the d_{v10} as a function of time shows this decrease in size very clearly (Figure 30). The phenomenon is reproducible as shown in Figure 31 and Table 20. The time at which the smaller particles appear is not the same in the both cases with a shift of 5 minutes. This is probably due to difficulties in reproducing mixing in the Malvern cell of 100 ml. This sudden appearance of a second population of fine particles < 500 nm is indicative of a second nucleation event.

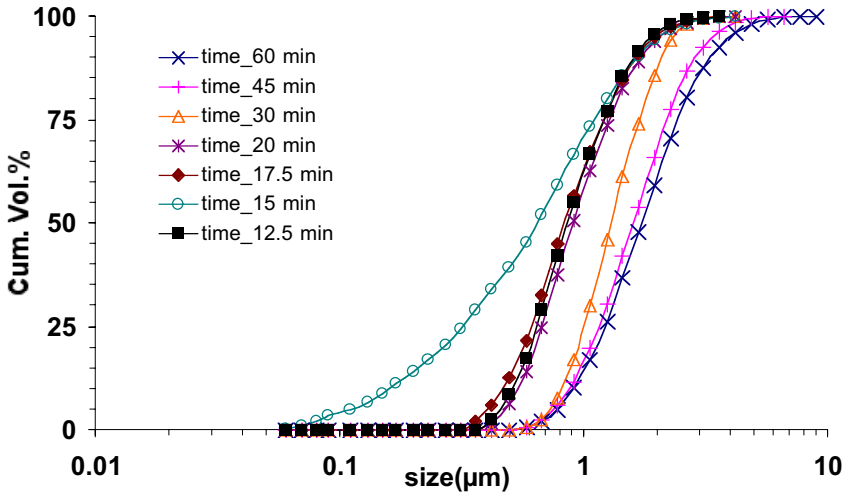

Figure 31: Evolution of particle size distribution of copper oxalate as a function of time

Table 21: Particle size distribution data in aqueous solution determined using Malvern instrument as a function of reaction time

Time (min)	d_{v10} (µm)	d_{v50} (µm)	d_{v90} (µm)	span
12.5	0.51	0.85	1.59	1.271
15	***0.16***	***0.64***	***1.64***	***2.313***
17.5	0.47	0.83	1.64	1.405
20	0.53	0.90	1.72	1.314
30	0.81	1.28	2.09	0.994
45	0.87	1.59	2.86	1.251
60	0.91	1.73	3.31	1.390

The smallest size that can be measured using the Malvern is 50 nm. To confirm this formation of small particles, 250-µL of suspension was filtered through 20 nm ceramic membrane and then analysed using HRSEM. For this microscope the samples are not coated to avoid the possible artefacts, by the deposition of gold on the particles surface. Figure 32 shows particles with an ageing time of 23 minutes. Two populations can be seen one with a size less then 200 nm (which look like random aggregation of primary particles) and others formed or under construction, as seen in the previous section, with a larger size of about 2 µm. These observation support the hypothesis of a second nucleation event after about 15-20 minutes.

a) 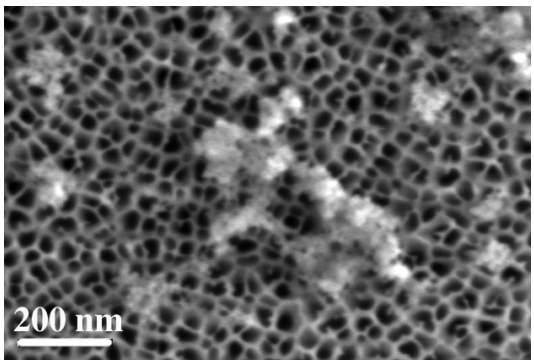

b) 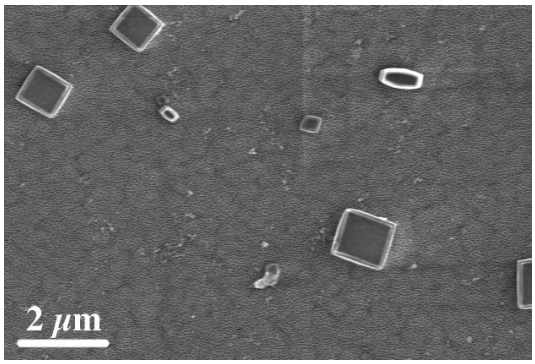

Figure 32: SEM images for copper oxalate precipitation with an ageing time of 23 minutes: a) particles with a size less then 200 nm b) a large distribution of "primary" particles, particles under construction

There are certain differences between the HRSEM images obtained from the mini-batch reactor and those from the Malvern *in-situ* measurements. Malvern showed particles with a larger size > 500 nm only after 15 minutes. The mini-batch (20 ml) showed after 2 min ageing time particles that reached a size of 500 nm and around 1 μm after 8 minutes. The fact that the Malvern *in-situ* measurements were made while stirring and the mini-batch experiments did not may contribute to these differences. The volume fraction of these large particles was however not possible to quantify perhaps they are too few to be measured in the Malvern. The stirring during the process of precipitation is an important factor that must be considered and also the supersaturation variation in the system must be taken into account. The PSD's support the model of several processes that are involved in the same time of reaction as e. g. nucleation from zero size, nuclei growth, growth by aggregation and second nucleation event as a consequence of the precipitation of malachite or the aggregation process.

The measurement of particles evolution obtained by laser diffraction at the end of precipitation shows particles with the expected cushion morphology.

D. Small Angle X-ray Scattering (SAXS)

To follow the particle formation in-situ from zero size to a certain value could help us to discern between different growth e.g. molecular attachment *vs.* agglomeration. At this time only few techniques are available such as SAXS, PCS and AUC. The SAXS technique yields information about the size of colloidal particles at a nanometric scale < 100 nm. SAXS can give new insights in to the early stages of precipitation on milliseconds scale. Therefore an attempt to follow the evolution of the copper oxalate precipitation *in-situ* during the first 2 minutes of precipitation was made using SAXS.

Using this technique the only limitation is given by the solid/liquid ratio that must be higher than 0.1% wt to ensure a reasonable signal/background ratio. For copper oxalate precipitation at a precursor concentration of 0.005 M after mixing the amount of powder collected at equilibrium is 0.56g/L (after 18 hours). This value is just below the range of detection of 1g/L. To meet these conditions the reactant concentration must be increased to access the SAXS domain. Six systems, for three different volume

fractions and for three organic additive concentrations are described in Table 22. Experiments were carried out in the mini-batch reactor (section 2.2.2) to provide final particle characteristics for comparison with the SAXS data.

Table 22: Samples investigated by SAXS

Name of sample	Precursor concentration (mol/L)	Organic additive HPMC (g/L)	Supersaturation	Mass (g/L)
B_000	0.025	0.000	1.02	3.743
B_125	0.025	0.125	1.02	3.743
B_500	0.025	0.500	1.02	3.743
B_1000	0.025	1.000	1.02	3.743
C_000	0.05	0.000	1.26	7.720
D_000	0.1	0.000	1.48	15.697

Increasing the precursor concentration the parameters of precipitation were changed. They influence the values of supersaturation (Table 22), the pH evolution as indicated in Figure 33.

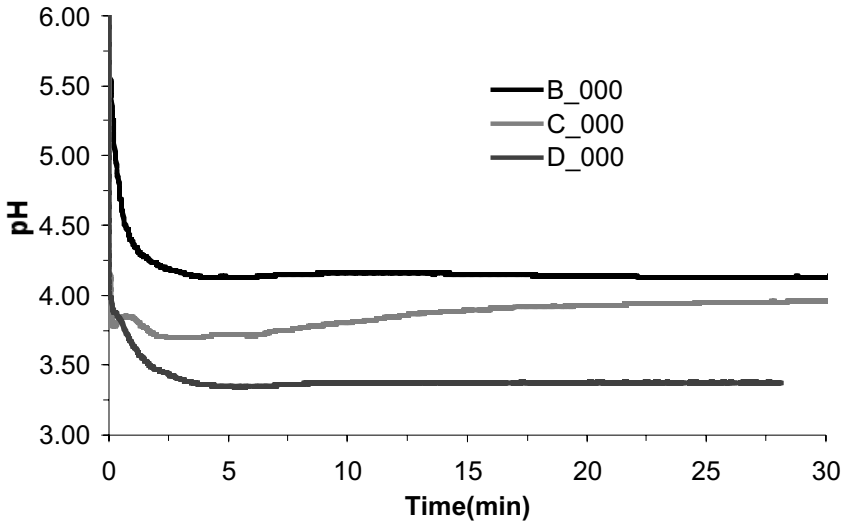

a)

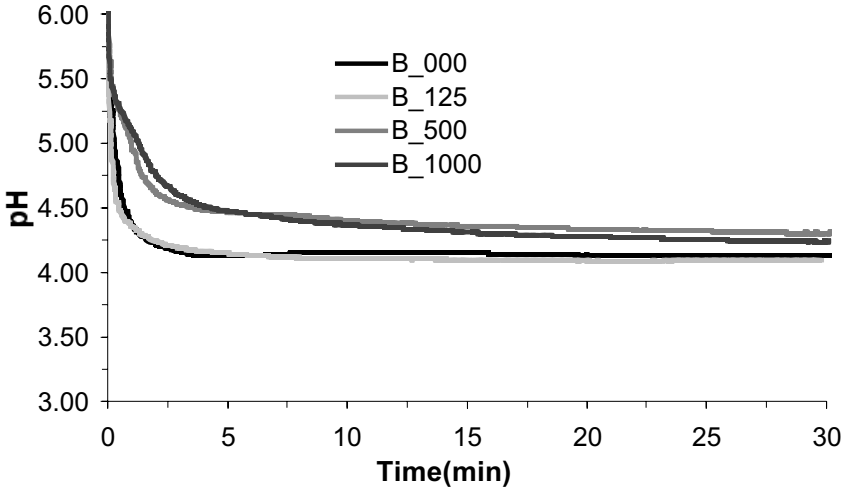

b)

Figure 33: pH evolution as a function of time: a) pH behaviour for three different concentrations of precursors; b) pH behaviour for the same precursor concentration and different amounts of organic additive

The final ageing time was established at 30 minutes, which coincided with a rapid sedimentation process. In the moment of mixing when the two precursors get in contact the formation of a colloidal suspension can be seen. Then the particles start to sediment in a short time range less then 1-minute depending on precursor concentrations. These pH curves as a function of time are in qualitative agreement with the curves obtained at a low concentration of 0.005M. The initial growth of the pH at a concentration higher than 0.005M happened in a short time range. Then it decreases rapidly as seen previously.

At a low concentration (0.005 M after mixing) the particle morphology is like cushion, whereas when the precursor concentration increase the morphology of particles change to spheres and their size decreases as shown in Figure 34.

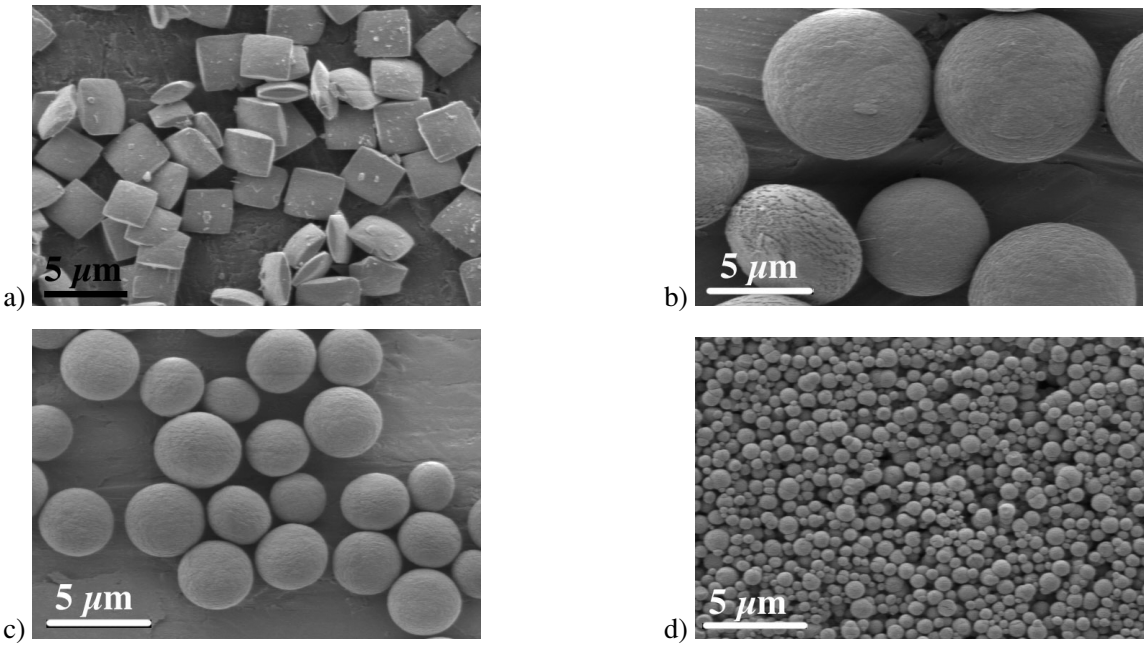

Figure 34: Morphology of copper oxalate particles for different reactive concentrations after mixing: a) 0.005 M; b) 0.025 M; c) 0.05 M; d) 0.1M

Higher S* leads to a higher nucleation rate and thus a higher primary particle density (number of particles per unit volume). If the final crystallites in the secondary particles are assumed to come from a single nucleation process, the XRD line broadening crystallite size can be used to estimate the total number of nucleation events (Table 23). The higher nucleation rates and nuclei number densities presumably affect the particle formation mechanism - assumed to be aggregation leading to the change in morphology and size. Increasing the precursors concentration the size of the primary particles decreases as shown in Table 23. The higher density of primary particles presumably leads to higher agglomeration rates. There is not enough time for the "organisation" of the crystallites as found for the lower concentrations. The "self-organisation" attachment of a primary particle is assumed to take place at a local energy minimum before "re-aligning" to find the global minimum. For the higher concentrations this "re-alignment" step seems to be perturbed either because of a change in the interaction potentials or by a rapid cementing due to a higher residual supersaturation.

The system at a reactant concentration of 0.025M has been studied in the presence of different amounts of an organic additive (HPMC). It is known that at a low concentration of 0.005 M the particle morphology and shape can be controlled by the HPMC concentration (chapter 2.2.4). At a higher supersaturation this polymer has less influence on particle morphology, because of the large number density of the primary particles in the system. This involves a rapid aggregation phenomenon and the time of polymer adsorption - desorption on the preferential particles surface may be reduced. Without polymer the morphology of particles is sphere like. When the amount of polymer increases the morphology moves to ellipsoid as depicted in Figure 35. For this system of 0.025M the size of primary particles varies little (Table 23) with polymer concentration.

a) 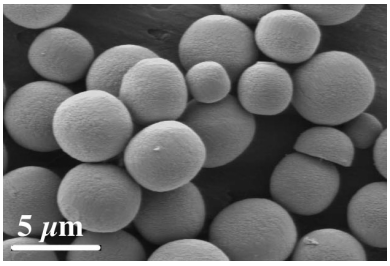

b) 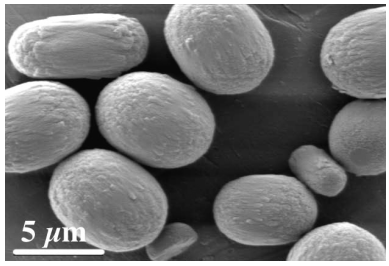

c) 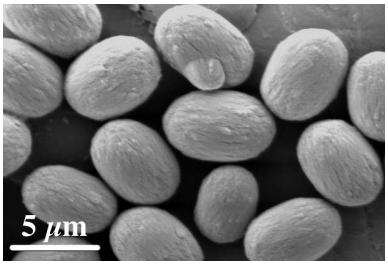

Figure 35: Morphology of copper oxalate particles: concentration 0.025 M after mixing in the presence of a polymer: a) 125 mg/L HPMC; b) 500 mg/L HPMC; c) 1000 mg/L HPMC

Table 23: Size of the crystallites determined by XRD

Name of the sample	Conc. after mixing (M)	Size of the crystallite (nm)
B_000	0.025	27.2
C_000	0.05	14.6
D_000	0.1	16.9
B_125	0.025	14.1
B_500	0.025	14.4
B_1000	0.025	11.5

Table 23 sums up the size of nanocrystallites for the six systems under investigation. For a concentration of 0.025 M the primary particle size is at 27 nm (B_000) and then decreases to 17 nm (D_000) for a concentration of 0.100 M. This behaviour is a function of the supersaturation ratio. For the same value of supersaturation but increasing the organic additive concentration the size of primary particles change from 27 nm (B_000) to 12 nm (B_1000) as seen previously[7].

In order to obtain information about the global evolution of the particles structure time resolved SAXS measurements have been conducted with Synchrotron radiation over the first minutes. The experimental conditions of SAXS investigation with a stopped flow cell have been described in section 2.2.3. B in more detail[83].

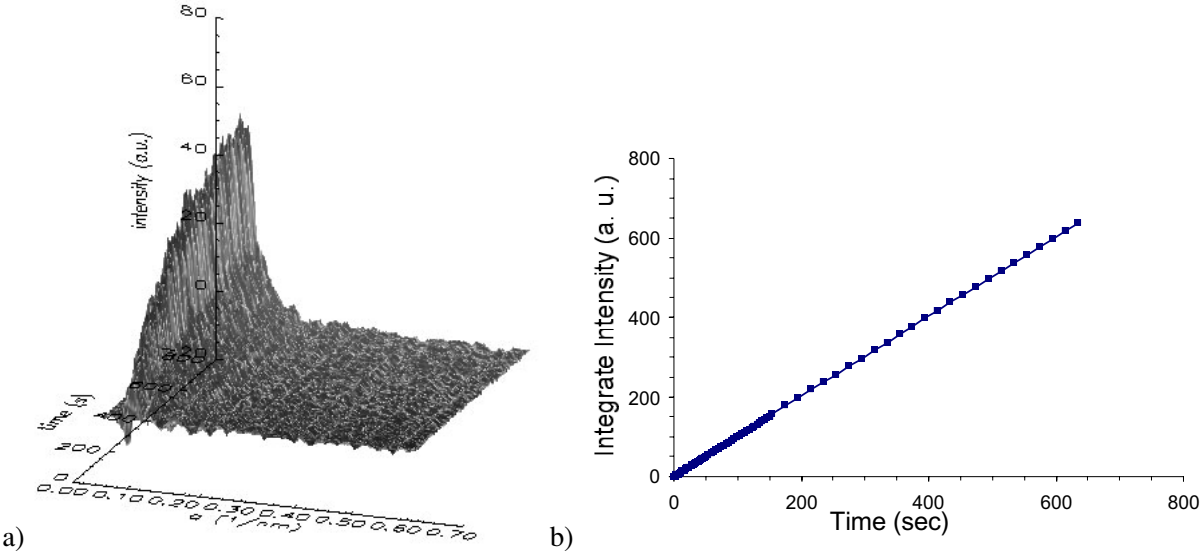

Figure 36: a) Raw SAXS profile of copper oxalate precipitation B_1000 in the first few seconds with a nano crystal size of about 25 nm[85]; b) Integrate intesity evolution as a function of reaction time

Figure 36 shows the in situ SAXS diffraction pattern measured during the precipitation of sample B_1000. A fast evolution particle growth can be observed in the first few seconds of measurements. In less than a few seconds the particles reach a size of 25 nm, which have been derived from the Guinier analysis, followed by growth over 100 nm, a process that occurs rapidly in 30 seconds. Therefore, in the

later stages of the precipitation reaction only the asymptotic Porod regime can be interpreted also to the limited resolution of the instrument.

For the other systems under investigation the same results were obtained with a fast formation of particles in times of subseconds. They rapidly grow to over 100 nm. Thus even using SAXS in-situ stop flow measurements it was not possible to elucidate the early stages of particle formation. It was hoped to be able to follow their growth to a certain size and then to see the growth by aggregation. Low concentrations of 0.010 M have been investigated but the ratio solid/liquid was too low to have a sufficient scattering to be measured.

2.2.5 Discussion and Mechanism of Copper Oxalate Precipitation

The precipitation of copper oxalate was simulated using the thermodynamic calculations. It was possible to follow experimentally the pH behaviour of precipitation in time (Figure 18). The kinetic measurements of pH evolution showed a rapid increase in pH, it reaches a maximum value and then decreases slowly in time. The first part of the pH behaviour, the increasing part, from the simulations corresponds to copper oxalate precipitation. This happened in a time range of less than 2 minutes. The second part of the pH evolution a slow decrease, could only be explained by the precipitation of malachite. In the first 2 minutes most of the copper oxalate precipitates, around 73% wt of the expected amount of powder that is predicted to be found at equilibrium. The amount of malachite at the end of precipitation was estimated to be around 0.4% wt.

In this time range, of 2 minutes, the HRSEM micrographs showed particles with a size of 500 nm under "construction" with steps and kink the same size as the crystallite size measured by XRD. These particles under "construction" are surrounded by nanoparticles with a size under 100 nm supporting the brick-by-brick growth mechanism previously proposed[6] and seen for other systems[23] (Figure 22 a). So within this time range of 2 minutes the nucleation, growth and the onset of agglomeration of primary particles takes place. The slow decrease in pH after 2 minutes (malachite precipitation) could only be simulated with a relatively constant copper oxalate supersaturation. This also fits in with the idea that most growth of copper oxalate nuclei takes places before 2 minutes. Then a much slower evolution of supersaturation during which agglomeration is the dominate growth mechanism. The micrographs with an ageing time higher then 2 minutes showed the particles with a size larger than 500 nm and others under 100 nm. This behaviour can be seen during a period of 15 minutes, then the small particles were no longer observed; coherent with the hypothesis that growth by aggregation dominates in this period. The cushion morphology of particles is formed at an early stage of precipitation of five minutes. Then, these particles grow from a size of 1µm to 2 µm. These particles showed two large surfaces (α-faces) and four small surfaces (ε-faces). The particles with an ageing time of around two weeks showed only the two large surfaces. The four small surfaces were no longer present (Figure 22 f). This fact could come for a ripening

process and the differences between the surface energies[6] of the terminating surfaces. The high energy "hydrophobic" β surfaces (small surfaces) slowly being eliminated, either by an Ostwald ripening or from the remaining species in solution as after 30 minutes from the solubility simulations show S=0.42. The solution should de-saturated slowly eliminating the high-energy surfaces and defects.

The earlier stage of precipitation nucleation and growth of particles was investigated using the SAXS technique. Unfortunately the supersaturation had to be increased from 0.70 to 1.22 to produce solid contents accessible in the SAXS domain. For the SAXS conditions particles were detected in a time range of milliseconds, then grew quickly and after 25 seconds the intensity of scattering remains constant. This means that the particles reached a size higher than 100 nm. These experiments are in general agreement with the thermodynamic evaluation of pH simulation, where the majority of the copper oxalates precipitates in less than 2 minutes.

The PSD of copper oxalate measured using the Malvern laser diffraction only showed the presence of particles after 15 minutes assumed to be because volume fraction and size were too low to scatter enough light for analysis. The particle diameter d_{v50} increases from 15 to 20 minutes then decreases for a short period of time of about 5 minutes and finally increases again. This behaviour could come from a difference between the concentration and hence scattering efficiency of small particles and large particles or could be due to a second nucleation event. On a filter membrane (Figure 32) two populations of particles < 200 nm and > 500 nm were seen - supporting a second nucleation event.

The internal substructure of copper oxalate with a cubic morphology showed a core of randomly organised crystallites and a shell well oriented crystallites (Figure 28 c). Also the cross section of aggregates showed a larger size in the outer shell than in the core (Figure 28 e). Also the copper oxalate particles showed an internal closed porosity independent of the particle morphology. A random core and an organised shell for all the particles of copper oxalate independent of the particles morphology seem probable. This random core of particles comes from the fact that at initial stage the number of particles is high. If we considered the particles size at around 50 nm from Brownian motion, the velocity of particles is in a range of 0.097 m/s. If all the particles precipitate in a short time as shown by SAXS, and the system reaches a concentration of 0.56 g/L; the number of particles in solution is around $6.53 \cdot 10^{14}$, and their mean separation is at about of 1000 nm. Thus the number of collisions will be at about $3.61 \cdot 10^{9}$ per second. The repulsive barrier energy to ensure kinetic stability needs to be around 22 kT. For the calculation the solution viscosity is not considered the value of pure water was used (Appendix chapter 2). If at this energy the particles are not stable because of the high ionic strength and low zeta potential then they should aggregate together. This high velocity of 50 nm particle diameter thus should induce a rapid agglomeration and consequently a random particle substructure. As the reaction time increases the number of free particles in solution decreases as a consequence of aggregation and at the end of the precipitation experiment the particles have the time to organise.

The curve in Figure 37 shows the theoretical evolution of the supersaturation with time calculated using the thermodynamic data.

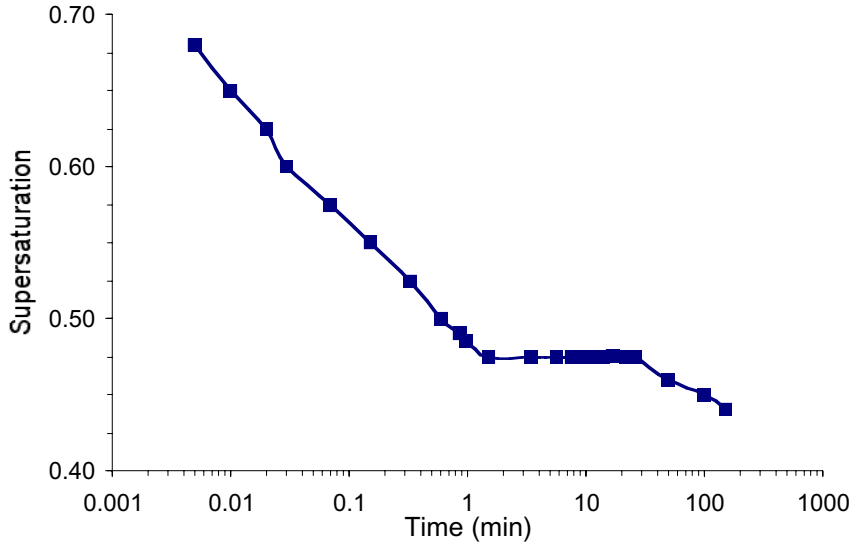

Figure 37: Supersaturation evolution as a function of time calculated using the thermodynamic data

Using the experimental data summarised above and the thermodynamic simulation made on the copper oxalate precipitation a possible mechanism of particle formation will be now proposed. This is represented schematically in Figure 38 as a function of supersaturation and time.

When the two precursors are mixed a high supersaturation level of 0.70 produces a burst of nucleation in a time of milliseconds point A (Figure 38). Then the nuclei grow to a critical size, when they become thermodynamically stable (Figure 38) B. From XRD the copper oxalates primary particles present an anisotropic form. The total system energy decreases quickly represented by the chemical potential change i.e. supersaturation decreases. Then these particles begin to agglomerate. The large number density of particles dispersed in solution may induce a random agglomeration of the particles. As well as relatively high ionic concentration of 0.01 M and thus a thin electric double layer, this process corresponds to the point C. When the particles aggregate in a random fashion by the simple contact no change on the total system energy would be expected as they would have an open porosity i.e. no reduction of surface are per unit volume. This random organisation of the particles is supported by the presence of an internal porosity of about 14% from pycnometry analysis and also from the TEM cross-section study.

To minimise the system free energy the particles start to aggregate in an ordered behaviour. The free surface energy of the system (per unit volume) decreases, thus decreasing the total free energy of the precipitating system. This more ordered or oriented attachment may become possible due to a decrease in the overall ionic strength (decreasing supersaturation) which would increase the electric double layer thickness. This could produce a local potential minimum, E_1, Figure 40, which attaches the primary particle to the larger particles but allows rotation to find the global energy minimum E_3, i.e.

crystallographically well aligned. In the earlier random agglomeration the local attractive potential is too deep, E_2, to allow rotation and alignment. When primary particles attach in an ordered fashion the ions that were in the electric double layer will be released into solution. When a significant quantity of "ordered" attachment has taken place thus the "released" ions may be numerous enough to increase the supersaturation and induce a second nucleation event-as modelled and proposed for nanoparticles aggregation by Nomura *et al*[84]. This behaviour corresponds to point D in Figure 38. Finally to move towards the equilibrium state of the system, the particles continue to aggregate and the free particle surfaces are further eliminated. The aggregation process takes place preferentially as a function of the anisotropic crystallographic structure of copper oxalate. The particle order was analysed by TEM cross-section, and XRD diffraction patterns, showing a preferential organisation in the 110 direction, which corresponds to the CuC_2O_4 ribbon axis (Figure 26 d).

After the initial burst of nucleation and growth, the solubility simulations suggest a small amount of malachite be expected to precipitate (point E). The amount of malachite is so small that the system's overall energy does not change as much as for the previous points as B or C. The particles of copper oxalate showed different sizes from several nanometre to 1µm as seen in Figure 39 a. The two populations are observed for a period of 15 minutes from micrograph analysis. Between 10-30 minutes the bigger particles showed a cushion-like morphology with four small surfaces and two large ones. In the Malvern laser diffraction an apparent second nucleation event between 12 to 20 minutes was also observed. This is coherent with the above discussion of ordered aggregation between 2 and 20 minutes and the electron microscopy observations. The smaller particles with a size less then 200 nm present equiaxed morphology as expected for the primary particles.

After 60 minutes of precipitation the particles reached a size of 2 µm Figure 39 b. The TEM cross-section for the particles with an ageing time of 60 minutes showed larger particles at the surface than in the core. 2-3 layers of particles form this thickness of larger crystallites. It is assumed a ripening process of the particles occurs, at this outer surface which spends more time in contact with the solution. Between 10-60 minutes the lateral faces (4 small surfaces) decrease in relative importance compared to the two large basal surfaces. Particles with an important ageing time of 2 weeks, point F (Figure 38), start to become larger in size and have change the morphology from cushions to plates Figure 39 b and c. The four small surfaces of the cushion-like particles have vanished and the particles are made up from the 2 large surfaces. The elimination of the smaller edge faces is both coherent with a slow de-saturation or ripening (as seen in TEM) and their "high energy" hydrophobic nature responsible for the early cushion shape as previously proposed[6].

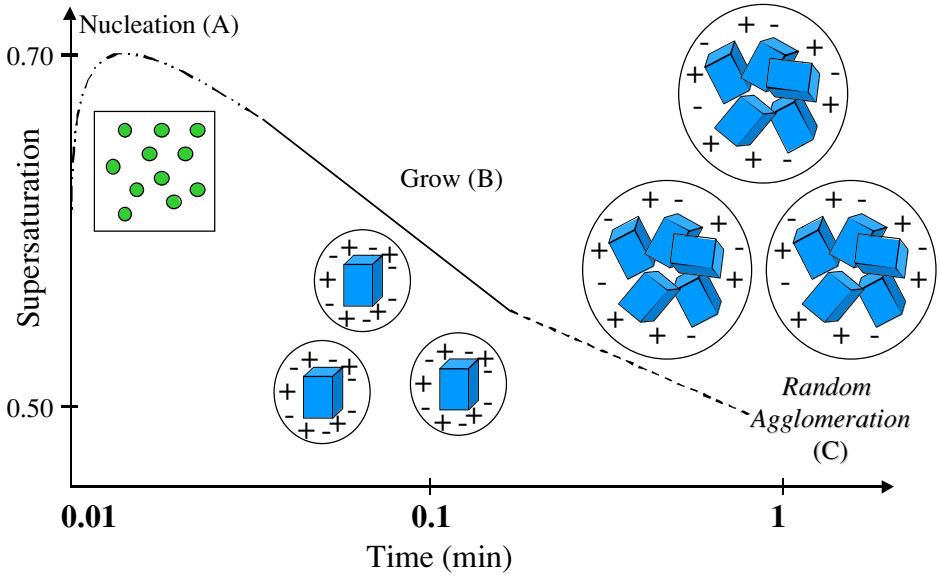
Nucleation (A)
0.70
Supersaturation
Grow (B)
Random
Agglomeration
(C)
0.50
0.01
0.1
1
Time (min)

a)

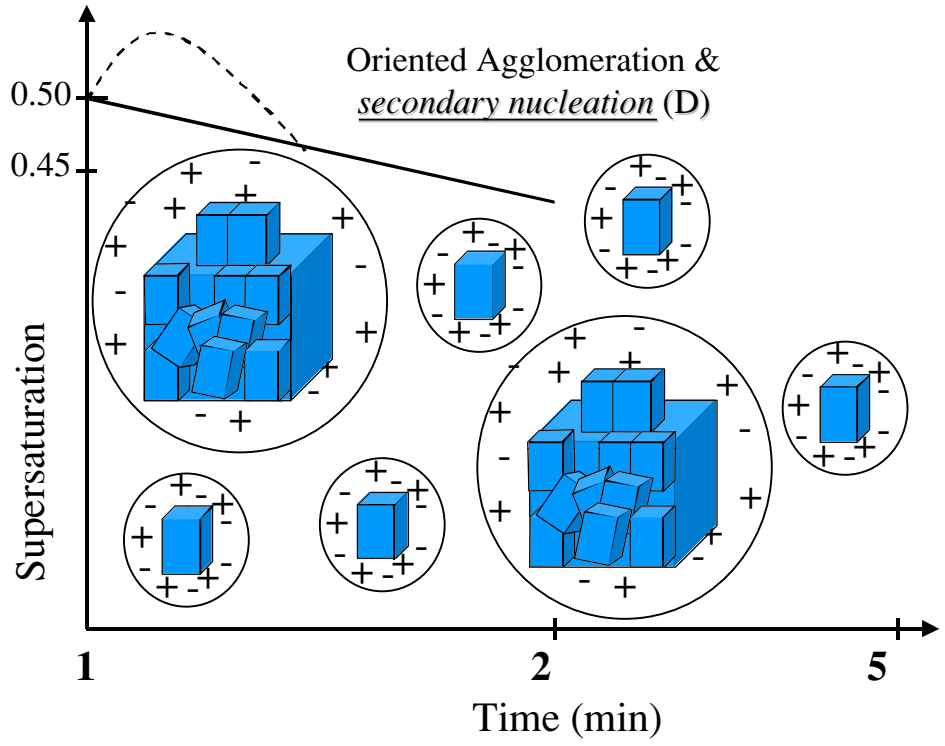
Oriented Agglomeration &
secondary nucleation (D)
0.50
0.45
Supersaturation
1
2
5
Time (min)

b)

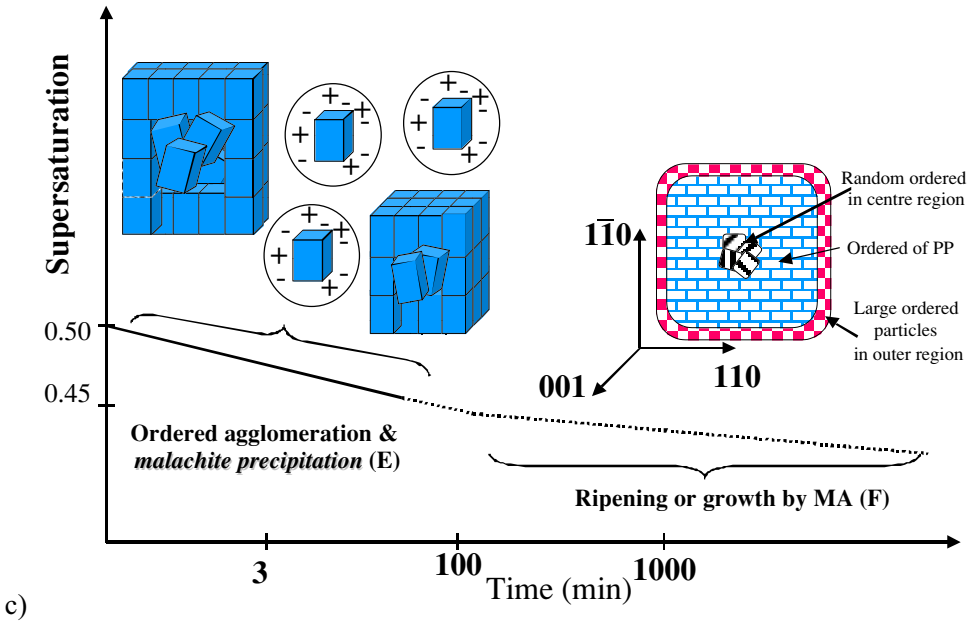

c)

Figure 38: Mechanism of copper oxalate formation from the initial stage to final particles. a, b evolution of supersaturation as a function of time; c) showed the evolution of particles assembly and a cross-section inner the particles

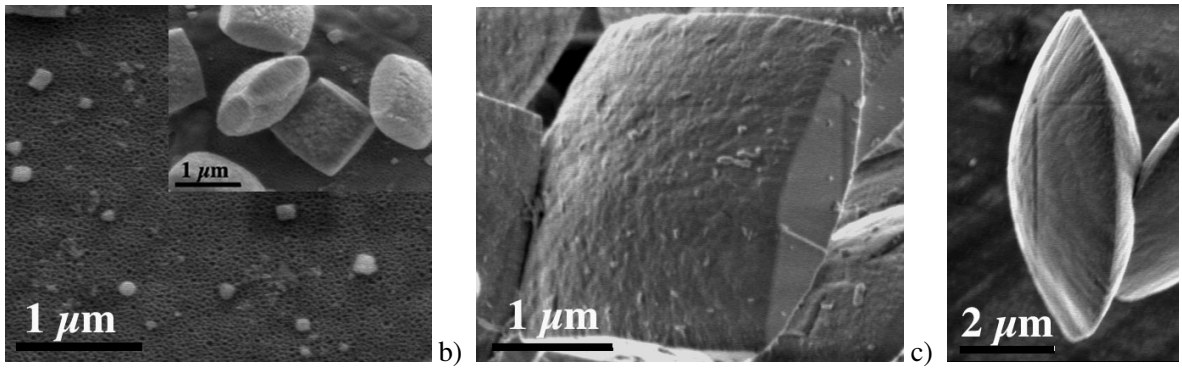

a) b) c)

Figure 39: HRSEM micrographs of copper oxalate evolution as a proof for the proposed mechanism depicted in the previous figure: a) the time of agglomeration and malachite precipitation; b) time of ripening; c) time of ripening with vanishing of the small surface

For an important increase in supersaturation the particle morphology changes from cushions to spheres (SAXS precipitation system). The number of primary particles per unit volume increases significantly, using the assumption that each crystallite comes from a single nucleation event. The mean separation moves to smaller values as the supersaturation ratio increases. As the particle size decreases their velocity increases, the mean separation decreases and thus collision frequency increases. Also nucleation from higher S will have-at least initially - a higher ionic concentration. The higher ionic concentration may lead to a random aggregation as discussed above for the early stage of CuC_2O_4 low S precipitation. At these higher supersaturation this period should last longer and the local potential minimum is too deep E_2 to allow particle orientation before more particles are attached. The particles aggregate as spheres to minimise the volume.

Table 24: Supersaturation of copper oxalate, number of particles in the precipitation system, their velocity and mean separation

Supersaturation ratio	Number of particles (1 dm^3)	Velocity (m/s)	Mean separation (nm)
0.70	$6.53 \cdot 10^{14}$	0.09	1082
1.02	$3.88 \cdot 10^{16}$	0.34	268
1.26	$6.33 \cdot 10^{16}$	0.86	101
1.48	$8.22 \cdot 10^{16}$	0.69	90

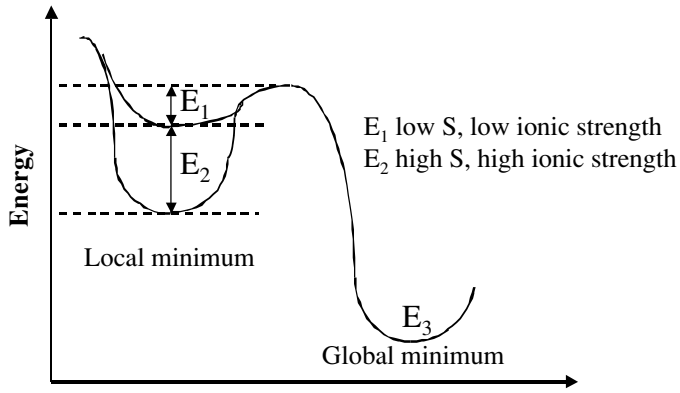

Figure 40: Variation of system energy of precipitation as a function of particles size

2.3. General conclusion of copper oxalate precipitation

During this chapter several avenues of investigation were made on copper oxalate precipitation from the early stages of precipitation to the final nanostructured particles. Using thermodynamic solubility data to simulate the pH as a function of supersaturation it was possible to model the kinetics of precipitation by experimentally following the pH behaviour. To explain the pH behaviour it was necessary to account for the precipitation of two solid phases, copper oxalate and malachite. The amount of malachite predicted is so low (0.4 % wt) that it was not possible to detect it experimentally.

The particle evolution and kinetics of precipitation were linked together to give a more detailed proposition for the mechanism of copper oxalate formation. The elucidation of the mechanism of particle formation was made on intermediate and final stages, the aggregation and growth. The initial stage of nucleation and growth of the primary particles is still difficult to elucidate even using the SAXS measurements, this stage took place in a few seconds not quite accessible by the SAXS system used. The mechanism proposed for this first step is that each nucleus grows to a certain size by molecular attachment. The mechanism of aggregation seems to involve more then one single process. The aggregation seems take place in two different regimes one characterised by a random organisation and the second by a specific organisation. The specific organisation involved a possible secondary nucleation. The

proposed mechanism was developed using the experimental data of microscopy and *in-situ* particle size measurement. These measurements from 2 minutes to 2 weeks generally confirm the previously proposed brick-by-brick agglomeration mechanism for intermediate times (2-30 minutes). After 2 weeks a disc or plate like morphology with only two curved surfaces indicate the equilibrium form has been achieved. Between 10 and 60 minutes, 4 small lateral higher energy surfaces are still presents giving a more cushion like morphology. This approach of using a small well-mixed batch reactor, following pH *in-situ* and using high resolution SEM and TEM cross section, *ex-situ* for specific time intervals has been successful in further elucidating the growth mechanism of copper oxalate.

Chapter 3: Transformation of copper oxalate into metallic copper particles

3.1. Introduction

This chapter describes the strategy applied and the possible kinetic mechanism for the reduction of copper oxalate nanostructured materials into metallic copper, with the aim of conserving of particles morphology and nanocrystals organisation. The copper oxalate was syntheses by precipitation as described in Chapter 2. Several studies were made on the kinetics of oxalate transformation into the oxide or metallic state, under different atmospheres and thermal treatments. Several mechanisms have been proposed in the literature from TGA curves, DSC/ATD measurements and mass spectrometer without a real understanding of nanostructured particles transformation as discussed in chapter 1.

This chapter will be divided into three parts:

- ✓ *first will treat the transformation of copper oxalate nanostructured materials under a reducing atmosphere of helium and hydrogen directly into metallic copper with variation of pressure and temperature;*
- ✓ *the second part describes the transformation of oxalate into oxide, with detailed characterisation of the particles evolution. Methods such as SSA, HRSEM, cross-section TEM and XRD were used;*
- ✓ *the third part investigates the transformation of copper oxide into metallic copper under a reducing atmosphere. The evolution of the particles nanostructure has been investigated with HRSEM from the initial stage, passing through intermediate states and ending with metallic copper. Using thermogravimetric analyses and particle characterisation, a possible kinetic model has been proposed to explain the mechanism of reduction.*

3.2.1. Copper oxalate nanostructure materials - characterisation

The copper oxalate nanostructured material was synthesised by an aqueous precipitation route in the presence of hydroxypropylmethylcellulose (HPMC). The particles showed a cubic morphology with a high internal anisotropy given by the crystallographic structure and the shape of the primary particles[6].

a) 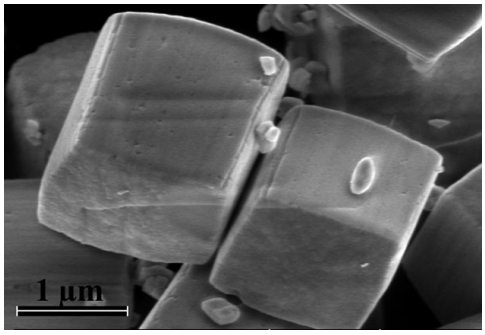

b) 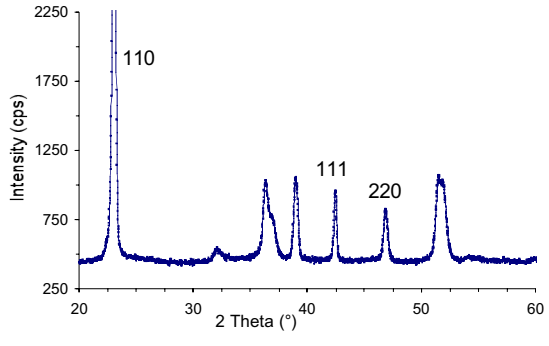

Figure 41: Micrographe HRSEM for copper oxalate nanostructure particles with four smooth surfaces (ε hydrophobic) and two rough surfaces (α hydrophilic); b) X-ray diffraction patterns of copper oxalate

The average crystallite diameters were calculated from peak broadening of the X- ray diffraction (XRD) patterns (Figure 41 b). The primary particle size was estimate using the Scherrer equation to be around 40 nm using software TOPAS 2000, for the refinement the copper oxalate anhydride structure was used (see chapter 2.2.4.B)

Figure 41a shows the cubic morphology of the copper oxalate with a size of about 1µm. HRSEM allowed distinguishing the six surfaces of the cubes with two slightly rough surfaces perpendicular to 001 axis (α-surface) and four smooth surfaces perpendicular to 110 axis (ε-surface) as illustrated in Figure 42. The adsorption of organic additive is expected to occur on the smooth surfaces[6].

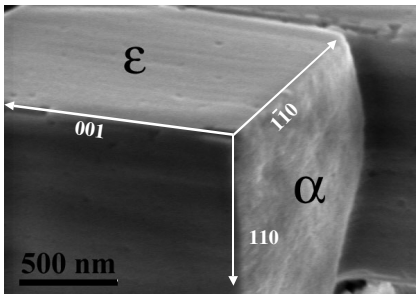

Figure 42: Copper oxalate particles at high resolution with the specific surface and the particles orientation

The copper oxalate precipitate showed a specific surface area of 3.3 m^2/g from nitrogen adsorption measurements, which is very close to the geometric surface area for particles with a width of 850 nm and a height of 1000 nm which is 2.5 m^2/g. This indicates that there is no, or very little, open porosity despite the slightly rough aspect of the two α-faces.

The physico-chemical characteristics of copper oxalate are given in Table 25.

Table 25: Physico-chemical properties of copper oxalate

	Density (kg/m^3)	SSA (m^2/g)
CuC_2O_4	3500	3.3

3.2.2. Copper oxide synthesis

Previous work on the transformation in air showed that the cubic morphology could be conserved when producing copper oxide[87]. The transformation into the oxide phase will not be studied in great detail as it is considered as a preparative step for the more difficult transformation into the metal studied in detail in a later section. Most of the transformation was thus made using a simple tube furnace. Some in-situ SAXS experiment were however carried out along with ex-situ characterisation of the powder after different thermal treatments in the tubular furnace.

The main goal was to conserve the particles morphology and the nanodomains dispersion inside the particles and also to produce powder with a high surface area. The transformation of the oxalate into oxide was made using a tubular oven (Linderberg), the air flow rate was 20 ml/min, and several ramps and dwells are described in (Figure 43).

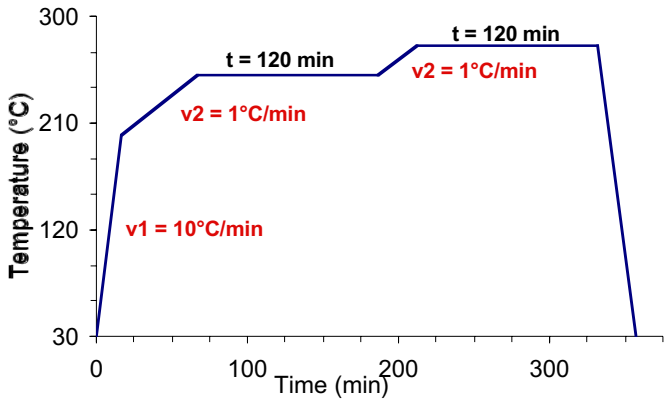

Figure 43: Thermal cycle for copper oxalate decomposition under air at 1 atm pressure

The SAXS measurements were performed with a classical Kratky camera installed on an X-ray tube. The powder was placed in a capillary tube with a diameter of 1 mm and wall thickness of 0.01mm, which was sealed. Thereafter the capillary was placed in a heating stage (KHR, Anton Paar, Graz, Austria) and heated with a heating rate of 10°C/min without any gas regeneration. The temperature was set at 250°C and measurements were provided during 3 hours each 30 minutes.

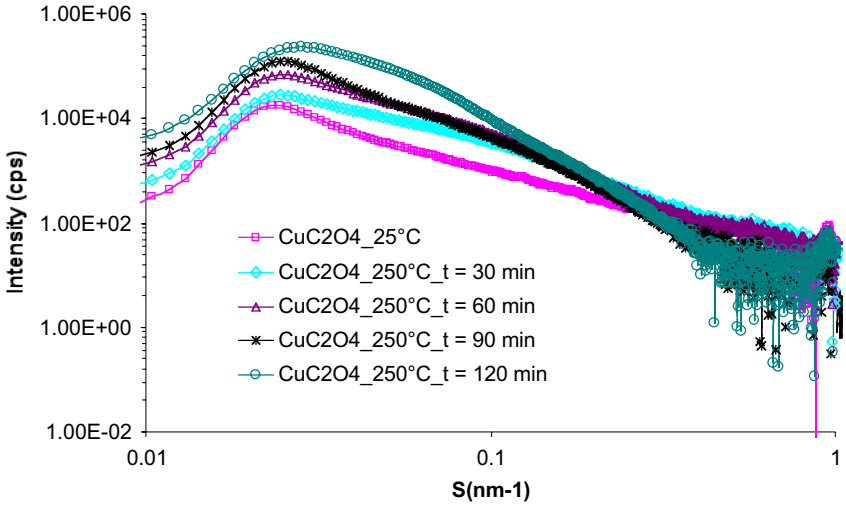

Figure 44: Diffraction pattern of copper oxalate under investigation, respectively it transformations into oxide at 250°C for different time of dwells[85]

Figure 44 depicts the diffraction patterns intensity versus the inverse of scattering vectors. The decrease of intensity for S approaching 1 come from the fact that initial powder copper oxalate has an internal porosity of about 14% and during the transformation this porosity increases as time. In the present case of a copper oxide with a final SSA of 70m^2/g the porosity was calculated to be 65%.

Copper oxide characterisation

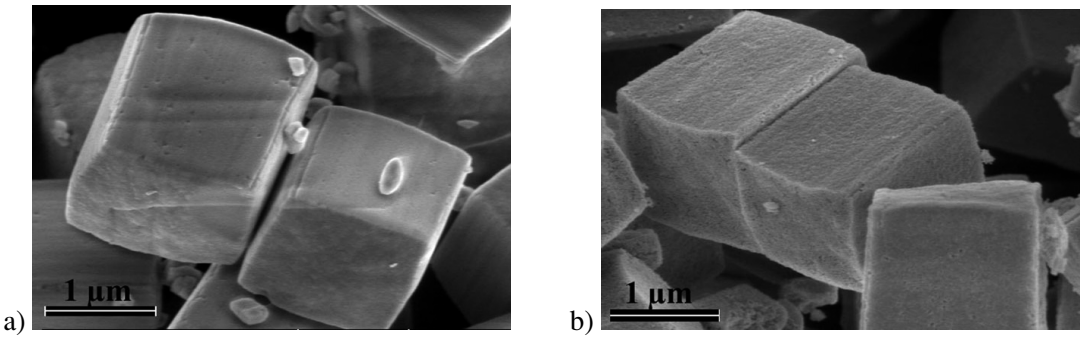

Figure 45: a) copper oxalate nanostructured particles with a cubic morphology used for decomposition under air; b) copper oxalate nanostructured particles obtain from copper oxalate after decomposition

Figure 45 shows the particles before and after transformation, particle morphology was well conserved. The oxide also shows a nanostructure resulting in the high surface area of about 70 m^2/g, with a d_{BET} equal to 13.5nm.

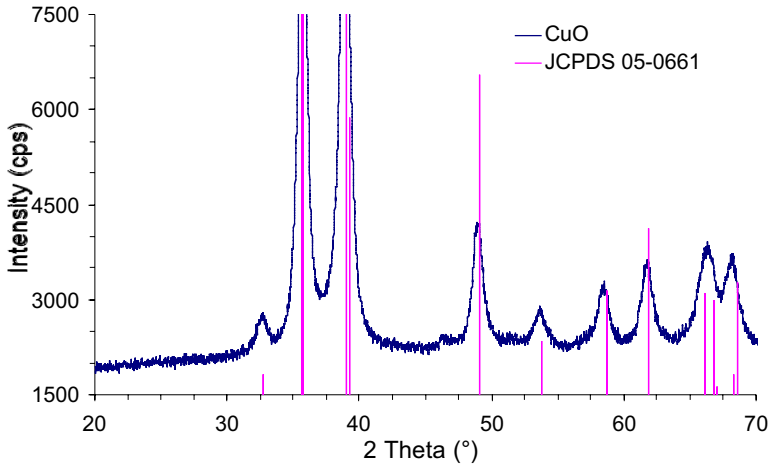

Figure 46: Diffraction patters of copper oxide nanostructure particles

Figure 46 shows the diffraction patterns of the resulting copper oxide, corresponding to a monoclinic crystallographic structure as, Tenorite, CuO phase (JCPDS 05-0661). The crystallite size was been fitted using the Software TOPAS 2000. The estimation of the primary particles size was of about 15 nm, which is similar to the d_{BET} indicating that the porosity is open and accessible to nitrogen. The spatial organisation of nanoparticles of copper oxide inside the particles was examined by TEM cross-section. The samples were prepared as previously described in 2.2.1.

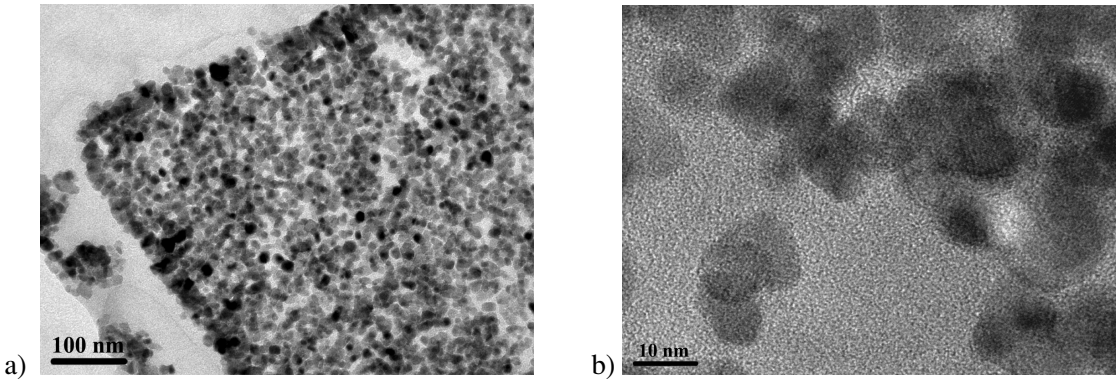

Figure 47: Micrographs TEM cross-sections of copper oxide particles used for the reduction to metallic copper

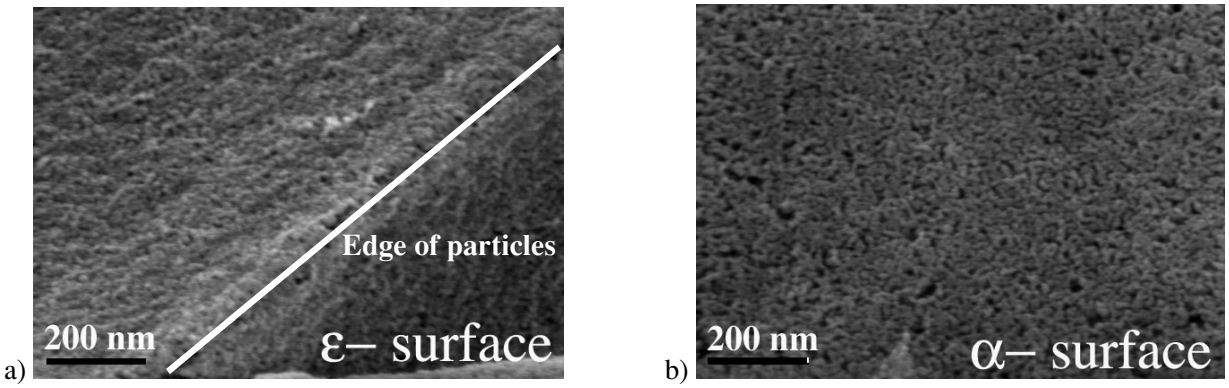

Figure 48: Copper oxide particles a) ε surface with a high density of primary nanoparticles; b) α surface showing a higher porosity than ε surface

Figure 47 a) shows particles with cubic shapes with well defined edges and corners, and a thin layer with a high density of particles at the outer surface expected to be the epsilon surface of the initial particles, from comparison with HRSEM images. Figure 47 b) shows primary particles of about 15 nm; the same order of magnitude estimated by XRD and specific surface area. We assumed that particles were observed on planes perpendicular to the 001 direction. The particles seem to be less dense towards the core, which is similar to the precursor copper oxalates particles (chapter 2 Figure 28 *a*)). The primary particles have a rounded appearance. Figure 48 a) shows the two distinct surfaces of copper oxide particles with differences in particles density: the ε-surface showing a higher density compared to the α-surface. The size of the pores was determined by nitrogen adsorption/desorption (NAD) with an average pore size of 12nm. The particles porosity was determined at around 12 nm by the NAD measurements.

Table 26: Physico - chemical characteristics of copper oxide synthesised by decomposition

Phase	S_{BET} (m^2/g)	Grain Shape	Diameter Size (nm)				Density (g/cm^3)
			XRD	SAXS	d_{BET}	TEM	
CuO (Tenorite) (JCPDS 05-0661)	70	Sphere	15	18	13	15	6.51 (JCPDS 05-0661)

Table 26, summarises the measured physical parameters of copper oxide as well as the theoretical powder density from JCPDS file 05-0661.

3.3. Thermogravimetric analysis

3.3.1. Copper oxalate investigation

The reduction of copper oxalate was studied using thermogravimetric analysis - SETARAM TG/ATD 92 in alumina crucibles. The TG trace was obtained at a heating rate of 5 K/min in a helium and hydrogen atmosphere in a ratio of 970 mbar to 40 mbar respectively. Figure 49 shows the evolution of the weight loss in (%) as a function of temperature. At the beginning of transformation the weight loss changes slowly between 30 and 250°C then an important decreases in weight is visible up to a temperature near 300°C. The total weight loss under reducing atmosphere is of 59.6% similar to values seen in a previous[87] study. The weight lost in the first part of decomposition corresponds to approximately 0.3 mole of water molecules per copper oxalate, which corresponds to the dehydration process (R_1) and close to the nominal 0.5 generally expected. The fast weight loss between 250-300°C was 58 % wt, which corresponds to the reduction of copper oxalate anhydride into metallic copper (R_2). This is in agreement with previous studies[86,87].

$CuC_2O_4 \cdot 0.3H_2O_{(s)} \rightarrow CuC_2O_{4(s)} + 0.3\ H_2O_{(g)}$ R_1

$CuC_2O_{4(s)} + H_2 \rightarrow Cu_{(s)} + 2\ CO_{2(g)} + H_{2(g)}$ R_2

The decomposition of copper oxalate proceeds ba a simple decomposition process with the easier break of M-O bond than C-O bond rupture, so it mainly produces CO_2 gas[88]. This can be explained by the foramtion energies for each gases[89]. At 215°C CO_2 is more stable than the reacting with hydrogen gas. So there are no formation of CH_4 and H_2O in the decomposition process of copper oxalate by gas-gas reaction. To study the kinetics of decomposition under isothermal conditions, the temperature was set at 215°C.

Isothermal curves were obtained by heating 15 mg of powder at 215°C under the same hydrogen and helium atmosphere. The tested samples were first heated up to 150°C under 1 atm helium pressure during 30 minutes for dehydration. Then the temperature was rapidly increased (20°C/min) up to 210°C and then at 5K/min up to 215°C. As soon as the isothermal conditions were established, the partial pressure ratio of helium and hydrogen gases was adjusted. In a first step the overall evolution of cooper oxalate (cubic morphology) to metallic copper was investigated. Close attention was paid to particle transformation as a function of reaction yield. The isothermal kinetic curves were interpreted qualitatively, however the influence of the hydrogen partial pressure was not investigated.

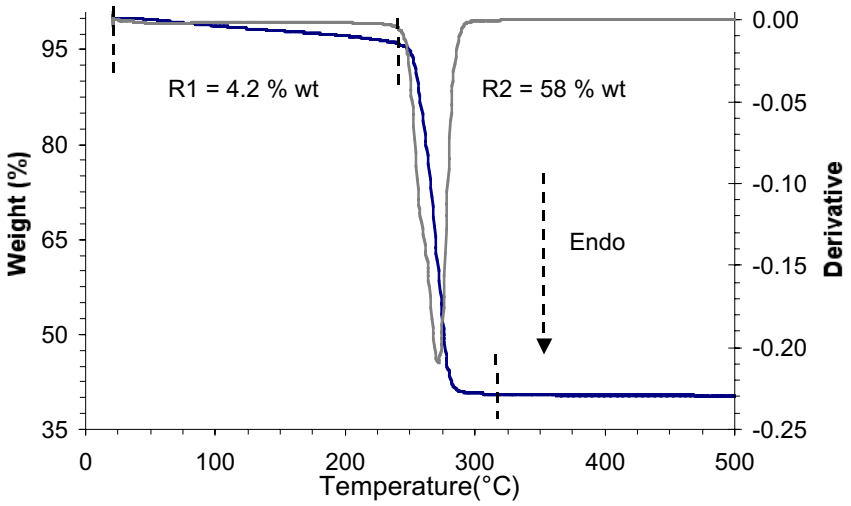

Figure 49: Typical trace of TG and DTG recorded simultaneously for the decomposition of copper oxalate under H_2/He atmospheres

The powders at the intermediate stage of transformation were characterised in ex-situ conditions using HRSEM, for morphology evolution, and XRD for the detection of the crystalline phases involved during the transformation, at various stages of the thermal cycle.

3.3.2. Characterisation of the transformation of copper oxalate particles into copper

For the different stages of transformation the samples were investigated by XRD, (Figure 50 and Figure 51). XRD analysis shows the presence of two phases only: copper oxalate and metallic copper. No

other intermediate phases such as oxides (Cu_2O or CuO) were identified. The reaction yield calculated from the peaks areas of the XRD analysis corresponds very well to the one calculated from the thermogravimetric weight loss data (±2% wt) assuming only 2 phases. We conclude therefore that the reduction passes directly from copper oxalate to metallic copper.

During this chapter the reaction yield of transformation will be noted as "α" ($0 < \alpha < 1$) for a simple transformation, for examples here the $CuC_2O_4 \rightarrow Cu + 2CO_2$, and α_{total} when the system goes through an intermediate step as, $2CuO \rightarrow Cu_2O + 1/2\ O_2$; $Cu_2O \rightarrow 2Cu + 1/2\ O_2$ (α_{total} is the product of the two intermediate transformations for the separate reaction in the case of simultaneously reaction see Apendix of Chapter 3).

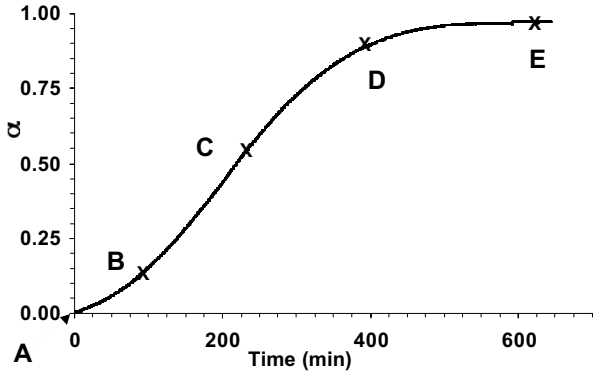

Figure 50: Reaction yields (α) as a function of time from TG analysis. The points A, B, C, D, E corresponds to conditions where the XRD and HRSEM analyses were performed

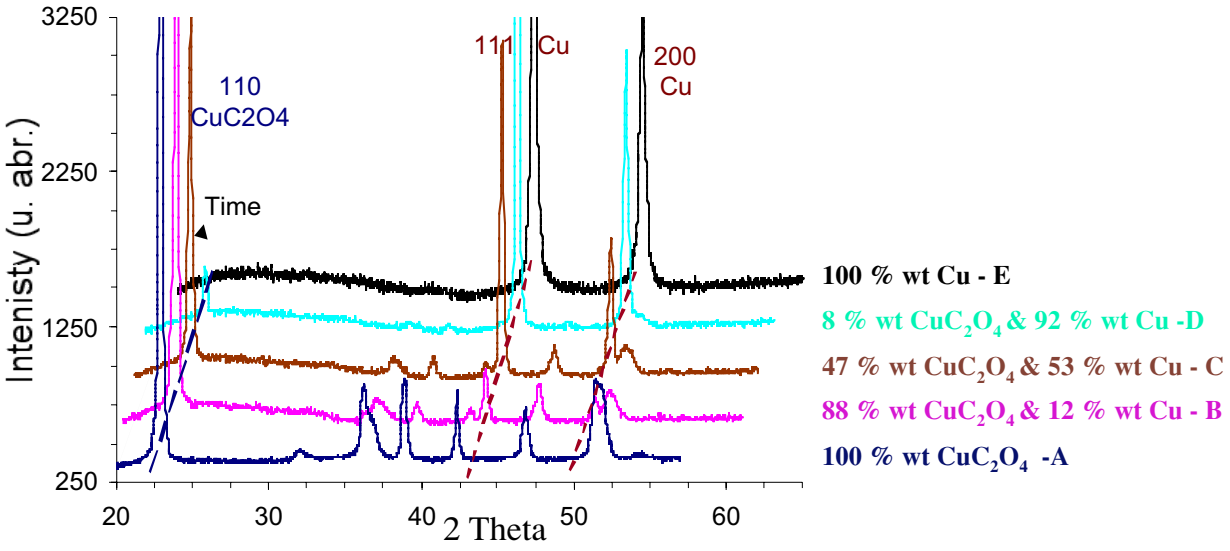

Figure 51: XRD patterns for copper oxalate reduction as a function of conversion

Figure 50 shows the reaction yield as a function of reaction time from TG analysis. Samples where XRD (Figure 51) and HRSEM analyses were performed are indicated from A to D. Figure 52 shows some particles transformed at 215°C for several degrees of conversion. We can see in Figure 52 (a)

(12% Cu) that the α-faces becomes very rough while the ε surfaces remain smooth and well defined. This suggests that the transformation seem to be initiated at the two extremities of the particle (α-faces). This corresponds to the axis parallel to the "molecular ribbons" of copper oxalate that makes up the crystal structure[90]. This behaviour may be explained by a difference in density of the primary nanoparticles at the particle surface as a result of the "brick by brick" growth process explained in Chapter 2. As mentioned earlier the smoother ε-faces are also the ones where HPMC is assumed to adsorb, leading to this cube-like morphology rather than the cushion-like morphology obtained without HPMC. Both, the possible differences in density of the two types of faces and the HPMC content could thus contribute to this apparently faster transformation of the α-faces. Also as the core of the particle may have up to 14% porosity, once this porosity is accessed, further acceleration of the reaction along this direction may be expected (Figure 52 (b)). Up to a conversion of 87% wt the architecture of the cubic morphology is kept under the isothermal reduction at 215°C. Although sintering between individual grains can be seen. For higher conversions the cubic shape is completely lost because of the high degree of sintering.

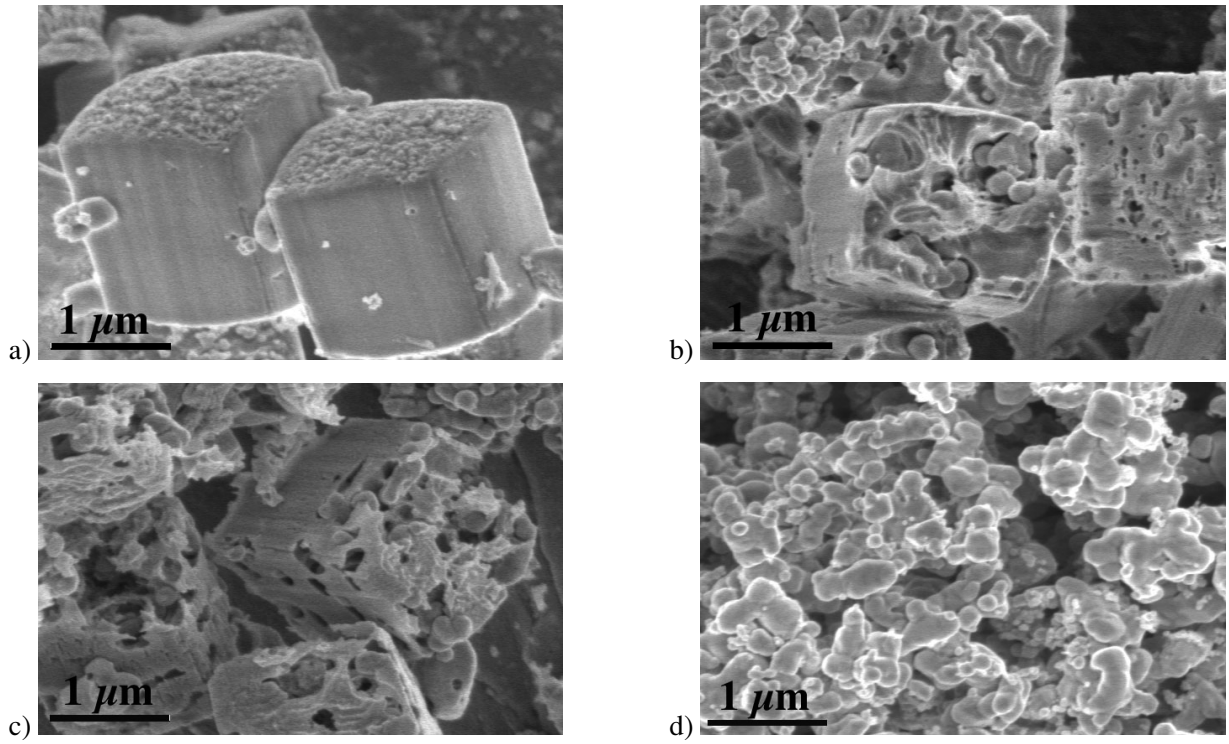

Figure 52: Copper oxalate reduction after different reaction yield: a) 0.12; b) 0.53; c) 0.88; d) 1.00

The reaction proceeds through a progressive transformation of the faces with propagation into the particle core. Measurement of the overall reaction rate (of product or of reactant consumption) do not necessarily provide sufficient information to completely described the kinetics of the reduction process of copper oxalate into metallic copper. The kinetic modelling of transformation must consider the reaction velocity as a function of time, the size of the initial particles and their texture[91,94].

3.3.3. Thermogravimetric analysis of the transformation of copper oxide to metal

The transformation of copper oxide particles into metallic copper with a high surface area under reducing atmosphere was studied in more detail.

The chemical reactions of the reduction of copper oxide are given by reactions R_3 to R_5:

$2\ CuO_{(s)} + H_{2(g)} \rightarrow Cu_2O_{(s)} + H_2O_{(g)}$ reaction yield α_1 *R_3*

$Cu_2O_{(s)} + H_{2(g)} \rightarrow 2\ Cu_{(s)} + 1/2\ H_2O_{(g)}$ reaction yield α_2 *R_4*

$CuO_{(s)} + H_{2(g)} \rightarrow Cu_{(s)} + H_2O_{(g)}$ reaction yield α_3 *R_5*

Reduction of copper oxide to metallic copper has been investigated in a SETARAM TAG single oven thermo-balance under reducing atmospheres (He: 970 mbar and H_2 40 mbar), in isothermal conditions at 124.5°C. The flow rate of the gas mixture was set at 2 l/h. Powder samples of around 20 mg were analysed in alumina crucibles. The sample was kept for 35 minutes at 30°C under (He &H_2) atmospheres, then heated up to 70°C with a rate heat of 10K/min, and then a faster rate of 20°C/min was applied up to 117.5°C, followed finally by 5K/min up to 124.5°C. All these rates were chosen to evaporate the possible water adsorbed at the surfaces of copper oxide particles that present a high surface area, and also to reach as soon as possible the isothermal conditions without any powder transformation. The weight loss (TG) was monitored as a function of time. Figure 53 depicts the total reaction yield evolution as a function of time and the heat flow curve.

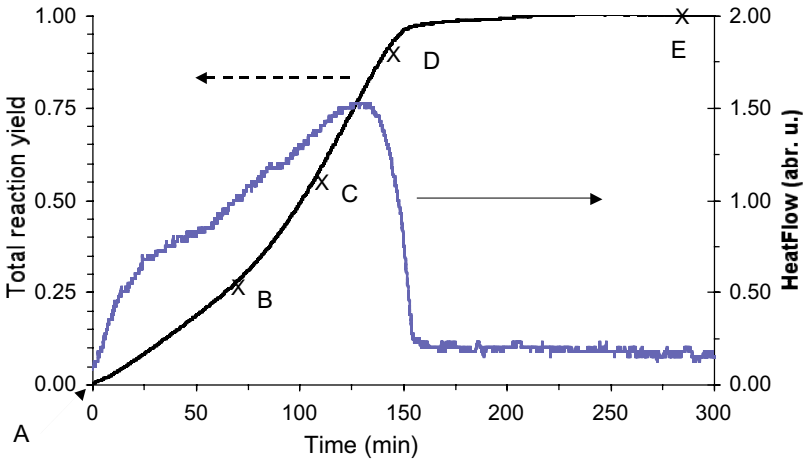

Figure 53: Reaction yield and heat flow as a function of time; Points A, B, C, D and E correspond to the conditions where the reaction was stopped and the particles under transformation were characterised using different techniques

The curve of heat rate shows three different slopes one before 0.30 of total transformation then at about 0.75 and finally an inflection point through the end of reaction. Figure 53 shows the curve $\alpha(t)$ only the isothermal part of the curves are shown from the point where the sample temperature effectively reached

124.5°C. A, B, C, D and E are the points where the reaction was stopped. The powder characterisation to the intermediate state was carried out using ex-situ conditions such as HRSEM, XRD, SSA and TEM cross-section. Point A corresponds to the copper oxide characterisation as described above in section 3.2.2.

The influence of water vapour pressure on the transformation was also investigated. In that aim water vapour was added to the flowing gases during the entire transformation. The measurements were performed at three different water partial pressures.

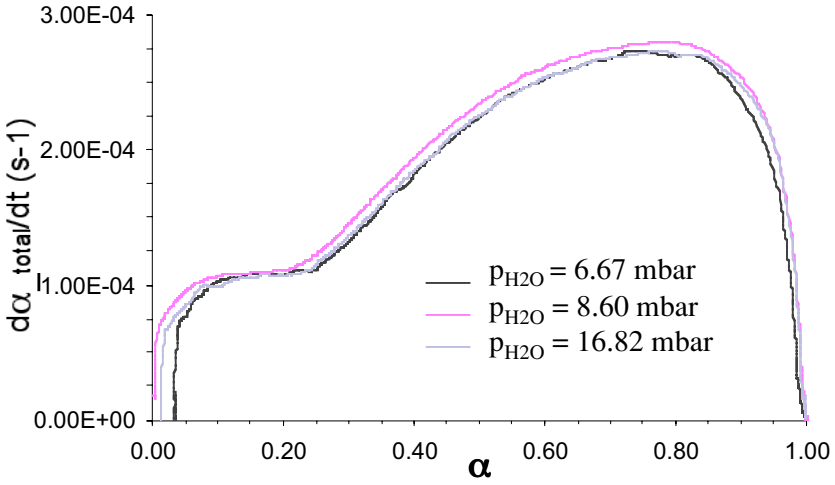

Figure 54: Derivative of α_{total} versus time as a function of total reaction yield for different water vapour partial pressures

Figure 54 shows the influence of water vapour partial pressure on the reduction process of the copper oxide transformation into metallic copper. The kinetic curves show very similar trends indicating that water partial pressure does not influence the mechanism of the transformation under these conditions.

3.3.4. Copper oxide intermediate product characterisation

After different degrees of conversion the samples were analysed using a Philips X-Pert Diffractometer as described in chapter 2. The diffractograms of the three distinct phases CuO, Cu_2O and Cu, correspond to the JCPDS files 004 -551, 004-557, and 004-836 respectively. The precursor products after transformation have been kept under argon atmosphere to avoid the possible oxidation of the Cu^+ or Cu under oxygen atmospheric pressure. The diffractograms for the different reaction yields are presented in Figure 55.

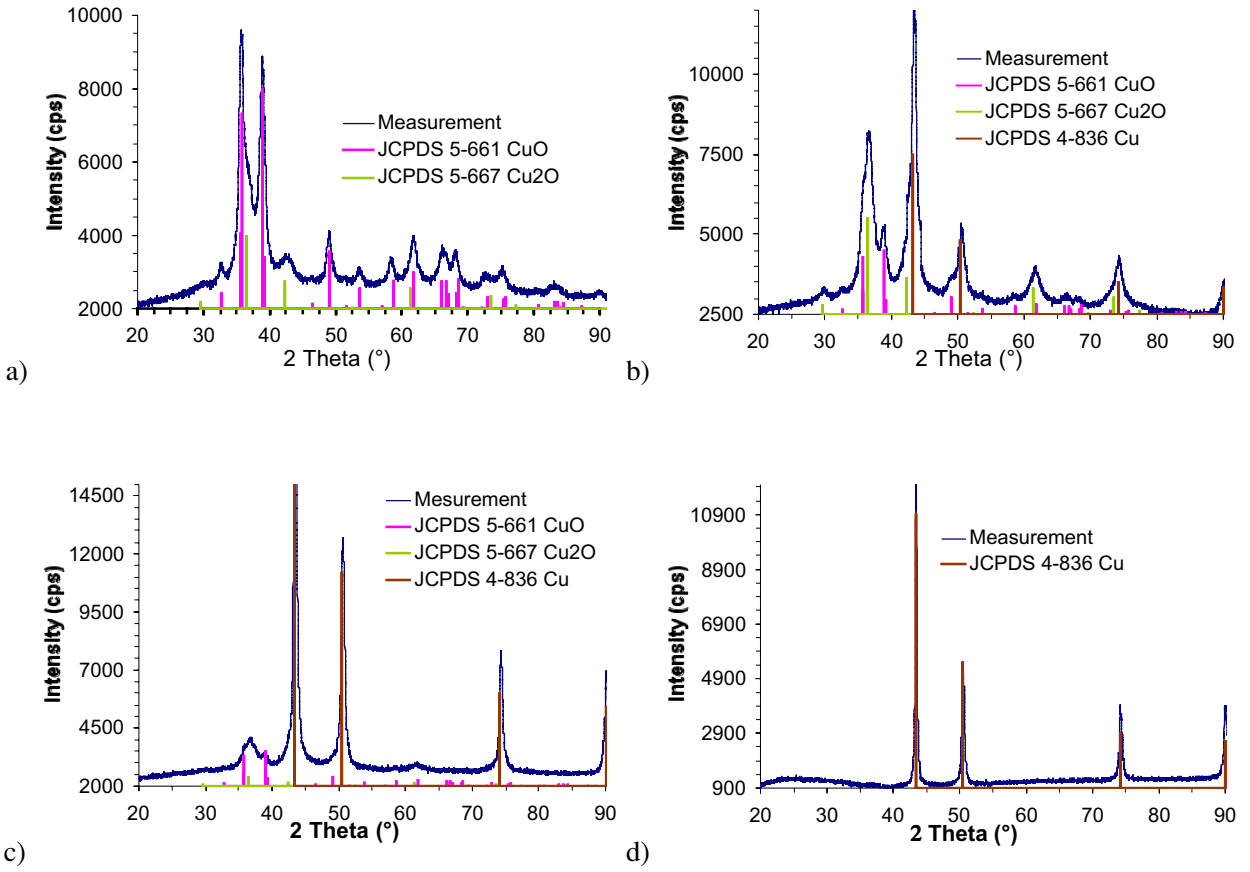

Figure 55 : X-ray diffraction patterns for the different stages of the conversion: a) CuO 62.3 % wt, Cu_2O 37.7 % wt; b) CuO 30.0 % wt, Cu_2O 33.0 % wt, Cu 37 % wt; c) CuO 4.0 % wt, Cu_2O 9.5 % wt, Cu 86.5 % wt, d) Cu 100 % wt[92]

The reaction yield was calculated using two methods: the thermogravimetric analysis and the XRD peaks intensity. The results for this analysis are summarised in Table 27. The measurements were carried out with an error of 3 nm.

Table 27: Summary of XRD data: percentage of each copper oxide phase during the reduction and crystallites size evolutions as a comparison with the total reaction transformation obtained using the TG results

TGA	0 .0	0.21		0.63		0.93		1.00	
yield		Percentage	*size (nm)*	Percentage	*size (nm)*	Percentage	*size (nm)*	Percentage	*size (nm)*
CuO	*15 nm*	62.32	*14.4*	33.7	*12.8*	4.3	*17.2*	-	
Cu_2O	-	37.68	*6.1*	30.5	*8.1*	8.9	*6.2*	-	
Cu	-	-		35.5	*11.5*	86.6	*30*	100	*42*
XRD		37.68		0.66		95.70		100	

Table 28: Specific Surface Area for the initial stage of copper oxide before transformation, final particles transformed into metal and an intermediate state where the three phases are in the same masse ratio[i]

TG	0.00	0.63	1.00
Percentage wieght of phases for distinct conversions of reaction			
CuO	100	33.7	
Cu_2O	-	30.5	-
Cu		35.5	100
SSA(m^2/g)	70	40.5	5
d_{BET}	14	-	135

Table 28 describes the SSA of the copper oxide before transformation going through an intermediate stage and finally to the metallic. The values for the reaction yield are higher for TGA than for the XRD peak intensity. This behaviour comes from the fact that Cu_2O and Cu can be distributed inside the particles that may modify the ratio between the peaks intensity, leading to an underestimation by XRD.

The physical characteristics of each phase such as the densities: CuO - 6.51 g/cm^3, Cu_2O - 6.1 g/cm^3 and Cu - 8.9 g/cm^3 were from the JCPDS files. These values allow the calculation of the volume ratio for each phase involved in the transformation using:

$$Z = {}^{V_f}\!/_{V_i}, \qquad \textit{Eq 27}$$

where Z is the coefficient of volume change, V_f is the molar volume of the final component (cm^3/mol) and V_i the molar volume of the initial component.

Table 29: Volume ratio of copper oxides and metallic copper

	Cu_2O/ CuO	Cu/ Cu_2O	Cu/CuO
Z	0.95	0.61	0.54

The theoretical values of Z are smaller then 1, the reaction must happen with a volume contraction. The XRD data given in Table 27 shows the primary particles size evolution from the oxides to the metal phase. XRD data shows an initial transformation of Cu_2O occurs at low reaction yield of 0.20. Then, the three phases are detected and remains visible till the end. The size of the CuO primary particles during the transformation changes a little from the initial 14 nm, decreases for a reaction yield of 0.63 to 12.8 and finally increases to 17.2nm for a reaction yield of 0.93. Moreover the size of Cu_2O also changes

[i] The total reaction yield of transformation was calculated using the wieght loss at a time t in ratio with the total weight loss as for the CuO reduction into Cu.

little from the initial stage of formation of a size of 6.2nm for a reaction yield of 0.21, increases to 8.1 nm for 0.63 and finally decreases to 6.2 nm towards the end of the reaction at α=0.93. However for the metallic copper the size increases from 11.5 nm up to 42 nm during the transformation as the reaction yield increases. These relatively stable sizes for the oxides suggest a rapid transformation of the primary particles once the transformation is nucleated. This behaviour suggests different rates of the transformation of the CuO to Cu_2O to Cu, or also, at the same time, CuO to Cu. Also the anisotropic nature of the particles may contribute to the kinetic as seen for the copper oxalate transformation. Each process is characterised by a particular reaction rate. We will discuss the kinetics of transformation more in detail in the next section of this chapter. Considering the kinetic curves of copper oxide transformation into metal the presence of the two domains were shown in Figure 54. For the first part only the transformation to an intermediate state of copper oxide Cu_2O is expected, up to a reaction yield of 0.20 then the three compounds CuO, Cu_2O and Cu are involved. The intermediate powder with a total reaction yield of 0.63 and the final metallic copper have been characterised by nitrogen adsorption measuring the specific surface area (SSA). The intermediate sample shows a surface area around 40 m^2/g while the copper shows only 5 m^2/g as described in Table 28.

From nitrogen adsorption measurements, the metallic copper shows a d_{BET} of 134 nm, which is high, compared to result obtained by the XRD. From HRSEM micrographs Figure 56 the size seems to be around to 100 nm. These results indicate the final Cu is polycrystalline with some sintering taking place towards the end of the transformation. Figure 56 shows HRSEM images of the copper oxide transformation from the initial stage to final metallic copper passing through various intermediate stages.

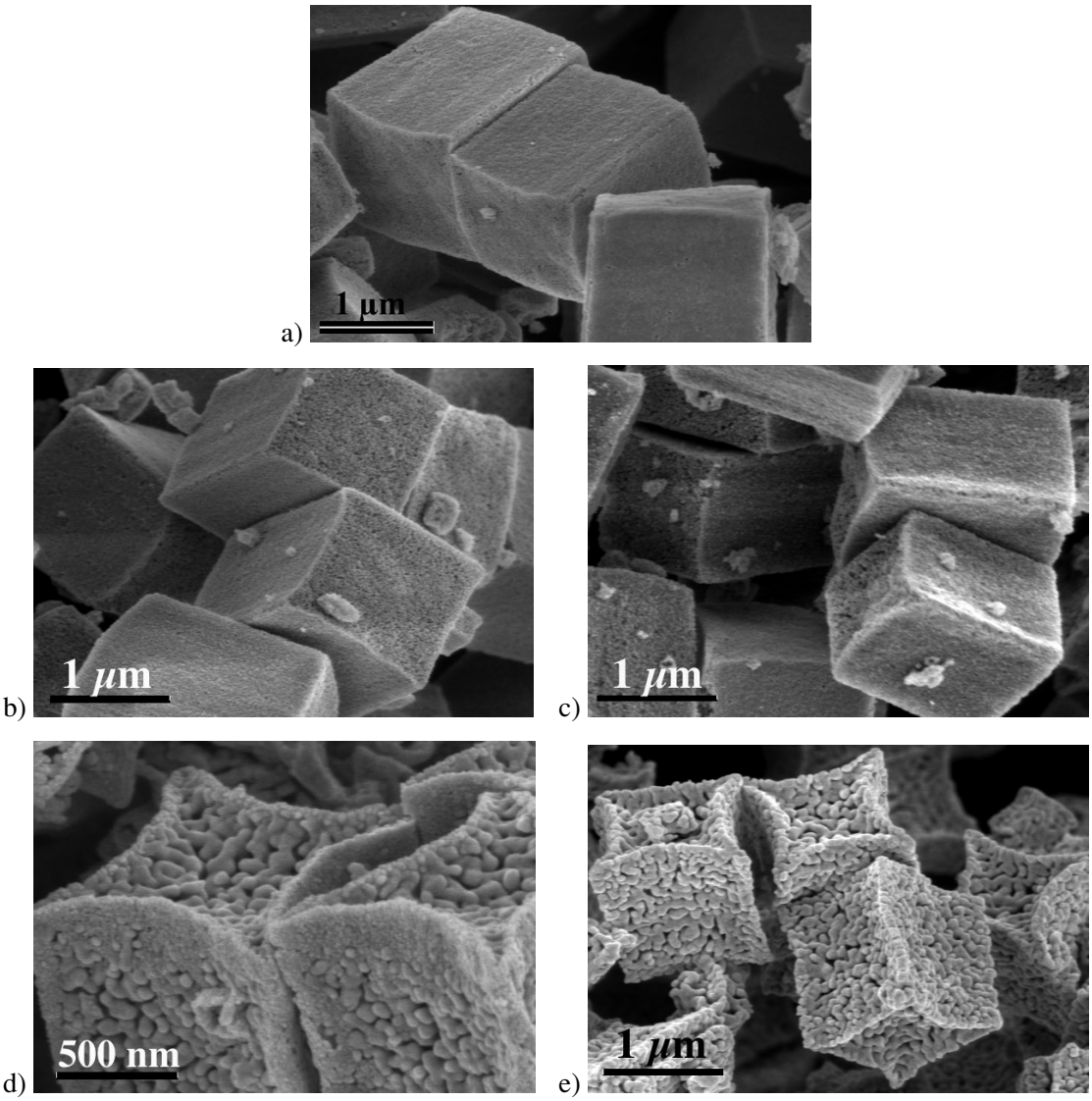

Figure 56: copper oxide reduction into metal: a) $\alpha_{total} = 0.0$; b) $\alpha_{total} = 0.21$; c) $\alpha_{total} = 0.63$; d) $\alpha_{total} = 0.93$; e) $\alpha_{total} = 1$

These HRSEM micrographs show that the reactions are initiated on the α-surface of the particles as also seen for the oxalate transformation. At a total reaction yield of 0.21, the α-surfaces show some changes in pore structure-slightly larger pore size but the particles remains well defined. Initial investigations show porous channels of 12 nm wide. During the transformation process the overall particles size changes little if the skeleton can support the stress involved in the transformation. As a consequence, the porous channels become larger and consequently diffusion in and out of these should become easier. At higher degrees of transformation the high density of particles at the edges (ε-surfaces) is clearly visible and finally sintering of metal copper is observed on both α and ε surfaces. At 0.63 conversion the metallic copper crystallites reach a size of about 30 nm (XRD), while the oxide particles size remains under 17 nm. Using HRSEM micrographs one can estimate the size of the metallic copper crystallites at total conversion is of about 100 nm similar to that calculated previously by SSA. Diffraction

patterns indicates that the size of the Cu_2O particles is at about 8 nm. The micrograph in (Figure 56 d) shows particles at the surface with this typical magnitude, in the "dense" shell of the ε-surfaces. This phenomenon may simply a slow process of transformation of particles at these dense surfaces. One can imagine that at the end of the reduction process, removal of O is difficult; some Cu_2O grains are coated by a fast-reduced Cu film, leaving oxygen trapped as seen in previous studies an films [93,99].

The partially transformed particles α=0.63 were also investigated in TEM cross-section. The goal was to understand the phase distribution in a thin layer of a sample and to estimate the size of the primary particles.

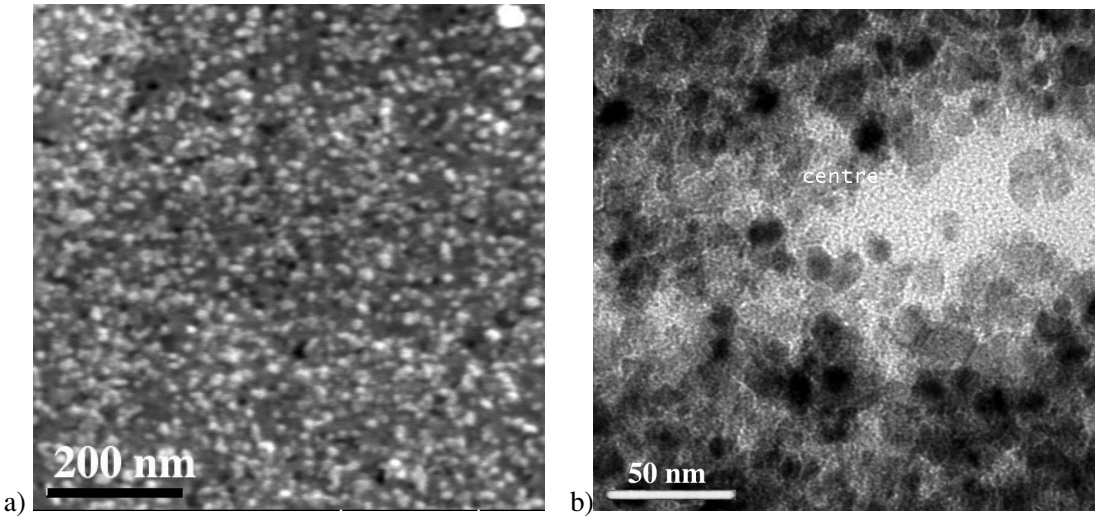

Figure 57: a)) HRSEM image of the same sample with some dots on the particles surface; b Cross section TEM of the sample with a mixture of oxides and metallic copper for α_{total}=0.63 reaction yield

The micrographs in Figure 57 shows primary particles with size from 7 to 17 nm for a total reaction yield of 0.63. These values are of the same order of magnitude as those calculated from XRD data. Figure 57 (a) depicts some dots on the particle surface, which have different contrast to the rest of the particle, suggesting both oxide and metal particles. The diffraction patterns of TEM of this sample was difficult to analyse because of the presence of the three phases involved at about 30% wt of each. The XRD peak intensity, HRSEM and TEM cross section of this level of transformation all show a mixture of crystallites of oxides and metallic copper. These measurements indicate a simultaneous transformation and that even for a high reaction conversion, the CuO is not totally transformed into Cu_2O and finally to Cu. The same kind of behaviour is discussed in the literature, in the case of calcium carbonate when the nucleation process takes a long time, compared to the transformation step [94].

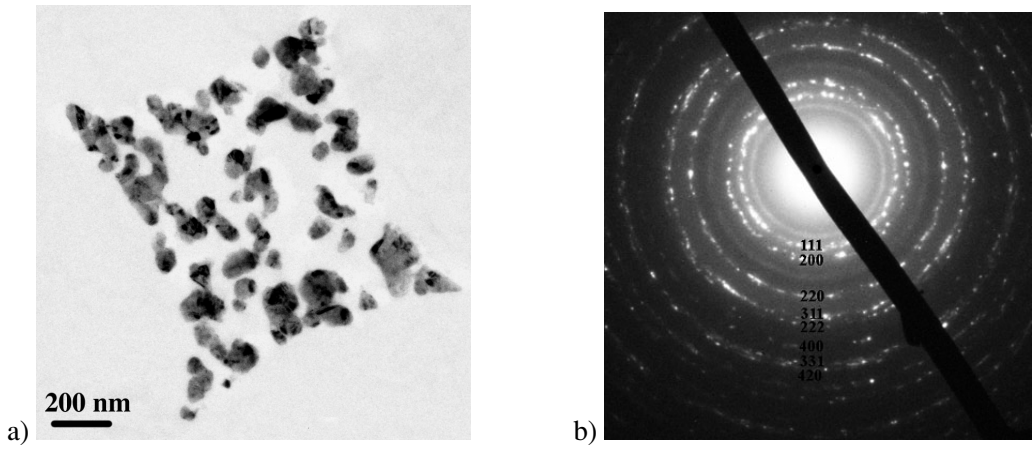

Figure 58: Metallic copper α = 1: a) TEM cross -section micrograph; b) TEM diffraction patterns

Figure 58 shows a TEM cross-section of the 100% Cu particles with a size up to around 100 nm. The rings observed in the TEM diffraction patterns indicates that no ordering of the nanoparticles within the overall cubic particle seemed is apparent and the Cu primary particles are polycrystalline and have undergone a certain degree of sintering.

In order to reach better understanding of the reduction process, a kinetic study of copper oxide transformation was carried out under controlled conditions for different hydrogen partial pressure and temperature.

3.4. Kinetic investigations

Several steps such as nucleation and growth and possible simultaneous sintering processes can describe the transformation of a solid phase under defined physico-chemical conditions. The nucleation step is defined as the starting point of the formation of a new phase. For examples, for the direct transformation (3.3.2) the copper oxalate is considered as the initial phase and the nuclei are the metallic copper. The nuclei are usually formed at the initial solid surface. Figure 59 illustrates the possible formation of Cu nuclei on the external α−surface and their growth at an early stage of the direct transformation of copper oxalate into copper.

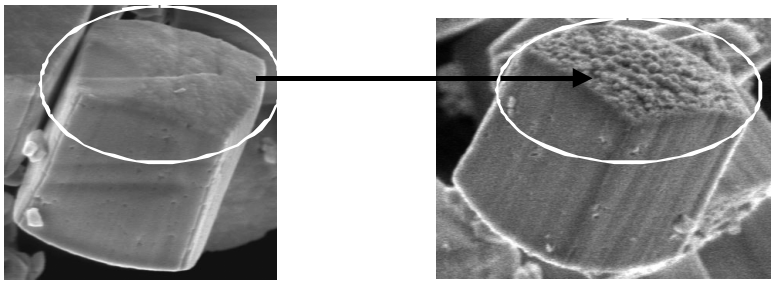

Figure 59: initial stage of copper oxalate before transformation, nuclei formation on the particles surface at an earlier stage of transformation

When nuclei are formed they start growing with respect to a crystallographic direction. The growth process is complex, involving several elementary steps, and it depends on the initial solid with an internal or external development of the new phase as described in Figure 60. For the kinetic model the rate-limiting step of growth can be considered as either diffusion or as an interfacial step:

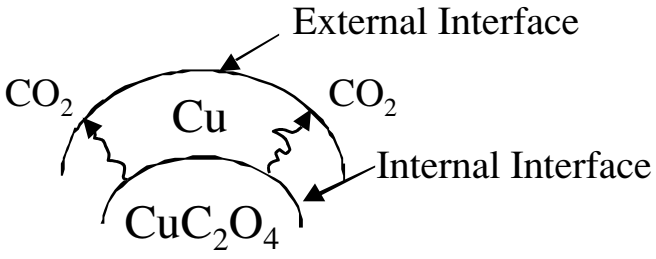

Figure 60: Scheme of the possible transformation of copper oxalate into copper and the types of surfaces involved during the transformation as external: between the gas and the new solid formed and internal between the two solids

Two interfaces exist, one between the two phases (internal interface) and one between the new phase and the gas atmosphere (external interface). For a reaction without intermediate phases such as the copper oxalate reduction to copper:

$CuC_2O_4 \rightarrow Cu + 2\ CO_2$

we can define the reaction yield such as :

$$\alpha = \frac{\xi}{n_0} = \frac{n_{cu(t)}}{n_0} = \frac{n_0 - n_{(ox)(t)}}{n_0} \qquad \textit{Eq 28}$$

where ζ_{CuC2O4} is the reaction advancement relative to the initial copper oxalate phase, n_0 is the initial number of moles (here of the copper oxalate) and n_t the number of moles of copper oxalate after a time t.

$$\xi = n_0 - n_t \qquad \textit{Eq 29}$$

Another term of importance is the "rate of transformation" R (1/s), this corresponds to the derivative of the reaction yield with respect to the time:

$$R = \frac{d\alpha}{dt} \qquad \textit{Eq 30}$$

For experiments that are made under isothermal conditions and at fixed partial pressures of all the gases and on the assumption of a rate limiting step, the rate can be expressed as the product of two function: $\Phi(Y_i)$, which is a function of the intensive parameters (temperature, partial pressures) and thus does not depend on time; and E (t) which is a function related to both shape and size of the region in which the rate-limiting step occurs.

$$R = \Phi\left(Y_i\right) \cdot E\left(t, Y_i(0,t)\right) \qquad \textit{Eq 31}$$

$\Phi(Y_i)$ is called reactivity (mol/m^2·s) and E (m^2/mol) the space function. As E depends on the size of the limiting region, it also depends on time and on the initial shape and size of the solid copper oxalate, as well as on the intensive parameters present from t = 0 to t.

As a consequence of equation 31, it will be possible to establish separate models for the kinetics of a reaction: those corresponding to the space function called " the geometrical model" and those corresponding to the processes of nucleation and growth called " the physico-chemical" model. For a reaction in which one of these two processes (nucleation and growth) is infinitely fast with respect to the other that only one of the physico-chemical models need be considered.

To verify the validity of equation 31, it is necessary to demonstrate that the reactivity $\Phi(Y_i)$ does not depend on time. This hypothesis can be confirmed by performing series experiments in set isothermal or isobaric physico-chemical conditions. For example at a time t_0 the system is under some Y_0 (p_0, T_0) conditions and after a time t_1, by suddenly changing Y_1 (p_0, T_1) will have T or p to another set of conditions. For this class of experiment the rate of transformation is measured just before and after this sudden change, with the assumption that the space function is constant. As a consequence of equation 31 one can write[95]:

$$R_l^1 = \phi\left(p_{H_2}, T_1\right) \cdot E\left(p_{H_2}, T_1, t_1\right)$$

$$R_r^1 = \phi\left(p_{H_2}, T_2\right) \cdot E\left(p_{H_2}, T_1, t_1\right)$$

$$R_l^2 = \phi\left(p_{H_2}, T_1\right) \cdot E\left(p_{H_2}, T_1, t_2\right)$$

$$R_r^2 = \phi\left(p_{H_2}, T_2\right) \cdot E\left(p_{H_2}, T_1, t_2\right)$$

where R_l^1 is the reactance measured on the left hand of the point of the sudden change (juste before the change on isobar or isothermal conditions) R_r^1 is the reactance measured on the right hand of the point of sudden change (just after the change in isobar or isothermal conditions). The index, 1, 2 and so on are for the series of measurements carried out. As the ratio of the rates before and after sudden change must be independent of time, one obtains:

$$\frac{R_r^1}{R_l^1} = \frac{R_r^2}{R_l^2} = \frac{\phi\left(T_2\right)}{\phi\left(T_1\right)} \qquad \textit{Eq 32}$$

In this case, it can be inferred that there exists a rate-limiting step of the growth process (in most of the cases except those corresponding to instantaneous growth explained in detail below 3.4.2.)

3.4.1. Sudden change kinetic analysis

A. System Copper Oxalate - Copper

For copper oxalate, the physico-chemical parameters were modified by a sudden change of temperature, as illustrated in Figure 61.

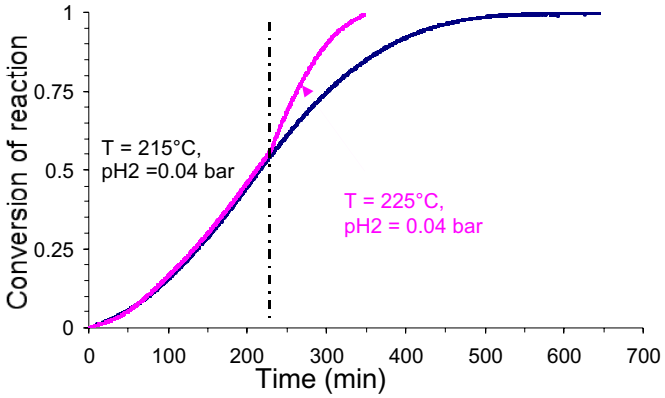

Figure 61: Sudden change of temperature for the copper oxalate transformation into metallic copper

The case of the direct transformation of copper oxalate into metallic copper was studied under p_{H2} = 0.04 bar at 215°C. The sudden change was realised under isobar conditions at pH2= 0.04 bar from 215°C to 225°C by a rapid increase in temperature, for different degrees of reaction yield. The heating took place in a short time (5°C/min) to avoid the possible transformation of powder and conserve the reaction yield (α). The rate was measured before and after the sudden changes (see Table 30). Figure 62 represents the ratios obtained for various values of α.

Table 30: Summary of the experimental sudden change on temperature for the various values of reaction yield of copper oxalate

Reaction Yield (α)	R_1 (s^{-1})	R_r (s^{-1})	R_r/R_1
0.23	$2.55 \cdot 10^{-3}$	$5.97 \cdot 10^{-3}$	2.34 ± 0.10
0.39	$2.87 \cdot 10^{-3}$	$6.17 \cdot 10^{-3}$	2.15 ± 0.10
0.56	$3.03 \cdot 10^{-3}$	$5.39 \cdot 10^{-3}$	1.77 ± 0.10
0.70	$3.22 \cdot 10^{-3}$	$5.11 \cdot 10^{-3}$	1.58 ± 0.10
0.79	$3.08 \cdot 10^{-3}$	$5.14 \cdot 10^{-3}$	1.67 ± 0.10

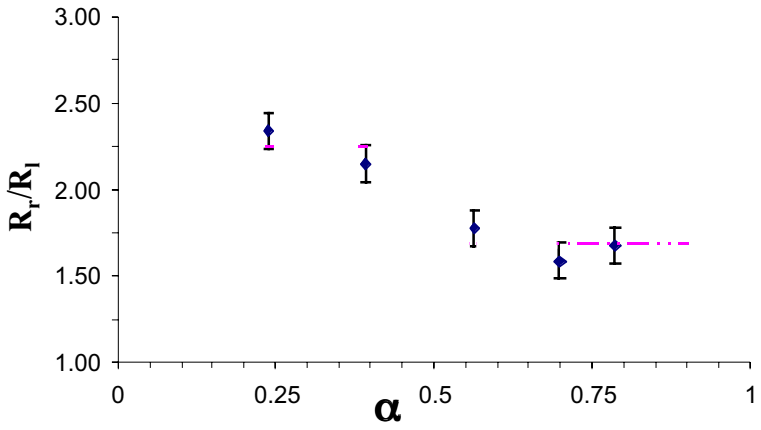

Figure 62: Velocity ratio calculated for various reaction yields of copper oxalate

Considering the experimental error for the direct transformation of copper oxalate into metallic copper, two domains can be distinguished, one domain before a yield of 0.50 and another towards the end of the transformation. This behaviour could suggest that a single rate-limiting step is not valid in the whole range of α.

B. System copper oxide - copper

The transformation under p_{H2} of copper oxide into metallic copper was investigated by sudden changes on temperature and hydrogen partial pressure for several degrees of reaction.

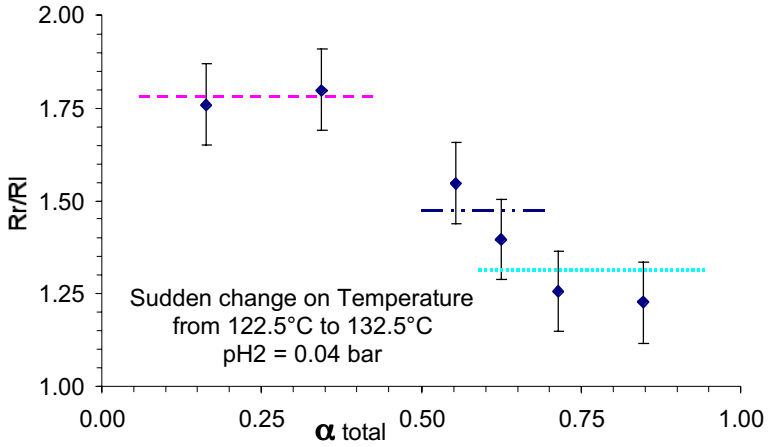

Figure 63: Sudden change method on isobar conditions for the copper oxide transformation into metallic copper for different extents of reaction

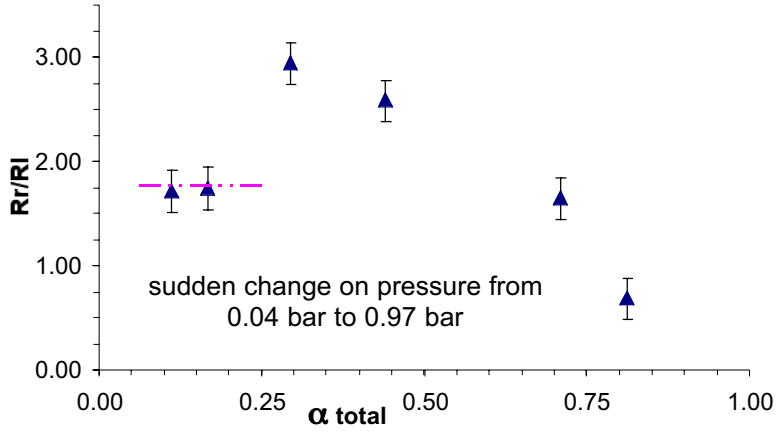

Figure 64: Sudden change on isotherm conditions for the copper oxide transformation into metallic copper for different extents of reaction

Figure 63 shows the isothermal experiments carried out under fixed partial pressure of hydrogen at 0.042 atm. The experiments were made first at a temperature of 125°C until a certain extent of reaction and then the temperature was changed to 135°C. The heating rate was of at 5°C/min to avoid the possible transformation during the heating up. The time for the system to reach the isothermal conditions is about 7 minutes. Similar experiments were carried out in similar conditions but the sudden change was made under isobar condition, for a sudden change of the hydrogen partial pressure from 0.042 up to 0.099 atm. The rate of conversion was calculated just before and after the sudden change for several extents of reaction as illustrated in Figure 64. In the both cases (Figure 63 and Figure 64) there exists a domain of conversion in which the ratio keeps the same value ($\alpha_{total} < 0.25$), thus in this range $d\alpha/dt$ can be expresses by the product of the two functions $\Phi \cdot E$. This is not true for the domain of a higher than 0.25. For both copper oxalate and copper oxide systems, the transformation into copper showed a dependence of the reactivity with the reaction time if one considers the whole range of variation of α between 0 and 1. Thus over the whole domain there is not one single mechanism on rate limiting step.

3.4.2. Nucleation and growth modelling

The model for the decomposition of copper oxalate under p_{H2}= 40 mbar in isothermal conditions assumes a process of nucleation and growth of the new metallic copper phase which nucleates at the surface of the initial particles, as shown in Figure 59. Two extreme cases where either nucleation or growth dominates can be described as follows:

1. $t_g \ll t_n$ (t_g-growth time, t_n- nucleation time) - initially, entire surfaces of the particles are very rapidly covered with a thin layer of the solid product. Then growth takes place towards the core of the particle. The particles are transformed in the same time with the same velocity, as described in (Figure 65 b).

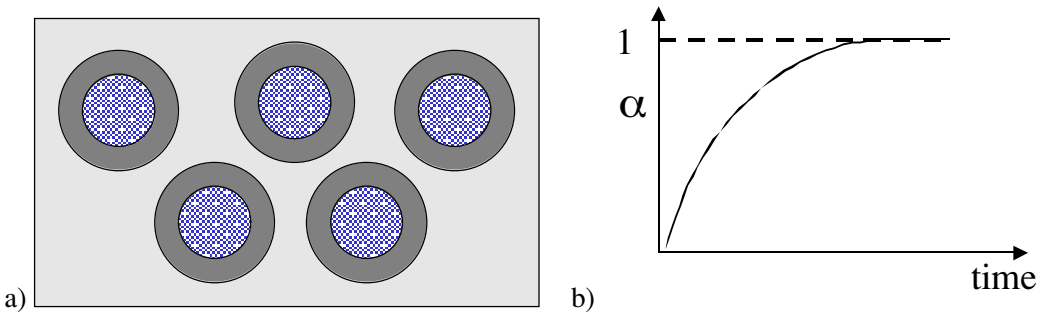

Figure 65: a) Scheme of instantaneous nucleation and growth toward the particles core at a constant velocity; b) reaction yield as a function of time for spheres

The surface of growth uniformly decreases in time with the assumption of an internal development and a rate-limiting step located at the internal interface. This model is known in the literature as the shrinking core model[72]. For this type of transformation the rate of conversion as a function of the reactivity and the reaction yield can be described as given in equations 7 and 8 depending on the particle shape:

$$\frac{d\alpha}{dt} = \frac{V_m \cdot \phi}{r_0}(1-\alpha)^{1/2} \qquad \textit{Eq 33}$$

$$\frac{d\alpha}{dt} = \frac{V_m \cdot \phi}{r_0}(1-\alpha)^{2/3} \qquad \textit{Eq 34}$$

where $d\alpha/dt$ is the rate of conversion (s^{-1}), V_m the molar volume, Φ the growth reactivity, α the reaction yield. Equation 7 is specific for particles with a shape as cylinder and equation 8 for the spheres. The kinetic curves of reaction yield as a function of time is shown in (Figure 65 b).

2. $t_g \gg t_n$ - the growth of the nucleus is fast. Nuclei appear on the particles surface and the transformation is completed in a short time. At an arbitrary time t, the system under investigation consists of a mixture of totally transformed particles and non-transformed particles.

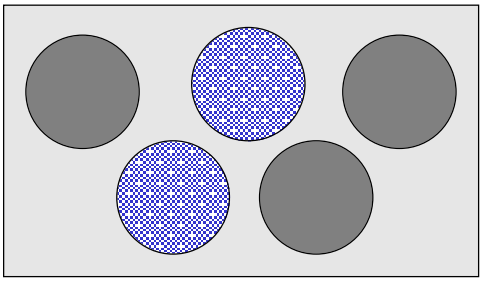

Figure 66: Scheme of particles transformation in the case of a spontaneous growth mechanism

The free surface for nucleation is represented by the total surface of non-transformed particles. The rate of conversion shows a decreasing behaviour and the rate law can be written as for equation 35:

$$\frac{d\alpha}{dt} = s_0 \cdot \gamma \cdot (1-\alpha) \qquad \textit{Eq 35}$$

where $d\alpha/dt$ is the rate of conversion (s^{-1}), s_0 is the initial surface available for nucleation, γ is the frequency of nucleation and α is the reaction yield. The curve of the reaction yield as a function of time shows the same kind of behaviour as for the previous case of spontaneous nucleation.

3. $t_g = t_n$ - mainly, when nucleation and growth of the nuclei occur at the same time, the geometrical model involves the frequency of nucleation and the reactivity growth in the same time[72]. The law of rate of reaction is more complicated, considering the two parameters of nucleation and growth. For this case the reaction yield as a function of time shows different rates of transformation for the reaction yield as time, as observed for the transformation of copper oxalate and copper oxide into metallic copper.

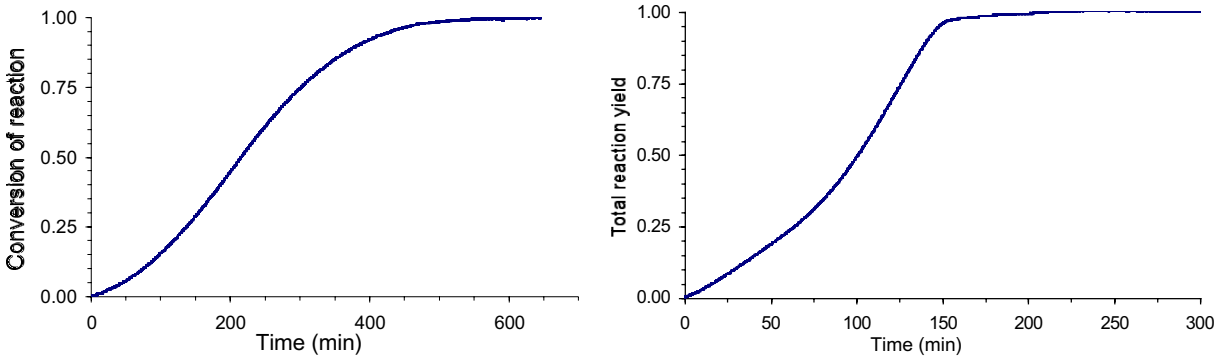

Figure 67: Curves for the reaction yield as a function of time: a) for the direct transformation of copper oxalate to metallic copper; b) for the transformation of copper oxide to metallic copper under helium & hydrogen gases

In that case, the rate $d\alpha/dt$ cannot be expressed using a single function of α as those in equation 35.

3.4.3. Type of Model of Transformation

In this section, we intend to investigate which type of model of transformation could be used to best explain our experimental curves. To choose between simple models (in which one of the two steps nucleation or growth is so fast that it can be considered "instantaneous") and complex ones (in which nucleation and growth occurs simultaneously), a very simple method can be adopted.

For example in the case of copper oxalate, two experiments can be made. Both of them start with different physico - chemical parameters, here the same hydrogen partial pressure but different temperature, 215°C and 225°C; and both must end in the same conditions 225°C and pH_2 = 40 mbar. This was carried out by a simple sudden change of temperature as illustrated in Figure 68. For copper oxalate this was carried out for the 5 different yields recorded in Table 30. Superposition was only observed from α=0.76 as shown in Figure 68 b.

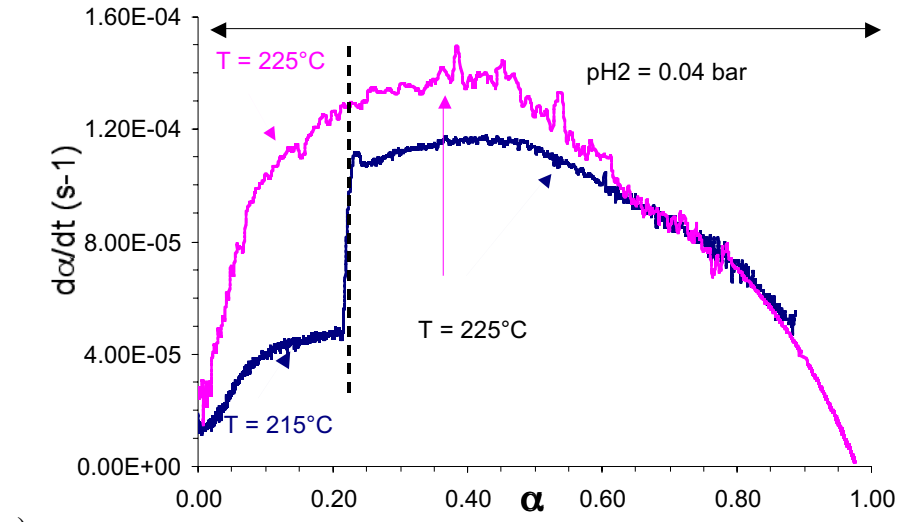

a)

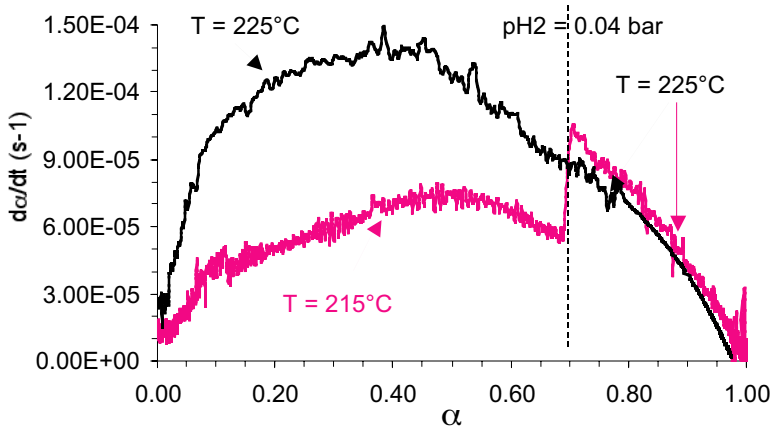

b)

Figure 68: Sudden change of temperature: dα/dt as a function of α for the copper oxalate transformation: a) for a reaction yield lower than 0.50; b) for a reaction yield higher than 0.50

If the model of transformation of the studied copper oxalate is a "simple" model, after the change in temperature, the portion of the curves under the same conditions temperature 225°C, and at constant pressure should superpose. Whereas a complex model should be chosen for conversion rates less than around 0.60 (Figure 68 a). So, the transformation of copper oxalate directly into the metal seems to occur with a "simple" rate model only after a certain transformation. Similar experiments were performed for the transformation of copper oxide into metallic copper, at different degrees of conversion.

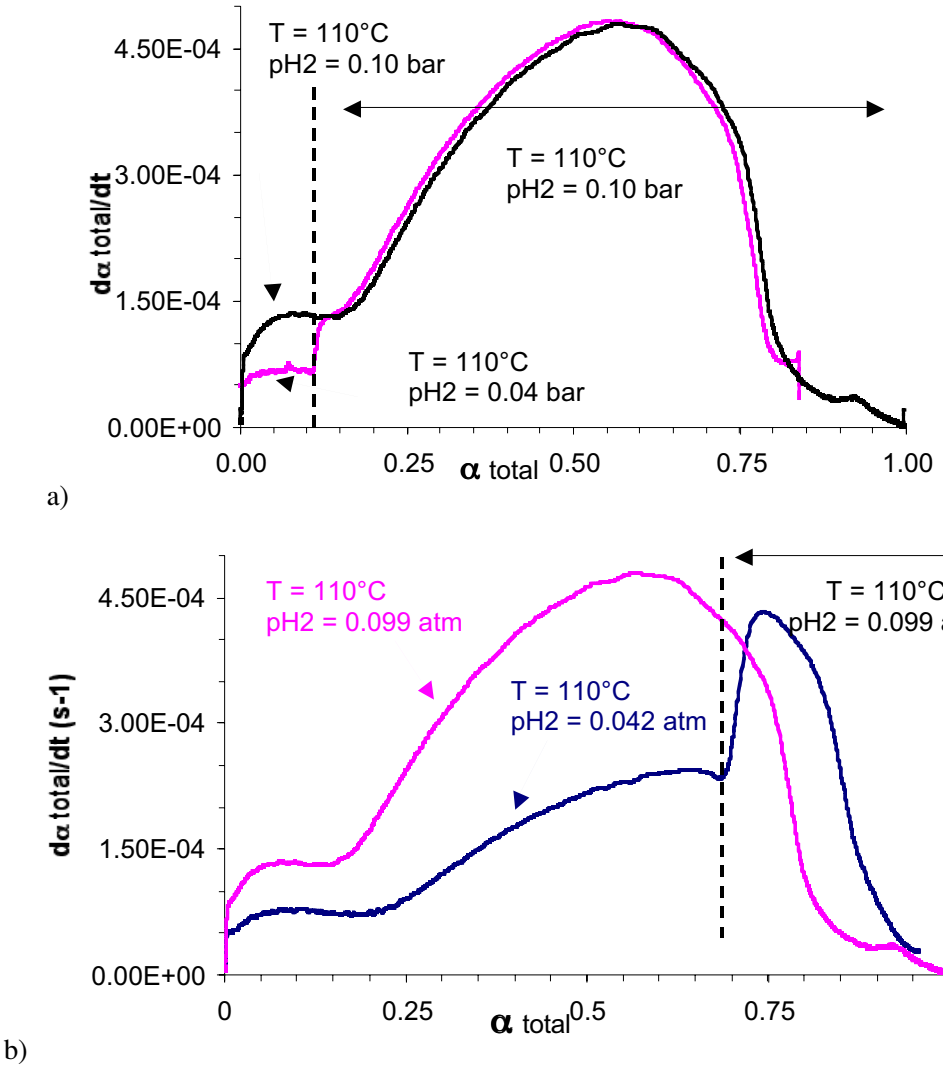

Figure 69: Sudden change method applied in isobar conditions from 40 mbar to 970 mbar for the transformation of copper oxide into metal for: a) reaction yield less then 0.25 and b) for a reaction yield at around 0.70

Figure 69 shows two such experiments with a sudden change of partial pressure of hydrogen from 0.04 bar to 0.97 bar at 110°C. Figure 69 a) shows the sudden change for α=0.12 and then the curves superpose, under same physico-chemical conditions (temperature and pressure) similar results were found for α<0.25. On the other hand, for a conversion of 0.70 (Figure 69 b) for the same physico-chemical conditions the curves do not present such a behaviour. These experiments indicate that in the second part of the transformation (α_{total} > 0.25) involves more then one process, contrarily to the first part (α_{total} < 0.25). This in not surprising since for α<0.25, the transformation involves only CuO -> Cu_2O and for α>0.25 the Cu_2O -> Cu reaction as well.

To gain a better understanding on mechanism of transformation the "sudden change" in isothermal conditions were performed for a reaction yield of 0.16. This point corresponds to the first part of transformation as shown above in Figure 54. Before 0.16 the XRD showed only two phases CuO and

Cu_2O. The goal was to set the space function and to study the variation of the reactivity with an intensive parameter, here the partial pressure, before elaborating a physico-chemical model. Using the initial conditions (p_{H2}= 40 mbar, t = 110°C) at α = 0.16, the pressure was changed to different values: 80 mbar, 120 mbar, 160 mbar and 200 mbar (Figure 70).

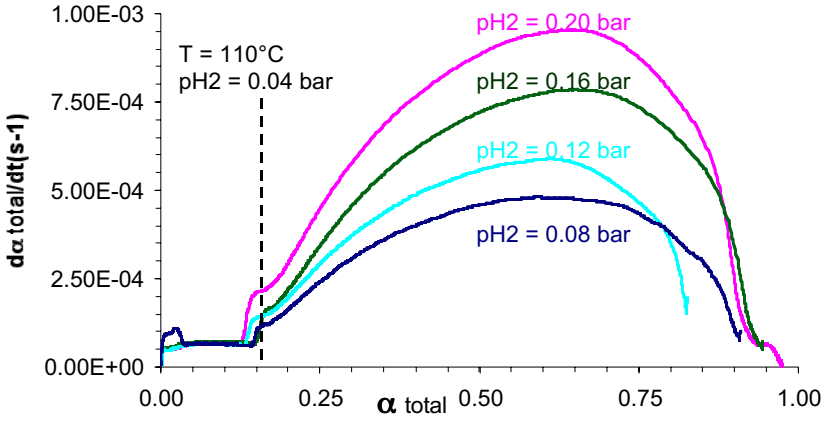

Figure 70: Sudden change method at reaction yield of 160mbar for isothermal conditions 110°C from 40 mbar bar to 200 mbar for copper oxide

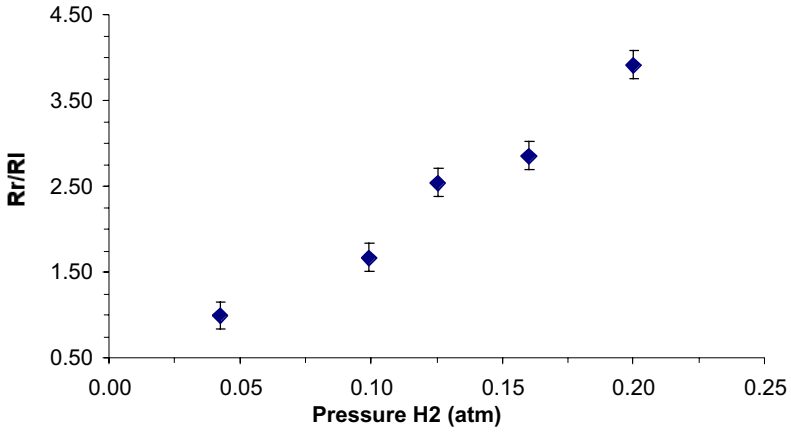

Figure 71: Variation of rates ratio as a function of hydrogen partial pressure on isothermal conditions 110°C for copper oxide

Figure 71 shows the reaction rate ration (before and after sudden change) obtained under isothermal conditions at 110°C for p_{H2} varying from 40 mbar to 200 mbar, with a sudden change for a constant α_{total} of 0.16. These data can now be used to test different kinetic models to be carried in the following sections.

3.5. Modelling

3.5.1. Geometrical model of copper oxalate transformation into metal

The direct transformation of copper oxalate under reducing atmosphere to metallic copper shows a complex mechanism. Kinetic data show a possible transformation where nucleation and growth are involved at the same time, with different rates. As mentioned previously, the mechanism of reaction shows two distinct domains: one before 0.60 reaction yield and another at high values of α.

The anisotropic structure and the inhomogeneous distribution of the copper oxalate primary particles can influence the process of transformation to metallic copper. The initial particles show 4 "smooth" or "dense" ε - surfaces and 2 "rough" or "open" α-surfaces and a small amount of the organic additive HPMC adsorbed on the ε - surfaces. The reduction process shows a high anisotropy during transformation by reacting first at the "rough" surfaces along the 001 crystallographic direction. It is assumed that the transformation starts at the zone of the particles characterised by a high defect concentration. The presence of an internal porosity in the core of the particles and traces of the organic polymer assumed to be adsorbed on the "smooth" surfaces might also contribute to this effect. The particle cubic morphology is conserved until reaction yield of 0.80. The molar volume ratio of copper oxalate to metallic copper is 0.17, which in terms of individual primary particles correspond to shrinkage phenomena.

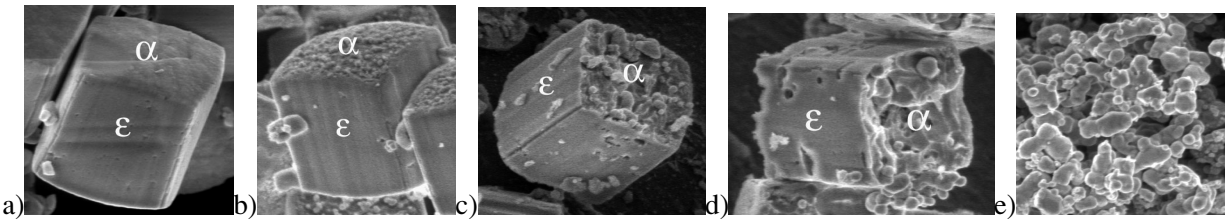

Figure 72: Particles evolution from the initial stage of copper oxalate to final metallic copper passing through all the intermediate stage of decomposition: a) initial stage copper oxalate α = 0% wt; b) α = 0.12; c) α = 0.21; d) α = 0.53; e) α = 1.00 metallic copper

Figure 72 shows the particle morphology evolution from the initial stage of copper oxalate passing through the intermediate stage of decomposition and finally into metallic copper, respect with the surfaces evolution[96]. Each copper oxalate particles is formed from small subunits. Each individual subunit will undergo the transformation (CuC_2O_4 -> Cu + 2 CO_2) influenced by two processes nucleation and growth. Using the XRD, HRSEM and kinetic curves results we propose a qualitative approach for copper oxalate transformation into metallic copper. Using the kinetic curves for copper oxalate transformation into metal and the model of sudden changes (Figure 62) $d\alpha/dt = \Phi \cdot E$ for the whole of α two distinct domains can be seen, characterised by two $\Phi_1 \neq \Phi_2$, with Φ_1, Φ_2 specific for each domain.

For a reaction yield less than 0.50 the kinetic curves (Figure 68 b) involves a complex model of nucleation and growth. However $d\alpha/dt = \Phi \cdot E(t)$ (with $E(t) \neq f(\alpha)$), may involve a transformation where the nucleation and growth do not take place in the same time as depicted in Figure 73. Some subunits starts to nucleate and grow and others are in the initial stage as copper oxalate. The nuclei are assumed to appear on the particles surfaces. Once a nucleus has been formed, the anisotropic transformation takes place. This behaviour was seen in the first part of transformation when the reaction start on α surfaces and ε surfaces do not seem to be transformed.

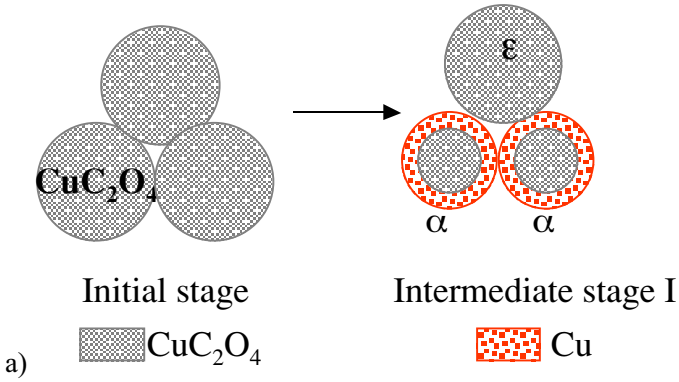

Figure 73: Model of subunits of copper oxalate transformation into metallic copper for α < 0.60

However for a reaction yield higher then 0.60 the theorem $d\alpha/dt = \Phi \cdot f(\alpha)$ (where E is a function of α) showed that all the subunits arrived at the same level of transformation. This is supported by the kinetic curve shown in Figure 68 a. When this point is reached all the subunits converge to final product with the same ratio as illustrated in Figure 74. For high reactions yield 0.80 the sintering process is apparent and the parent particle cubic morphology is lost.

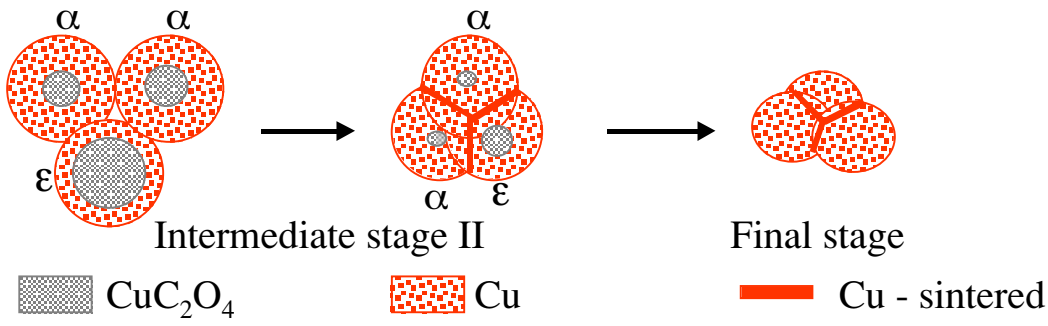

Figure 74: Model of CuC_2O_4 & Cu evolution to the final stage of metallic copper α > 0.60

One can conclude according to these data that the transformation mechanism involves two distinct steps one of the nucleation and anisotropic growth for α<0.60 and only a single growth mechanism for α>0.60. The first stage the surfaces nucleate and transform followed by the ε-surfaces. Once a certain Cu layer has been formed (α>0.6) the internal interface controls the reaction for both α and ε particles. To advance further towards the goal of copper metallic particles conserving a cubic morphology, a second pathway has been explored via the copper oxide.

3.5.2. Physico-chemical model of copper oxide transformation

The hydrogen diffusion in the copper oxide with a specific surface area of 70 m^2/g should not be a rate-limiting step. The effect of total pressure on diffusion of gases in pores depends on the relative importance of Knudsen diffusion. The value of the Knudsen diffusion[97] was estimated to be 0.0056cm^2/s in the copper oxide 12 nm pores size and this should not be rate limiting.

In the first domain of transformation (reaction yield less then 0.20), the formation of the intermediate oxide Cu_2O takes place; then all the three compounds, the two oxides and the metal, are contained in the system. The physico-chemical mechanisms of reduction can be modelled "simply" on the first domain of the transformation, when only the two oxides are present, before a total reaction yield of 0.20.

The reduction of the metal oxide can be considered as a heterogeneous reaction. The reactants are hydrogen and oxygen ions of the metal oxide. Hence, the reduction of metal oxide goes through an adsorption procedure, surface reaction and desorption. The reduction of metal oxide needs some starting points (nuclei) such as defects, a surface oxygen vacancy or a weakly bonded surface oxygen ion.

Taking into account kinetic measurements for the first part of transformation governed by a transformation to an intermediate oxide Cu_2O/CuO. We shall use a physico-chemical model to understand the variation of the growth reactivity, Φ, with the respect to hydrogen pressure. The two solid phases' Cu_2O and CuO will be described using the Kröger notation[98]:

For the copper oxide, CuO, with copper ions in a divalent form is noted (Cu_{Cu}), and oxygen ions noted (O_O). The oxygen ions in interstitial position are noted as: (O''_i).

The mechanism proposed implies several elementary steps. At the external interface, the grain surface is in contact with the hydrogen atmosphere and two steps are considered.

1) adsorption step on a surface site noted "s"

$$H_2 + s \rightarrow H_{2-s} \qquad \text{(i)}$$

2) hydrogen dissociation step:

$$H_{2-s} + s \rightarrow 2\,H_{-s} \qquad \text{(ii)}$$

3) diffusion of oxygen ions to an interstitial position and the formation of a water molecule:

$$2\,H_{-s} + O''_i + 2h^* \rightarrow H_2O + 2s \qquad \text{(iii)}$$

4) interstitial oxygen is transported from the internal to the external surface with at the same time, the electron holes formation and their movement. The electron hole is noted as h*:

$$O''_{i\,int} \rightarrow O''_{i\,ext} \qquad h^*_{int} \rightarrow h^*_{ext} \qquad \text{(iv)}$$

where "ext" represents the external interface and "int" represents the internal interface

5) transformation of CuO into Cu_2O.

$$2\,(Cu_{Cu})_{CuO} + 2\,(O_0)_{CuO} \rightarrow 2\,(Cu_{Cu})_{Cu2O} + O''_{i\ Cu2O} + 2h^* + (O_0)_{Cu2O} \qquad (v)$$

All these reactions (i) to (v) are characterised by different equilibrium constants noted K_j and velocity constant of the direct rection noted k_i.

In this particular case, limiting rates corresponding to steps (i), (ii), and (iii) that can be considered: the hydrogen adsorption and dissociation on the surface and the surface water desorption.

Therefore the variation of growth reactivity for the physico-chemical model considers first the hydrogen adsorption, and then the water desorption, while the other reactions are in equilibrium. For the three steps of reaction that can be considered as rate limiting, one can write the following kinetic expressions (these are in fact the possible expressions for Φ) :

$$v_1 = k_1 \cdot \frac{p_{H_2}}{1 + \frac{p_{H_2O}}{K_2 K_3 K_5} + \frac{p^{1/2}{}_{H_2O}}{(K_3 K_5)^{1/2}}}$$ H_2 adsorption *Eq 36*

$$v_2 = k_2 \cdot K_1 \cdot p_{H_2} \cdot \left(\frac{1}{1 + K_1 p_{H_2} + \frac{p_{H_2O}^{1/2}}{\sqrt{K_3 K_5}}} \right)^2$$ H_2 dissociation *Eq 37*

$$v_3 = k_3 \cdot K_5 \cdot \frac{K_1 K_2 p_{H_2}}{\left(1 + K_1 p_{H_2} + \sqrt{K_1 K_2} \cdot p_{H_2}^{1/2}\right)^2}$$ H_2O desorption *Eq 38*

These equations describe the kinetic laws of partial reduction of CuO into Cu_2O under the assumption of a rate-limiting step at the external interface between the solid and the gas. The two first laws depend on p_{H2} and p_{H2O} (equation 36 and 37). Equation 38 is not a function of p_{H2O}.

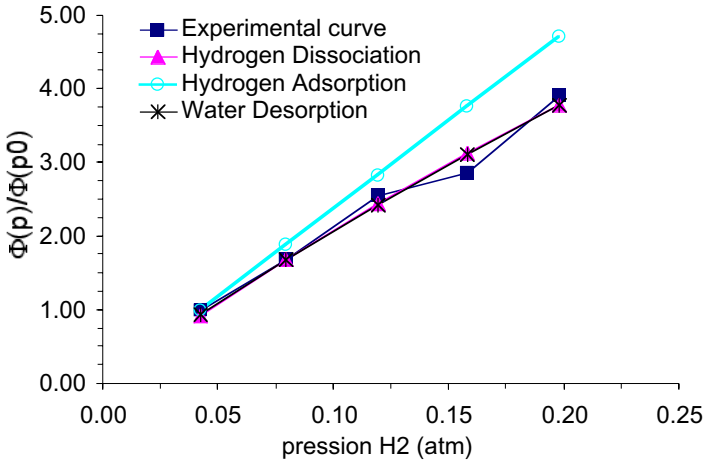

Figure 75: Experimental and theoretical data for the three equations: 36, 37, 38 experimental data come from sudden change experiments shown in Figure 71

Figure 75 shows the plots of the three equations possible as rate-limiting steps. The first equation is the hydrogen adsorption onto the copper oxide. This limiting-step is too far away to be considered as a rate-limiting step. Steps (ii) and (iii) governed by equations (36) and (37) fit well with the experimental data for both H_2 dissociation and H_2O desorption respectively. The experimental curves of the copper oxide reduction to metal performed in the presence on different water vapour partial pressure showed no influence of the kinetics of transformation as described in 3.3.3. Therefore one can assume as the rate-limiting step, the hydrogen dissociation at the solid oxide surface.

So the proposed mechanism for the copper oxide transformation into the intermediate state of Cu_2O at 110°C and p_{H2} of 40 mbar, is described in Figure 76.

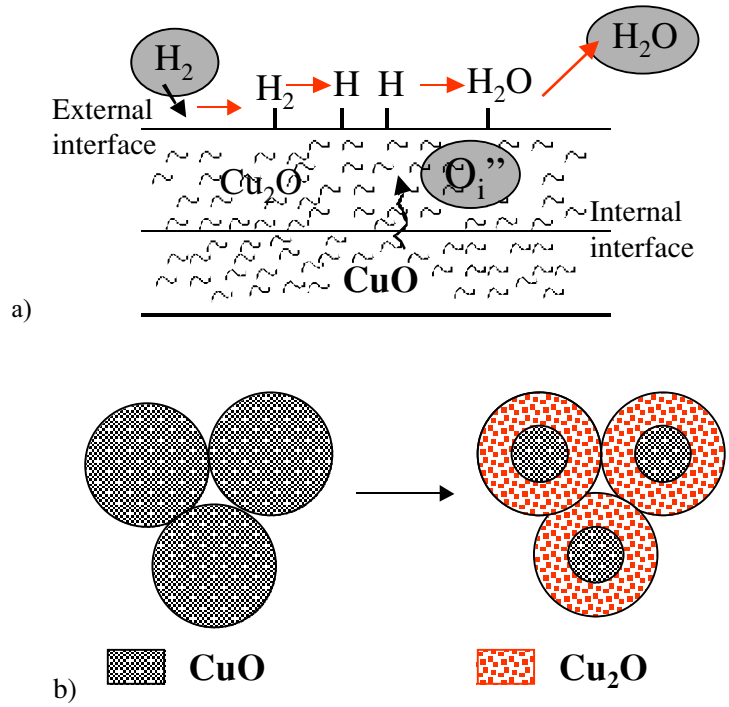

Figure 76: Physico-chemical mechanism of copper oxide reduction into Cu_2O for α_{total} <0.2: a) the model of hydrogen adsorption; b) reaction at nanoparticles level

The rate-limiting step of growth of partial reduction of copper oxide to Cu_2O is found to occur at the external solid gas interface associated with the hydrogen dissociation step.

For a transformation higher than 0.20, the three solids seen previously using the XRD and cross section TEM analysis are present. The modelling of the transformation reaction is more complex, involving different rates of transformation (CuO -> Cu_2O; Cu_2O -> Cu; CuO -> Cu), the preferential organisation of nanoparticles and theirs inhomogeneity distribution on the particles surfaces (α low density and ε high density). The presence of all 3 phases' fits well with a simultaneously growth of Cu_2O/Cu. This is also supported by the fact that oxide crystallite sizes change little during the transformation. The two possible geometric models are described in Figure 77 and 78. The first is a shrinking core type model, the second an inhomogeneous nucleation model. Geometrical mechanisms on the particle scale can be considered using the XRD data.

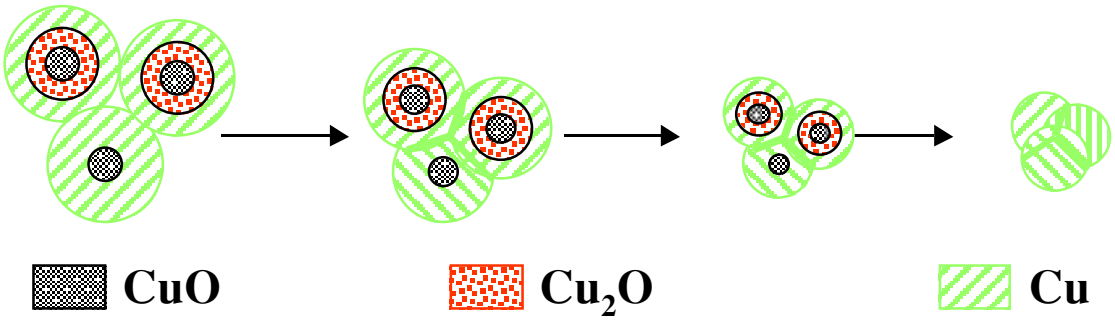

Figure 77: Mechanism of mixt CuO and Cu_2O reduction into metal state of Cu α>0.20

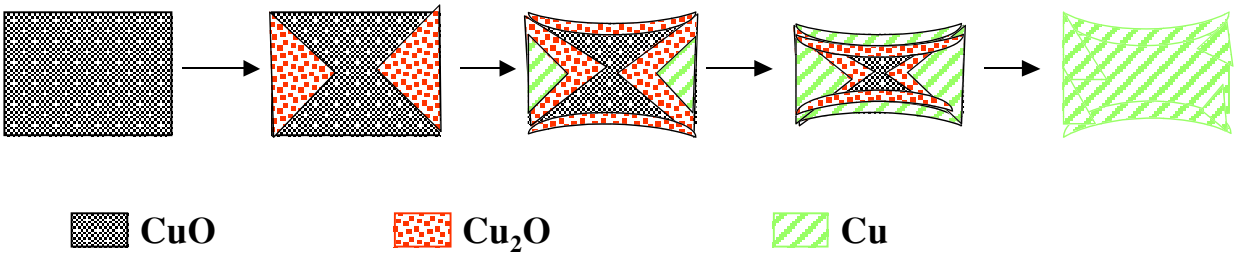

Figure 78: Copper oxide particle evolution at macroscopic scale

For the first model at a high level of total transformation the layers of Cu_2O and Cu formed on CuO nanoparticles may prevent the hydrogen access to the inner surface and delay the process advancement. Also a sintering process takes place at a total reaction yield higher then 0.63 again reducing H_2 access. The second model considers the inhomogeneity of the copper oxide with a high density of particles on shell the transformation could proceed differently from the core towards the shell. The nucleation event per copper oxide particles varies on core and shell. The presence of the copper oxide during all the transformation, with a size which change little, could also come from the inhomogeneity of the initial product i.e. the larger crystals and denser structure in the ε surfaces. Reaction R_5 is clearly dominant for an advanced isothermal time at 125°C. This behaviour have seen previously for in-situ XRD copper oxide reduction powder[99].

3.5.3. Conclusions

In summary the transformation of copper oxide, nanostructured materials with a high surface area, under reducing atmosphere of helium and hydrogen in isothermal conditions at 124.5°C show a complex behaviour. The characterisations of samples for different degrees of transformation initially show the formation of an intermediate oxide: Cu_2O. As the reaction yield increases, the two oxides and metallic copper are present before finally reaching the metallic state. The initial powder presents a surface area of

70 m^2/g. Then for a total reaction yield of 0.63 (TGA) this surface decrease to $40m^2/g$ and finally to copper of $5m^2/g$. This decrease is a result of a sintering effect of copper nanograins, observed both in HRSEM and TEM cross-section micrographs (Figure 56 c and Figure 58). The macroscopic particle morphology is conserved until the metallic state is reached with well-defined particle edges and particle corners. The copper oxide reduction seems to be faster on the α - surfaces given by the higher residual porosity seen in the precursor, then passes through the ε - surfaces, which also show pore growth as the reaction proceeds. Macroscopic particles show a small change in size around 5%. The initial CuO had pores of 12 nm whereas the final Cu product showed pores of 100 nm, estimated from the TEM cross-section (Figure 58 a).

For the first domain of transformation for reaction yields of less than 0.20, a kinetic model of transformation fits well the data for a growth model with hydrogen dissociation as the rate-limiting step.

The second part of the reaction, where the three compounds are involved, is more difficult to model. According to the analyses of the shape of the kinetic curves obtained and gaseous and solid products, the decomposition mechanism is a complex one and the global decomposition process consists of a number of simultaneous, parallel reactions. Observing the results of the TEM cross - section of samples at an intermediate stages, it remains difficult to distinguish between the exact nature of the grains. The anisotropic nanostructure and difference between the different surfaces also seem to contribute suggesting a spatially inhomogeneous nucleation and growth rate. To distinguish between individual grains a powerful method like nanodiffraction is needed to better characterise to be the reaction pathway. The transformation via copper oxide allows the initial cubic morphology to be conserved with a specific surface area of 5 m^2/g for the final metallic copper.

3.6. General Conclusion of Transformation

Copper oxalate can be transformed in air under isothermal conditions at 275°C produce an oxide CuO with a high surface area of 70 m^2/g. The particles morphology as cubes is conserved during all the transformation. On the other hand the cubic morphology of the oxalate is lost during the direct metallic copper synthesis, under a He & H_2 atmosphere from copper oxalate at 215°C. The micrographs for the copper oxalate intermediate stage illustrated a morphology conservation up to 0.80 reaction yield, then the sintering process controls the evolution toward the final copper. The early stage of transformation from the kinetic analysis suggests a complex transformation mechanism of the subunits. For a reaction yield higher than 0.50 the growth takes place and kinetic analysis via one single mechanism where the reaction interface control the rate of transformation.

For the CuO transformation into metallic copper under an H_2 & He atmosphere at 110°C the cubic particle morphology can be conserved from the initial stage to the final stage. The intermediate powders

analysis showed the presence of CuO and Cu_2O metallic copper for a global transformation > 0.20. The kinetic analysis showed two domains of transformation: one for a low transformation at 0.20 and then above 0.20. The first domain shows the formation of Cu_2O, as an intermediate oxide and the rate-limiting step of growth mechanism were found to be the hydrogen dissociation on the CuO surface.

The total transformation from CuO to Cu_2O then to Cu seems to involve a more complex model, due of the different rates of reaction linked to the anisotropic particle structure. The very high surface area of the CuO ($70m^2/g$) should show interesting catalytic[100] properties and are currently being evaluated in another laboratory. The copper polycrystalline particles are used as catalyst for degradation of nitrophenols, and with some minor optimisation the cubic, porous Cu particles produced via the oxide route may be a promising candidate.

Chapter 4. Co-precipitation

4.1. General Introduction

This chapter describes preliminary attempts to synthesise mixed cobalt-copper oxalate nanostructured composite material. The goal was to produce 3D mosaic particles of cobalt-copper oxalate, then via the reduction process to obtain finally the metallic composite cobalt-copper. This mosaic particle formed by nanoparticles of cobalt with a size of 5-20 nm well encapsulated in the conducting matrix of copper is expected to present a Giant Magneto Resistance (GMR) effect. The design of the build of mosaic nanostructured materials of copper and cobalt oxalate is shown schematically in Figure 79. To produce mosaic particles of cobalt and copper oxalate the sizes have been estimated from the density variations expected on transformation for the copper oxalate at 40nm and for the cobalt oxalate at 20 nm. If the final particles are considered with a cubic morphology as described in chapter 3, the mass of cobalt oxalate has to be 10.95 % wt in the copper oxalate matrix. As precursor reactants for the oxalate co-precipitation copper and cobalt nitrate and sodium oxalate were used. A second route was also investigated where cobalt oxalate or cobalt oxide seeds were used as heterogeneous sites for copper oxalate.

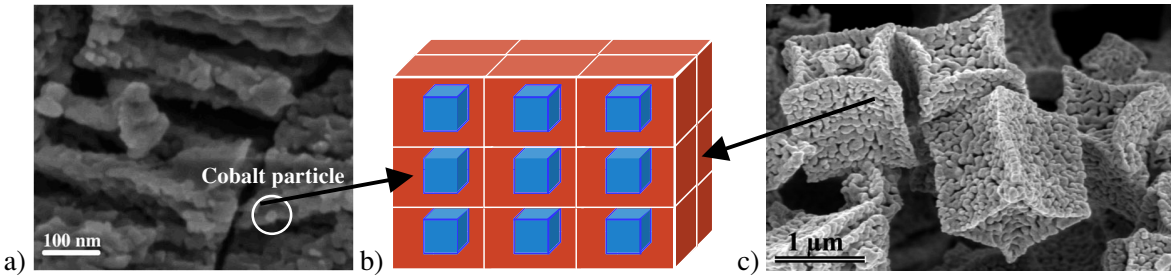

Figure 79: Design of the copper- cobalt oxalate mosaic particle with a size of the primary particles of 20 nm for cobalt oxalate and 40 nm for the copper oxalate

4.2. Physico-chemical data of cobalt oxalate precipitation

Precipitation of cobalt oxalate has been studied in detail in recent years[54,101]. Precipitated particles at low supersaturation (S=0.741) show a complex nanostructure. A mechanism of the particles assembly has been proposed by Pujol[101] (2004), using cryogenic HRSEM it was possible to follow the particle evolution with time.

The cobalt oxalate precipitate shows a core-shell structure with an amorphous core and an ordered polycrystalline shell. The shell organisation occurs in the last part of particle growth by a brick-by-brick mechanism. At this stage the system has a lower ionic strength and lower supersaturation inducing slower kinetics and hence more ordered particle assembly. This system showed a gradient of particle crystallinity from the core (disordered - amorphous) to the shell (crystallites of 10nm). Finally ripening takes place[9] producing a smooth external surface. The final particles have parallelepiped morphology with a length of 5µm and width of 400 nm with four smooth surfaces and two rough surfaces.

The two precipitates copper and cobalt oxalate seems to present the appropriate physico-chemical parameters to attempt a co-precipitation as described in Table 31. The kinetics of copper oxalate precipitation was investigated in detail in chapter 2. This system shows a fast burst nucleation in a time of milliseconds for a concentration of 0.005M after mixing of reactants. After 2 minutes of precipitation on the ceramic membrane analysed by HRSEM one can distinguish two types of particles some at about 500 nm and others less then 100 nm. Cobalt oxalate showed formation of amorphous or poorly crystalline particles in times less than 1 second of precipitation[9] and then these particles formed the disordered cores for the final particles.

Table 31: Physico-chemical characterisation of copper and cobalt simple oxalates

Characteristics	$CoC_2O_4 \cdot 2H_2O$	$CuC_2O_4 \cdot 0.3H_2O$
pKs	8.572	9.655
Conc. of Co/Cu at eq	$2.13 \cdot 10^{-4}$	$2.02 \cdot 10^{-4}$
Density (g/cm3)	2.30	3.65
Crystallographic structure	$P2_1/m$ a= c=0.66nm b=0.78nm β=131.57°	Pnnm a=0.54 b=0.55 c=0.25
Radius ionic	0.6 nm (Co^{2+})	0.6 nm (Cu^{2+})

4.3. Co-precipitation of mosaic copper-cobalt oxalate composite

4.3.1. Experimental section

A. Precipitation and Thermodynamic calculations

Preliminary experiments were made for the coprecipitation of a cobalt-copper oxalate using the minibatch reactor of 20 ml volume by the injection method (see chapter 2). The organic additive HPMC has been added in the nitrate solution to produce cubic shaped particles. The two-reactant solutions nitrate and oxalate have been prepared with the same precautions as described for the copper oxalate, using decarbonatated water and the solutions were filtered through 200nm membranes. The ageing time of

precipitation was established at one hour then the suspension was filtered and dried over silicagel until constant weight. Table 32 shows the experimental conditions of precipitation investigated as well as, the supersaturation values of each simple oxalate and the analytic concentration of Co and Cu at equilibrium.

Table 32: Summary table of the co-precipitation experiments of mosaic particles cobalt-copper oxalate, the experimental conditions and the techniques used for the powder characterisation

Experiment	A	B	C
Conc. $Na_2C_2O_4$	0.0100	0.0075	0.0075
Conc. $Cu(NO_3)_2$	0.0050	0.0050	0.0025
Conc. $Co(NO_3)_2$	0.0050	0.0025	0.0050
pH initial		5.332	5.48
pH final		5.87	5.70
Supersaturation CuC_2O_4	0.584	0.652	0.346
Supersaturation CoC_2O_4	0.588	0.367	0.671
{Co} eq		$3.34 \cdot 10^{-4}$	
{Cu} eq		$3.00 \cdot 10^{-4}$	

The supersaturation values for the three systems were calculated assuming the presence of both the copper and cobalt in the precipitation system. The analytic concentration at equilibria of each compound was calculated from the conditions of supersaturation values $S_{CuC2O4} = S_{CoC2O4} = 0$.

The higher sodium oxalate concentration thus creates a higher supersaturation, which should increase the kinetics of precipitation, which should favour a co-precipitation. For the precipitation process of the two oxalates and on the assumption that equilibrium is achieved, the finally concentration of copper and cobalt are higher than the separate single precipitation of oxalates. The calculations have been made considering the presence of all known complexes that can be formed in solution.

The calculated concentration of the main species in solution as a function of pH have been made using the solubility isotherms data for the system $Cu(OH)_2$ - $Co(OH)_2$ - $H_2C_2O_4$ - HNO_3/NaOH - H_2O at 25°C for the initial experimental concentrations as given (Table 32). Using this type of tool, first of all the pH of solution was calculated, then the pH was varied towards acid and basic values by adding HNO_3 or NaOH to the system, and the resulting complex compositions computed.

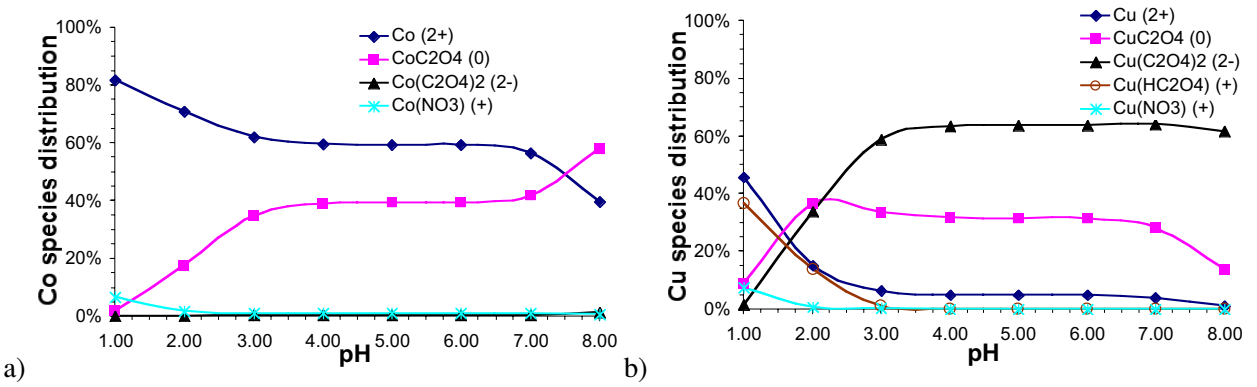

Figure 80: Species distribution for the experiment A: a) cobalt species distribution in the presence of the copper ions; b) copper species distribution in the presence of the cobalt ions

The Figure 80 shows the ionic species distribution in solution as a function of pH. The final experimental pH measured for these cases of precipitation was between 5-6 pH. For the cobalt oxalate, the two major species are Co^{2+} and $CoC_2O_4^0$, the other ionic or complex species formed are in low concentrations. Pujol showed that cobalt oxalate precipitation is little influence by the presence of other species such as carbonate[101], which was shown in chapter 2, an important effect on copper oxalate. In similar conditions of pH evolution but for the copper oxalate precipitation, as treated in detail in chapter 2, the major species are $Cu(C_2O_4)_2^{2-}$ (63%), $CuC_2O_4^0$ (31%). This shows that complexing of the precipitating cation Cu^{2+} with oxalate leads to a limited concentration of free Cu^{2+} cations in solution.

Similar calculations were done for the experimental conditions of samples B and C (Table 7) as presented in Figure 81 and Figure 82.

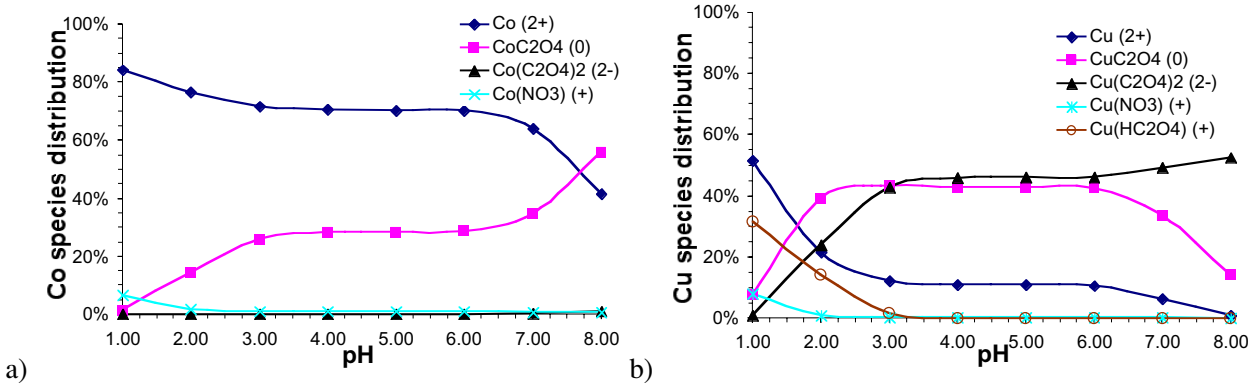

Figure 81: Species distribution for the experiment B: a) cobalt ions distribution in the presence of the copper ions; b) copper ions distribution in the presence of the cobalt ions

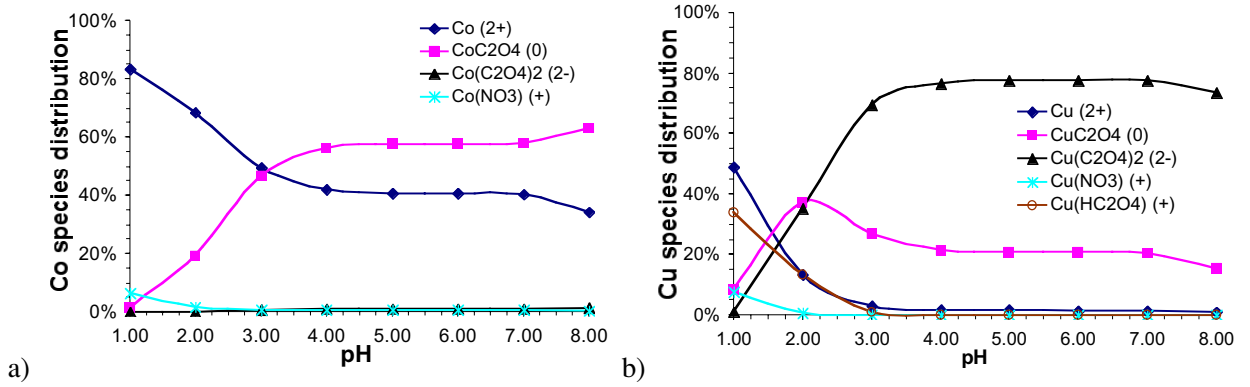

Figure 82: Species distribution for the experiment C: a) cobalt ions distribution in the presence of the copper ions; b) copper ions distribution in the presence of the cobalt ions

In a pH range 5-6 for experiment B (Figure 81 a) most part of the cobalt is present as Co^{2+} (70%) with the CoC_2O_4 in a low concentration than case A, the copper (Figure 81 b) the dominant species being $CuC_2O_4^0$ and $Cu(C_2O_4)_2^{2-}$ in roughly equal quantities. Changing the ratio of cobalt and copper nitrate concentration (experiment C), the cobalt ions are now mostly in the form $CoC_2O_4^0$ (Figure 82 a) with a high amount around 40% as Co^{2+}, an inversion of the case for solution B. In the case of copper ions the complex $Cu(C_2O_4)_2^{2-}$ (Figure 82 b) dominates with only around of 20% as $CuC_2O_4^0$ again a modification with respect to experiment B where Cu is in excess with respect to Co. Thermodynamically it is possible to precipitate the two oxalate phases. The simulations have been made on the assumption that all reactions are at equilibria and no rate limiting step controls the mechanism of co-precipitation.

B. XRD analyses

The X-ray diffraction patterns of the three precipitates show two phases copper oxalate and cobalt oxalate. No changes in peak position and hence lattice parameters were discernible.

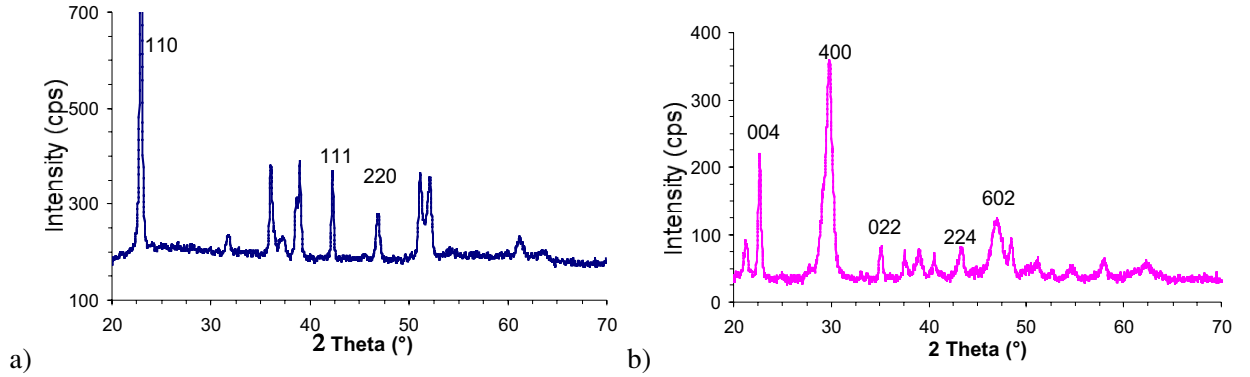

Figure 83: X-rays diffraction patterns for the precipitates: a) experiment B copper oxalate; b) experiment C cobalt oxide

Figure 83 shows the diffraction patterns for the samples B and C. For the experiment A XRD shows the two phases copper and cobalt oxalate whereas diffractograms of B and C show the precipitation

of one single phase. In the case (experiment B) for the ratio Cu/Co=2 only the copper oxalate is observed, in the second case for (experiment C) for the ratio Cu/Co=0.5 only the cobalt oxalate is observed.

C. SEM Analyses

The precipitates were analysed using the SEM micrographs. Figure 84 shows the precipitate morphology as a function of copper/cobalt ratio. For a Cu/Co ratio of 1 (Figure 84 a), the two-oxalates precipitate separately with a change of the copper oxalate morphology from cubes (without cobalt ions in solution) to oblates. For case of copper excess (Figure 84 b) shows the precipitate particles like ellipsoids or plates, which are expected to be copper oxalate. When Co is in excess (Figure 84 c) precipitate particles with an elongated morphology as expected for the cobalt oxalate precipitation alone (Pujol[9]).

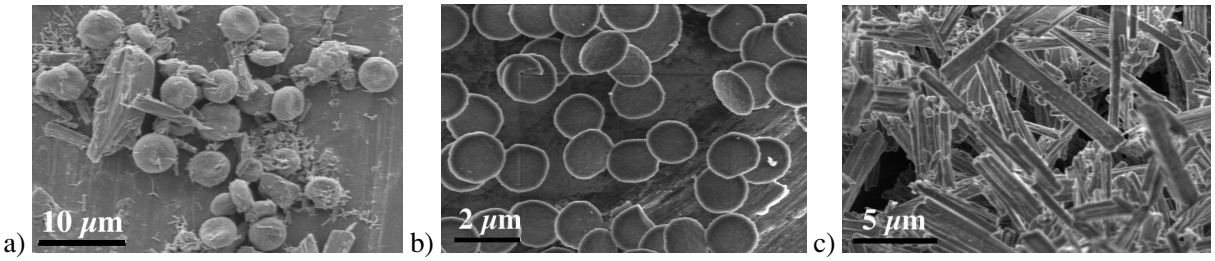

Figure 84: Particles shape for the three experiments described in table2: a) the experiment A: Cu/Co=1: 1; b) experiment B Cu/Co=2:1; c) experiment C Cu/Co=1:2

They all show 5-10 μm sized particles with two types of morphology, one like plates or spheroids that are expected to be the copper oxalate and one like rods expected to be cobalt oxalate. The SEM micrographs confirmed the XRD analysis. The copper oxalate in the presence of the organic polymer often present a cubic morphology, here the morphology is more like plates or spheres. However the cobalt oxalate morphology is conserved as rods.

D. Discussion

Thermodynamic calculation of soluble species of copper and cobalt oxalate suggest that the two solid compounds can form independent of the copper-cobalt ratios used in this study.

Changes in various species in solution when mixing Cu and Co were predicted by solubility calculations. Netherless the S remains high (from 0.67 to 0.34) for all three experiments for both cobalt and copper oxalate. The expected co-precipitation does not however take place except for case A. For B and C a possible explanation for the seemingly “separate” precipitation can be put forward from a kinetic point of view. Perhaps once nucleation of one phase takes place the S is diminished below the critical S for a nucleation of the other by consumption of the oxalate species. Thus S is too low for the secondary phase precipitation.

Co-precipitation via the aqueous route from the copper and cobalt nitrate and sodium oxalate at 25°C was not fruitful. In the literature at this moment only one solid solution of cobalt-copper oxalate[54] is known obtained at 50°C. The general composition of the co-precipitated Co-Cu oxalates is $Co_xCu_{1-x}C_2O_4 \cdot nH_2O$. These oxalates were prepared in the presence of oxalic acid 0.10 M and 0.10M solution of metal nitrate in the required molar ration of Co^{2+} and Cu^{2+}. Five compositions with this formula were prepared (x= 0, 0.3, 0.5, 0.7, 1). The samples were analysed using X-ray diffraction. The compounds with x = 0.3 and 0.5 follow the behaviour exactly like their mechanical mixtures of the two separate oxalates. This indicates that these compositions did not form a solid solution by co-precipitation. Whereas for the compound with x = 0.7 the pattern display new lines for the XRD, that may be attributed to a new phase of the solid solution. The authors studied in detail the thermal decomposition of the mixed oxalate and the catalytic properties of mixed oxides in the rate of decomposition of H_2O_2 at 30°C [102]. For this compound the authors did not investigate in detail the nanostructure of this mixed oxalate $Cu_{0.3}Co_{0.7}C_2O_4$. The crystallographic arrangement of atoms in the unit cell is not determined to the present considering the difference of the unit cell of the two simple oxalates as monoclinic for cobalt oxalate and orthorhombic for copper oxalate. Using this method of precipitation is only possible to co-precipitate an oxalate with a high ratio of cobalt the other co-precipitates did not formed a solid solution at a low concentration of cobalt dispersed in solution. However the goal of this work is to obtain a composite with a ratio Cu:Co = 90:10. The metallic cobalt particles must be well dispersed in the conducting copper matrix as depicted in Figure 79.

The route of co-precipitation a copper-cobalt oxalate single solid to does not seem to be fruitful.

4.4. Heterogeneous precipitation using seeds

4.4.1 Cobalt Oxalate seeds

The precipitation of 8 nm calcite seeds from a high surface area (35m2/g) calcite has been shown to allow great control over subsequent calcite precipitation[12]. A similar approach has been attempted to produce cobalt oxalate seeds from a nanostructured cobalt oxalate, by partial dissolution to weaken of the nanocrystallites followed by an ultrasonic treatment to dislodge nanoparticles from the parent particle.

A. Seeds preparation

The seeds used for heterogeneous precipitation have been prepared using nanostructured cobalt oxalate precipitates obtained from the precipitation of cobalt nitrate and sodium oxalate with or without an organic additive, polyacrylicacid (PAA)[101] (Table 3). A previous study on cobalt oxalate precipitation showed an effect on particle morphology in the presence of this additive as a function of the ratio of cobalt

and acrylic acid groups (defined by R = Co/AA). The pH of PAA solutions were modified using NH_3 and was defined in the previous work as R' = NH_3/AA = 1.5 [103].

The different cobalt oxalate seeds were prepared by dispersing 200 mg of cobalt oxalate powder 250 ml solution of sodium oxalate of 0.01M. The suspensions were kept for 24h in a thermostatic bath agitated at 25°C. Then the suspensions were treated in an ultrasonic bath for 15 minutes to try to dislodge and disperse the primary particles of cobalt oxalate that are expected to have a size between 10 to 30 nm[101]. From solubility calculations around 59 % wt of the cobalt oxalate should dissolve and weaken the binding of the nanocrystallites within the particles. The cobalt ions concentration should be $2.05 \cdot 10^{-3}$M if the dissolution reaction under these conditions reaches the equilibrium state.

Experiments LOT_D and E are considered as reference samples, to check the influence of the additive PAA and the effect of the NH_3 on copper oxalate particles morphology. The PAA additive is used with NH_3 for the cobalt oxalate precipitates, for LOT_A, B and C, whereas for the LOT_E the cobalt oxalate precipitates particles was carried out in the presence of PAA with NaOH, keeping the same ratio of 1.5. The cobalt oxalate particles morphology does not change if either NaOH or NH_3 is used to control the pH [103].

Table 33: Summary of the experimental conditions for the cobalt oxalate preparation as a function of AA/Co and NH_3/AA ratio

Name of sample	R=Co/AA	R'	$Co(NO_3)_2$	$Na_2C_2O_4$
LOT_A	0.5	NH_3/AA = 1.5	0.01 M	0.01 M
LOT_B	1	NH_3/AA = 1.5	0.01 M	0.01 M
LOT_C	1	NH_3/AA = 1.5	0.01 M	0.01 M
LOT_D	0	NH_3/AA = 0	0.01 M	0.01 M
LOT_E	0.5	NaOH/AA = 1.5	0.01 M	0.01 M

The seed suspensions were separated into three types of particle range by filtration through either 450 nm, 200 nm or 20 nm membranes, to remove the micron sized seed source particles. This produced 3 types of seed suspension (supernatant) for each cobalt oxalate sample (Lots A to C).

The seed suspension were analysed for cobalt concentration using ICP which is carried out in dilute nitric acid (Chapter 2.2.3 H) and would therefore include solid and dissolved Co in the seed suspension to confirm the presence of cobalt seeds in these different supernatants Table 34.

Table 34: Cobalt concentration and pH measurement for the cobalt oxalate solution in supernatant as a function of the pores size of the membrane

Name of sample	Size of filtered	R = Co/AA	pH	Cobalt conc. supernatant
Lot A_450	450 nm	0.5	8.67	$1.35 \cdot 10^{-3}$ M ± $1.41 \cdot 10^{-6}$
Lot A_200	200 nm	0.5	9.32	$1.31 \cdot 10^{-4}$M ± $7.07 \cdot 10^{-6}$
Lot A_020	20 nm	0.5	8.79	$1.32 \cdot 10^{-4}$M ± $7.98 \cdot 10^{-6}$
Lot B_450	450 nm	1	9.30	$0.70 \cdot 10^{-4}$M ± $1.16 \cdot 10^{-6}$
Lot B_200	200 nm	1	9.19	$0.70 \cdot 10^{-4}$M ± $3.21 \cdot 10^{-6}$
Lot B_020	20 nm	1	9.00	$0.78 \cdot 10^{-4}$M ± $3.43 \cdot 10^{-6}$
Lot C_450	450 nm	1	9.00	$0.96 \cdot 10^{-4}$M ± $1.01 \cdot 10^{-6}$
Lot C_200	200 nm	1	9.00	$1.06 \cdot 10^{-4}$M ± $9.89 \cdot 10^{-6}$
Lot C_020	20 nm	1	9.00	$1.00 \cdot 10^{-4}$M ± $5.31 \cdot 10^{-6}$

The ICP measurements of cobalt concentrations in the supernatant did not change as a function of the filter diameter. A difference is observed with respect to R and when HPMC is present in LOT_C. With HPMC 100 the oxalate reactant solution produces a slight change in the cobalt concentration in the supernatant. It has been shown that the organic additives can have an influence on the dissolution process[12]. The above results show that the Co supernatant concentrations are lower then the expected value from solubility calculations, which was $2.05 \cdot 10^{-3}$ M. According to the values obtained by ICP and the lack of any influence of the types of filter membrane, the supernatant should have no solid particles with a size larger than 20 nm. No direct evidence of the presence of such solid phase seeds could be determined from TEM or PCS. The cobalt present could be in the form of solid seeds or simply in a dissolved state.

B. Precipitation

The copper oxalate precipitation took place in the presence of an organic additive HPMC to obtain particles with a cubic morphology. The HPMC was added in the copper nitrate solution as for the samples LOT_A, B, D and E and in the oxalate suspension in the case of sample LOT_C. For LOT_C seeds HPMC was added with view to dispersing the cobalt oxalate nanocrystallites in the solution and to maintain their colloidal dispersion CoC_2O_4 stable.

Experiments of precipitation were investigated for various conditions of cobalt oxalate seed preparation. 50 ml of each precursor solution copper nitrate and sodium oxalate (containing cobalt oxalate seeds) was mixed for 5 minutes at 500 rpm. The ageing time of reaction was set at 24 hours. The suspension is filtered through a 200-nm membrane and the powder dried over silicagel till constant weight. The supernatants of each precipitation experiment were analysed by ICP in order to determined

the cobalt concentration and compared them with the initial values as given in (Table 34). All the precipitates have a blue colour exactly as for copper oxalate.

The initial conditions of the precipitation, the supersaturation for the two solids phases cobalt and copper oxalate were determined theoretically using the solubility calculations. The results are given in Table 35.

Table 35: Supersaturation values for the cobalt & copper oxalate precipitation for the conditions as described above

Name of sample	S_{CoC2O4}	S_{CuC2O4}
Lot A_450	0.016	0.68
Lot A_200	0.008	0.68
Lot A_020	0.010	0.68
Lot B_450	-0.143	0.69
Lot B_200	-0.143	0.69
Lot B_020	-0.118	0.69
Lot C_450	-0.069	0.69
Lot C_200	-0.044	0.68
Lot C_020	-0.058	0.68
Lot D_450	***-0.049***	***0.66***
Lot E_450	***-0.039***	***0.67***

For all experiments the supersaturation values of cobalt oxalate are under saturated except for the LOT_A. Whereas in the case of copper oxalate the values of supersaturation are at around 0.70. Table 36,Table 37 and Table 38 summarise the experimental conditions of the precipitation with the initial ratio of copper and cobalt concentrations in solution measured by ICP and the amount of solids calculated to be present in the precipitate. All calculations for the powder composition were made by difference between, the amount of cobalt and copper found in the supernatant compared to the starting solutions. The quantity of Co in the precipitate is generally much lower than the 0.11 fraction desired for the GMR composites.

Table 36: Summary of the initial ratio of copper and cobalt by ICP measurement for R = 1 and the expected powder to precipitates

	Lot A_450	Lot A_200	Lot A_020
CoC_2O_4 (g/L) precipitate	$2.58 \cdot 10^{-3}$	$1.18 \cdot 10^{-2}$	$1.68 \cdot 10^{-2}$
CuC_2O_4 (g/L) precipitate	$6.29 \cdot 10^{-1}$	$7.53 \cdot 10^{-1}$	$5.49 \cdot 10^{-1}$
Ratio Cu/Co initial	6.99	7.08	7.77
Ratio Co/Cu powder	0.004	0.016	0.031

Table 37: Summary of the initial ratio of copper and cobalt by ICP measurement for R=0.5 and the expected powder to precipitates

	Lot B_450	Lot B_200	Lot B_020
CoC_2O_4 (g/L) precipitate	$1.75 \cdot 10^{-2}$	$1.52 \cdot 10^{-2}$	$2.01 \cdot 10^{-2}$
CuC_2O_4 (g/L) precipitate	$7.19 \cdot 10^{-1}$	$7.37 \cdot 10^{-1}$	$7.42 \cdot 10^{-1}$
Ratio Cu/Co initial	13.55	13.19	13.22
Ratio Co/Cu powder	0.024	0.021	0.027

Table 38: Summary of the initial ratio of copper and cobalt measured by ICP- the seeds were prepared in the presence of HPMC (R=1) and the expected powder to precipitates

	Lot C_450	Lot C_200	Lot C_020
Co C_2O_4 (g/L) precipitate	$5.32 \cdot 10^{-3}$	$1.22 \cdot 10^{-2}$	$2.13 \cdot 10^{-2}$
Cu C_2O_4 (g/L) precipitate	$5.75 \cdot 10^{-1}$	$5.48 \cdot 10^{-1}$	$5.39 \cdot 10^{-1}$
Ratio Cu/Co initial	9.96	10.59	6.04
Ratio Co/Cu powder	0.009	0.022	0.039

The samples under investigation were analysed by SEM for the particle morphology as illustrated in figures 85, 86 and 87.

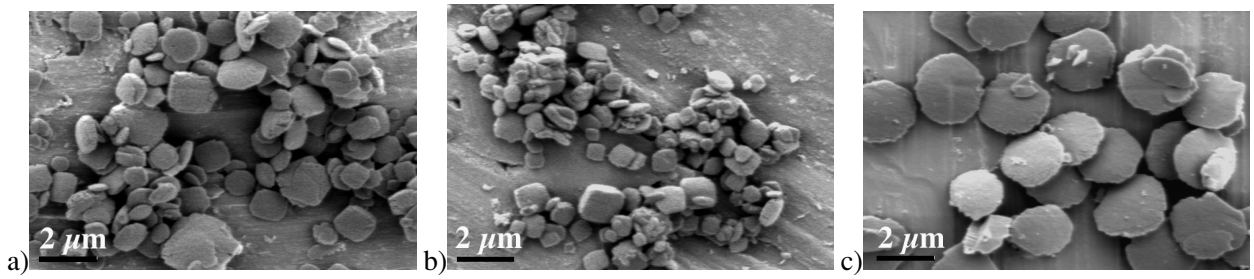

Figure 85 : SEM images of LOT_A as a function of filtrate membrane used for cobalt oxalate preparation seed source filtration through : a) 450 nm ; b) 200 nm ; c) 20 nm

Figure 85 shows the particles morphology as a function of the size of filtration membrane for the seed samples LOT_A. The presence of cobalt changes the particles morphology towards plates instead of cubes. Similar particle morphologies have been observed for the precipitated particles obtained in the experimental conditions of LOT_B seeds, (Figure 86).

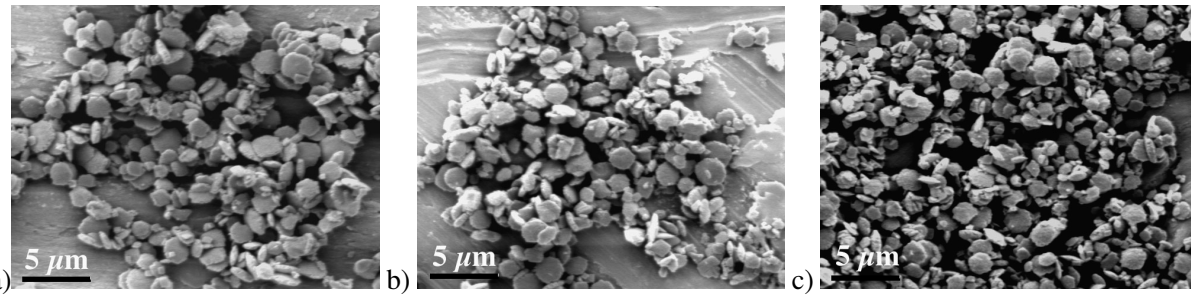

Figure 86: SEM images of LOT_B as a function of filtration membrane used for cobalt oxalate precipitation seed source filtration through: a) 450 nm; b) 200 nm; c) 20 nm

A significant change of particles morphology was observed for the LOT_C seeds where the HPMC was dispersed in the oxalate solution (Figure 87) rather that in the nitrate solution (LOT_B, Figure 86) for the same cobalt concentration.

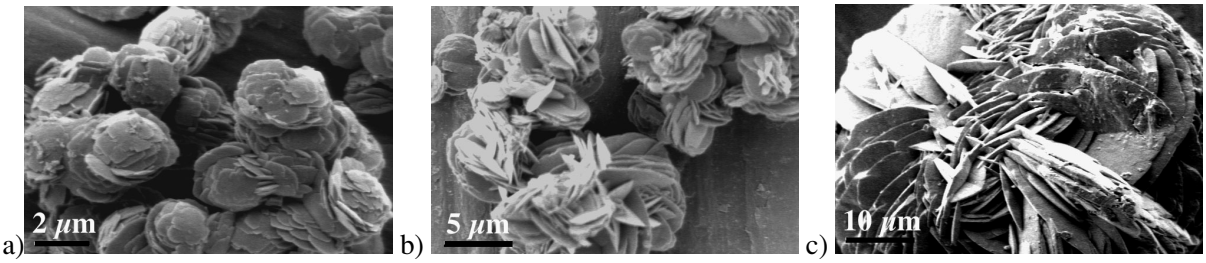

Figure 87 : SEM images of precipitates particles as a function of filtered membrane seed source filtration through : a) 450 nm ; b) 200 nm ; c) 20 nm

The particle morphology may be influenced by the PAA and/or NH_3 and also by the cobalt present in the system of precipitation. It is known that the NH_3 can complex the copper ions in solution and change the complex balance, on the other hand cobalt complex formation could also be possible. Therefore the two lots D and E were precipitated using the conditions developed by O. Pujol[103], to see if these parameters influence copper oxalate precipitation alone. One was prepared using precursors of cobalt nitrate and sodium oxalate (no PAA and no NH_3 LOT_D) and a second one in the presence of PAA and NaOH (LOT_E). The seed suspension of cobalt oxalate were then prepared in the same manner as described for the LOT_A, B, and C, and the filtration was made only through 450 nm diameter of pore filter (Table 39) to remove the cobalt oxalate seed source.

Table 39: Summary of the initial and final concentration of copper and cobalt measured by ICP- for the standard samples: LOT_D seed prepared without PAA, LOT_E seed prepared with AA/NaOH

	LOT_D (450 nm)	LOT_E (450 nm)
CoC_2O_4 (g/L) precipitate	$1.75 \cdot 10^{-2}$	$1.82 \cdot 10^{-2}$
CuC_2O_4 (g/L) precipitate	$7.26 \cdot 10^{-1}$	$6.35 \cdot 10^{-1}$
Ratio Cu/Co initial	9.70	9.84
Ratio Co/Cu powder	0.024	0.028

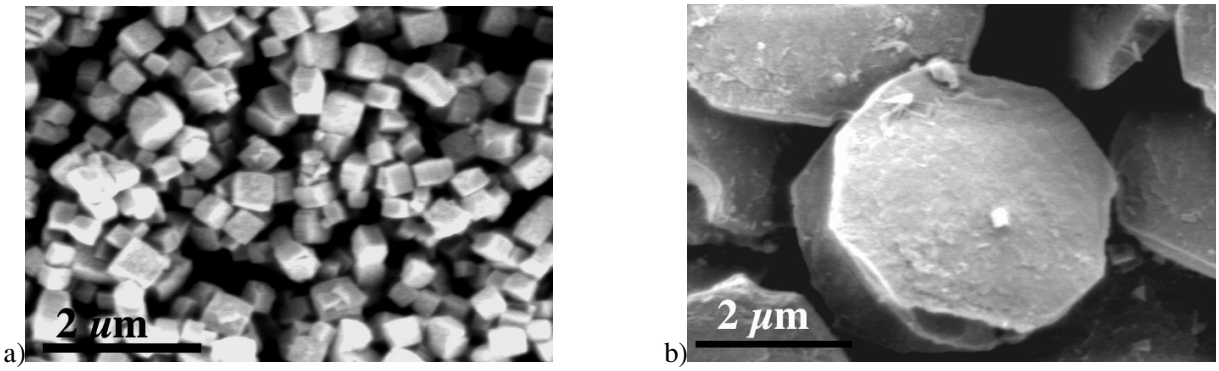

Figure 88: SEM images of LOT_D and E : a) copper oxalate precipitation in the presence of the cobalt oxalate seed without AA additive; b) copper oxalate precipitation in the presence of AA and NaOH

Figure 88 depicts the copper oxalate particle morphology precipitated in the presence of the LOT_D and LOT_E cobalt oxalate seeds. Figure 88 a) illustrates particles with a cubic morphology as for the copper oxalate precipitation in the presence of HPMC 100, and Figure 88 b shows the particles with a more plate-like morphology as observed for the precipitation of the LOT_A and B. The cobalt content in the samples LOT_D was analysed using TEM (CM200) EDS. For this samples the cobalt concentration was established qualitatively at around 3% wt, which it agrees with the ICP analysis.

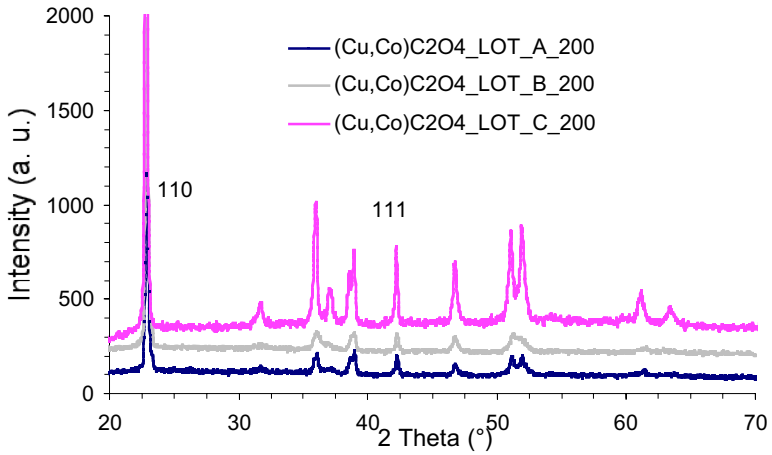

Figure 89: XRD diffractogramme of the three types of precipitates in the presence of cobalt oxalate seeds filtered through 200 nm

Figure 89 presents the XRD measurements for the samples precipitated in the presence of cobalt seeds filtered through 200 nm. Only the presence of copper oxalate crystallographic phase was observed. From ICP analyses a small amount of cobalt oxalate was expected to be present in 1-3 wt % but not observed by XRD measurements possibly being below the limit of detection. Cobalt oxalate could also be in an amorphous state or incorporated in the crystallographic structure of copper oxalate.

D. Discussion

The solubility calculations showed a low supersaturation value for cobalt oxalate in the presence of copper oxalate for LOT_A and an under saturated solution (ratio Co/Cu) for the other two cases LOT_B and C. According to the ICP analysis a small amount of cobalt oxalate up to 2.6 % wt, could be present in the final precipitates but it was not possible to detect them using the XRD analysis.

The SEM (Figure 85, Figure 86, Figure 87) images showed an important change in copper oxalate particles morphology when precipitated took place in the presence of cobalt (LOT_A, LOT_B and LOT_C) forming more plate like particles rather then the expected cubes. This behaviour may come from the fact that the kinetics of copper oxalate precipitation is affected by the nature of different complex formation of copper and possible cobalt ions in solution, and their evolution during the process of precipitation. On the other hand this behaviour could also be influenced also by the presence of the two additives PAA and HMPC. Further more the presence of the HPMC in the oxalate solution seems to have an important influence on the particles morphology. This is the case of samples LOT_C the particles morphology changed as a function of membrane filter pore size, the higher the pores size the smaller precipitated particles. ICP analyses for these samples showed no modification in cobalt concentration.

Precipitation of copper oxalate in the presence of cobalt oxalate seeds prepared without PAA (LOT_D) presents more or less a cubic morphology as expected for the copper oxalate precipitation. The size of the particles is smaller by a factor 10 than the simple precipitation of copper oxalate without cobalt oxalate seeds. For this samples TEM analysis shows a small amount of cobalt at about 3% wt. This decrease in size could be influenced by the presence of the cobalt in solution. Further more the kinetic of copper oxalate precipitation may changed from a simple precipitation to a more complex one.

Also copper oxalate precipitation in the presence of PAA/NaOH the particles morphology is plate like very similar to the experiments LOT_A and B. This change in particle morphology from cube to plate is mainly induced by the presence of PAA.

The amount of Co possibly present in the precipitates was much lower 2-3% than the target quantity of 7-15% to reach the magnetic conditions. The production of Co oxalate seeds has not resulted in the precipitation of useful precursors for the metallic Co/Cu composite envisaged. Further investigation into the nature of the seed solutions is needed to improve this route. As part of the screening of possible routes of cobalt-copper nanocomposite development a final system was investigated via the use cobalt oxide seeds.

4.4.2. Precipitation using cobalt oxide seeds

A. Cobalt oxide seeds preparation

A cobalt oxide with a high surface area was prepared by thermal decomposition of cobalt oxalate precipitates with a rod like morphology. The decomposition process takes place under air with a flow rate of 20 ml/min and well-defined heating sequence summarised in Table 40.

Table 40: Thermal treatment of cobalt oxalate to transform to oxide with a high specific surface area

Temperature initial (°C)	Temperature final (°C)	Rate (°C/min)	Dwell (min)
50	300	5	-
300	300	-	60
300	350	2	-
350	350	-	120
350	50	50	-

After decomposition the powder was analysed by XRD and SEM (Figure 90). XRD exhibits an important amorphous part, indicative of low crystallinity of least some of the final product in the conditions of transformation. The crystalline final product is Co_3O_4 the most stable cobalt oxide in air.

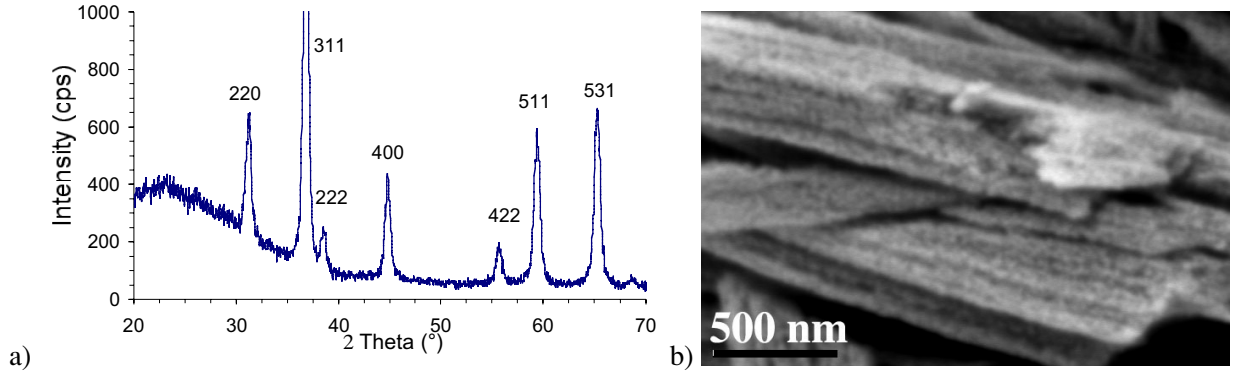

Figure 90: a) Cobalt oxide XRD; b) images of cobalt oxide after decomposition

The primary particle size of the resulting cobalt oxide has been estimated by nitrogen adsorption at around 22 nm, the same size can be estimate by SEM analyses show in (Figure 90 b) and XRD of 25 nm. The SEM shows nanostructured particles with primary particles size below 25 nm.

20 mg of the cobalt oxide was dispersed in 50 ml of PAA with three different concentrations given (Table 41). The PAA has the same characteristics as for the precipitation of cobalt oxalate (molecular weight 2000). The dispersion of the primary particles to then use as seeds was first attempted by a simple

ultrasonic treatment. The PAA is expected to help dispersion of the primary particles that may be dislodged from the cobalt oxide mother particle.

Table 41: Summary of the cobalt oxide dispersion in different PAA concentration and pH measurements

PAA (g/L)	R=AA/NaOH	pH
0.05	1	7.60
0.20	1	9.30
2.00	1	12.10

The colloidal dispersions, thus produced have been filtered through a 200 nm membrane to remove the mother particles. The analysis of particle size distribution on the suspension that passed through the filter was carried out using PCS and SEM micrographs (Figure 91 and Figure 92).

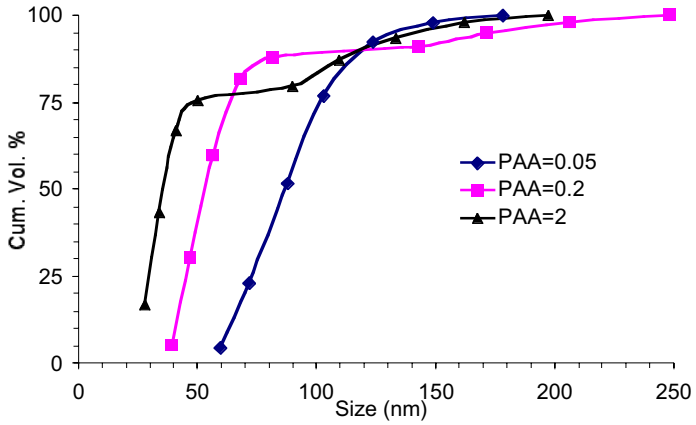

Figure 91: Particles size distribution of cobalt oxide seeds after passing a 200 nm filter measured by PCS

Table 42: PAA concentration and d_{v50} and span measured for the cobalt oxide seeds

PAA concentration (g/L)	d_{v50} (nm)	Span = $d_{v50}/(d_{v90}-d_{v10})$
0.05	87	0.61
0.20	53	1.5
2.00	35	2.77

The PAA concentration seems to have an influence of the PSD, increasing the organic additive concentration the particles size decreased approaching the d_{BET} at the highest PAA concentration. To evaluate in more detail the cobalt oxide particles, a small amount of suspension was filtered through 20-nm ceramic membrane (Whatman) in order to check the particles size range and morphology by SEM analysis (Figure 92).

a) 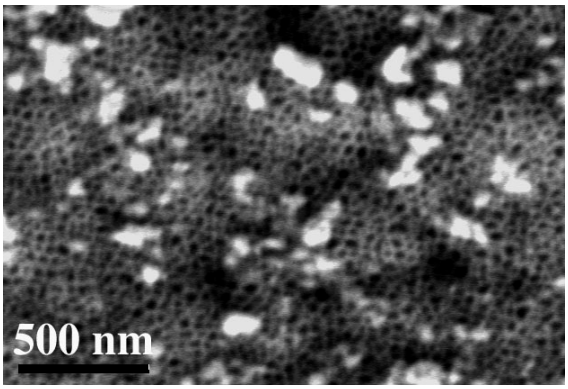

b) 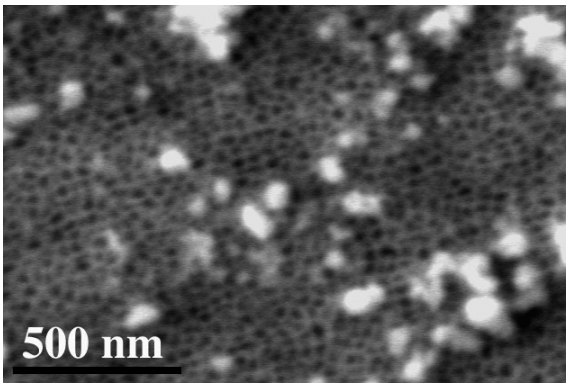

Figure 92: SEM analysis of cobalt oxide suspension in the presence of the additive: a) PAA 2% wt; b) 0.2% wt

SEM images of the two samples show particles with sizes between 30 and 150 nm with perhaps more particles under 50 nm with the 2% PAA solution coherent with the PCS results.

B. Results of precipitation using the cobalt oxide seeds

Precipitation was carried out using 2 ml of concentrated cobalt oxide suspension dispersed in 50 ml sodium oxalate solution 0.01M. The final concentration of cobalt oxide dispersed in the sodium oxalate solution was estimated to be around 12 mg/L. The two precursors have been mixed by stirring for 5 minutes. The precipitation ageing time was established at 24h. The experiments used to investigate the system are given in Table 43. The resulting precipitates were filtered over 200 nm and then dried over silicagel till a constant weight.

Table 43: experimental samples under investigation as a function of cobalt oxide size

Name of sample	PAA (g/L)	d_{v50} (nm) cobalt	Conc. Cu (mol/L)	Conc. C2O4 (mol/L)	PAA for precipitation (g/L)
A_2	2	35	0.01	0.01	0.40
A_0.2	0.2	53	0.01	0.01	0.04
A_0.05	0.05	87	0.01	0.01	0.01

The precipitation process of copper oxalate takes place in the presence of both the cobalt oxide nanoparticles and the organic additive PAA/NaOH used to disperse the cobalt oxide (Table 43). For the three samples as described in (Table 43) two formed precipitates A_0.05 and A_0.2, that could be filtered. The A_2 formed a colloidal suspension and the standard filtration is not possible. The precipitates were analysed by XRD, TGA and SEM. Figure 93 shows the diffraction patterns of sample A_0.2 which corresponds to the copper oxalate with an certain amorphous contribution.

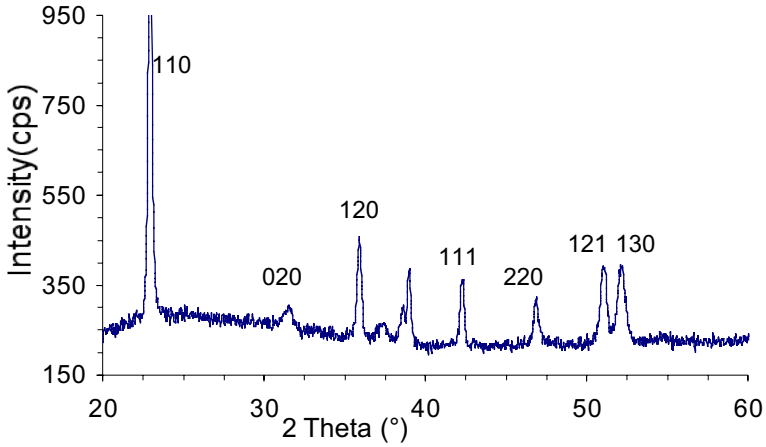

Figure 93: XRD for the sample A_0.2, of copper oxalate

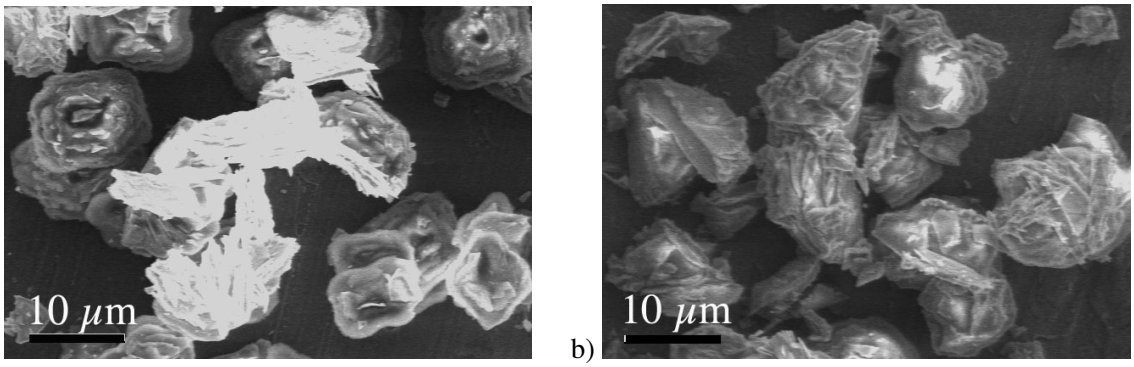

Figure 94: Particles morphology precipitated in the presence of cobalt oxide seed: a) sample precipitated in PAA 0.05 g/L; b) sample precipitated for the conditions: PAA 0.4 g/L

Figure 94 illustrate the particles morphology after precipitation with a size around 10 µm and a rose like morphology, whereas it was expected to be cushion like. The samples were analysed by thermogravimetric analysis in order to determine the possible inclusion of PAA during particles formation, which may influence the morphology. The measurements have been made in nitrogen atmosphere with a rate flow of 20 ml/min and a heat rate of 10°C/min from 30°C to 800°C. TG analysis correspond exactly to copper oxalate. The decomposed powder was analysed by XRD to try and discern the presence of cobalt oxide (Figure 94). This analysis showed only copper oxide with an important amorphous contribution. The final amount of cobalt oxide precipitates in the copper oxalate powder must be around 10% wt, from filtrate analysis (ICP) which showed negligible quantities of cobalt.

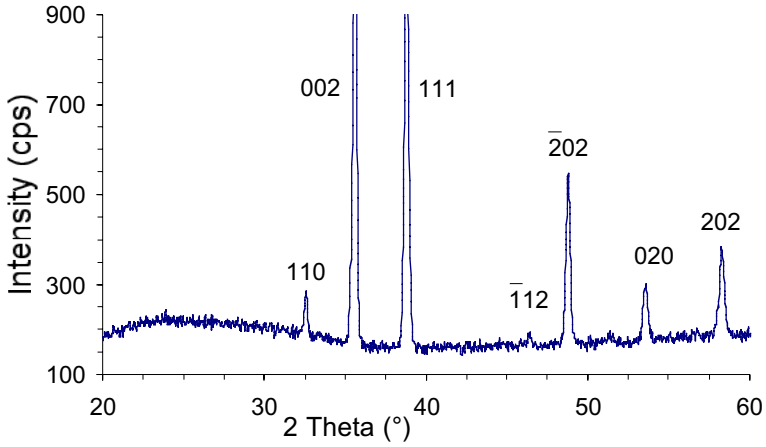

Figure 95: XRD of sample A_0.2 after thermal treatment under nitrogen atmosphere showing CuO (JCPDS 5-0661)

According with the method of powder characterisation it is difficult to estimate the presence or not of cobalt oxide inside the copper oxalate/oxide matrix, preliminary investigation using TEM has shown a cobalt signal but further studies need to be made to quantify the amount.

C. Discussions

Cobalt oxide seeds can be produced from high surface area oxides using ultrasonic treatment. By this method is possible to modify the particles size as a function of PAA concentration presumably due to the better dispersion of primary particles of 25 nm, as the PAA concentration is increased giving a more complete surface coverage.

The isoelectric point of cobalt hydroxide is at 11.4 [104], cobalt oxide in a basic environment should have a similar value. For the sample A_2 the pH is slightly higher than the isoelectric point of the cobalt oxide and the polymer should adsorb in a more extended conformation on a negative surface[105]. For the other samples the pH is below the isoelectric point of the cobalt oxide and the polymer may present a pancake or mushroom conformation for A_0.05 and A_0.2, this would be less efficient in preventing agglomeration of the "dislodged" primary particles.

During the precipitation of copper oxalate in the presence of the cobalt oxide seeds it is presumed that the growth process of copper oxalate is on the cobalt oxide nanoparticles. For the sample A_2 a high amount of PAA may be free in suspension and interact with the copper nitrate. The particles morphology is thus changed from sample A_0.05 to A_0.2. As seen above the PAA has an influence on the particles morphology producing more morphology plate-like. Here the particles morphology is more rose like and this change in morphology is assumed to come from the combined presence of the cobalt oxide and PAA. PAA polymer has also been observed to influence cobalt oxalate particles morphology[101] presumably by a specific adsorption mechanism.

4.5. General Conclusion

Preliminary experiments for the co-precipitation of cobalt-copper oxalate/oxide showed a compatibility of the two systems. The similarity of the thermodynamic data and the nanostructure of two single oxalate copper/cobalt systems seem to be affected when the precipitation process takes place in the presence of the two ions. Furthermore single-phase precipitation occurred if the ratio of the Co/Cu content was far from 1. At concentration close to 1 the two solids formed separately.

Using cobalt seeds either in the form of oxalate or oxide the final product was found to be the copper oxalate. For these systems the particles morphology were affected when compared with the simple precipitation of copper oxalate. For the cobalt oxalate seed route the total amount of the cobalt detected in the particles was 3% wt under the target of 10 % wt, further studies to elucidate the nature of the cobalt oxalate seed suspensions is needed to verify if the route is worthwhile. For the cobalt oxide incorporated in the copper oxalate the amount was also around 3% lower than the predicted the 10% wt, the target for GMR applications. It should be remarked that the cobalt oxide was difficult to detect in the copper oxalate matrix. Only the TEM cross-section will be able to detect the cobalt oxide nanoparticles in the copper matrix. To improve this oxide route, which seems the most promising the use of attrition milling in a solution of basic pH where the oxide is "slowly" dissolved may help obtain the 20 nm primary particles needed. For further investigations it would be interesting to attempt the transformation of the copper oxide / copper oxalate composite precursors into the metallic state.

The PAA used in the various routes was seen to have a significant effect on copper oxalate particle morphology. Further investigation on the exact nature of the CuC_2O_4-PAA interaction is needed to fully understand the complexation with Cu ion that may be important.

Chapter 5. Conclusions and Outlook

One of the main goals of the thesis was to synthesise a nanostructured metallic composite of copper and cobalt. A possible application of this composite is as a giant magneto resistance (GMR) for read/write devices. Attempts to produce such composites were made via 3 routes by co-precipitation of the oxalates or via the use of seeds of cobalt oxalate or oxide. Both the copper and cobalt oxalate precipitates show the type of nanostructure 20-70 nm that is coherent with the Co magnetic domain sizes (10-20 nm) desired for GMR applications.

In the field of precipitation a better understanding of the copper oxalate mechanism was needed. Before this thesis work the mechanism of particle formation was understood as a simple "brick by brick" mechanism. This model was described as a nucleation, followed with a growth by molecular attachment and finally a growth process by aggregation. The copper oxalate crystallographic structure shows a distinct anisotropy: one type of terminating (ε) surface is hydrophobic and another in nature (α) hydrophilic which gives rise to anisotropic properties of the particles. This anisotropy gives the cushion-like particles morphology studied in chapter 2 in the present thesis work.

For a better understanding of the copper oxalate precipitation mechanism, to allow better control for composite synthesis, both solubility calculations and kinetic investigations were made. The pH was followed as a function of time and using the solubility calculations it was possible to link the pH and precipitation yield of copper oxalate. For the precipitation of a single phase, copper oxalate, the solution simulations showed initially a sharp rising of the pH then a more gradual rise to a plateau. Experimentally the sharp rise was monitored but then a gradual decrease of the pH rather than an increase was observed. This pH behaviour could be simulated using solubility calculations by the precipitation of a secondary phase malachite ($CuCO_3 \cdot Cu(OH)_2$). The formation of malachite is possible due to the presence of a small amount of carbonate in the initial solution (from atmospheric CO_2) and a slightly non-stoichiometric sodium oxalate.

The precipitation mechanism was further elucidated by stopping the reaction after different time intervals and the resulting precipitate analysed by HRSEM and TEM cross-section. The HRSEM micrograph observations supported the "brick by brick" particle formation in the early stages of precipitation (2 minutes). Also at this time can be observed many "primary" particles or "bricks" with a sizes less then 100 nm around the larger polycrystalline particles. The cushion morphology is clearly formed after 5 minutes of precipitation. These particles present two large surfaces characterised by low energy surfaces hydrophilic (α) and four small surfaces with a high energy hydrophobic (ε). The cushion

morphology is conserved for a period of time and finally the residual supersaturation eliminates the small surfaces high-energy probably by a molecular attachment growth mechanism.

TEM cross-section analysis showed a possible core-shell assembly of these copper oxalate particles. The core of the particles showed a random organisation and a certain order on 110 axis particularly towards the particle surface. The size of the crystallites is larger on the surface or shell (40 nm) than the core (25 nm). Also the cross-section TEM showed two particles density as a function of the surface nature, denser on the ε surfaces than the α surfaces for cubic particles produced in the presence of hydroxypropylmethyl cellulose (HPMC).

SAXS measurements were made in the aim of a better understanding of the early stage of precipitation, nucleation and growth mechanism before 2 minutes, which remain unclear at the moment. To have precipitated volume fractions measurable by SAXS the precursor concentrations were increased which increases supersaturation producing a high nucleation rate in a shorter time. Unfortunately this gave initial nucleation and growth kinetics that produces particles >100 nm, greater than the SAXS upper size limit in just a few seconds. Therefore the "brick" or primary particle growth mechanism remains to be elucidated in future work. Detailed qualitative mechanisms have been proposed for copper oxalate precipitation, which takes into consideration all the experimental observations. This mechanism creates a link between the supersaturation (solubility calculation) and particles evolution as a function of time in a detailed manner.

Copper oxalate particles with a cubic morphology were used for the thermal transformation into metallic copper. These particles were precipitated in the presence of an organic additive (HPMC). The polymer seems to be adsorbed only on the lateral external hydrophobic ε−surfaces. The particles showed an important anisotropy given by the surface nature with 2 hydrophilic α−surfaces and 4 hydrophobic ε−surfaces.

Previous studies on the copper oxalate transformation in different gases were found in the literature but without characterising the nanostructure evolution. The thermal decomposition was investigated using two routes, one the direct transformation of the oxalate to metallic copper and the second via the oxide.

The main goal of transformation was to conserve the cubic particles morphology from the oxalate through to metallic copper and control the nanostructure evolution. For the direct transformation the nanostructure evolution was investigated as a function of reaction yield. More investigations were carried out on the kinetics of transformation using the sudden change in temperature method. The curves of transformation showed two distinct domains one for a reaction yield, $\alpha<0.6$ and one for higher values. The first domain involved a complex mechanism where it was difficult to distinguish between the nucleation and growth or a possible rate-limiting step. However the second part, $\alpha>0.60$, could be described by a

geometrical model taking into consideration the particles nanostructure and the particles anisotropic structure.

The second route to metallic copper cubic particles formation was via the oxide. The copper oxalate transformation into an oxide with a high surface area (70 m^2/g) was achieved in air at 275°C. Investigations were carried out on the nanostructure evolution from the initial stage of oxide to the final metallic copper. A kinetic characterisation was made by the "sudden change" approach for both pressure and temperature. As for the copper oxalate transformation, the copper oxide transformations presents also two domains, one before $\alpha_{total}<0.20$ and the second for higher transformation. In the first part ($\alpha_{total}<0.20$) the intermediate oxide, Cu_2O, is the only product. For the second part all the three solids CuO, Cu_2O and Cu are present up to $\alpha_{total}=0.96$. The initial part of the transformation ($CuO \rightarrow Cu_2O$) was understood as a nucleation and growth, shrinking core model, with a rate-limiting step of growth associated with the hydrogen dissociation step. Furthermore looking at the macrostructure of the particles the transformation starts on two the less "dense" surfaces (α) and then proceeds towards the inner area of the particles.

The second part of transformation for $\alpha_{total}>0.20$, is complex, for this part was possible to propose only a "geometrical" model considering all the experimental observation and particle characterisation. A link between the internal nanostructure and yield of transformation was proposed. The inhomogeneity of the copper oxide with a high density of particles in the outer shell, the transformation could take place differently from the core towards the shell. The nucleation event per copper oxide primary particle probably varies between the core and the shell. Also a sintering of the copper nanograins takes place for $\alpha>0.63$, with an increase in the Cu crystallite size, whereas the size of the oxides change little during all the transformation. This supports a sluggish nucleation and more rapid growth mechanism. The particles morphology as cubes is conserved with only a slight change, of around 5% shrinkage, but the SSA changes from the oxide of 70 m^2/g to metallic copper of 5 m^2/g with the primary particle or crystallite size increasing from 8 nm to around 42 nm, respectively.

Thermodynamic considerations of a possible co-precipitation of cobalt-copper oxalate were made for different ratios of Cu/Co. The solubility calculations showed similar supersaturation and thus the possible formation of the two solids independent of the Cu/Co ratio. Unfortunately, experimentally no solid solution coprecipitate was found and the two distinct phases were observed only for a ratio of 1. For other Cu/Co ratios only one single phase was observed. If Cu/Co>1, only the copper oxalate precipitated, or if Cu/Co<1 only the cobalt oxalate precipitated. A significant change in particle morphology was observed for the copper oxalate (i.e. in the presence of Co). The cobalt oxalate morphology was not influenced and produced rods each time.

A second preliminary route on possible composite formation was carried out via heterogeneous precipitation using cobalt oxalate or cobalt oxide seeds. When cobalt seeds either in the form of oxalate or oxide the final product was found by XRD to be copper oxalate. The amount of cobalt detected by TEM in

the precipitated particles, from either oxalate or oxide seeds, was around 3% wt, lower than the target of 10%. Furthermore for these systems the particle morphology was affected when compared with the simple precipitation of copper oxalate. The most promising route seems to be the use of oxide seeds, because of a control of the seed size was shown to be possible by using poly acrylic acid (PAA) as a dispersing. Their low solubility in the pH range of copper oxalate precipitation whereas the oxalate seeds have a significant solubility and may have a tendency to dissolve.

Outlook

For the copper oxalate assembly mechanism the early stage of precipitation is still unclear. The mechanism proposed involves nucleation, and each nucleus grows by molecular attachment, but an alternative path to be investigated could be a coalescence of nuclei. This could possibly be made using a combined dynamic / static light scattering (DLS/SLS) approach if multiangled detectors and a powerful pulsed laser were available Another possible route may be the use of cryogenic TEM methods, trying to stop the reaction at 1-5 seconds. The extreme beam sensitivity of the copper oxalate could however render analysis difficult.

To place the detailed qualitative model proposed for the copper oxalate growth mechanism on a more quantitative basis mass and population balance modelling should prove fruitful. For such modelling an estimation of an interfacial energy as a function of the particles anisotropy needs to be made. Furthermore a link between the supersaturation and the dominant species trapped in the double layer, which changes with time could be fruitful for the secondary nucleation proposed in the model. However the pH evolution and thus the solution composition must be followed while simultaneously measuring the PSD for example by using the Malvern MasterSizer or a combined DLS/SLS approach.

For the copper oxide transformation to an intermediate oxide (Cu_2O) nanodiffraction may be a way to elucidate between a shrinkage core or total transformation of each 12 nm grain of CuO into Cu_2O. The copper oxides produced as an intermediate product with a high surface area have an important application as catalyst for degradation of nitrophenol. Further improvements in the SSA of the copper particles nanostructured produced via the oxide route should be possible and may render them interesting as catalysts for methanol synthesis.

For the possible formation of the copper/cobalt composite first of all the presence of the cobalt oxide in the copper oxalate/oxide matrix must be confirmed using the TEM cross-section method. To produce the cobalt oxide as seeds with a size near to 20 nm a possible way could be a chemical mechanical dispersion in the presence of an additive. Further investigation should be done on the cobalt oxide characterisation and their surface nature. This would help towards understanding of the nature of the copper oxalate/cobalt oxide interface in the presence of the additive needed to disperse the 20 nm seeds.

When the composite with the desired ratio Cu/Co is formed the reduction process to metal of cobalt oxide must be made and finally to test the magnetic properties. When the precipitation mechanism is well understood some investigations on the magnetic property variation as a function of the cobalt size and quantity dispersed in the copper conducting matrix would be of great interest.

This thesis work has improved our understanding of the copper oxalate growth mechanism showing it to be more complex than a simple nucleation, growth and aggregation pathway as previously proposed. The copper oxalate presents an anisotropic structure with a core-shell substructure, with varying density and crystallite size.

Metallic copper particles are produced successfully passing via the oxide, the nanostructure and the shape were conserved to a certain degree. Following the direct transformation of copper oxalate to metallic copper the particles morphology was lost.

The most promising route to form a Co/Cu composite seems to be via the cobalt oxide seeds using the heterogeneous precipitation route.

[1] M.N. Baibich, J.M. Broto, A. Fert, F. Nguyen Van Dau, F. Perroff, "Giant Magnetoresistane of (001)Fe/(001) Cr magnetic superlattice" *Physical Review Letters*, **1988**, 61, 2472-2475

[2] J.C. Cezar, M.C. Martins Alves, D.Z. Cruz, F.C. S. da Silva, M. Knoble, H. Tolentino, "EXAFS characterization of cobalt nanoparticles embeded in a copper matrix", *Materials Science Forum*, **1999**, 302, 38-42

[3] J. Wecker, R. von Helmolt, "Giant magnetoresistance in melt spun Cu-Co alloys", *Allplied Physics Letters*, **1993,** 62, 1985-1987

[4] R.H. Yu, X.X. Zhang, J. Tejada, "Magnetic and magnetoresistance properties in Co_5Cu_{95} melt-spun alloys" *Journal of Applied Physics*, **1995**, 78, 392-397

[5] J.A. Dirksen, S. Benjelloun, T.A. Ring, "Modeling the precipitation of copper oxlate aggregates", *Colloid and Polymer Science* **1990**, 268, 864-876

[6] N. Jongen, P. Bowen, J. Lemaintre, J.C. Valmalette, H. Hofmann, "Precipitation of self-organized copper oxalate polycrystalline particles in the presence of hydroxypropylmethylcellulose (HPMC); Control of morphology" *Journal of Colloid Interface Science*, **2000**, 226, 189-198

[7] N.Jongen, Thesis no. 1864 " Contrôle de la composition, de la morphologie et de la granulométrie des oxalates de Y, Ba et Cu précipités en milieu aqueux", Lausanne **1998**, Suisse

[8] V. Privman, D.V. Goia, J. Park, E. Matijevic, "Mechanism of formation of monodispersed colloids by aggregation of nanosize precursors" *Journal Colloid and Interface Science*, **1999**, 213, 36

[9] O.Pujol, P. Bowen, P.A. Stadelmann, H. Hofmann, "Growth and Self-Assembly of Nanostructured $CoC_2O_4{\cdot}2H_2O$ Particles", submitted to *Journal Physics Chemistry B*, **2004**

[10] M.O.Habbache, S.G. Fritsch, J.Sarrias, A. Rousset, P. Bowen, "Contrôle de la precipitation des oxalates mixtes de Mn et de Ni en regim continu" *internal report*

[11] V.K. LaMer, "Nucleation in Phase Transitions" *Ind. Eng. Chem.*, **1952**, 44, 1270

[12] M Donnet, these no. 2623, "Précipitation de $CaCO_3$ en réacteur tubulaire: rôle des germes pour le contrôle de la granulométri et de la sélectivité" **2002** EPF Lausanne, Switzeralnd

[13] A.S. Myerson, "Molecular modeling applications in crystallization" Cambridge University Press 1999

[14] J.A. Dirksen, T.A. Ring, "Fundamentals of Crystallisazation:Kinetic Effects on Particles Size Distribution and Morphology" *Chemical Engineering Science*,**1991**, 46, 2389-2427

[15] J. Garside, "Industrial Crystallization from solution", *Chemical Engineering Science,* **1985**, 40, 3-26

[16] A.Testino, M.T. Buscaglia, V. Buscaglia, M. Vaini, C. Bottino, P. Nani, "Kinetics and Mechanism of aqueous synthesis of $BaTiO_3$ particles" *Chemistry Materials*, **2004,** 16, 1536-1543

[17] M. Ocana, R.R. Clemente, C. J. Serna, "Uniform Colloidal Particles in Solution: Formation Mechanism" *Advanced Materials*, **1995**,7, 212-216

[18] G. Porod, in O.Kratky, O. Glatter, *Small Angle X-rays Scattering*, Academic Press London, **1982**

[19] M.S. Tokumoto, S.H. Pulcinelli, C.V. Santilli, A.F. Craievich, "SAXS strudy of the kinetics of formation of ZnO colloidal suspension", *Journal of Non Crystalline Solids*, **1999**, 247, 176-182

[20] W.R. Meyer, S.H. Pulcinelli, C.V. Santilli, A.F: Craievich, "Formation of colloidal particle of hydrous iron oxide by forced hydrolysis", *Journal of non-Crystalline Solid*, **2000**, 273, 41-47

[21] H. Colfen and H. Schnablegger, "Particle Growth Kinteics in Zirconium Sulfate Aqueous Solutions Followed by Dynamic Light Scattering and Analytical Ultracentrifugation: Implication for Thin Film Deposition" *Langmuir*, **2002**, 18, 3500-3509

[22] H. Colfen, T. Pauck, "Determination of particle size distribution with anström resolution" *Colloid and Polymer Science*, **1997**, 275(2), 175-180

[23] H. Colfen, S. Mann, "Higher -order organisation by mesoscale self-assembly and transformation of hybrid nanostructures", *Angewandte Chemie-International,* Edition **2003**, 42 (21), 2350-2365

[24] O. Söhnel, J Garside, *Precipitation Basic Principles and Industrial Applications,Butterworth Heinemann*, **1992**

[25] N. Bowden, A. Terfort, J. Carbeck, Whitesides GM,"Self-assembly of mesoscale objects into ordered two-dimensional arrays" *Science*, **1997**, 276, 233-235

[26] Y. Guyodo, A. Mostrom, R.L. Penn, Banerjee SK, "From Nanodots to Nanorods: Oriented Aggregation and magnetic evolution of nanocrystallite goethite"*, Geophysical Research Letters*, **2003**, 30, 1512

[27] S.Kim, C. F. Zukoski, "A model of Growth by Hetero-Coagulation in Seeded Colloidal Dispersion", *Journal of Colloid and Interface Science*, **1990**, 139, 198-212

[28] J.F. Banfield, S.A. Welch, H. Zhang, Ebert T.T., Penn R.L., "Aggregation-based crystal growth and microsctructure development in natural iron oxyhydroxide biomineralization products" *Science*, **2000**, 289(4), 751-754

[29] D. Eichert, H. Shifi, M. Banu, S. Cazalbou, C. Combes, Ch. Rey, "Surface Structure of Nanocrystalline Apatites for Bioceramics and Coatings" *CIMTEC 2002 Proceeding, 10th Inter, Ceramic Congress & 3rd Forum of New Materials*, **2002,** Florence, Italy, July, 14-18,

[30] R.L. Penn, J.F. Banfield, " Imprefect Oriented Attachment: Dislocation Generation in Defect -Free Nanocrystals" *Science*, **1998**, 281 (14), 969- 971

[31] H.F. Lieberman, L. Williams, R.J. Davey, R.G. Pritchard, "Molecular Configuration at the Solid-Solid Interface: Twinning in Saccharin Crystals" *J. Am. Chem. Soc*, **1998**, 120, 686-691,

[32] R.L. Penn and J.F. Banfield, "Morphology development and crystal growth in nanocrystalline aggregates under hydrothermal conditions: Insights from titania" *Geochim. Cosmochim. Acta* , **1999**, 63, 1594

[33] B. Judat, M. Kind, "Morphology and internal structure of barium sulfate-derivation of a new growth mechanism" *Journal of Colloid and Interface Science*, **2004**, 269, 341-353

[34] Sugimoto T., "Preparation of monodispersed colloidal particles" *Advanced Colloid Interface Science*, **1987**, 28, 65-108

[35] R.L. Penn, G.Osakm, T.J. Strathmann, Searson P.C., Stone A.T., Veblen D.R., "Epitaxial assembly in aged colloids", *Journal Phys. Chem. B*, **2001**, 105, 2177-2182

[36] D.L.Van Hyning, W.G. Klemperer, C.F. Zukoski, "Silver nanoparticle formation: prediction and verification of the aggregative growth model" *Langmuir*, **2001**, 17, 3128-3135

[37] F. Huang, H. Zhang, J.F. Banfield, "Two-stage crystal-growth kinetics observed during hydrothermal coarsening of nanocrystalline ZnS" *Nano Letters*, **2003**, 3, 373-378

[38] A. Taubert, Ch. Kubel, D.C. Martin, "Polymer-induced microstructure variation in zinc oxide crystals precipitated from aqueous solution", *Journal Physical Chemistry B*, **2003**, 107, 2660-2666

[39] Schmittler H, "Comments on the structure of copper (II) Oxalate: Discussin of X-ray Powder Diffraction and EXAFS Results as a Basis for the Interpretation of Magnetic Properties" *Crystal Res. Technology*, **1984**, 19, 1225-1230

[40] Mei Li, H. Schnablegger, S. Mann, *Nature*, "Coupled synthesis and self-assembly of nanoparticles to give structures with controlled organization" **1999**, 402, 393-395

[41] J. Rieger, J. Thieme, C. Schmidt, "Study of Precipitation Reaction by X-ray Microscopy $CaCO_3$ Precipitation and the Effect of Polycarboxylates", *Langmuir,* **2000,** 16, 8300-8305

[42] W.M. Jung, S.H. Kang, W. S. Kim, C. K. Choi, "Particle morphology of calcium carbonate precipitated by gas-liquid reaction in a Couette-Taylor reactor", *Chemical Engineering Science*, **2000**, 55, 733-747

[43] A.P. Collier, C.J.D. Hetherrington, M.J. Hounslow, "Alignment mechanism between particles in crystalline aggregates" *Journal of Crystal Growth*, **2000**, 208, 513-519

[44] A.P. Alivisatos, "Biomineralization-Naturally aligned nanocrystals" *Science*, **2000**, 289, 736-738

[45] V.F. Puntes, K.M. Krishnan, A.P. Alivisatos, "Colloidal nanocrystla shape and size control: The case of cobalt" *Science***, 2001,** 291, 2115-2117

[46] M.P. Morales, T. Gonzales Carreno, C.J. Serna, "The formation of Alpha-Fe_2O_3 monodispersed particles in solution" *Journal of Materials Research Society*, **1992**, 2538-2545

[47] S. Rubattel, J. Lemaitre, P. Bowen, T.A. Ring, "Aqueous solubility of Y, Ba and Cu oxalates in the system ($Y(OH)_3$, $Ba(OH)_2$, $Cu(OH)_2$)-$H_2C_2O_4$-(HNO_3/NaOH)-H_2O", *Journal of Crystal Growth*, **1994**, 135, 135-144,

[48] M.J.Hounslow, A.S. Bramley, W.R. Paterson, "Aggregation during precipitation from solution. A pore diffusion-reaction model for calcium oxalate monohydrate" *Journal of Colloid and Interface Science*, **1998**, 203, 383-391

[49] R. Vacassy, S. M. Scholz, J. Dutta, Ch. J.G. Plummer, R. Houriet, H. Hofmann, " Synthesis of Controlled Spherical Zinc Sulfide Particles by Precipitation from Homogeneous Solutions"*, Journal American Ceramic Society,* **1998,** 81, 2699-2705

[50] A. Testino thesis, "*$BaTiO_3$ Sintesi in Fase Acquosa di Nanopolveri Studio Sperimentale e Sviluppo di un Modello Cinetica*" Universita degli Studi di Genova, Italy, **April 2004**

[51] A.L. Randolph, M. A. Larson, "Theory of Particulate Processes", *London*, **1971**

[52] M.J. Hounslow, R.L. Ryall, V.R. Marshall, "A Discretized Population Balance for Nucleation, Growth and Aggregation" *AIChE Journal*, **1998**, 34, 1821-1832

[53] A.S. Bramley, M.J. Hounslow, R.L. Ryall, "Aggregation during precipitation from solution: A method for extracting rates from experimental data" *Journal of Colloid and Interface Science,* **1996,** 183, 155-165

[54] A.M. Donia, Dollimore D., "Preparation, identification and thermal investigation of solid solutions of cobalt-copper oxalates", *Thermochmica Acta*, **1997**, 290(1), 139-147

[55] T. Sugumote and Y. Wamg, "Mechanism of the Shape and Structure Control of Monodispersed a-Fe2O3 Particles by Sulfate Ions", *Journal of Colloid and Interface Science*, **1998**, 207, 137-149

[56] D. Dollimore, "The production of metal and alloys by the decomposition of oxysalts" *Thermochimica Acta*, **199**1, 177, 59-75

[57] D. Dollimore and K.H. Tonge,, *Proceedings of the Fifth International Symposium on Reactivity of Solids*, Munich, **1964**, 97

[58] D. Dollimore, D.L. Griffiths, *Journal of Thermal Analysis*, **1970**, 2, 229-250

[59] D. Dollimore, "The thermal-decomposition of oxlates-A review", *Thermochimica Acta*, **1987**, 117, 331-363

[60] M.E. Brown, D. Dollimore, A.K. Galwey, *Comprehensive Chemical Kinetic*, Vol 22, Reaction in the Solid State, Eds. C.H. Bamford, C.F.H. Tipper, Elsevier, Amsterdam **1980**

[61] V.V. Boldyrev, I.S. Nev'yantsev, Y.I. Mikhailov, E.F. khairetdinov, *Kinet. Katal.*, **1970**, 11, 367

[62] K. Honda and T Stone, *Sci. Rept. Tohoka Imp. Univ.*, **1914**, 3, 139

[63] D. Dollimore and J. Mason, "Thermal-decomposition of oxlates. Effect of container material on DTA results for thermal-decomposition of magnesium oxalate", *Thermochimica Acta*, **1981**, 43, 183-187

[64] D. Dollimore and D.L. Griffiths, *Journal of Thermal Analysis*, **1970**, 2, 229,

[65] D. Broadbent, J. Dollimore, D. Dollimore, T.A. Evans, "Kinetic-study of the thermal decomposition of copper oxalate", *Journal Chemical Society*, **1991**, 87, 161-166

[66] D. Dollimore, D.M. Tinsley, "Thermal Decomposition of Oxalates. Thermal decomposition of Lithium Oxalate" *Journal of Chemical Society A*, **1971**, 3043

[67] J. Bandara, J. Kiwi, C. Pulgarin, Pajonk GM, Elaloui A, Albers P., "Novel cyclic process mediated by copper oxides active in the degradation of nitrophenols: Implications for the natural cycle" *Environmental Science and Technology*, **1996**, 30, 1261-1267

[68] M.D. Bharadwaj, J.C. Yang, "The Reduction of Copper Oxide by Water Vapor Visualized by in-situ UHV-TEM, *Scripta Materialia*, **2001**, 44, 2557-2561

[69] J.Y. Kim, J.A. Rodriguez, J.C. Hanson, A.I.Frenkel, P.L. Lee, " Reduction of CuO and Cu_2O with H_2: H Embedding and Kinetic Effects in the Formation of Suboxides" *Journal of American Chemical Society*, **2003**, 125, 10684-10692

[70] J.A. Rodriguez, J.Y. Kim, J.C: Hanson, M.Perez, A.I. Frenkel, "Reduction of CuO in H_2: *in-situ* time-resolved XRD studies" *Catalysis Letters*, **2003**, 85,247-254

[71] D. Dollimore, P. Spooner, "Sintering Studied on Zinc Oxide" *Transaction of the Faraday Society*, **1971**, 74, 2750

[72] M. Soustelle, *Modelisation Macroscopique des Transformation Phyico-chimiques,* Masson, Paris, **1990**

[73] M. Soustelle, M. Pijolat, "Experimental methods useful in the kinetic modelling of heterogeneous reactions" *Solid State Ionics*, **1997**, 95, 33-40

[74] C. Brun, F. Valdivieso, M. Pijolat, M. Soustelle, "Reduction by hydrogen of U_3O_8 into UO_2: Nucleation and growth, infleunce of hydration" *Phys. Chem. Chem. Phys.*, **1999**, 1, 471-477

[75] S. Perrin, M. Pijolat, F. Valdivieso, M. Soustelle, "Kinetic study of the effect of a sudden change in temperature during the reduction of U_3O_8 into UO_2 by hydrogen" *Solid State Ionic*, **2001**, 141-142, 109-115

[76] A.K. Galwey, M.E. Brown, Thermal Decomposition of Ionic Solids, *Elsevier*, **1999**

[77] M.J. Hounslow, A.S. Bramley, W.R. Paterson, "Aggregation during precipitation from solution. A pore diffusion-reaction model for calcium oxalate monohydrate", *Journal of Colloid and Interface Science*, **1998**, 203, 383-391

[78] S. Rubattel, J. Lemaître, P. Bowen, T. A. Ring, "Aqueous solubility of Y, Ba, and Cu oxalates in the system($Y(OH)_3$, $Ba(OH)_2$, $Cu(OH)_2$-$H_2C_2O_4$-(HNO_3/NaOH)-H_2O", *Journal of Crystal Growth*, **1994**, 135, 135-144

[79] S. Kotrly, L. Sucha, *Handbook of chemical euqilibria in analytical chemistry*, Ellis Horwood , England **1985**

[80] H.P. Klug and A.L. Alexander, X -ray Diffraction Procedures for polycrystalline and amorphous Materials, (Wiley, New York, 1954)

[81] N Jongen, "Control de la composition, de la morphologie et de la granulometrie des oxlate de Y, Ba, et Cu precipités en milieu aqueux", PhD Thesis N°. 1846, Swiss Federal Institute of technology of Lausanne (EPFL), Lausanne 1998, Suisse

[82] P.Bowen, J.A. Dirksen, R.H. Baker, L. Jelinek, "An Approach to Improve the Accuracy of Submicron Particle-Size Distribution Measurement Using the HORIBA-CAPA-700", *Powder Technology*, 74, **1993**, 67-71

[83] L.C.Soare, N. Jongen, P. Bowen, V. Buscalia, H. Amenitsch, "Epitaxial Self Assembly of Nanocrystallites-A New Particle Growth and Design Mechanism", *Annual Report*,**2002,** IBR/ ELETTRA, page 65-67

[84] T. Nomura, Y. Kousaka, M. Alonso, M. Fukunaga, T. Satoh, "Precipitation of zinc sulfide particles from homogeneous solutions", *Journal of Colloid and Intrface Science*, 221, **2000**, 195-199

[85] H. Amenitsch, Institute of Biophysics and X-ray Structure Research, Austrian Academy of Science, Scmiedlerstr. 6, 8042 Graz, Austria

[86] A. Coetzze, Brown M. E., Eve D. J. Strydom C.A. "Kinetics of the thermal dehydrations and decompositions of some mixed -Metal Oxalates"*, Journal of Thermal Analysis*, 41, **1994**, 357-385

[87] N. Jongen, P. Bowen, J. Lemaitre, H. Hofmann, "Calcination and morphological evolution of cubic copper oxalate particles", *Journal of Materials Science Letters*, 19, **2000**, 1073-1075

[88] J.H. Yu, H.S. Ahn, J.S. Lee, L.C. Soare, H.Hofmann, "Decomposition and Microstructural Development of Copper and Cobalt Oxalate Precipitate Particles in Hydrogen Atmosphere", article in preparation for *Thermocimica Acta*

[89] O. Kubaschewski, C.B. Alcock, Metallurgical Thermochemistry, Pergamon Press, Oxford, 1979

[90] Schmidler, "Comments on the Structure of Cu(II) Oxalate: Discussion of X-ray Powder Diffraction and EXAFS Reuslts as a Basis for the Interpretation of Magnetic Properties" *Crystal Res & Technology*, 19, **1984**

[91] M. Tupin, M. Pijolat, F. Valdivieso, M. Soustelle, A. Frichet, P. Barberis, "Differences in reactivity of oxide growth during the oxidation of zircoloy-4 in water vapor before and after the kinetic transition", *Journal of Nuclear Materials*, 317, **2003**, 130-144

[92] F. Kubel, Institute of Chemical Technologies and Analytics, Vienna University of Technology, Getreidemarkt 9/164 1060 Vienna, Austria

[93] J.Y. Kim, J.A. Rodriguez, J.C. Hanson, A.I. Frenkel, P.L. Lee, "Reduction of CuO and Cu_2O with H_2: H Embedding and Kinetic Effects in the Formation of Suboxides", *Journal of American Chemical Society*, 125, **2003**, 10684-10692

[94] V. Bouineau, thesis 179 TD, *"Experimentation et modelisation des reactions de decomposition isotherme et isobar des solides. Application au sulfate de lithium monohydrate et au carbonate de calcium*" 1998, St Etienne France

[95] M. Soustelle, M. Pijolat, "Experimental methods useful in the kinetic modelling of heterogeneous reactions", *Solid State Ionics*, 95, **1997**, 33-40

[96] L.C.Soare, P.Bowen, J. Lemaître, H. Hofmann, M. Pijolat, F. Valdivieso, "Assembly of nano-domain builgings blocks of copper oxalate with a cubic morphology", *Materials Reserch Society Symposium Proceedings*, vol. 788, *Materials Research Society* **2004**

[97] A.P.Satterfield and V.H. Sherwood, *The role of diffusion in catalysis*, Addison-Wesley, 1963

[98] Kröger F.A. *The chemistry of imperfect crystals*, 2nd Ed. , 3 vols. (North Holland Publ. Co., Amsterdam)1973

[99] J.A. Rodriguez, J.Y. Kim, J.C. Hanson, M.Perez, A.I. Frenkel, "Reduction of CuO in H_2: *in-situ* time-resolved XRD studies", *Catalysis Letters*, 85, **2003**, 247-254

[100] J. Bandara, J. Kiwi, C. Pulgarin, P. Peringer, G. M. Pajonk, A. Elaluoi, P.Albers, "Novel cyclic process mediated by copper oxides active in the degradation of nitrophenols: Implications for the natural cycle", *Environmental Science and Technology*, 30, **1996**, 1261-1267

[101] O. Pujol, EPF Lausanne thesis "Etude par microscopie électronique des particules nanostructure d'oxalate de cobalt dihydrate précipite en milieu aqueuse" **2004**

[102] A.M. Donia, N.R.E. Radwan and A.A. Atia, "Preparation of mixed Co and Cu oxides via thermal decomposition of their oxlates, and study of their catalytic properties", *Journal of Thermal analysis and Calorimetry*, 61, **2000**, 249-261

[103] O.Pujol, Internal Report of Thesis

[104] G.A. Parks, "Isoelectric points of solids oxides solid hydroxides and aqueous hydroxo complex systems", *Chemical Reviews*, 65, **1965**, 177-198

[105] H. G. Pedersen, L. Bergström, "Forces Measured between Zirconia Surfaces in Poly(acrylic acid) Solutions", *Journal of American Ceramic Society*, 82 (5), **1999**, 1137-1145

Appendix of Chapter 2

The particle size evolution is difficult to ensure with the low statistics of SEM. The next section describes the use of ensemble technique to try and follow the particle size evolution as a function of time. The measurements have been carried out by laser diffraction and Small Angle X-rays Scattering (SAXS). For laser diffraction investigations the estimation of a refractive index of copper oxalate is necessary. No optical data was found to be available at the moment in the literature about the copper oxalate powder.

A. Refractive index of Copper Oxalate

The PSD obtained by photocentrifuge for particles sedimentation using the Horiba - is less sensitive to optical parameters for particles smaller than 1 µm of precipitates[1]. To make this measurement only the physical parameters such as the powder density and solvent viscosity are needed. The limits of the distribution can be determined by scanning electron microscopy (SEM).

The PSD obtained by laser diffraction (Malvern) gives us information about the volume distribution of the particles. To describe the results the percentiles d_{v10}, d_{v50}, d_{v90} and the span were used, where the span is defined as:

$$span = \frac{d_{v90} - d_{v10}}{d_{v50}} \qquad eq\ 1$$

A comparison between the PSD's measured using Malvern and Horiba was made. The refractive index used to model the Malvern was adjusted to give results close to those of Horiba and SEM. In both cases calculated PSD are based on the assumption of spherical particles (Figure 1 b). To make as good an estimation as possible of the refractive index a special powder of copper oxalate was precipitated with spherical morphology. These particles were synthesised at high concentration of 0.05 M of each precursor (copper nitrate and sodium oxalate). This was made under the same conditions as described above for the kinetic measurements in section 2.2.2.

For the sedimentation measurements 10 mg of the spherical copper oxalate were dispersed in 200 ml of the saturated solutions of copper oxalate filtered through a 20 nm membrane. It is expected that the possible dissolution does not take place. The background was made with the saturated solution of copper oxalate.

The value of the refractive index calculated by laser diffraction that gave a good correspondence with the HORIBA and SEM data was estimated to be 1.77 for the real part and 0.01 for the imaginary part.

a)

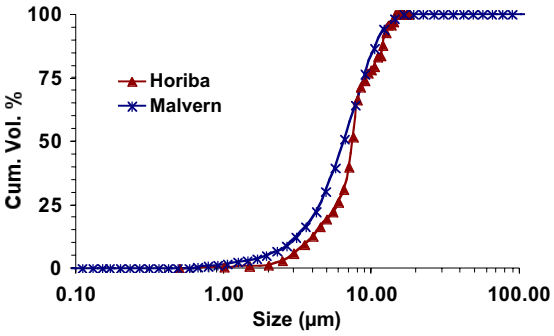

b)

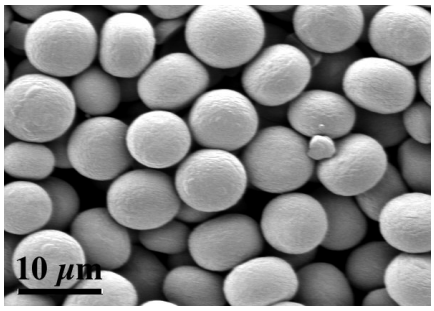

Figure 1: a) PSD obtained by a sedimentation method and by laser diffraction; b) SEM image of particles under investigation

The results of the simulation are summarised in Table 1 for the two methods used.

Table 1: Data of particle size distribution obtained by Malvern and Horiba using the optical data 1.77 real part and 0.01 imaginary part

Method	d_{v10}(µm)	d_{v50}(µm)	d_{v90}(µm)	Span
Malvern (laser diffraction)	2.80	6.45	11.15	1.272
Horiba (sedimentation)	3.25	7.42	13.05	1.303

B. Copper Oxalate Dissolution

The copper oxalate dissolution was studied in order for the nanostructure and the influence of HPMC on the dissolution mechanism. The studied was carried out using a statistical design $3x2^2$. For the dissolution was chosen three types of morphology as: cushion, cubes and rods. The factors under investigation are: particles morphology, time and concentration as described in Table 2:

Table 2: Definition of the statistical design for the copper oxalate dissolution

	Low level	**High level**	
Time (h)	2	24	
Concentration(mg/10ml)	3.9	8.1	
Morphology	**Cushion**	**Cubes**	**Rods**

Figure 2 shows the oxalate particles evolution as time for a concentration of 8.1 mg/10 ml, for a time of 24 hours. The dissolution mechanism of particles stars on the α surfaces (large) which corresponds to the 001 direction, where it is expected a less order of the primary particles.

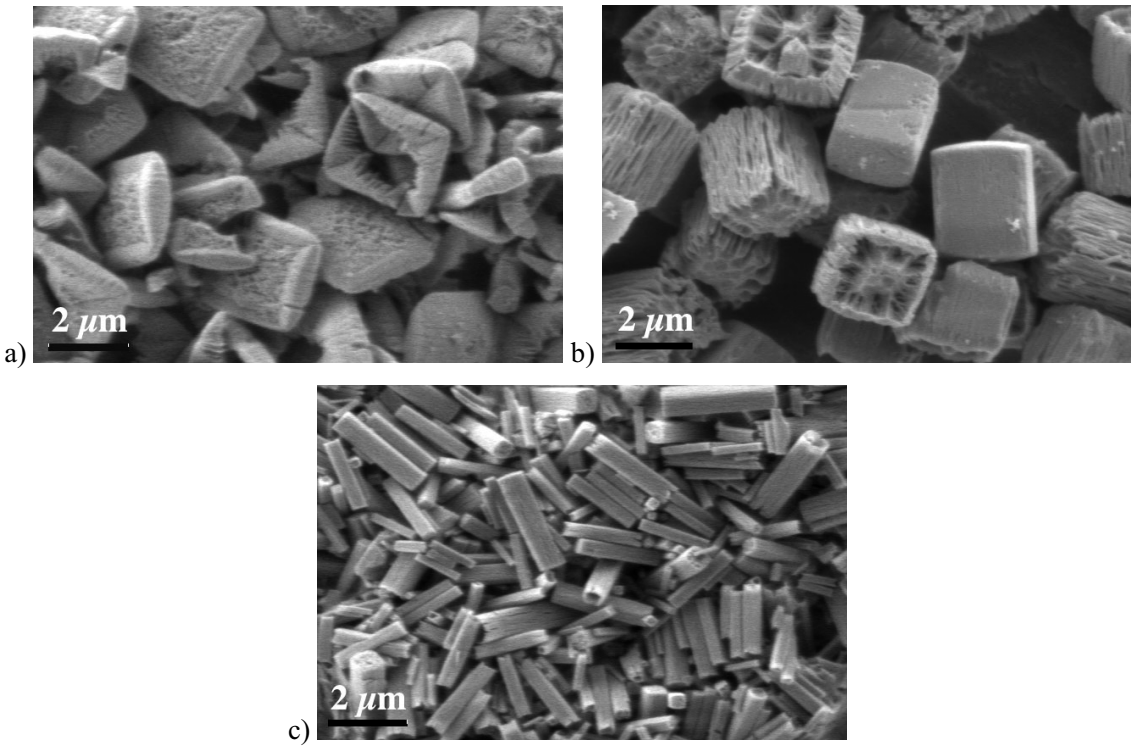

Figure 2: Dissolution of copper oxalate as morphology: a) cushion after 24 hours; b) cubes after 24 hours; c) rods after 24 hours

The investigations were made on the analytical concentration of copper measured by ICP-ASE. The Figure 3 showed an important dissolution of the cushion as time and concentration. However the dissolution of the rods seems to happen in a large time. This fact come may be from the polymer, which is adsorbed on the external surfaces and keep so well the nanounits linked.

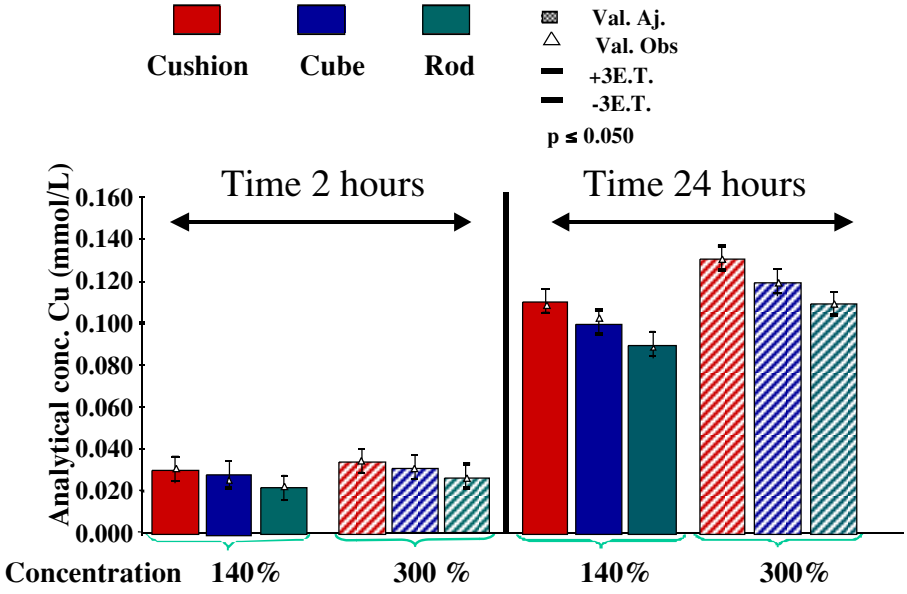

Figure 3: Statistical design of the copper oxalate dissolution

C. Calculation of the barrier energy

The mean Brownian velocity, v, per particles is given by the equation 2

$$\tfrac{1}{2}mv^2 = kT \qquad \textit{Eq 2}$$

For the present case the copper oxalate particles with a size of 70 x 70 x 50 nm, with a density of 3500 kg/m^3 and a particles dispersion of 0.56 g/L. This value of the particles concentration in solution was taken considering the solubility data as described in detail in chapter 2. It is possible to calculate the number of particles dispersed in the volume per unit volume to be of $6.53 \cdot 10^{14}$ and their weight of one particle is $8.57 \cdot 10^{-19}$ kg. The particle velocity is 0.097 m/s. For these conditions the mean separation is about 1000 nm. Thus the time between collisions will be about $3.61 \cdot 10^9$ collisions per second.

We therefore require the condition that the probability of two colliding particles overcoming their barrier energy ΔW should be less than $(1/3.61 \cdot 10^9) = 2.77 \cdot 10^{-10}$. Putting $2.77 \cdot 10^{-10} = \exp(-\Delta W/kT)$ we obtain $\Delta W/kT = 22$. Thus the energy barrier should be in excess of about 22 kT to ensure kinetic stability.

D. Crystals Structure

D. 1. Copper Oxalate

Space group Pnm (Nr. 58) - orthorhombic was developed by Schmittler as shown in Table 3.

Table 3: Lattice parameters of copper oxalate in Å[i]

a	b	c	α = β = γ
5.403	5.571	2.546	90°

Lattice parameters of copper oxalate $CuC_2O_4 \cdot 0.3H_2O$ in Å for the precipitate powder as described in Chapter 2, measured using an X-Pert Philips device with a copper radiation[ii]. The lattice parameters obtained are summarised in Table 4. The measurements were carried out also for the anhydride powder as described in Table 5.

Table 4: Lattice parameters of copper oxalate precipitate powder

a	b	c	α = β = γ
5.4122	5.5843	2.5576	90°

Table 5: Lattice parameters of copper oxalate anhydride powder

a	b	c	α = β = γ
5.4254	5.5775	2.5568	90°

The lattice parameters were calculated using the powder diffraction refined TOPAS 2000. A small but significant differences could be observed between the unit cell parameters *a* and *b* and just a slightly change for the parameter *c*. The presence of water in crystallographic structure was not possible to quantify exactly. The water seems to be dispersed random and did not change so much the lattice parameters.

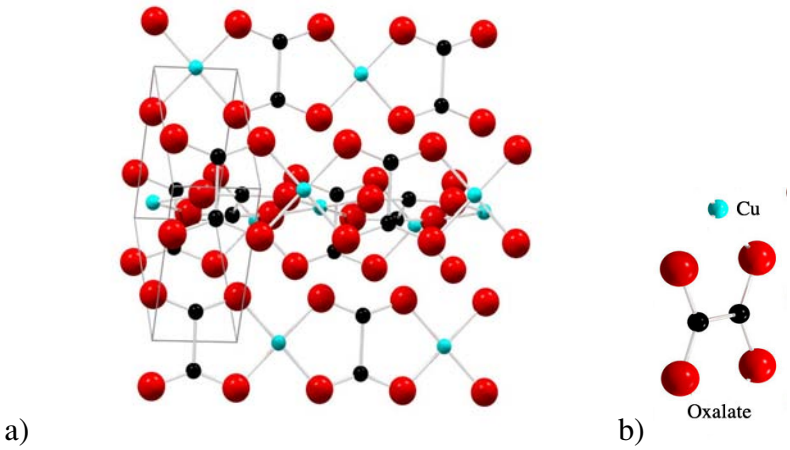

Figure 4: Copper oxalate structure with the ribbons channel fitted using the powder diffraction: a) disordered structure; b) copper oxalate unit

D. 2. Structure of Copper Oxides and Copper

Single crystals of CuO were obtained by a flux method. Commercial powder of copper oxide was mixed in equimolar proportions with sodium carbonate and melted in a platinum crucible, heated in a conventional furnace. The melt was kept at 900°C for 20 hours and then cooled to 500°C at a rate of 1.5°C/min. The solidified material was then air quenched and the sodium carbonate dissolved in hot water. The residue consisted of small, needle-shape, dark, highly reflecting crystals of CuO. The dimensions of the crystal were 0.057x0.013x0.010 mm, the long edge being parallel to the c axis[iii]. The single-crystal X-ray diffraction intensities were measured with a General Electric Datex automatic four circles diffractometer, the crystal being rotated around the c axis. According with the measurements copper oxide (Tenorite) crystallises in the monoclinic space group C2/c (No. 15) with four CuO units in the unit cell. The unit-cell dimension for the Tenorite structure are: a=4.6837A, b=3.4226A, c=5.1288A, β=99.54, D_x=6.515g/cm^3. Some slightly difference on crystallographic parameters can be found in the literature as a function of method preparation of sample[iv]. The crystal structure of Tenorite can be interpreted, as the building elements are the oxygen coordination parallelograms, which forms chains by sharing edge. Such

chains traverse the structure in the 110 and -110 directions, the two types of chains are stacked in the 010 direction with the separation between of about 2.7A the chains. At this distance no bonding should occur. Each individual chain in a group of stacked chains of 110 type is linked to each chain in the two adjacent groups of -110 type by corner sharing, as showing in figure 3a.

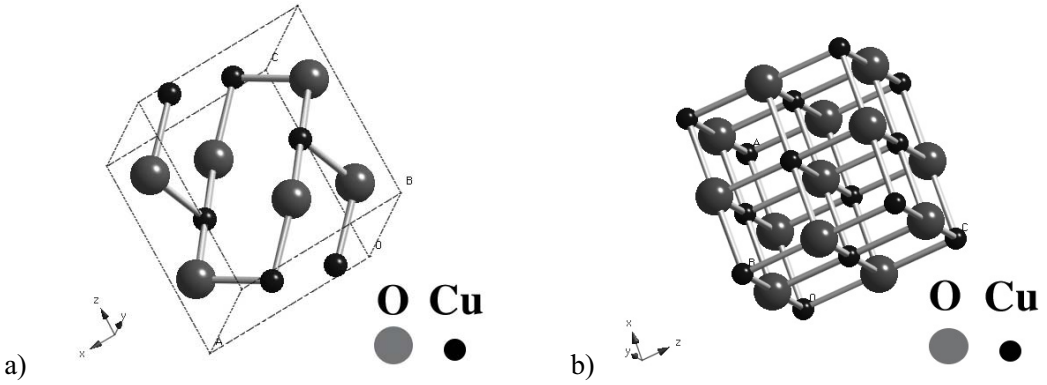

Figure 5: Copper oxide structure with two different crystallographic unit cell: a) Tenorit monoclinic; b) copper oxide cubic

Spherical crystals of Cu_2O were prepared with a crystal grinder (Enraf-Nonius) from a natural specimen of imprecisely specified origin (eastern USA). A sphere of diameter 0.105 mm was chosen for data collection at 100K on an Enraf-Nonius CAD-4 diffractometer using LiF monochromated Ag $K\alpha$ radiation ($\lambda\alpha_1$=0.55941), a nitrogen gas flow cooling device and the 2Θ-ω scan technique. The lattice complexes formed by Cu and O in the cubic Pn3m (224) structure of the semiconductor cuprite are F and I respectively. The lattice parameter is 4.627A and density D_x=6.11 g/cm^3. These f.c.c. and b.c.c. substructures interpenetrate in such a way that O is tethehedrally coordinated by four copper and copper linearly by two oxygen as illustrated in Figure 6 a. The Cu-O distance is 1.848A, whereas the distances between like atoms are much longer, 3.107A for Cu-Cu and 3.695A for O-O. The structure is in fact uniquely defined by requiring a linear coordination of close-packed Cu: the stoichiometry then requires the occupancies of tetrahedral sites by O; any other stacking variant but the cubic one, or occupation of tetrahedral sites other than those of the actual structure leads to O-Cu-O angles, different from 180°. The structure with the exact 2:1 stoichiometry is therefore not expected to be disordered[v].

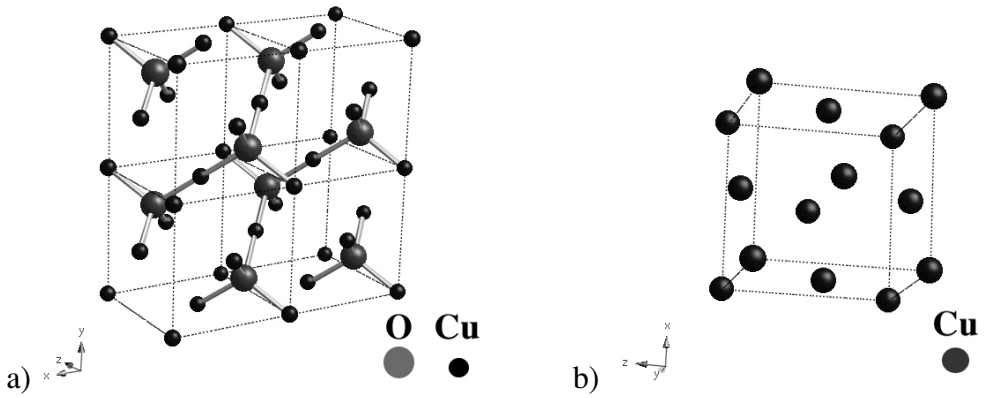

Figure 6: Structure: a) Cu_2O (cuprit) and b) Cu

[1] P. Bowen, J.A. Dirksen, R.H. Baker, L. Jelinek, "An Approach to Improve the Accuracy of Submicron Particle-Size Distribution Measurement Using the HORIBA-CAPA-700" *Powder Technology*, **1993**, 74, 67-71

[i] Schmittler H., "Comments on the structure of copper (II) Oxalate: Discussion of X-ray Powder Diffraction and EXAFS Results as a Basis for the Interpretation of magnetic Properties, *Crystal Res. & Technology*, **1984**, 19, 1225-1230

[ii] F. Kubel, Institute of Chemical Technologies and Analytics, Vienna University of Technology, Getreidemarkt 9/164 1060 Vienna, Austria

[iii] S. Asbrink, J.L. Norrby, *Acta Crystallographica Section B*. 26, **1970**, 8-15

[iv] Gmelin, Handbook for Copper, Vol. 60 B, 72-73

[v] R. Restori, D. Schwarzenbach, *Acta Crystallographica Section B*, 42, **1986**, 201-208

Appendix of Chapter 3

Table 1: Phyisico-chemical properties of phases used for investigation in Chapter 3

Name	CuC_2O_4	CuO	Cu_2O	Cu
Molar Masse (g/mol)	169.54	79.54	143.09	63.546
Density (theoretical) (g/dm^3)	3.50	6.51	6.10	8.91
Density (experimental) (g/dm^3)	3.00	-	-	-
Molar Volume (dm^3/mol)	48.44	12.21	23.45	7.13

Table 2: Volume ratio of several compounds

	CuO/CuC_2O_4	Cu_2O/CuO	Cu/Cu_2O	Cu/CuO
Z	0.25	0.95	0.60	0.58

The chemical reaction studied in Chapter 3 and calculation of volume ratio for one mole of compound for different cases as described below:

$CuC_2O_4 + H_2 \rightarrow CuO + 2\,CO_2 + H_2$ (R_1) $\quad Z = \frac{V_{CuO}}{V_{CuC_2O_4}}$

$2\,CuO + H_2 \rightarrow Cu_2O + H_2O$ (R_2) $\quad Z = \frac{V_{Cu_2O}}{V_{CuO}} \cdot \frac{1}{2}$

$Cu_2O + H_2 \rightarrow 2\,Cu + H_2O$ (R_3) $\quad Z = \frac{V_{Cu}}{V_{Cu_2O}} \cdot 2$

$CuO + H_2 \rightarrow Cu + H_2O$ (R_4) $\quad Z = \frac{V_{Cu}}{V_{CuO}}$

Calculation of reaction yields for simultaneously transformation as R_2, R_3 and R_4:

R_2: $\alpha_1 = \frac{n_0 - n_{CuO(t)}}{n_0} = \frac{2n_{Cu2O(t)} + n_{Cu(t)}}{n_0}$

R_3: $\alpha_2 = \frac{n_{Cu(t)}}{2n_{Cu2O(t)} + n_{Cu(t)}} = \frac{n_{Cu(t)}}{\alpha_1 \cdot n_0}$

$\alpha = \alpha_1 \cdot \alpha_2 = \frac{n_{Cu(t)}}{n_0}$

The mechanism proposed in Chapter 3, section 3.5.2.. It was described by five chemical reactions:

1) Adsorption step on a surface site noted "s":

   $H_2 + s \quad H_{2\text{-}s}$

2) Hydrogen dissociation step:

   $H_{2\text{-}s} + s \quad 2\,H_{\text{-}s}$

3) Diffusion of oxygen ions to an interstitial position and the formation of a water molecule:

   $2H_{\text{-}s} + O''_i + 2h^* \quad H_2O + 2s$

4) Interstitial oxygen is transported from the internal to the external surface with at the same time, the electron holes formation and their movement. The electron hole is noted as h* :

   $O''_{i\ int} \quad O''_{i\ est}$; $h^*_{int} \quad h^*_{ext}$

where "ext" represents the external interface and "int" represents the internal interface

5) transformation of CuO into Cu2O

   $2\,(Cu_{Cu})_{CuO} + 2\,(O_0)_{CuO} \quad 2(Cu_{Cu})_{Cu2O} + O''_i + 2h^* + (O_0)_{Cu2O}$

The chemical reactions are characterised by a velocity constant of the elementary step for the direct reaction: k_i and an equilibrium constant K_i. The K_i is the ratio of the velocity constant of the direct (k_i) and indirect reaction (k_{-i}):

$$K_i = \frac{k_i}{k_{-i}} \qquad \textit{Eq 1}$$

For the five reactions can be write constant equilibrium expressions:

$$K_1 = \frac{(H_{2-s})}{p_{H_2} \cdot (s)} \qquad \textit{Eq 2}$$

$$K_2 = \frac{(H_{-s})^2}{(H_{2-s}) \cdot (s)} \qquad \textit{Eq 3}$$

$$K_3 = \frac{p_{H_2O} \cdot (s)^2}{(H_{-s})^2 \cdot (O_i^{"}) \cdot (h^*)^2} \qquad \textit{Eq 4}$$

$$K_5 = (O_i^{"}) \cdot (h^*)^2$$

The reactions velocities are:

$$v_1 = k_1 \cdot p_{H_2} \cdot (s) \qquad \textit{Eq 5}$$

$$v_2 = k_2 \cdot (H_{2-s}) \cdot (s) \qquad \textit{Eq 6}$$

$$v_3 = k_3 \cdot (H_{-s})^2 \cdot (O_i^{"}) \cdot (h^*)^2 \qquad \textit{Eq 7}$$

Conservation of site on the surface:

$$(s)+(H_{-s})+(H_{2-s})=1 \qquad \textit{Eq 8}$$

All velocities reaction must be express as a function of partial pressure of hydrogen and water:

The v_1 must be express as a function of K_i, k_i and the partial pressures:

$$K_3 \cdot K_2 = \frac{p_{H_2O} \cdot (s)^2}{(H_{-s})^2 \cdot (O_i^{"}) \cdot (h*)^2} \cdot \frac{(H_{-s})^2}{(H_{2-s}) \cdot (s)} \qquad \textit{Eq 9}$$

$$(H_{2-s}) = \frac{p_{H_2O} \cdot (s)}{K_2 \cdot K_3 \cdot K_5} \qquad \textit{Eq 10}$$

$$(H_{-s}) = \frac{p_{H_2O}^{1/2} \cdot (s)}{(K_3 \cdot K_5)^{1/2}} \qquad \textit{Eq 11}$$

The equations 10 and 11 are introduce in equation 8 as a condition of site consideration on the surface:

$$(s)\left[1+\frac{p_{H_2O}}{K_2 \cdot K_3 \cdot K_5}+\frac{p_{H_2O}^{1/2}}{(K_3 \cdot K_5)^{1/2}}\right]=1 \qquad \textit{Eq 12}$$

With the value of *s* it is possible to express v_1 as follow:

$$v_1 = k_1 \cdot \frac{p_{H_2}}{1+\frac{p_{H_2O}}{K_2 \cdot K_3 \cdot K_5}+\frac{p_{H_2O}^{1/2}}{(K_3 \cdot K_5)^{1/2}}} \qquad \textit{Eq 13}$$

The same algorithm was made for the v_2 and v_3:

$$v_2 = k_2 \cdot (H_{2-s}) \cdot (s) \qquad \textit{Eq 14}$$

$$(H_{2-s}) = K_1 \cdot p_{H_2} \cdot (s)$$

$$(H_{-s}) = \frac{(p_{H_2O})^{1/2} \cdot (s)}{(K_3 \cdot K_5)^{1/2}} \qquad \textit{Eq 15}$$

Condition of sites conservation on the surface:

$$(s) \cdot \left[1+K_1 \cdot p_{H_2}+\frac{p_{H_2O}^{1/2}}{(K_3 \cdot K_5)^{1/2}}\right]=1 \qquad \textit{Eq 16}$$

$$v_2 = k_2 \cdot K_1 \cdot p_{H_2} \cdot (s)^2 \qquad \textit{Eq 17}$$

The value of v_2 as a function of k_i, K_i and partial pressures of hydrogen and water:

$$v_2 = k_2 \cdot K_1 \cdot p_{H_2} \cdot \left(\frac{1}{1 + K_1 \cdot p_{H_2} + \frac{p_{H_2O}^{1/2}}{\sqrt{K_3 \cdot K_5}}} \right)^2 \qquad \textit{Eq 18}$$

Equation of v_3 as a function of site free on the surface and hole formed:

$$v_3 = k_3 \cdot \left(H_{-s}\right)^2 \cdot \left(O_i^{"}\right) \cdot (h*)^2 = k_3 \cdot \left(H_{-s}\right)^2 \cdot K_5 \qquad \textit{Eq 19}$$

$$K_1 \cdot K_2 = \frac{\left(H_{2-s}\right)}{p_{H_2} \cdot (s)} \cdot \frac{\left(H_{-s}\right)^2}{\left(H_{2-s}\right) \cdot (s)} \qquad \left(H_{-s}\right) = \sqrt{K_1 \cdot K_2} \cdot \sqrt{p_{H_2}} \cdot (s) \qquad \textit{Eq 20}$$

$$\left(H_{2-s}\right) = K_1 \cdot p_{H_2} \cdot (s) \qquad \textit{Eq 21}$$

Condition of sites conservation on the surface:

$$(s)\left[1 + K_1 \cdot p_{H_2} + \sqrt{K_1 \cdot K_2} \cdot \sqrt{p_{H_2}}\right] = 1 \qquad \textit{Eq 22}$$

The value of v_3 as a function of the k_i, K_i and partial pressure:

$$v_3 = k_3 \cdot K_5 \cdot \frac{K_1 \cdot K_2 \cdot p_{H_2}}{\left(1 + K_1 \cdot p_{H_2} + \sqrt{K_1 \cdot K_2} \cdot \sqrt{p_{H_2}}\right)^2} \qquad \textit{Eq 23}$$

The v_3 does not depend on the partial pressure of water.

Symbols

c	-	concentration	(mol/L)
d_{v90}	-	spherical diameter for 90 % of particles in volume	(µm)
d_{v50}	-	average volume spherical diameter	(µm)
d_{v10}	-	spherical diameter for 10% of particles in volume	(µm)
d_{BET}	-	particles diameter calculated by BET	(µm)
E	-	space function	(m^2/mol)
ΔG	-	Gibbs free energy	(J/mol)
h	-	electron hole	(-)
I	-	ionic strength	(Mol/L)
K	-	Scherrer factor of correction	(-)
K_s	-	Solubility constant	((Mol/L)$^{\alpha}$)
k	-	reaction constant	(m/s)
M_i)	-	ion activity	(mol/L)
$[M_i]$	-	ion concentration	(mol/L)
$\{M_i\}$	-	total analytical concentration	(mol/L)
N	-	Number of particles density	(particles/m^3)
n	-	refractive index	(-)
n_0	-	initial number of moles	(-)
n_t	-	number of moles at time t	(-)
P_s	-	Solubility product	((Mol/L)$^{\alpha}$)
p	-	pressure	(bar)
q	-	scattering vector	(nm^{-1})
S	-	supersaturation	(-)
S*	-	reduced supersaturation	(-)
s	-	site of adsorption	(-)
s_0	-	area surface	(m^2)
R	-	rate of transformation	(1/s)
r_0	-	radius	(nm)
t	-	time	(s)
t_n	-	time of nucleation	(s)
t_g	-	time of growth	(s)
T	-	temperature	(K)
U	-	tension	(V)
V	-	Volume	(m^3)

V_m	-	Molar volume	(m^3/mol)
Z_i	-	valency of ion	(-)

Greeks Symbols

α	–	reaction yield	(-)
β	–	width of pic for X rays diffraction	(rad)
γ	–	interfacial tension	(J/m^2)
ε	–	solvent dielectric constant	(-)
θ	–	diffraction angle	(deg)
ρ	–	density	(g/cm^3)
Φ	–	reactivity	($mol \cdot m^{-2} \cdot s^{-1}$)
λ	–	wavelength	(nm)

Abbreviations:

AFM	-	Atomic Force Microscopy
BET	-	Brunauer-Emmett-Teller
DDSA	-	Dodecenyl succinic anhydride
DMP 30	-	2,4,6-tri (dimethylamonimethyl) pHenol
DLS	-	Dynamic Laser Sacttering
GMR	-	Giant Magneto Resistance
HPMC	-	Hydroxypropylmethyl cellulose
HRSEM	-	High Resolution Scanning Electron Microscopy
MNA	-	Methyl Nadic Anhydride
NAD	-	Nitrogen Adsorption Desorption
PAA	-	Poly acrylic acid
PCS	-	Particles Correlation Spectroscopy
PSD	-	Particles Size Distribution
SAXS	-	Small Angle X-ray Scattering
SLS	-	Static Laser Scattering
SSA	-	Specific Surface Area
SEM	-	Scanning Electron Microscopy
TEM	-	Transmission Electron Microscopy
TGA	-	Thermogravimetric analysis
UHV	-	Ultra High Vacuum
XRD	-	X-rays Diffraction

Lucica Cristina SOARE

Av. Davel 21
CH - 1004 Lausanne
June 15, 1977, Romania
Mobile phone: 41 78 832 30 91
E-mail: lsoare@yahoo.com

University Education

2000 - 2004 **PhD Thesis,** Swiss Federal Institute of Technology (EPFL), Materials Science and Engineering, Powder Technology Laboratory, Lausanne, Switzerland "*Precipitation and Transformation of Nanostructured Copper Oxalate and Copper/Cobalt Composite Precursor Synthesis*"

1999 – 2000 **Masters Degree** in Materials Physics, University Paul Sabatier, Toulouse, France, "*Temperature Optimisation of LSMO thin layers, epitaxial with STO and MgO*"

1995 – 1999 **Degree**: Physics and Chemistry , University Dunarea de Jos, Galati, Romania

Professional Experience

2000–2004 **Assistant** at Powder Technology Laboratory, Swiss Federal Institute of Technology (EPFL), Lausanne, Switzerland - Teaching of practical work "Ceramics Processing", Supervision of 4 undergraduate projects:

2002 (6 months), Participation in an **industrial project** between Powder Technology Laboratory and a pharmaceutical company (Germany): "*Crystallisation of **organic** drug substance*"

Languages: French (fluent), English (fluent), Rumanian (mother tongue)

Hobbies: Skiing, Hiking, Classical music

Publications:

J. F. Bobo, Ch. Fery, S. Dubourg, B. Warot, D. Basso, ***C. Soare***, B. Diouf, A. R. Fert, J. C. Ousset, E. Snoeck, Ch. Roucau, " Sputter growth, structural, magnetic, magneto-optic and transport properties of epitaxial oxide thin films an heterostructure for spin electronic", Proceeding, OXSEN, Paris, May 2000

L.C. Soare, P. Bowen, J. Lemaitre, H. Hofmann, M. Pijolat, F. Valdivieso, "Assembly of nanodomain buildings blocks of copper oxalate with a cubic morphology" Proceeding, *Mat. Res. Soc. Symp. Proc.* Vol. 788, 2004 Materials Research Society

Conferences:

Journée de la Société Physique Francaise, Poitiers, France, 23-26 August 2000, poster presentation, D. Harabrovsky, ***C. Soare***, J.F. Bobo, A.R. Fert, J.C. Ousset, " Propriétés magnétiques et magnéto-optiques des filmes minces de LSMO monocristallin",

IUVSTA Workshop of Nanoparticles, Stratford upon Avon, U.K. 8-12 July, 2001, oral presentation, ***L.C. Soare***, N. Jongen, J. Lemaitre, P. Bowen, H. Hofmann, "Precipitation of Copper Oxalate Polycrystalline Particles as a Precursor for Co-Cu magnetic Nanocomposites"

Nanoparticles COST Meeting, Sevilla, Spain, 3-4 October 2002, oral presentation, ***L.C. Soare***, N. Jongen, J. Lemaitre, P. Bowen, C.J.G. Plummer, H. Hofmann, "Precipitation of self-assembly of copper oxalate nanoparticles as a precursor for Co-Cu magnetic nanocomposite"

11th Annual Meeting of Swiss Colloid Group (SGCIS) Nano-and Meso- Particle assembly, Ilford, Marly, Switzerland, 12th March, 2003, oral presentation, ***L.C. Soare***, N. Jongen, P.Bowen, J. Lemaitre, H. Hofmann, "Self-organisation of Copper Oxalate nanoparticles as a Precursor for Cu-Co magnetic nanoparticles"

Euromat, Lausanne, Switzerland, 1-4th September, 2003, oral presentation, ***L.C. Soare***, P. Bowen, J. Lemaitre, H. Hofmann, "Design of magnetic Nanocomposites Assembly of Nanosized Building Blocks"

Materials Research Society (MRS), Boston, USA 1-5th December 2003, oral presentation, ***L.C. Soare***, P. Bowen, J. Lemaitre, H. Hofmann, M. Pijolat, F. Valdivieso "Assembly of Nanodomain Buildings Blocks of Copper Oxalate with a Cubic Morphology"